Experimental Investigation of Electronic and Magnetic Properties of $LaAlO_3$-$SrTiO_3$ Interfaces

Dissertation zur Erlangung des Doktorgrades
der mathematisch-naturwissenschaftlichen Fakultät
der Universität Augsburg

vorgelegt von
Christoph Richter
am 28.11.2012

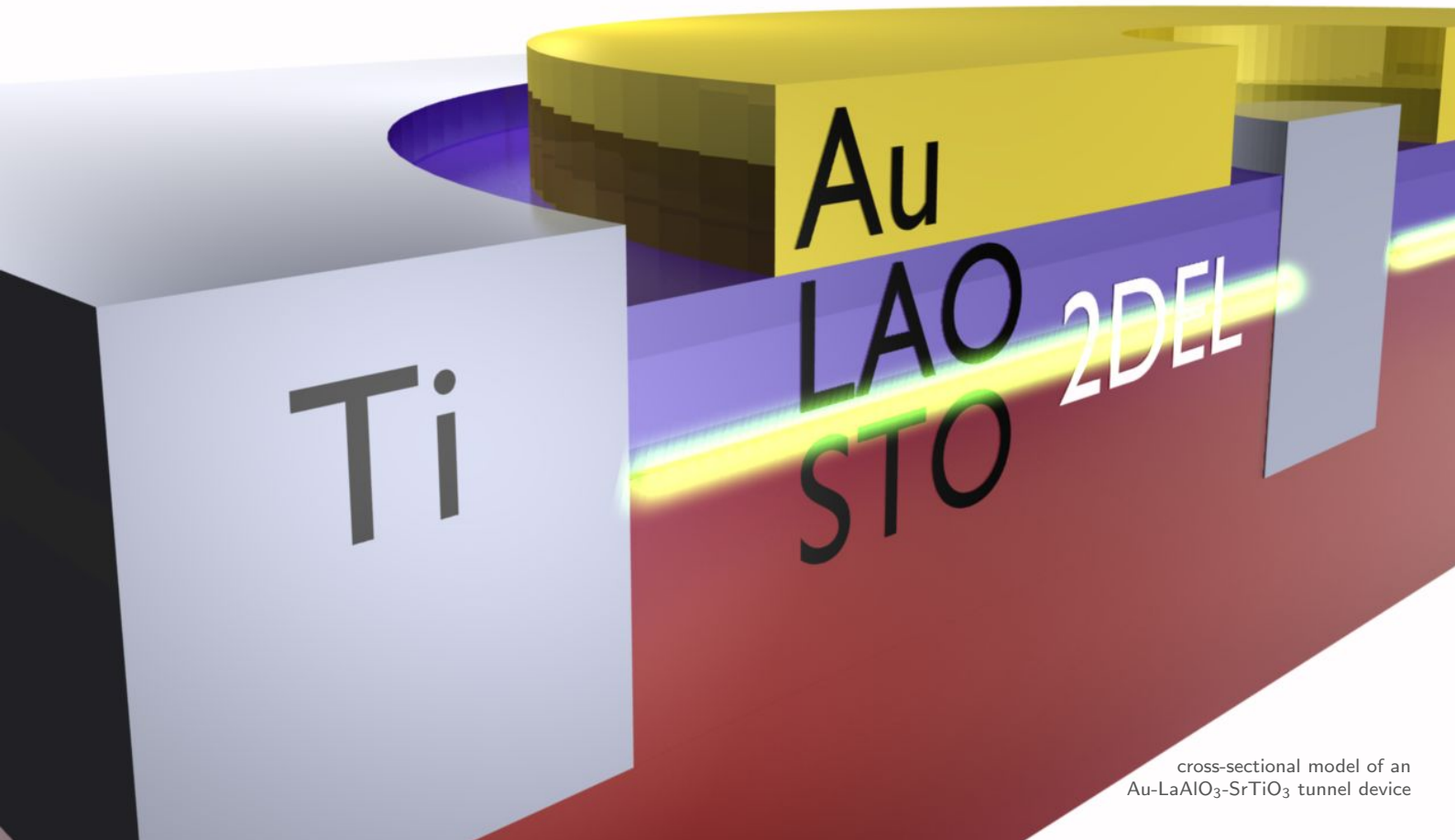

cross-sectional model of an
Au-$LaAlO_3$-$SrTiO_3$ tunnel device

Erstgutachter:	Jochen Mannhart
	(Max Planck Institut für Festkörperforschung, Stuttgart)
Zweitgutachter:	Achim Wixforth
	(Universität Augsburg)

Die mündliche Prüfung fand statt am 8. Februar 2013.

Contents

1. Introduction

This thesis is about interfaces. It compresses and conveys my scientific accomplishments of the past years. In this sense, this thesis in itself is an interface.

Through interfaces we interact, communicate and collaborate. We can thereby achieve feats that for an individual are impossible to attain. This thesis can be taken as an example: I could not have accomplished it without collaborating, without interfacing. It demonstrates how interfaces between individual people can enable something extraordinary.

The material interface that this thesis is about enables something extraordinary, too, phenomena that can be found in neither of its individual components. Superconductivity emerges between insulators. Magnetism is generated between non-magnetic materials. Both effects are found simultaneously in the same system. They characterize the $LaAlO_3$-$SrTiO_3$ heterostructures that I have grown and explored for this thesis. Both effects, and the question how they can coexist, are investigated using cantilever-based torque magnetometry to determine the magnetism, and tunneling spectroscopy to measure the low-energy spectral density of states of normal-conducting and superconducting $LaAlO_3$-$SrTiO_3$ interfaces.

Thesis organization This chapter introduces $LaAlO_3$, $SrTiO_3$ and the basic properties of $LaAlO_3$-$SrTiO_3$ interfaces. The second chapter is concerned with the experimental concept, methods, and the sample fabrication. The third and fourth chapter report and discuss the experimental results of the tunneling spectroscopy and torque magnetometry, respectively. The fifth, final chapter summarizes those results and gives and outlook.

In addition, the appendix contains information regarding possible applications of $LaAlO_3$-$SrTiO_3$ interfaces as field-effect transistors in integrated circuits (Appendix A), as well as extensive experimental results concerning alternative growth procedures and related material systems (Appendix D).

1.1. $LaAlO_3$ and $SrTiO_3$: Two band insulators and their interface

The interface between $LaAlO_3$ (LAO) and $SrTiO_3$ (STO) is at the heart of this thesis. Its exceptional scientific development began in 2004, eight years ago, when Akira Ohtomo and Harold Y. Hwang discovered[25] that the two band insulators can generate a high-mobility electron gas at their interface. This seminal discovery has lead to a plethora of exciting research investigating the origin, physics and potential applications of the two-dimensional electron system.

This introductory chapter will present the bulk properties of $LaAlO_3$ and $SrTiO_3$ as well as additional key features relevant to the LAO-STO interface and this thesis. The requirements for conductivity at the LAO-STO interface will be discussed. These will motivate the prevailing model to explain the phenomenon of a conducting interface between insulating oxides.

1.1.1. $LaAlO_3$: lanthanum aluminate

$LaAlO_3$ is surely the less prominent, less investigated of the two materials. At the same time, though, $LaAlO_3$ is without doubt better understood than $SrTiO_3$. As a single-crystal, $LaAlO_3$ is transparent with a hue of pale pink to russet. It is a non-magnetic (diamagnetic[26]) material.

Crystal structure $LaAlO_3$ is a perovskite. Below 435 °C, the perovskite structure is rhombohedrally distorted, which leads to twinning. At room temperature, a pseudo-cubic unit cell, containing one $LaAlO_3$ formula unit, has a lattice constant of 3.790 Å[27].

Its lattice constant matches that of many high-temperature superconductors. This fact, together with a low dielectric loss and high crystal quality at relatively low costs attainable by Czochralski-growth, made $LaAlO_3$ a popular substrate material[28, 29]. Throughout this thesis, however, $LaAlO_3$ has not been used as a substrate. It was frequently grown as a thin film, though.

Electronic properties Owing to its wide band gap of 5.6 eV[30], $LaAlO_3$ is an electrical insulator[1]. Since its dielectric constant of 24[33] is about 6 times higher than that of SiO_2, it is used as a high-κ oxide. Even in its amorphous state, $LaAlO_3$ retains a high dielectric constant and low dielectric loss, which make $LaAlO_3$ an appealing material as a gate-dielectric in field-effect devices.

1.1.2. $SrTiO_3$: strontium titanate

$SrTiO_3$, which as a substrate is the fundamental building block of $LaAlO_3$-$SrTiO_3$ interfaces, is definitely the more interesting of the two materials. On the one hand, as a

[1] At high temperatures above about 900°, $LaAlO_3$, when doped with Sr or Mg, develops good ionic and electronic conductivity[31] with potential applications in solid state fuel cells[32].

popular substrate it has enabled a tremendous amount of research on all kinds of functional oxide thin-films. On the other hand, it has many unique and interesting properties in itself.

Crystal structure Like $LaAlO_3$, $SrTiO_3$ belongs to the perovskite family. Above 105 K its crystal structure is of cubic symmetry with a room-temperature lattice constant of 3.905 Å[34]. Commercial $SrTiO_3$ crystals are almost exclusively grown by the Verneuil method (flame fusion), which is known to produce crystals of inferior quality compared to e.g. the Czochralski method. Nevertheless, $SrTiO_3$ has gained a great deal of popularity as a standard substrate, in part because of its lattice match to many interesting materials. The other notable reason for $SrTiO_3$'s popularity is a tried and trusted recipe[35, 36] to create a chemically single-terminated $SrTiO_3$ surface. The $SrTiO_3$ crystal lattice can be imaged as a stacking of alternating layers of SrO and TiO_2. The (001) surface of a mechanically polished $SrTiO_3$ substrate contains a mix of both species. If, however, such a substrate is exposed to first water and then buffered fluoric acid (BHF), the SrO dissolves; it is removed from the surface, and only TiO_2 remains. After a high-temperature anneal the substrate surface is structurally and chemically well-defined—a perfect starting point for countless thin-film growth experiments.

Magnetic properties $SrTiO_3$ is non-magnetic. Its magnetic susceptibility is partly diamagnetic and partly (Van Vleck) paramagnetic.[37]

Dielectric properties $SrTiO_3$ has remarkable dielectric properties. It is a quantum-paraelectric, an incipient ferroelectric, which remains paraelectric at all temperatures. $SrTiO_3$ can be driven ferroelectric by very slight alterations of the crystal lattice, e.g. by epitaxial strain[38], nonstochiometry[39] and doping[40] or even by oxygen isotope exchange with ^{18}O[41].

The dielectric constant of pristine $SrTiO_3$ is 300 at room temperature and increases massively, to values exceeding 10000, upon cooling to 4 K[42]. Unfortunately, the technical potential of this very high-κ material, e.g. for energy storage in high-κ capacitors is limited, since the dielectric constant is lowered considerably by the application of electric fields[43].

Semi- and superconducting properties $SrTiO_3$ is a semiconductor with a wide indirect band-gap of 3.2 eV[44]. To that extent, $SrTiO_3$ is comparable to the more familiar semiconducting oxide ZnO (zinc oxide), which has a direct band-gap of 3.3 eV[45]. Like a typical semiconductor, $SrTiO_3$ is susceptible to doping. Substituting La^{3+} for Sr^{2+} or Nb^{5+} for Ti^{4+}, for example, n-dopes $SrTiO_3$ with electrons and eventually renders it metallic. Like in ZnO n-doping in $SrTiO_3$ can also be achieved by removing oxygen from the crystal. This reduction process is often referred to as a doping of the crystal with *oxygen vacancies*: each oxygen atom that is removed from the lattice, leaves behind an oxygen vacancy plus two excess electrons.

Not only is doped $SrTiO_3$ electrically conducting, for an electron concentration between around 5×10^{18} /cm^3 and 5×10^{20} /cm^3, F.R. Schooley, C.S. Koonce and others found the ground state of $SrTiO_3$ to be superconducting[46, 47]. The superconducting transition temperature T_c of reduced $SrTiO_3$ was found to be a non-monotonous function of charge-carrier density with a maximum of around $T_c = 0.3 - 0.4$ K. Whereas from a technological standpoint such a low transition temperature is not too exciting, superconductivity in a semiconducting oxide, especially at such low carrier-densities, was a novelty, a scientific breakthrough. F.R. Schooley's discovery of superconducting $SrTiO_3$ in 1964 thereby surely inspired the search for other superconducting oxides, which finally lead to the seminal discovery of high-temperature superconductivity in the cuprates two decades later by J.G. Bednorz and K.A. Müller.

Besides chemical substitution and oxygen vacancies there is a third route to doping stoichiometric $SrTiO_3$ into a conducting and superconducting state. This route is electrostatic doping utilizing the electric field-effect. In 2008, K. Ueno and his colleagues from Sendai and Tokyo, Japan, demonstrated how electric double layer (EDL) gating can induce sheet carrier densities up to 10^{14}/cm^2 in a pristine $SrTiO_3$ single-crystal.[48] Strikingly, this field-effect doping also turns on superconductivity in the normally insulating $SrTiO_3$.

EDL-gating is a special field-effect setup, by which high electric fields can be applied to the $SrTiO_3$ surface. The working principle is analogous to that of a field-effect transistor (FET), in which a gate-dielectric separates a gate electrode from the transistor-channel. The voltage applied between gate and channel generates an electric field, which penetrates the gate-dielectric and controls the density of mobile charge inside the channel.

In 2004, four years before Ueno's publication, Akira Ohtomo and Harold Y. Hwang published[25] the surprising results of an experiment that conceptually started out very similar to that of Ueno. Instead of using EDL, Ohtomo and Hwang had pursued a traditional field-effect configuration with an undoped $SrTiO_3$ channel and epitaxially grown $LaAlO_3$ as a gate-dielectric.

1.1.3. A conducting interface between two insulators

To their surprise, A. Ohtomo and H.Y. Hwang did not need any gate voltage to turn their $LaAlO_3$-$SrTiO_3$ field-effect devices conducting. In fact, they did not even need a gate electrode. As if the electric field was somehow built into the $LaAlO_3$ thin-film, they found the interface between $LaAlO_3$ and TiO_2-terminated $SrTiO_3$ to be intrinsically conducting. A conducting interface between two band-insulators[25].

Considering the aforementioned doping sensitivity of $SrTiO_3$ to oxygen-vacancies or La, plus the fact that Ohtomo had grown the $LaAlO_3$ films by pulsed laser deposition at a very low oxygen background pressure (10^{-6} mbar), the observed conductivity could in principle have been caused by an unintended doping of the $SrTiO_3$ substrate. Another observation renders this possibility extremely unlikely, though: The interface conductivity depended sensitively on the substrate termination. Only a TiO_2 substrate surface would generate a conducting interface (TiO_2-LaO); if a single unit cell of SrO was inserted between TiO_2-terminated substrate and $LaAlO_3$ film, the samples remained insu-

lating (SrO-AlO_2 interface)[25]. Next to unintended substrate doping, another possible explanation for the n-type conductivity at the TiO_2-LaO interface was the $LaTiO_3$ monolayer, which constitutes the interface between $LaAlO_3$ and TiO_2-terminated $SrTiO_3$. Depending on its exact stoichiometry, $LaTiO_{3+\delta}$ is metallic[49, 50], even ultra-thin layers of $LaTiO_3$ are conducting, at least when they are embedded in $SrTiO_3$[51]. $LaTiO_3$ is present at the TiO_2-LaO interface, but not at the SrO-AlO_2 interface. $LaTiO_3$ therefore lends itself to explain the diametrically different electronic properties of the two related systems.

Critical $LaAlO_3$ thickness

In 2006, an important experimental observation was made by Stefan Thiel and others, which refuted interfacial $LaTiO_3$ as the sole cause for the conducting $LaAlO_3$-$SrTiO_3$ interface: the $LaAlO_3$ thickness is of critical importance for the interface conductivity[52]. Samples with zero, one, or two unit cells (uc) of $LaAlO_3$ grown on TiO_2-terminated $SrTiO_3$ remain insulating. Samples with four or more unit cells generate a quasi two-dimensional electron system like that found by Ohtomo and Hwang. The 3 uc case is special: These interfaces are normally insulating, but can be switched with a gate voltage. The switching between conducting and insulating state is reversible, albeit with a peculiar memory effect[52, 53]. Thiel's observation of a critical $LaAlO_3$ thickness has since been reproduced in numerous laboratories. It proves that the conducting interface can not be explained by a single $LaTiO_3$ unit cell alone: this unit cell exists in $LaAlO_3$-$SrTiO_3$ interfaces of any $LaAlO_3$ thickness $d \geq 1$, but only for $d > 3$ uc is the interface conducting. It cuts the chance that oxygen vacancies might somehow be responsible for the conductivity: the growth process involved in the fabrication of a 4 uc sample is almost identical to that of a 3 uc sample, so both should have the same level of oxygen deficiency. Yet only the 4 uc sample is conducting. The same reasoning applies to the idea that an unintended chemical doping in the form of an intermixing of La and Sr at the interface might be responsible for the conductivity. On the one hand the level of intermixing should be nearly identical for a 3 uc and a 4 uc sample grown under otherwise identical conditions. On the other hand, the growth conditions may vary appreciably between different labs and research groups; yet the same critical $LaAlO_3$ thickness is universally found.

Instead, the critical thickness demonstrates the functional importance of the $LaAlO_3$ on the interface properties and on the emergence of the high-mobility electron system. The "secret ingredient" lies in the $LaAlO_3$ film, not in the substrate. As will be shown, Harold Hwang's and Akira Ohtomo's initial intuition of a built-in electric field in the $LaAlO_3$ is a starting point for the very successful model of an *electronic reconstruction* in response to a polar discontinuity between the polar $LaAlO_3$ and the non-polar $SrTiO_3$. This model will be explained in the following. It was proposed by Ohtomo and Hwang themselves, to explain the observations in their seminal paper[25]. Yet about 8 years and more than 800 citations[54] later, it still stands as the most widely accepted model with the highest level of compatibility among the multitude of experimental facts gained from this fascinating oxide-interface.

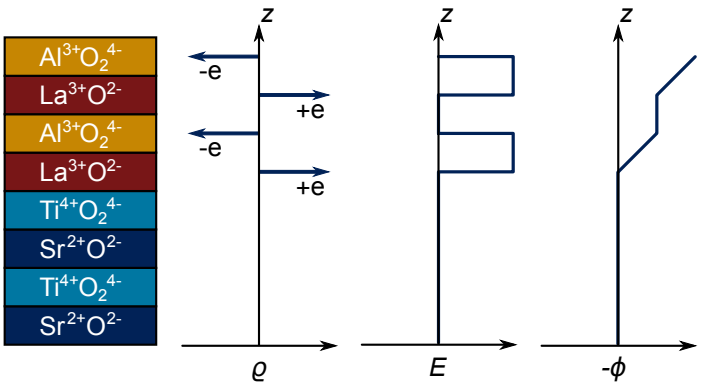

Fig. 1.1: Illustration of the *polar catastrophe* scenario (after Nakagawa et al. [57]). The figure sketches the situation of an unreconstructed $LaAlO_3$-$SrTiO_3$ interface, in which the net charge $\varrho(z)$ of the $(LaO)^+$ and $(AlO_2)^-$ planes of $LaAlO_3$ cause an electric field $E(z)$ and a divergent electric potential $\phi(z)$.

Electronic reconstruction and polar catastrophe

The term "electronic reconstruction" was coined in 2000 by Ronald Hesper, Hao Tjeng, Arend Heeres and George Sawatzky to explain the compensation of a polar (111) surface of K_3C_{60} by an electronic charge rearrangement[55]. In 2004 Satoshi Okamoto and Andrew J. Millis suggested "that this useful phrase be applied more generally to denote electronic phase behavior that is fundamentally different at a surface from in bulk"[56].

In the context of $LaAlO_3$-$SrTiO_3$ interfaces electronic reconstruction explains how a divergent electrostatic potential generated by growing $LaAlO_3$ on a TiO_2-terminated $SrTiO_3$ surface can be compensated by a transfer of half an elementary charge per unit cell towards the interface. The ABO_3 perovskite lattice of $LaAlO_3$ and $SrTiO_3$ is composed of sheets of AO and BO_2, which alternate along the [001] crystal direction. For $SrTiO_3$, these sheets are SrO and TiO_2; both are formally neutral. For $LaAlO_3$, the sheets are $(LaO)^+$ and $(AlO_2)^-$; they both carry a non-zero net charge. Figure 1.1 illustrates this situation, with the polar $LaAlO_3$ adjoining the non-polar, TiO_2-terminated $SrTiO_3$: An electric field E and a diverging electrostatic potential $\phi(z)$ arises from the net-charges of the $(LaO)^+$ and $(AlO_2)^-$ sub-layers. One way to compensate the divergence, the so-called polar catastrophe, is to rearrange the charge-distribution as shown in Figure 1.2. If half an elementary charge per unit-lattice is transfered from the $LaAlO_3$ surface to the $LaAlO_3$-$SrTiO_3$ interface, $\phi(z)$, instead of diverging, oscillates around a finite value. This charge transfer formally changes the valency inside the topmost AlO_2 layer from $Al^{3+}{O_2}^{4-}$ to $Al^{3+}{O_2}^{3.5-}$, and the valency inside the TiO_2 layer at the interface from $Ti^{4+}{O_2}^{4-}$ to $Ti^{3.5+}{O_2}^{4-}$, in turn.

Experimental confirmations of the electronic reconstruction scenario

The electronic reconstruction scenario correctly predicts the interface to be n-type, i.e. the itinerant charge carriers at the interface are electrons. It also sets an upper boundary of 0.5 electrons per unit lattice or about $3.5 \times 10^{14}\,/\mathrm{cm}^2$ on the charge carrier density

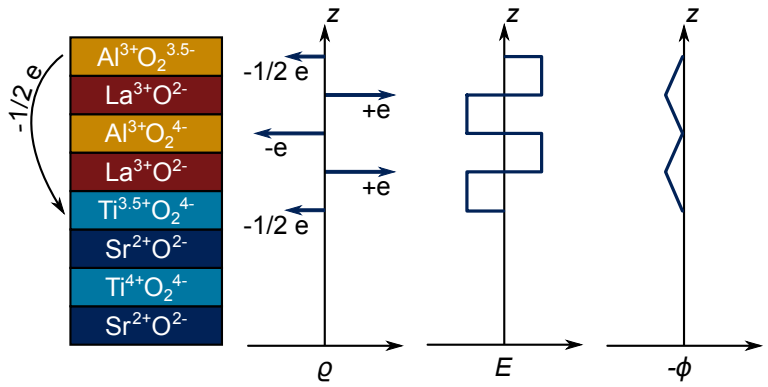

Fig. 1.2: Illustration of an electronic reconstruction to avoid the *polar catastrophe* (after Nakagawa et al. [57]). The figure sketches the situation of a $LaAlO_3$-$SrTiO_3$ interface, electronically reconstructed by the transfer of half an elementary charge e from the topmost AlO_2 layer to the TiO_2 layer at the interface. The net charge $\varrho(z)$ of the $(LaO)^+$ and $(AlO_2)^-$ planes of $LaAlO_3$ cause an electric field $E(z)$ and a finite, oscillating electric potential $\phi(z)$.

expected at an electronically reconstructed interface. Experimentally, the density of *itinerant* electrons at conducting LAO-STO interfaces has been found well below that limit: values of $2 - 4 \times 10^{13}$ /cm^2 have been determined by Hall-measurements on our samples. In collaboration with research groups from Naples, Bonn and Würzburg we were able to verify key predictions of the polar catastrophe scenario (underlined citations denote my co-authored publications):

- The degree of electronic polarization of LAO-STO interfaces rises abruptly as a function of LAO thickness at or around a thickness of 3 uc[6]. This fact has been derived from the non-linear optical response (second harmonic generation) of LAO-STO interfaces and is attributed to the Ti 3d orbitals of the interfacial $SrTiO_3$ layers[12].

- The fraction of Ti^{3+} at the interface increases as a function of LAO thickness. This we have learned from hard x-ray photoelectron spectroscopy[58] and resonant inelastic x-ray spectroscopy[8] at BESSY, Berlin. The amount of charge transferred to the interface, which can be derived independently from both experiments, rises monotonously as a function of LAO thickness d, even beyond $d = 4$ uc. For $d \geq 6$ uc the electronic density settles at around 1×10^{14} /cm^2.

- The electronic reconstruction is accompanied by an orbital reconstruction of the Ti 3d orbitals at the interface. X-ray absorption spectroscopy measurements at the ESRF, Grenoble, revealed that the degeneracy of the 3d orbitals is fully removed.[5]

Magnetism or superconductivity?

A central challenge in understanding the physics at $LaAlO_3$-$SrTiO_3$ interfaces is to identify the magnetic ordering in these two-dimensional electron systems. A closely related question is about the $LaAlO_3$-$SrTiO_3$ interface's electronic ground state.

The latter had been resolved in 2007 in a collaboration with Jean-Marc Triscone's group at the University of Geneva. This pioneering research[3] found a superconducting electronic ground state with a transition temperature of about 200 mK. A superconducting ground state does normally rule out magnetic ordering, so both questions appear to be answered.

A paper also published in 2007, however, gave some evidence for magnetism at $LaAlO_3$-$SrTiO_3$ interfaces[59]. Alexander Brinkman and coworkers from the group of Hans Hilgenkamp at the University of Twente, the Netherlands, had found hysteresis in magnetotransport measurements, and $R(T)$-characteristics reminiscent of the Kondo-effect[60] in $LaAlO_3$-$SrTiO_3$-samples prepared under certain $LaAlO_3$ growth conditions.

Clearly, the two observations are in direct opposition. The magnetic and superconducting samples had been grown under different conditions, though, and neither could magnetoresistive hysteresis be proven for the superconducting samples, nor were the magnetoresistive samples superconducting.

The generally accepted conclusion[61] was that the sample growth conditions had an influence not only on the electronic, but also on the magnetic properties of $LaAlO_3$-$SrTiO_3$ interfaces. Theoretical investigations with density-functional and first-principles methods have given some insights into the possible mechanisms behind magnetic ordering at polar oxide-interfaces[62, 63]. Recently published DFT-calculations[64] could elucidate the role of oxygen vacancies, as they enhance the TiO_2 interface layer's tendency towards ferromagnetism. In lack of experimental data on the occupied part of the $LaAlO_3$-$SrTiO_3$ interface density of states that could be compared to the theoretical results, though, there was no objective criterion to judge the theories' appropriateness. What is more, a direct measurement of the LAO-STO interface's magnetic properties through a direct measurement of its magnetization had not yet been achieved.

2. Experimental concept, methods and setup

The phenomenon of a conducting high-mobility electron system at the interface between two insulators, $LaAlO_3$ (LAO) and $SrTiO_3$ (STO) has triggered a tremendous amount of theoretical and experimental research in recent years. Still, two essential physical properties of LAO-STO interfaces had not yet been explored directly, its magnetic properties and the spectral density of states of its conduction band, which directly governs its electronic properties. The main part of this thesis is going to address these very points.

Magnetism Measuring the magnetic moment of a two-dimensional electron system requires extremely sensitive instruments, because the volume of the investigated system is extremely small: The typical area of PLD-grown $LaAlO_3$-$SrTiO_3$ interfaces is $5\,\mathrm{mm} \times 5\,\mathrm{mm}$. A magnetic moment of one Bohr magneton μ_B on every Ti site at the $LaAlO_3$-$SrTiO_3$ interface would add up to just $1.4 \times 10^{-9}\,\mathrm{Am}^2 = 1.4 \times 10^{-6}$ emu for the whole sample. Currently available commercial superconducting quantum interference device (SQUID) magnetometers top out at a sensitivity of $1 \times 10^{-11}\mathrm{Am}^2$[65]. Such instruments should thus be able to measure the magnetization of LAO-STO interfaces, if the magnetic moment of the interface is sufficiently large ($\gtrapprox 0.1\,\mu_\mathrm{B}$ per Ti-site).

An even more sensitive magnetometry method is cantilever-based torque magnetometry. The technique can resolve magnetic moments on the order of $10^{-12} - 10^{-13}\,\mathrm{Am}^2$[66, p. 62] and is particularly sensitive to anisotropic systems (interfaces). For this technique, the sample to be examined is attached to a cantilever tip. An external magnetic field is applied and interacts with the sample's magnetic moment to develop an aligning torque. When this torque bends the cantilever, the deflection of the cantilever is a measure of the sample's magnetic moment.

In a collaboration with Lu Li and Prof. Ray Ashoori at the Massachusetts Institute of Technology (MIT) we have applied this technique to directly determine the magnetic moment of $LaAlO_3$-$SrTiO_3$ interfaces, which I have prepared in Augsburg.

Density of states The spectral density of states (DOS) can be regarded as the most fundamental property of any electronic system. It is also the pivotal feature targeted in computational material design using, e.g., density-functional theory. There are two well-established experimental methods to access the density of states of a material: tunneling spectroscopy and photoelectron spectroscopy (PES). The buried nature of the LAO-STO interface, which in its conducting state is covered by at least 4 monolayers of $LaAlO_3$, complicates the application of PES to access the interface DOS. Only very recently, exploiting the resonance enhancement at the Ti L edge, could PES, or more specifically soft x-ray resonant PES, be used to map the occupied part of the DOS of LAO-STO interfaces[21].

Tunneling spectroscopy, on the other hand, has previously been successful in mapping the DOS of LAO-STO interfaces[9]. Martin Breitschaft used scanning tunneling spectroscopy (STS) to measure the density of empty states at LAO-STO interfaces in an energy range of about 0.5 eV to 2 eV. His measured spectra coincide nicely with density-functional calculations (LDA+U). The key for the theoretical DOS to match the experimental results in detail is the on-site repulsion parameter U, which semi-empirically introduces electronic correlations into the local-density approximation (LDA). In particular, a pure, mean-field LDA calculation can not reproduce the measured spectra. The authors therefore conclude[9] that the LAO-STO interface is a correlated electron system and should be understood as a two-dimensional electron liquid (2DEL) rather than a two-dimensional electron gas (2DEG). For this reason, the acronym "2DEL" will often be used throughout this thesis to denote the conducting electron system at the $LaAlO_3$-$SrTiO_3$ interface.

Up to present, *scanning* tunneling spectroscopy on LAO-STO has two shortcomings, which I want to address. First, its accessible energy range does not include the occupied and near-Fermi-energy part of the conduction band of the LAO-STO interface; and second, it can not easily be used at temperatures below the superconducting transition temperature ($T_c \approx 200\,\mathrm{mK}$[3]) of LAO-STO interfaces. To extend the energy range accessible by tunneling spectroscopy into the low (mV) and ultra-low (µV) energy range, I have developed solid state planar tunnel devices, which can be used at arbitrarily low temperatures. The development and application of these tunnel devices to access the near Fermi-energy electronic DOS in the normal- and superconducting state of LAO-STO interfaces is the second central subject of this thesis.

Chapter organization The chapter opens with a basic introduction to tunneling spectroscopy and torque magnetometry, the two pivotal experimental methods employed. Next, the conception and design of the tunneling- and magnetometry-samples is discussed. While this point is rather trivial for the magnetometry samples, the proper implementation of planar tunnel devices required intensive planning and preliminary experimentation to succeed. The next section covers the sample preparation. The focus of this section is on the tunneling samples, as these represent a new development. The magnetometry samples need only a subset of the processing steps necessary for the tunnel devices. In the final section, the microstructure of the tunnel junctions and the electronic transport properties of the LAO-STO interfaces inside of tunnel devices are characterized. This preliminary characterization is necessary in order to assess the influence of the newly developed processing steps on the LAO-STO interface.

2.1. Experimental Methods

2.1.1. Sample growth and morphological characterization

I have employed several thin-film growth and patterning techniques to fabricate high-quality $LaAlO_3$-$SrTiO_3$-based samples for this research. These techniques include pulsed laser deposition (PLD) with *in-situ* growth control by reflection high-energy electron diffraction (RHEED) as well as DC- and RF-sputtering for film-growth, photolithography for pattern transfer, and Ar-ion milling for dry-etching. To characterize the surfaces and cross-sections of the grown heterostructures atomic force microscopy (AFM) and scanning transmission electron microscopy (STEM) was used, respectively. Although all of these methods are essential for the presented research, they do not per se represent a novel development of this thesis. A description of these techniques and their application to $LaAlO_3$-$SrTiO_3$ interfaces can be found, e.g., in Stefan Thiel's doctoral thesis[67].

2.1.2. Tunneling spectroscopy

When two materials are brought into close contact, electrons can tunnel in between. Since the tunneling probability depends on the materials' density of states (DOS), their spectral DOS can be derived from an analysis of the tunneling current and its voltage dependency. Tunneling spectroscopy has revealed the gapped quasiparticle density of states of conventional superconductors[68] and thereby confirmed a key prediction of the BCS-theory. It has also disclosed the pseudogap in high-T_c superconductors[69]. Recently, scanning tunneling spectroscopy has been applied to $LaAlO_3$-$SrTiO_3$ interfaces[70, 9, 11], too.

Working-principle

In this thesis tunneling spectroscopy is used as a tool to gain information on the low-energy DOS of $LaAlO_3$-$SrTiO_3$ interfaces in their normal-conducting and superconducting state. The theory and physics behind tunneling spectroscopy will be introduced on a very basic level only. More in-depth information can be found elsewhere[71, 72]. Using Bardeen's transfer Hamiltonian approach (see e.g. Refs. [73], [72, p.768], [74] or [75, p.30]), the steady-state (elastic) tunnel current between two electrodes with their respective electronic densities of states ϱ_l, ϱ_r can be derived and expressed as:

$$I_e(V) = \frac{2\pi \mathrm{e}}{\hbar} \int_{-\infty}^{\infty} \mathrm{d}E \varrho_r(E) \varrho_l(E + eV)[f(E) - f(E + eV)]|\mathcal{M}|^2 \tag{2.1}$$

$f(E) = (1 + \exp \frac{E}{\mathrm{k_B}T})^{-1}$ is the Fermi-distribution at temperature T. The term $[f(E) - f(E + eV)]$ limits the tunneling energy window to a band-width of eV between the electrochemical potential of the left-hand ($\mu_l = \mathrm{e}V$) and right-hand ($\mu_r = 0$) electrode. $\mathcal{M}$ is a tunneling matrix element. $|\mathcal{M}|^2$ measures the transmissivity of the tunnel barrier.

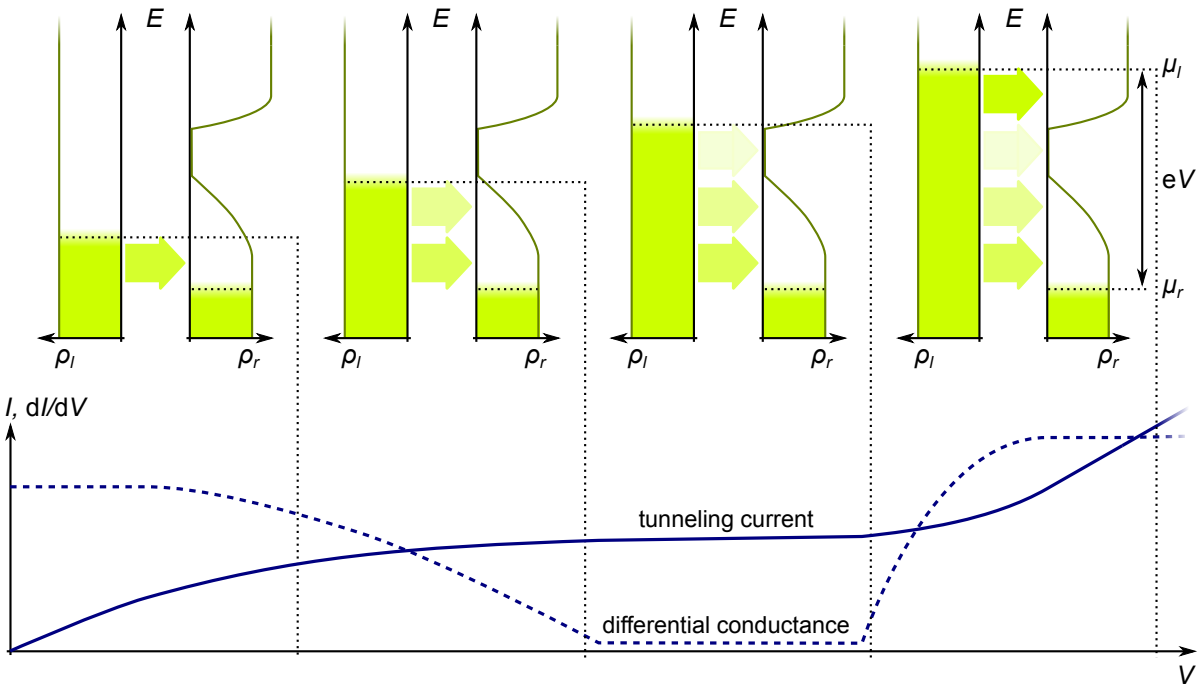

Fig. 2.1: Illustration of elastic tunneling between a metal with constant DOS (left, $\rho_l(E) = \text{const.}$) and a material with arbitrary DOS (right, ρ_r). The electrodes left and right of a tunnel barrier are represented by the graphs $\rho_l(E)$ and $\rho_r(E)$, which indicate their respective DOS (dark green solid line). Occupied states are represented by the bright green filling. A voltage V applied between the electrodes separates the electrochemical potentials μ_l, μ_r by an energy eV. Where occupied states on the left face empty states on the right, elastic tunnel currents flow, which are represented by green arrows. The current density per energy interval depends on $\rho_l(E)$ and $\rho_r(E)$ and is encoded in the arrow color. The $I(V)$ graph sketches the expected current-voltage characteristic and its derivative, the differential conductance.

In tunneling spectroscopy a metal, e.g. in form of an STM tip, is usually used as a probe. The density of states of the tip is often assumed to be constant in the investigated energy range. This case is sketched in Figure 2.1: If one DOS is flat (in this case ρ_l), the voltage derivative of the tunneling current, the differential conductance $\mathrm{d}I(V)/\mathrm{d}V$, is a direct measure of the density of states ρ_r[68]:

$$\frac{\mathrm{d}I_e(V)}{\mathrm{d}V} \propto \int_{-\infty}^{\infty} \mathrm{d}E \frac{-\partial f(E+\mathrm{e}V)}{\partial E} \varrho_\mathrm{r}(E) \approx \int_{-\infty}^{\infty} \mathrm{d}E \delta(E+\mathrm{e}V)\varrho_\mathrm{r}(E) = \varrho_\mathrm{r}(\mathrm{e}V). \tag{2.2}$$

That is, assuming the temperature is sufficiently low to treat the Fermi-function derivative $-\partial f/\partial E$ as a Dirac δ-function. Moreover, the tunnel voltages have to be small, such that ρ_l, ρ_r and $|\mathcal{M}|^2$ are all independent of the applied voltage.

Measurement technique

To acquire $\mathrm{d}I(V)/\mathrm{d}V(V)$ differential conductance spectra, I have employed two different techniques: an AC- and a DC-method.

DC-method The DC-method is to record $I(V)$ characteristics, which are differentiated numerically. The $I(V)$ characteristics can be acquired by either sourcing a voltage and measuring a current, or by sourcing a current and measuring a voltage. Keithley source-measure-units (e.g. models 2400, 2636 or 6430) and self-developed measurement software were used for that purpose. The voltage-source method is expedient, when a fixed voltage or energy resolution with equidistant V-stepping is desired. The current-source method is advantageous for 4-wire measurements, in which separate contacts are used for sourcing current and measuring voltage. There are hybrid solutions in which, e.g., a measured voltage is used as a feedback signal controlling the current source.

The DC-method is simple and reliable. In contrast to the AC-method, it is insensitive to capacitive contributions, if appropriate timing is provided. In principle, its resolution is limited only by the voltage- and current-resolution of the instrumentation used. In practice, though, the numerical differentiation of measured $I(V)$ curves amplifies noise severely. The relative noise in the measured differential conductance is primarily given by the ratio between the noise of the voltmeter δV and the stepping of the voltage sweep ΔV. Consequently, to acquire a meaningful $\mathrm{d}I(V)/\mathrm{d}V$ curve with a relative noise $< 5\,\%$, a stepping $\Delta V > 20\delta V$ is required. The resolution of the DC-method to infer differential conductance spectra is thereby limited primarily by the noise of the used instrumentation.

AC-method The AC-method can be used to directly (without numerical differentiation) measure the differential conductance by measuring the AC-response (e.g. $\mathrm{d}V$) to an AC-excitation (e.g. $\mathrm{d}I$). It is an add-on to the DC-method: a DC-voltage or -current is stepped as described above, but a small AC-voltage or -current is added to the DC-bias. This is best explained for a 4-wire current-based measurement.

A DC current-source provides a bias I_{DC}. An AC current-source is interconnected in parallel, such that an overall current $I(t) = I_{DC} + I_{\mathrm{AC}} \sin(\omega t)$ is sourced through the device under test (DUT). The DUT develops a voltage $V(t) = V_{\mathrm{DC}} + V_{\mathrm{AC}} \sin(\omega t + \Delta\varphi)$ in response. DC- and AC-voltage can be separated and amplified before the measurement by frequency-selective filters (e.g. Stanford Research 550, 560). Lock-in amplifiers (Princeton Applied Research EG&G 5210, Stanford Research 830) were used to record the AC-signal. Their phase-sensitivity and dual-phase capability allows for measuring the capacitive (out-of-phase) and resistive (in-phase) contributions concurrently.

The amplitude of the AC-input represents a small excitation $\mathrm{d}I = I_{\mathrm{AC}}$. The response is the measured AC-signal with amplitude $\mathrm{d}V = V_{\mathrm{AC}}$. This way the AC-method can determine the differential conductance $\mathrm{d}I/\mathrm{d}V = I_{\mathrm{AC}}/V_{\mathrm{AC}}$ directly at each DC-bias step.

The signal-to-noise ratio of the AC-method can be adjusted with the amplitude of the AC input signal. A larger input reduces the relative measurement noise at the expense of spectral resolution, since V_{AC} defines the window size over which the measured

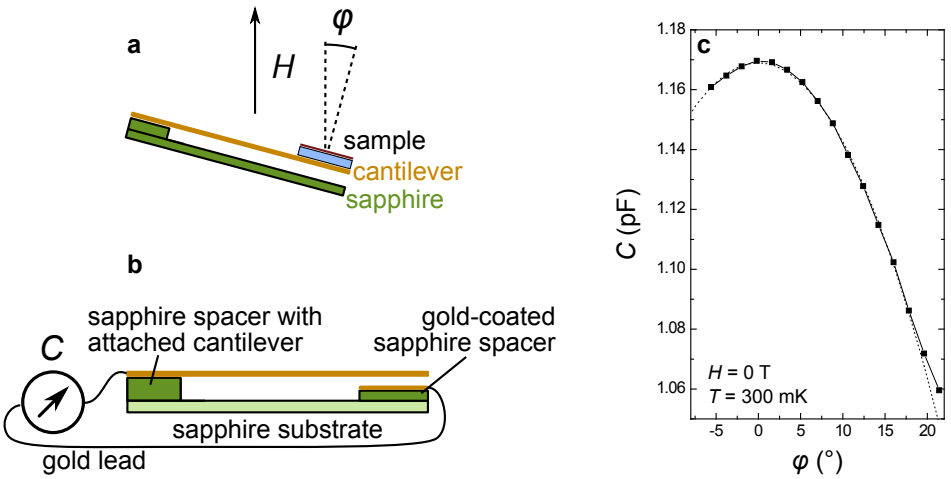

Fig. 2.2: Schematic setup of cantilever-based torque magnetometer (**a,b**) (after Li [66, Fig. 3.1]), and exemplary zero-field ($H = 0$) measurement (**c**) of the capacitance C as a function of tilt angle φ to calibrate the spring constant of the cantilever.

differential conductance is averaged. The AC-method was used for measurements on a µV scale concerning the superconducting state of LAO-STO interfaces, to achieve an improved signal-to-noise ratio as compared to the DC-method. Typical measurement frequencies employed were 8.33 Hz to 133 Hz. See Figure B.1 in Appendix B for typical parameters.

2.1.3. Cantilever-based torque magnetometry

Torque magnetometry measures the magnetic aligning torque $\vec{\tau}$ that develops between an applied magnetic field $\vec{H}$ and the magnetic moment $\vec{m}$ of a sample. This way $\vec{m}$ can be inferred from the measured $\tau(H)$ curves. In the cantilever-based approach we are using, τ is measured as the deflection of a cantilever to which the sample under investigation is attached. The deflection is measured capacitively. The cantilever consists of a gold or brass foil, which is 25 µm or 50 µm thick. The principal setup is sketched in Figure 2.2. The cantilever is mounted above a gold-coated sapphire spacer, from which it is electrically insulated. Cantilever and sapphire surface form a plate capacitor, whose capacitance is a measure of their distance. If the cantilever is bent, e.g. by the gravitational force of the sample mass or a magnetic torque, the deflection can be measured by tracking the capacitance. Capacitance bridges were employed for that purpose. Detailed technical information can be found in Li [66, chap. 3].

To quantitatively derive the torque from a capacitance change, a calibration curve is first recorded in zero magnetic field. The whole setup is rotated, such that the cantilever is bent by the gravitational force of the known mass of the sample. From this measurement the cantilever's spring constant can be derived. An exemplary capacitance C versus tilt-angle φ calibration curve is shown in Figure 2.2c.

When a magnetic field is applied to the setup, a magnetic torque $\vec{\tau}$ develops, which is the cross-product ($\times$) between magnetic field $\vec{H}$ and the sample's magnetic moment $\vec{m}$:

$$\vec{\tau} = \mu_0 \, \vec{m}(\vec{H}) \times \vec{H} \Rightarrow \tau = \mu_0 m(H) H \sin\theta, \tag{2.3}$$

where θ denotes the angle between $\vec{m}$ and $\vec{H}$. Note that the magnetization $\vec{M}$ and thus the magnetic moment $\vec{m}$ itself usually depend on $\vec{H}$. For an isotropic magnetic susceptibility, which is approximately found in many bulk materials, $\vec{m}$ is aligned either parallel (paramagnetic) or antiparallel (diamagnetic) to $\vec{H}$. In such cases the magnetic torque is zero: $\tau = \mu_0 m(H) H \sin 0° = 0$. This fact is highly welcome for interface magnetometry: Although the small volume and magnetic moment of the interface is often negligible with respect to the large volume and magnetic moment of the surrounding bulk, torque magnetometry is most often sensitive to the interface only, because only the interface has an anisotropic susceptibility and magnetization.

2.2. Experimental concept and sample design

This section describes the concept and design of the samples which I have fabricated for the magnetometry and tunneling experiments. Most of this section is concerned with the development of planar tunnel devices for the tunneling experiments, since these are technically and conceptually more complex than the magnetometry samples.

2.2.1. LAO-STO direct magnetization measurement

The cantilever-based torque magnetometry experiments put no special requirements on the sample design. Plain $LaAlO_3$-$SrTiO_3$ samples of our standard size 5 mm × 5 mm × 1 mm can readily be handled in the MIT setup[66]. For electronic transport measurements of the LAO-STO interfaces, small ohmic contacts to the 2DEL were prepared near the sample edges. Niobium (Nb) was chosen as a contact material, as it gives excellent contact to the 2DEL. Neither the paramagnetic susceptibility of its normal-conducting state, nor the diamagnetic contribution of its superconducting state is expected to enter the measurement, since torque magnetometry senses only anisotropic susceptibilities. Its influence can, in principle, be quantified nevertheless by making use of niobium's critical temperature of $T_c = 9.2\,\mathrm{K}$ or its critical field $H_{c2} \approx 0.5\,\mathrm{T}$.

Another important natural prerequisite for LAO-STO magnetometry samples is to exclude any spurious magnetic contributions. Care must be taken, for example, not to contaminate the samples with ferromagnetic materials. To this end, all magnetometry samples have been handled with carbon tweezers only. In some situations direct contact to (stainless) steel, e.g. of the resistive PLD heater or the tip of our wire-bonder, is inevitable. Instead of somehow working around these contributions, e.g. by grinding off the possibly contaminated sample regions, a series of control samples without a 2DEL was grown and treated in exactly the same manner as the investigated LAO-STO samples. The purpose of these control samples was to deduce the magnetization of the $SrTiO_3$ substrate, the contacts, the $LaAlO_3$ film and its surface in addition to spurious sources introduced during the sample processing.

2.2.2. LAO-STO low-energy tunneling spectroscopy

In principle, tunneling as an experimental technique to access the density of states (DOS) of a material is relatively straightforward, both conceptually and from an experimental point of view: Approach the electronic system under investigation with an STM tip, and measure the differential conductance between tip and sample as a function of tip-sample voltage bias. In practice, scanning tunneling spectroscopy (STS) on the LAO-STO interface turned out to be challenging.

My then-colleague Martin Breitschaft pioneered the first such experiments. The big challenge with STS on $LaAlO_3$-$SrTiO_3$ is the 15 Å thick $LaAlO_3$ layer covering the conducting interface. This $LaAlO_3$ thickness, the equivalent of 4 uc, is required for the conducting electron system to be generated at the interface[52].

First, the $LaAlO_3$ film constitutes a natural spacer between the 2DEL and the STM

tip and gives a lower boundary for their separation. For scanning tunneling spectroscopy, 15 Å is a relatively large distance already. Second, the $LaAlO_3$ surface exposes intrinsic as well as extrinsic sources of spurious tunneling signals. The $LaAlO_3$ surface is in between the 2DEL and the STM tip. Electronic surface states may thus have a big impact on the tunneling currents. These surface states might be intrinsic oxygen-$2p$ states of the $LaAlO_3$ surface or result from a molecular surface adsorbate.

Those are the major hurdles for scanning tunneling spectroscopy on $LaAlO_3$-$SrTiO_3$ interfaces. The first limits the spectroscopically accessible voltage range: For voltages below about 0.5 V, tunneling currents are just too small to be detected reliably. The second mainly hampers experimental reproducibility. Extensive surface- and tip-preparation and an ultra-high vacuum STM were employed to counteract adsorbate layers. Nevertheless, in order to distinguish features that are characteristic to the 2DEL from random fluctuations due to $LaAlO_3$ surface states, extensive sets of measurements were required.

2.2.3. Planar tunnel device concept

Both hurdles can be cleared with planar tunnel junctions: The basic idea is to replace the STM tip with a solid, planar metal electrode. The contact area between the planar electrode and the 2DEL is orders of magnitude larger than the point-like STM tip. The area can be scaled to obtain measurable tunneling currents even at very low voltages. By proper *in-situ* processing, the tunnel electrode can be applied directly to the clean, as-grown $LaAlO_3$ surface, thereby avoiding the adsorbate- and surface-state problem altogether.

A welcome additional advantage of planar tunnel junctions over the STM setup is that no moving parts are involved, as all essential functionality can be implemented in the solid-state devices, with multiple devices on a single chip. As a consequence, the tunnel devices can be mounted and investigated in about every imaginable probe or setup from simple bench-top experiments over bath- or flow-cryostats to ^{3}He- and dilution-refrigerators, from vacuum over different gas atmospheres to high-pressure cells, in high-field magnets, x-rays or light. From this tremendous amount of possibilities, the research presented in this thesis concentrates mainly on the temperature degree of freedom. In dilution cryostats, for example, my tunnel devices have been used to learn about the nature of the superconducting state ($T_c \approx 200$ mK) of LAO-STO interfaces.

2.2.4. Tunnel-electrode material constraints

In implementating LAO-STO tunnel devices, the choice of material used for the top electrode is of great consequence.

Chemical compatibility This experiment is designed to investigate the electronic structure of LAO-STO interfaces. Naturally, the top-electrode material must not alter the electronic structure under investigation in any way. The optimal electrode material is

chemically inert; it does not impair the $LaAlO_3$ film or change the oxygen stoichiometry at the $LaAlO_3$-$SrTiO_3$ interface. In this respect, noble metals seem a safe choice.

Epitaxy From a structural point of view, an epitaxially grown electrode material would provide the most well-defined heterostructure. On the other hand, epitaxy alters the strain level inside the $LaAlO_3$ and requires high growth temperatures, which facilitate interdiffusion. Both effects will likely have an impact on the $LaAlO_3$-$SrTiO_3$ interface and its electronic properties and should be avoided. Moreover, possible metallic perovskites like $SrRuO_3$, $YBa_2Cu_3O_7$ or $LaNiO_3$ that could be grown on LAO/STO epitaxially, have a rather complicated band-structure, which would complicate the tunneling spectroscopy data analysis.

Band structure The main objective in developing the tunnel-devices is to study the density of states of LAO-STO interfaces. This is possible because tunneling currents are mainly controlled by a folding of the DOS of the two tunnel electrodes. A featureless, approximately constant spectral density of states inside the top-electrode therefore greatly facilitates disentangling the two DOS contributions and extracting the LAO-STO interface density of states from the measured spectra. Most elementary metals meet that requirement in the targeted energy range.

Patterning While not strictly necessary for the simplest possible device layouts, the ability to pattern (e.g. wet-etch) the electrode material is advantageous. It enables advanced, more practical and closer packed designs, as will be explained in the next subsection. While etching recipes exist for almost any material, not every recipe is compatible with $LaAlO_3$-$SrTiO_3$ interfaces. The etch must not affect the $LaAlO_3$-$SrTiO_3$ interface. Thankfully, $LaAlO_3$ is quite inert against many etchants. But especially for 4 uc thin $LaAlO_3$ layers, the removal of fractions of a unit cell is already detrimental to the interface conductivity. It should be noted that the 4-wire tunnel-device design, which will be introduced in the following, can tolerate relatively high-ohmic "supply conductors", as long as the interface beneath the top-electrode, which is naturally unaffected by etching, is intact.

2.2.5. Tunnel device layout

The device layout is the principle shape of the device, the geometry of the planar tunnel-electrode and the placement of ohmic contacts to the 2DEL. Two principle layouts have been developed and used throughout this thesis, the *circular design*, with ring-shaped tunnel-electrodes and the *linear design*, with a cross-bar like architecture.

The common objective behind both designs is a 4-wire measurement of the tunnel-resistance. To this end, each device has two contacts on the top-electrode, and at least two contacts to the 2DEL, on opposite sides of the tunnel-electrode; "opposite" in the topological sense, that on the sample surface there is no path connecting the two 2DEL contacts, that does not cross the tunnel-electrode. This is sketched in Figure 2.3. The

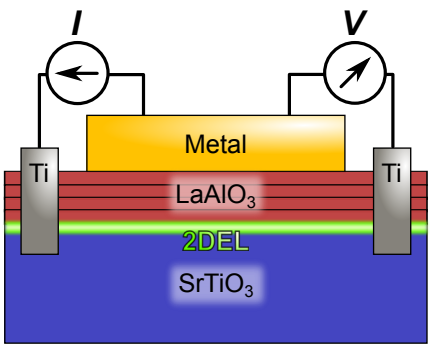

Fig. 2.3: Illustration of the 4-wire design principle of planar LAO-STO tunnel devices. The "Metal" is the tunneling counter-electrode to the 2DEL, to which the Ti plugs provide ohmic contact. Current is sourced from one side of the tunnel junction, voltage is measured on the opposite side to exclude resistive contributions of the 2DEL.

idea is that a current sourced onto the tunnel-electrode from one (e.g. left) side of the junction will eventually encounter the electrical resistance of the 2DEL (and the contact resistance of the ohmic contact). It will therefore generate a voltage drop along its path, before it tunnels through the $LaAlO_3$ into the top-electrode. This voltage drop, plus the actual tunneling voltage, would be measured in a 2-wire measurement, with a voltmeter in parallel to the current source. The voltage between the top-electrode and the other (right) side of the junction, though, is free from any resistive contributions of the 2DEL. This voltage therefore marks the minimum potential difference $\Delta\Phi$ between the two tunnel-electrodes. The aforementioned 2-wire voltage measurement on the left side of the junction limits $\Delta\Phi$ from above. Using a third contact, separate from the current carrying contact, on the left-hand side of the junction, $\Delta\Phi$ can be narrowed down even more, as then the contact resistance of the current-contact does not enter the measured voltage. The 4-wire design enables us to measure the potential difference between the left- and right-hand side of the tunnel junction, which should be negligible for well-defined tunneling spectroscopy. In addition, it provides us with the possibility to do transport measurements of the $LaAlO_3$-$SrTiO_3$ interface covered by the top-electrode. This is necessary in order to judge if the deposition or the existence of the top-electrode impairs the transport properties of the interface, a topic of the next section. Such in-plane transport measurements will furthermore become relevant for experiments with superconducting interfaces.

Circular design

The circular design uses ring-shaped tunnel-electrodes, directly on top of unpatterned $LaAlO_3$-$SrTiO_3$ interfaces. The 4-wire design rule is naturally fulfilled, as a ring naturally separates its outside ("left contact") from its inside ("right contact"). The design is not very demanding: it requires neither a patterning of the conducting LAO-STO interface (i.e. through patterning the $LaAlO_3$ thickness[1]), nor strictly a compatible wet-etching procedure for the top-electrode material, and in principle it can be implemented using only a single lithographic step. In its simplest implementation, an array of rings is transferred onto the surface of an as-grown $SrTiO_3$-$LaAlO_3$-metal sample by photolithography (or even using washers as a hard-mask). An Ar-ion-beam then dry-etches away the metal, the $LaAlO_3$ and a bit of $SrTiO_3$. The ion-milled $SrTiO_3$ becomes

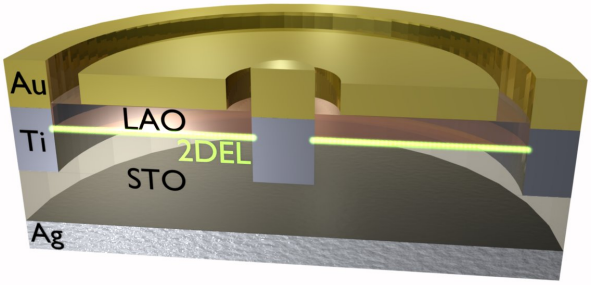

Fig. 2.4: Cross-sectional sketch of a circular tunnel device. The device is comprised of a broad ring-shaped tunnel-counterelectrode with ohmic contact-plugs to the 2DEL (LAO-STO interface) on its outside and inside. The bottom of the STO substrate is covered with silver-paste to be used as a back-gate electrode.

conducting due to the ion-bombardement and creates a good ohmic contact to the 2DEL.

If a compatible chemical etch is available and multiple steps of photo-lithography can be afforded, circular tunnel-devices similar to the cross-section in Figure 2.4 can be created. The figure already reflects the final design and selection of materials for most of the (circular) tunnel-device samples used throughout this thesis. Its simplicity makes the circular design elegant and appealing. It has certain drawbacks, though, which can mostly be overcome with slightly more complicated designs. For example, the ring-shaped tunnel electrodes can not be contacted by wedge-bonding like the ohmic 2DEL-contacts. The $SrTiO_3$-$LaAlO_3$-metal heterostructure is too fragile to sustain the pressure exerted by a wire bonder. Consequently, the rings have to be glue-bonded manually without applying any pressure. This also imposes certain limitations on the scaling of the rings and therefore limits the number of devices per chip.

The design sketched in Figure 2.4 does not allow for 4-wire transport measurements of the Au-covered 2DEL inside the devices. The two contacts inside and outside of the ring allow for 2-wire measurements only.

Linear design

The linear design improves on these points. It is more complicated to implement, as it requires a patterned 2DEL, i.e. the ability to restrict the conducting 2DEL to defined sample areas. Moreover, a way to pattern the top metal contact, e.g. by wet-etching, is mandatory. The basic building block of the linear design is a cross-bar between the 2DEL and the metallic tunnel counter-electrode. A wide 2DEL channel is crossed by a number of relatively narrow top electrodes. These top electrodes begin and end on regions in which the $LaAlO_3$-$SrTiO_3$ interface is insulating. On the insulating regions, the top electrodes can be wedge-bonded safely, as a cracking of the underlying $LaAlO_3$ film does not risk a shortcut to the conducting interface. Inside the regions with conducting 2DEL, in between the top electrodes, a number of pads provides ohmic contact to the 2DEL. They enable 4-wire measurements both for tunneling and in-plane measurements. A true to scale outline of the lithographic design is given in Figure 2.5.

Compared to the circular design, the linear design allows for more closely packed devices of smaller dimensions and thus more devices per sample. In addition, Hall-bars can be implemented on the same chip, which facilitates determining the charge carrier

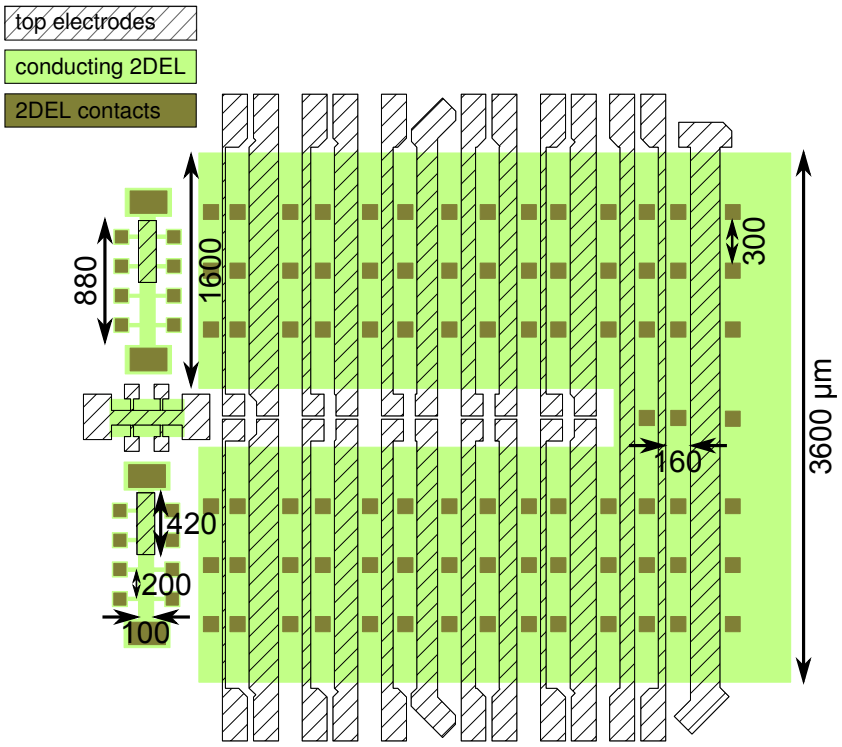

Fig. 2.5: Outline of the linear design for LAO-STO tunnel devices. The areas shaded in green represent conducting LAO-STO interfaces (2DEL). The filled brown rectangles are ohmic contacts, which penetrate the LAO. The striped areas are tunnel-contacts ontop of the LAO film. The dimensioning is given in units of 1 µm. The layout is designed for a 5 mm × 5 mm sample area. The large 2DEL field hosts 23 tunneling cross-bars of varying tunnel-electrode width. Left of that field are Hall-bars for diagnostic purposes.

density of the $LaAlO_3$-$SrTiO_3$ interface. In the design used throughout this chapter, these Hall-bars had open (plain LAO-STO) as well as metal-covered regions, in order to directly compare their electronic properties.

2.3. Sample preparation

This section describes the preparation of the LAO-STO samples as they were used for torque magnetometry and tunneling experiments. As can be anticipated from the experimental concept, the fabrication of tunnel devices involves more processing steps than the fabrication of a plain LAO-STO sample for the magnetization measurements. For the tunneling samples, two different principal layouts, which have been introduced in the previous section, were used. For the tunnel-counter-electrode, overall six different materials have been investigated: $SrRuO_3$, $YBa_2Cu_3O_7$, Au, Co, Nb and Ti. Of these materials, gold has been found to be most practical: Since it is a noble metal, there is no chemical interaction with either $LaAlO_3$ or $SrTiO_3$. It can be deposited by PLD or sputtering and can be patterned with a iodine-based etch, which does not attack the $LaAlO_3$. Co, Nb, Ti and $SrRuO_3$, on the contrary, are difficult to wet-etch, which precludes the linear tunnel-device design. $YBa_2Cu_3O_7$ (YBCO) is easy to etch, but alters the electronic properties of the LAO-STO interface: For YBCO on an LAO film of less than 8 uc, insulating LAO-STO interfaces were obtained. Even with thicker LAO layers, the YBCO has a depleting effect on the LAO-STO interface[76, 16].

As will be shown, Au does not affect the electronic properties of the LAO-STO interface. All of the extensive results following throughout this chapter have been achieved with Au-$LaAlO_3$-$SrTiO_3$ tunnel junctions. The preparation of such Au-$LaAlO_3$-$SrTiO_3$ tunnel devices, starting from a commercially obtained $SrTiO_3$ substrate, will be explained in the following. For plain LAO-STO samples, like those used for torque-magnetometry, only a subset of the preparation steps is necessary.

2.3.1. TiO_2-terminated $SrTiO_3$ substrate

$SrTiO_3$ substrates were bought from CrysTec GmbH, Berlin (Germany). The as-supplied single-crystalline substrates are grown by the Verneuil method, and usually have a single polished (001) oriented surface. The common size of these substrates is $10 \times 10 \times 1\,\mathrm{mm}^3$. In most cases, they were cut into 4 pieces of the more practical size of $5 \times 5 \times 1\,\mathrm{mm}^3$ before further processing. A wire-saw (Well) was used for this purpose. A brushed-on film of photo-resist (AZ®1512 HS) protects the substrate surface from microscopic splinters, which the saw might break off.

The photo-resist and residue of the hot-melt adhesive, which is used to fix the substrate during sawing, are removed from the cut substrates by ultrasonic cleaning in acetone. After another 10 min ultrasonic cleaning step in fresh acetone, the substrates are wiped in isopropanol on soft lens cleaning tissue (Whatman). Finally, the substrates are again cleaned ultrasonically for 2×10 min—first in acetone, then in isopropanol.

At this stage, the sample surface is already very clean and smooth, but chemically not well defined: it is a mix of SrO and TiO_2. To obtain a pure TiO_2 termination, a well established recipe[36] is used, which involves mainly water and buffered fluoric acid (BHF) followed by an annealing step. More information on this recipe and an alternative BHF free procedure can be found in section D.3.

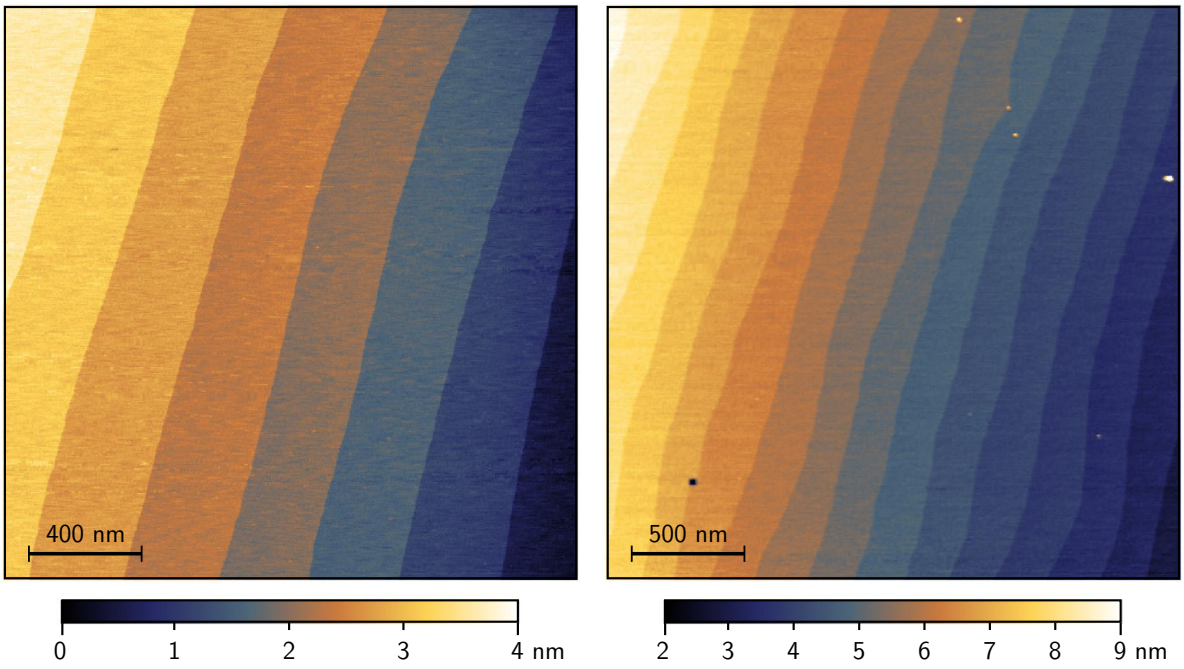

Fig. 2.6: AFM topographic images of typical TiO_2 terminated $SrTiO_3$ substrates. A step-and-terrace like structure with 0.2 - 0.4 µm wide terraces and 0.4 nm high steps is observed. The step height corresponds to one unit cell of $SrTiO_3$ (3.9 Å). Left: standard CrysTec substrate; right: mono-isotopic $SrTi^{18}O_3$.

One sample (T36) is based on a $SrTi^{18}O_3$-substrate of size $5\,\text{mm} \times 5\,\text{mm} \times 0.6\,\text{mm}$. The substrate was obtained from Christof W. Schneider (PSI, Switzerland) and was treated in a special manner, to exchange its natural ^{16}O isotope for the heavier ^{18}O: A batch of substrates was initially bought from CrysTec, annealed at 1100 °C for one week in a $^{18}O_2$ atmosphere to completely exchange the substrates' natural oxygen isotope mixture for ^{18}O. The substrates have then been sent back to CrysTec, where they were polished to achieve an atomically flat (100) surface. Back in Switzerland the substrates received the usual termination procedure[36] (BHF), they were again annealed in $^{18}O_2$ for 7 h at 950 °C. Apart from the isotopically clean oxygen gas, this is the same procedure we use to fabricate TiO_2-terminated substrates. Additional information can be found in Ref. [77].

The surfaces of all of the substrates used have been characterized by atomic force microscopy. Only substrates with high-quality step-and-terrace surfaces, as shown in Figure 2.6 were used to fabricate LAO-STO tunneling samples.

2.3.2. PLD-grown $LaAlO_3$ film

$LaAlO_3$ thin films were grown in our PLD following our usual recipe, which is based on the original works of Stefan Thiel. Detailed information regarding this process can be

found in his doctoral thesis[67]. The substrate was heated to 780°C in 3×10^{-4}mbar of oxygen. The $LaAlO_3$ film was ablated from a single-crystalline target by 450 mJ pulses at a frequency of 1 pulse per second from our KrF-Excimer-Laser ($\lambda = 248$ nm). The background oxygen pressure was 1×10^{-4}mbar during the deposition. The film growth is monitored *in-situ* by reflection high energy diffraction (RHEED). The $LaAlO_3$ thin film grows in the layer-by-layer (Frank-Van der Merwe) growth mode[78, 79]. The growth of every single $LaAlO_3$ monolayer is therefore accompanied by a full oscillation period of the RHEED specular reflection spot. The deposition is stopped after a fixed number of intensity oscillation periods, which corresponds to the desired $LaAlO_3$-thickness. Typical RHEED-patterns and -oscillations during $LaAlO_3$-growth, as well as further information can be found in subsections D.3.3 or D.4.3.

Next, the sample is cooled in an oxygen atmosphere ($p_{O_2} = 400$ mbar), with 2 annealing steps: one at 600 °C for one hour and another one at 420 °C again for about one hour. After the second annealing step, the heating current is normally switched off. In this case, the sample cools from 420 °C to room temperature in the high-pressure oxygen atmosphere, before the PLD is evacuated to unload the sample via our transfer system. At this point, a typical reference $LaAlO_3$-$SrTiO_3$ sample, as it was used for many collaborative projects (section H.1) including the torque magnetometry, would be finished, unless, e.g., interface contacts are required.

If a tunnel-electrode is to be grown on top of the $LaAlO_3$ film, an optimized cooling procedure is employed, to prevent adsorbates on the $LaAlO_3$ surface: With the oxygen pressure still at $p_{O_2} = 0.4$ bar, the sample temperature is first reduced from 420 °C to 360 °C. At this point, the pumps are started and the valves opened to evacuate the PLD chamber. At the same time a constant flow (12 sccm) of high-purity ($10^6 : 1$) oxygen is upheld, that keeps the dynamic oxygen pressure inside the chamber at 0.03 mbar, at minimum. To keep the temperature stable at ≈ 350 °C, the heating current has to be adjusted constantly, as convective heat losses are radically reduced, when the pressure lowers from 10^{+2} mbar to 10^{-2} mbar. After about 1 h of pumping, the sample heating is switched off. The sample then cools freely for at least 1 h (to $T \approx 60$ °C), before the oxygen flow is stopped. In response, the pressure inside the PLD chamber drops to $\approx 3 \times 10^{-7}$ mbar rapidly, which demonstrates the cleanliness of the vacuum chamber.

The technique resembles Martin Breitschaft's sample treatment for STM experiments on LAO-STO interfaces[9]: To achieve reproducible surface conditions after the samples were transferred in air to the preparation chamber of his scanning probe microscope, they were radiatively heated to ≈ 400 °C in an oxygen pressure of 10^{-2} mbar (background pressure $\approx 5 \times 10^{-7}$ mbar).

While this treatment proved to be a necessity for reproducible STM results, one might be inclined to consider it superfluous between the PLD and sputtering steps, because intuitively, the PLD vacuum chamber appears to guarantee a clean atmosphere and inhibit any sample surface contamination. When cooling the sample in 400 mbar of oxygen after the PLD-growth, though, all valves of the PLD chamber are shut. As a consequence, contaminants that inevitably evaporate from the chamber walls are not

pumped off, they accumulate in the oxygen atmosphere. Moreover, even with high-purity oxygen gas, at 400 mbar a purity of $10^6 : 1$ implies a background pressure of at least 4×10^{-4} mbar, which consists mostly of N_2, Ar, CO, CO_2, H_2 and H_2O.[80] The resulting background pressure is thus large with respect to the base pressure of the pumped PLD chamber. A (thin) layer of adsorbents is therefore expected to form on the $LaAlO_3$ surface, if the sample is cooled to room-temperature in the contaminated atmosphere. Pumping the PLD chamber while the sample is hot should counteract the emergence of such an adsorbate layer, as it reduces the background pressure to the base pressure of the system ($\approx 10^{-7}$ mbar) *before* the sample cools to room-temperature.

2.3.3. Patterned $LaAlO_3$-$SrTiO_3$ interfaces

The PLD-process, including the sample heating and cooling, can be repeated to grow parts of the $LaAlO_3$ film in multiple steps. If a hard-mask of amorphous $LaAlO_3$ is applied to parts of the sample before the $LaAlO_3$ is grown beyond the critical thickness of 4 uc, those parts of the sample will stay insulating. We have developed this technique to constrict the conducting interface to select sample areas. A detailed description can be found in Refs. [67, 1, 2].

2.3.4. Sputtered Au top-electrode

Directly after the optimized cooling procedure, the sample is transferred—without leaving the vacuum—from the PLD through our transfer system into the sputter chamber, which is well pumped to a pressure of $p < 10^{-7}$ mbar.

The top-electrode is made by sputtering gold at parameters chosen to impede penetration of high-energetic Au ions into the sample. The sample is relatively cold ($T \approx 50\,°C$), the Ar-background pressure relatively high ($p_{Ar} = 0.1$ mbar) and the RF-sputtering-power very low ($P_{RF} = 10$ W) to keep the bias voltage as low as possible ($V_{bias} = 110$ V). The sample is also kept at a rather large distance from the target ($d \approx 10$ cm). This parameter set results in very low deposition rates: Sputtering for 15 min yields an Au-film thickness of around 30 nm. The sputtered films are semi-transparent, with a dark green tint of the transmitted light. In reflection, the films appear metallic with the familiar golden gloss. Their electrical conductance was verified by 2-wire measurements, with R_s on the order of $1 - 50\,\Omega$.

2.3.5. Au-tunnel-electrode patterning

Defined by photo-lithography, the ring-shaped or linear tunnel-electrode structures are masked by photo-resist. The unmasked part of the Au-film gets etched off by a I_2+KI aqueous solution (I_2:KI:H_2O = 1:4:40), the etching time is 25 s. Previous tests found this etching procedure to not have any measurable influence on the $LaAlO_3$-$SrTiO_3$ interface for $LaAlO_3$-films. Repeated or prolonged etching on samples with 4 uc thin $LaAlO_3$ films can lead to a drastic increase of the interface sheet resistance, though.

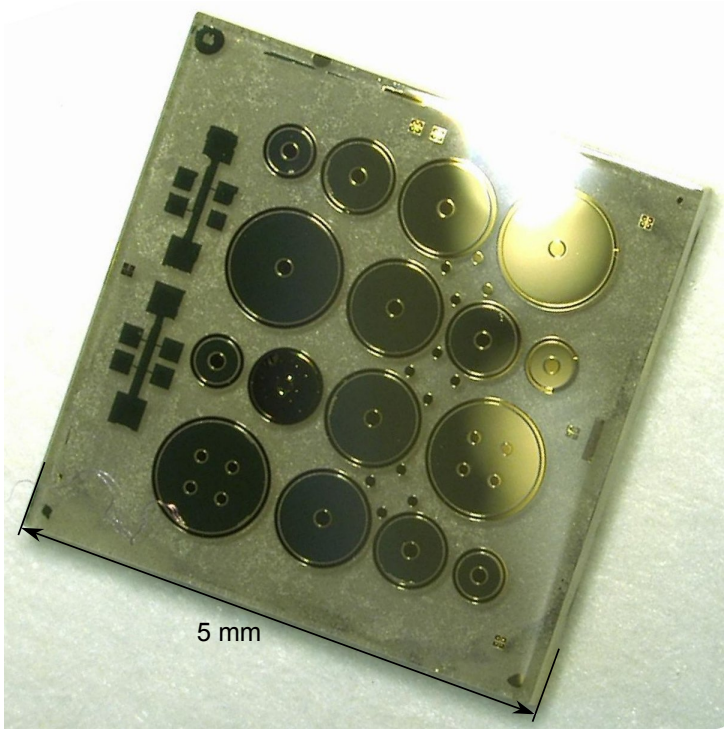

Fig. 2.7: Photo of the finished ring-design tunneling sample T36 (5 mm × 5 mm × 0.6 mm). The transparent crystal is a $SrTiO_3$-substrate covered with four unit cells of $LaAlO_3$. The broad golden rings are tunnel-electrodes made of sputtered Au, on top of the $LaAlO_3$-film. The smaller, slightly darker dots and circles are sunk-in contacts to the $LaAlO_3$-$SrTiO_3$-interface made of sputtered titanium and covered by gold.

2.3.6. $LaAlO_3$-$SrTiO_3$-interface contacts

Another photo-mask defines contacts to the conducting LAO-STO interface. The contact areas are etched by an Ar-ion-beam. The resulting 40 nm deep pits are filled with 20 nm of sputtered Ti ($P_{\mathrm{DC}} = 30\,\mathrm{W}, p_{\mathrm{Ar}} = 0.025\,\mathrm{mbar}, t = 6\,\mathrm{min}$), which is subsequently covered by 150 nm of sputtered Au ($P_{\mathrm{RF}} = 30\,\mathrm{W}, p_{\mathrm{Ar}} = 0.05\,\mathrm{mbar}, t = 4\,\mathrm{min}$). In some cases, notably for all of the magnetometry samples, DC-sputtered Nb ($P_{\mathrm{DC}} = 40\,\mathrm{W}, p_{\mathrm{Ar}} = 0.01\,\mathrm{mbar}, t = 8\,\mathrm{min}$) was used instead of Au/Ti as a contact material. After soaking the samples in warm acetone for at least 30 min, a final lift-off in acetone in an ultrasonic bath takes away the photo-mask alongside the excess metal on it. A photo of a finished sample is shown in Figure 2.7.

2.3.7. Wire-bonding

While the sunk-in interface-contacts can be wedge-bonded, special care must be taken not to compromise the thin and fragile tunnel-junctions. The gold on the thin $LaAlO_3$ film is very soft; a cold-welded wire-bond readily breaks through and creates an electric short to the conducting $LaAlO_3$-$SrTiO_3$ interface. For this reason, at least on the ring-design samples with unpatterned $LaAlO_3$, wires had to be gently attached to these contacts manually with silver-epoxy or conductive silver paint (Figure 2.8). On the linear-design samples with patterned $LaAlO_3$ the tunnel-electrodes can, just like the 2DEL-contacts, be wedge-bonded conveniently: For that purpose, each tunnel-electrode is connected to a bond-pad, which is situated above an insulating part of the $LaAlO_3$-$SrTiO_3$ interface, with less than 4 unit cells of epitaxial $LaAlO_3$. Of course, also in this

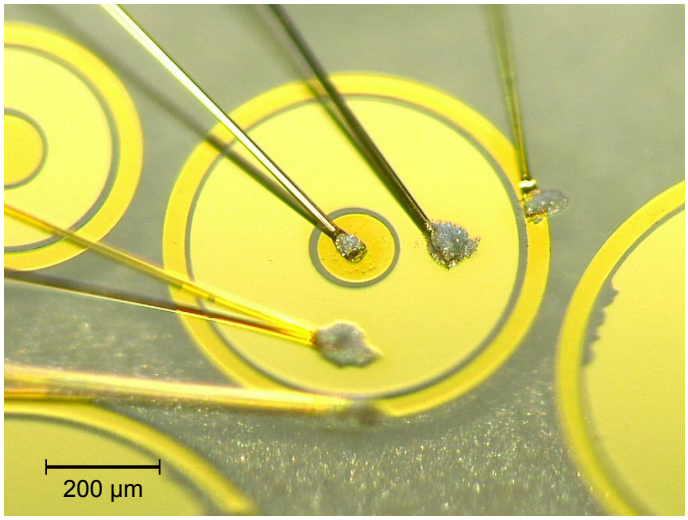

Fig. 2.8: Photo of a wire-bonded circular design ring-shaped tunnel device on sample T36. The broad golden ring is an Au tunnel-electrode on top of a 4 monolayer thin $LaAlO_3$ film. The Au wire-bonds are glued to that electrode (Marion Hagel, MPI). The narrower, slightly darker rings and circles are sunk-in ohmic Ti/Au contacts to the $LaAlO_3$-$SrTiO_3$ interface. They are wedge-bonded.

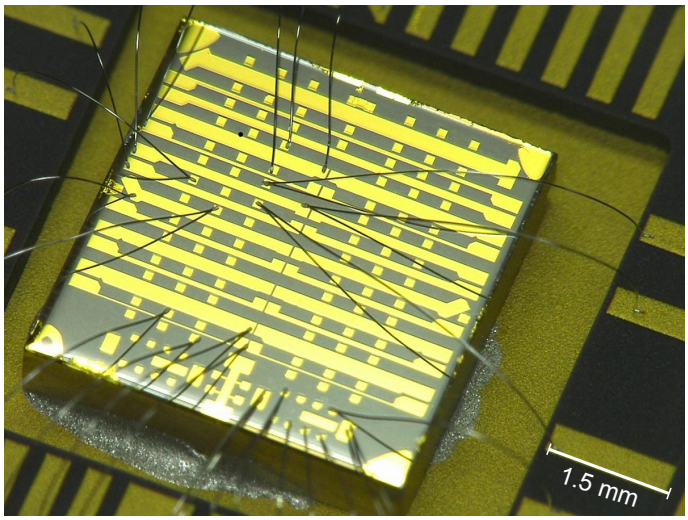

Fig. 2.9: Photo of the linear design tunneling sample T32, glued and wire-bonded to a chip-carrier. The thin, long, golden contacts are tunnel-electrodes on top of the 5 monolayer thin $LaAlO_3$ film. The small, golden squares are sunk-in ohmic Ti/Au contacts to the $LaAlO_3$-$SrTiO_3$ interface. Near the lower edge of the sample, test structures in the form of Hall-bars are located.

case, care must be taken to restrict the bond to the insulating regions in order to avoid an unintended shortcut to the conducting 2DEL. This is complicated by the fact that there is no optical contrast between conducting and insulating regions. A wire-bonded linear-design tunneling sample is shown in Figure 2.9.

2.4. Preliminary characterization of tunnel-junctions

In order to learn from my tunnel experiments fundamental properties of the LAO-STO interface, an important natural requirement has to be met: the tunnel counter electrode must not alter the electronic properties of the LAO-STO interface. Neither the existence, nor the deposition of the electrode material on top of the 1.6 nm thin $LaAlO_3$ layer should have any impact on the properties of the LAO-STO interface.

Two separate effects have to be considered, structural side-effects of the electrode material growth ("collateral damage") and an intrinsic interplay between this material and the electronic reconstruction, which creates the conducting electron system at the interface.

Intrinsic influence Even without an additional overlayer, the $LaAlO_3$-$SrTiO_3$ interface electronic properties react sensitively to the $LaAlO_3$ thickness, below[6, 12] and above[8] the critical thickness of 4 uc[52]. An overlayer on the $LaAlO_3$ surface can alter the LAO-STO interface in many ways:

- A $SrTiO_3$-$SrCuO_2$ overlayer can massively enhance the 2DEG low-temperature mobility[81], enabling the observation of quantum oscillations at the LAO-STO interface[82].
- A $SrTiO_3$ overlayer can reduce the critical LAO thickness[83].
- An $YBa_2Cu_3O_7$ overlayer depletes the interface and increases the critical LAO thickness[76, 13, 16].
- Density functional theory (DFT) calculations[84] predict a metallic overlayer to alter significantly the electric field within the polar $LaAlO_3$ film with significant implications on the LAO-STO interface.

It is therefore mandatory to carefully check the LAO-STO interfaces after the application of the tunnel counter-electrode. This is best done by comparing the transport properties of covered interfaces to that of uncovered regions on the same sample and reference $LaAlO_3$-$SrTiO_3$ samples like the plain LAO-STO samples prepared for torque magnetometry.

Structural side-effects The thin-film growth techniques which are available in our PLD lab are DC- and RF-sputtering and, of course, pulsed laser deposition. These techniques have in common that the target material usually impinges the substrate surface with high kinetic energies. A high kinetic energy enables the ablated ions to be implanted into the sample (possibly near the LAO-STO interface) and to damage the thin $LaAlO_3$ layer. Depending on the substrate temperature, diffusion of the electrode material into the sample is another issue. All of these effects compromise the integrity of the LAO-STO interface and might alter its electronic properties. The best way to check for such effects in my samples is to directly image cross-sections of the grown Au-LAO-STO heterostructure.

2.4.1. TEM results of Au-LAO-STO junctions

A direct method to image the local crystal structure and chemistry at oxide heterostructures with atomic precision is state-of-the-art scanning transmission electron microscopy (STEM). The TEM specimen preparation and microscopy was done mainly by Lena Fitting Kourkoutis at David Muller's group at Cornell University, Ithaca, USA. For this experiment, I grew a large ($10 \times 10\,\mathrm{mm}^2$) Au-LAO-STO sample with a nominal thickness of 5 uc $LaAlO_3$ (as counted from RHEED oscillations). Cross-sections of the Au-LAO-STO heterostructure were prepared using a Focused Ion Beam (FIB). These cross-sections were oriented and scanned in a Nion SuperSTEM. Two of the resulting images, which were acquired in a Z-contrast high-angle annular dark field mode, are shown in figure 2.10. The images present cuts from different positions on the sample, with different crystal orientation. In both images, the $LaAlO_3$-$SrTiO_3$ interface is nicely visible, as the heavy $_{57}$La gives a good contrast over the lighter $_{38}$Sr. Consequently $_{79}$Au appears brightest and takes the yellow band of the false color scale, while $_{22}$Ti and $_{13}$Al appear much darker. The $LaAlO_3$-$SrTiO_3$ interface is quite sharp in both images, with only minimal intermixing of La and Sr. In both images, though, there are 6 (or at least $5\frac{1}{2}$) rows of $LaAlO_3$, whereas only 5 RHEED oscillations have been counted during the $LaAlO_3$ growth. There are two likely explanations for this discrepancy, inhomogeneous $LaAlO_3$ growth and $SrTiO_3$ step-edges.

Inhomogeneous $LaAlO_3$ growth On a $10\,\mathrm{mm} \times 10\,\mathrm{mm}$ large sample, the $LaAlO_3$ growth rate can vary appreciably across the sample surface, because of the limited extent of the PLD plasma plume. The RHEED-oscillations provide a local measure only, the incident electron beam is about 1 mm in diameter. Hence, it is natural to assume a slightly uneven film thickness, which on large samples can vary locally from the nominal thickness counted from RHEED oscillations.

$SrTiO_3$ step edges The $SrTiO_3$ substrates have a polished TiO_2 surface, which is oriented almost perfectly perpendicular to the [001] crystal direction. A slight vicinal angle of $0.1 \pm 0.02°$ results in a step-and-terrace structure on the $SrTiO_3$ surface. The terraces are about 200 nm wide and can be seen in AFM images of the $SrTiO_3$ substrate surface (e.g. Figure 2.6).

The FIB-prepared lamellae have a finite thickness, so they might include a substrate step. This step is then also crossed by the TEM electron beam, which at the $LaAlO_3$-$SrTiO_3$ interface could travel on the $SrTiO_3$ side before the step, and on the $LaAlO_3$ side afterwards. The resulting image would have rows in which La and Sr overlay. In this case La probably dominates the contrast due to its larger Z. The apparent result of this would be one extra La row at the $LaAlO_3$-$SrTiO_3$ interface and, depending on the $LaAlO_3$-Au interface morphology, possibly another La row at the $LaAlO_3$ surface, i.e. between Au and $LaAlO_3$. A close look at the $LaAlO_3$-Au interface in 2.10a indeed reveals an additional darker $LaAlO_3$ layer right below the gold, which could be indicative of a step-edge in the imaged specimen.

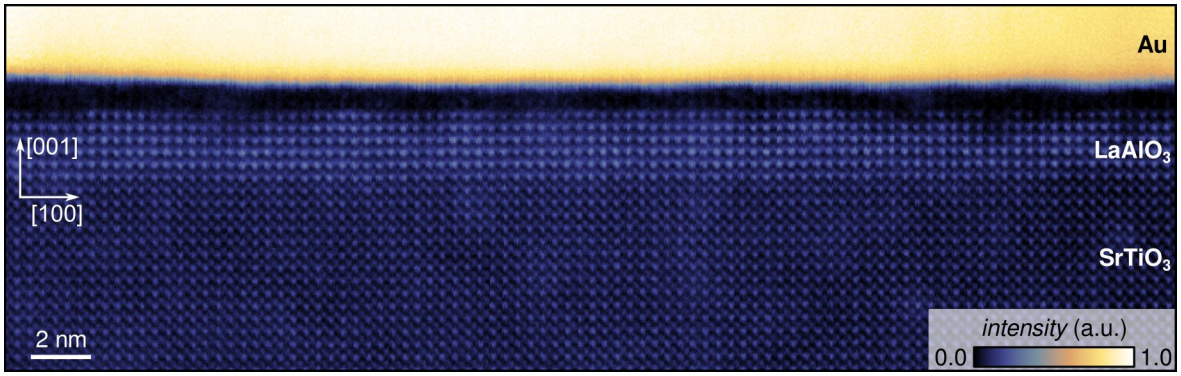

a *Z*-contrast STEM image of Au-LAO-STO heterostructure, with (010) image plane

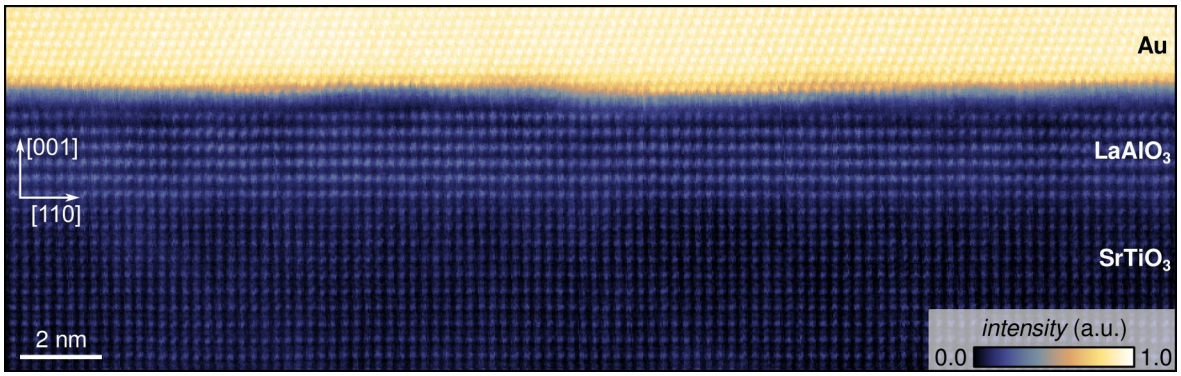

b *Z*-contrast STEM image of Au-LAO-STO heterostructure, with (-110) image plane

Fig. 2.10: *Z*-contrast STEM images of Au-$LaAlO_3$-$SrTiO_3$ heterostructures. The two imaged lamellae are cut from different positions on a sample with a nominal $LaAlO_3$ tickness of 5 uc. They are oriented perpendicular to the [010] **(a)** or [−110] **(b)** direction of the perovskite lattice. (Preparation and microscopy by L. Fitting Kourkoutis, Cornell)

Of the two effects the growth inhomogeneity is probably more relevant than $SrTiO_3$ step edges in this case. Consequently, a possibly inhomogeneous $LaAlO_3$ growth is an error source for the interpretation of tunnel-spectra in the following sections. Since a tunneling current scales exponentially with the inverse tunnel barrier thickness, even a slight inhomogeneity of the $LaAlO_3$ thickness is expected to result in large variations of the tunneling current density across the sample area. As a countermeasure, samples of $5 \times 5\,\mathrm{mm}^2$ or smaller, for which the expected inhomogeneity is only fractions of a unit cell, were manufactured for tunneling experiments.

The principle motivation for the TEM investigation of my Au-LAO-STO tunnel junctions was to ascertain, if the Au deposition process impaired the $LaAlO_3$ film structurally. While the TEM images have revealed imperfections in the form of a possibly inhomogeneous $LaAlO_3$ thickness and a disorder layer of variable thickness at the $LaAlO_3$-Au interface, the $LaAlO_3$ film and the $LaAlO_3$-$SrTiO_3$ interface were both found to be pristine. No pinholes penetrating the $LaAlO_3$ layer have been observed. Hence, the structural requirements of the tunnel-junction experimental concept are fulfilled.

2.4.2. Normal conductivity of Au-covered LAO-STO interfaces

A characteristic property of conducting LAO-STO interfaces is their sheet resistance R_s and its quadratic temperature dependence $R_\mathrm{s} \propto T^2$. The sheet resistance of Au-covered $LaAlO_3$-$SrTiO_3$ interfaces, when prepared according to the recipe given in the previous section, was identical to that of standard, plain $LaAlO_3$-$SrTiO_3$ interfaces. Figure 2.11 shows a typical $R(T)$ characteristic of a gold covered LAO/STO Hall-bar (outline in Figure 2.5. It features the familiar parabolic $R \propto T^2$ shape, at least for $T < 200\,\mathrm{K}$. The sheet resistance is $0.24\,\mathrm{k\Omega}$ at $4.2\,\mathrm{K}$ and $8.2\,\mathrm{k\Omega}$ at $200\,\mathrm{K}$; a quadratic fit to the data at $T < 200\,\mathrm{K}$ extrapolates to $18\,\mathrm{k\Omega}$ at $300\,\mathrm{K}$.

For $T > 200\,\mathrm{K}$ the curve changes slope and flattens. This effect is not intrinsic to the LAO-STO interface and disappears, when the voltage drop across the Au-covered interface channel is limited to a few millivolts, i.e. smaller currents or larger aspect ratios (wider channels) are used. The flattening is due to the current taking a shortcut over the gold electrode covering the Hall-bar. The resistance of the gold itself can be neglected, the asymptote which the sheet resistance approaches at high T is therefore given by about twice the (highly non-ohmic) tunnel resistance: Before crossing any of the remote voltage contacts, the current tunnels from the 2DEL into the gold, flows through the gold traversing the voltage contacts before it tunnels back into the 2DEL.

This way, the gold effectively shunts the $LaAlO_3$-$SrTiO_3$ interface, but only as long as the interface resistance is larger than the tunnel resistance. Because of the exponential $I(V)$ characteristic of a tunnel contact, this condition applies at high voltages in general, and high temperatures (high LAO-STO sheet resistance) in particular.

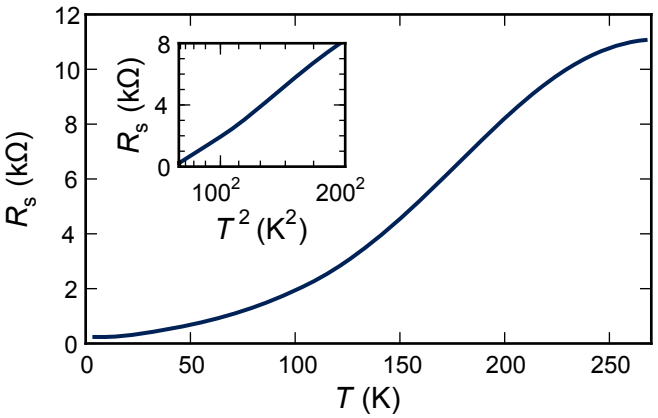

Fig. 2.11: Temperature dependence of sheet-resistance $R_s(T)$, measured on a Au-covered LAO-STO Hall-bar on a linear tunnel device sample with 4 uc of patterned $LaAlO_3$. For $T < 200\,K$, $R \propto T^2$, as is demonstrated by the $R_s(T^2)$ plot in the inset. For $T > 200\,K$ the resistance of the interface becomes comparable to the tunnel-resistance; the Au cover becomes an alternative current path and limits the measured resistance to approx. twice the tunnel resistance.

2.4.3. Transport properties at millikelvin temperatures

Since one of the major objectives behind developing the tunnel devices was to investigate the two-dimensional superconducting state at LAO-STO interfaces, their transport properties were investigated in dilution cryostats with base-temperatures of $30 - 50\,mK$ at the University of Geneva and the Max-Planck-Institute for Solid State Research in Stuttgart.

At millikelvin temperatures, samples with patterned $LaAlO_3$ turned out to be different from samples with unpatterned $LaAlO_3$. In contrast to unpatterned circular design samples, a number of patterned linear-device tunnel samples have been found to be not or only partially superconducting. I used the partially Au-covered Hall-bars of one 5 uc sample, to compare the transport properties of Au-covered LAO-STO interfaces to that of uncovered, plain LAO-STO interfaces. At 0.3 K, in the normal conducting state, the sheet resistances of covered and uncovered regions were practically identical. At base-temperature, though, the regions differed: the half not covered by gold clearly had superconducting properties, the Au-covered half was still normal conducting. Figure 2.12 displays these measurements, which were done on a double Hall-bar with 4 contacts lined up equally spaced along either side of the bar's long edges, half of which (lengthwise) is covered by Au. An explanation for the different behavior of covered and open interfaces could only be guessed at this point; out of 3 patterned linear device samples tested at millikelvin temperatures, none had a superconducting interface beneath their Au electrodes.

Unpatterned samples using the circular design were found to be less delicate: All 3 samples that I have tested were superconducting. An obvious difference between the circular- and linear-device samples, which might affect the interface, is the one-step growth of $LaAlO_3$ without the intermediate patterning step[1] needed for the linear design. Another subtle difference lies in the substrate: Only for patterned samples, alignment markers, defined near some of the sample edges by conventional photo-lithography, are ion-milled into the as-bought substrates. This processing step takes place before the initial thorough cleaning and polishing, but might still be detrimental to the substrate surface quality.

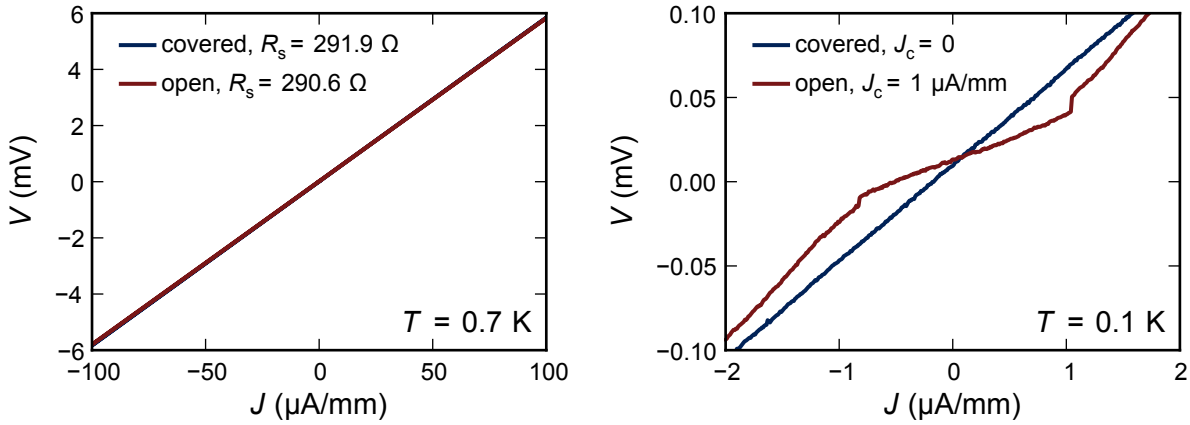

Fig. 2.12: Low-temperature current-voltage $V(I)$ measurement on a double Hall-bar on T32, a linear tunnel device sample with patterned 5 uc of $LaAlO_3$. One half of the Hall-bar is covered by Au (blue curves), the other half is plain LAO-STO (red curves). At 700 mK the resistivity of both halves is identical to within 0.5 % (left graph), but only the uncovered region is superconducting at $T \lessapprox 100$ mK (right graph).

The circular tunnel devices have one major flaw over the linear device samples: inside the ring-shaped devices no 4-wire measurement of the in-plane interface conductivity can be made, because each device has two contacts to the 2DEL only (see e.g. Figure 2.4 and Figure 2.7). Inside of the devices, one therefore has to resort to 2-wire transport measurements.

For 4-wire measurements, the samples feature dedicated structures with 4 small contacts arranged on a square (shown, e.g. in Figure 2.7) in Au-covered, as well as in open regions. Such contacts were used for $R(T)$ measurements and to determine critical currents, as shown in figure 2.13. The $R(T)$-measurements in that figure show a clear superconducting transition for both Au-covered and uncovered sample regions. The 4-wire $V(I)$ measurements in Figure 2.13 provide further prove, that open (2.13b) as well as Au-covered (2.13e) sample regions are superconducting. Most importantly, 2-wire measurements directly inside the circular tunnel devices exhibit very similar $V(I)$ characteristics, when the resistive contribution of the leads, electronic filters and contacts is subtracted (2.13c,f). While such 2-wire measurements can never prove a zero-resistance state directly, they provide very strong evidence and allow for the extraction of a critical current.

With $T_c \approx 100$ mK, the critical temperature of both samples is low compared to the value of $T_c \approx 200$ mK reported by Nicolas Reyren et al.[3]. The lower T_c is not necessarily connected to the additional sample processing imposed by the Au overlayer. Similarly low critical temperatures were also found in other (plain) LAO-STO samples, which others or myself have recently grown in our PLD. In particular, LAO-STO samples grown for the torque-magnetometry[14] collaboration had a critical temperature of about 120 mK. For this reason, the T_c spread is most likely attributed to a drifting quality of

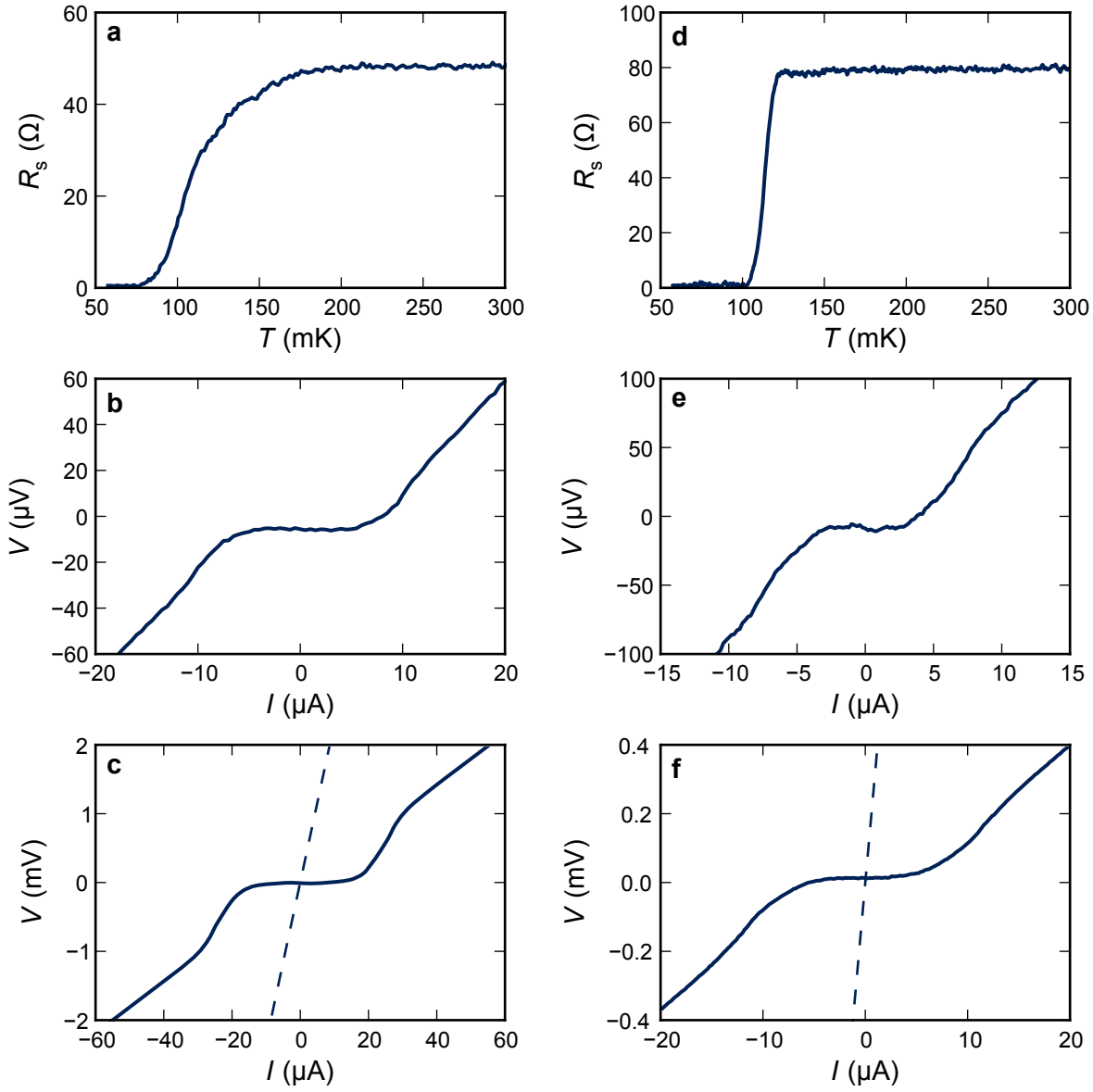

Fig. 2.13: Low-temperature transport data of two LAO-STO samples with circular tunnel devices (unpatterned 4 uc $LaAlO_3$). Left column **(a-c)**: $LaAlO_3$-$SrTi^{18}O_3$ sample T36, right column **(d-f)**: $LaAlO_3$-$SrTi^{16}O_3$ sample T41. **(a,d)** sheet resistance R_s vs. temperature T, **(b,e)** 4-wire *V(I)* measurements, both measured on a square arrangement of 4 contacts. In **(a,b)**, the probed region was the plain LAO-STO interface, in **(d,e)** it was covered by Au. **(c,f)** 2-wire *V(I)* measurements along the LAO-STO interface in circular tunnel devices. Linear *V(I)* functions, which are represented by the dashed lines, were subtracted from the data to account for the cable- and contact-resistances.

the $SrTiO_3$-substrates or our $LaAlO_3$-target or a drifting $LaAlO_3$ stoichiometry due to variations of the oxygen pressure, laser fluence and the geometric arrangement between target, plume, and substrate.

2.4.4. Conclusion

The decisive point, which the preliminary characterization of my tunnel junctions should clarify, was if the a posteriori deposited Au electrode or its deposition process would alter the $LaAlO_3$-$SrTiO_3$ interface in a measurable way. A state-of-the-art atomic resolution STEM characterization found the LAO-STO microstructure in a pristine shape. So the Au sputter deposition, which was intentionally tuned to be most gentle, fulfilled its requirements and did apparently not impair the thin $LaAlO_3$ film.

Electrical transport measurements along the Au-covered $LaAlO_3$-$SrTiO_3$ interfaces gave the typical values of sheet resistance with its typical quadratic temperature dependence. In most situations, the sheet resistance of uncovered sample regions was quasi indistinguishable from that of nearby Au-covered interfaces.

The superconducting properties of Au-covered LAO-STO interfaces are a more complex issue. Here, samples with patterned $LaAlO_3$ (linear design) and Au were found to not become superconducting, at least not below the Au electrodes. Unpatterned samples (circular design) were superconducting, albeit with a relatively low critical temperature ($T_c \approx 100\,\mathrm{mK}$). A similarly low critical temperature was measured in plain LAO-STO samples, which I have fabricated for torque magnetometry measurements.

With no collateral influence of the Au electrode on the properties of LAO-STO interface under test, tunneling spectroscopy with planar Au-$LaAlO_3$-$SrTiO_3$ tunnel junctions can be regarded as a local probe technique, just like *scanning* tunneling spectroscopy. Consequently, the tunnel spectroscopy that I am going to present in the following sections is going to explore the native electronic system at $LaAlO_3$-$SrTiO_3$ interfaces. In particular, the same electronic system will be investigated with tunnel spectroscopy and torque magnetometry.

3. LAO-STO tunneling spectroscopy

This chapter reports on the experimental results achieved using the Au-$LaAlO_3$-$SrTiO_3$ tunnel devices, whose concept, fabrication, and preliminary characterization has been described in the previous chapter. The experiments are categorized and sorted by their voltage- or energy-scale into three separate sections covering the µV, the mV, and the V range. In the microvolt range the quasiparticle density of states of superconducting LAO-STO interfaces is explored. In the millivolt range the normal-state sub-band structure near the Fermi-level is investigated. In the 1 volt range the aim is to reproduce the previous scanning tunneling spectroscopy results of M. Breitschaft et al.[9].

The reason for sorting the experiments in ascending order of their tunneling voltage is that with increasing tunneling voltage the interpretation of the respective tunnel spectra becomes increasingly complicated as well. On a microvolt scale the tunnel spectra can be interpreted quite directly as a DOS. On a millivolt scale inelastic tunneling and tunnel barrier effects become apparent. On a volt scale in addition to barrier effects the resistance of the 2DEL at the LAO-STO interface impedes exact tunneling spectroscopy. The chapter closes with a brief summary of the results.

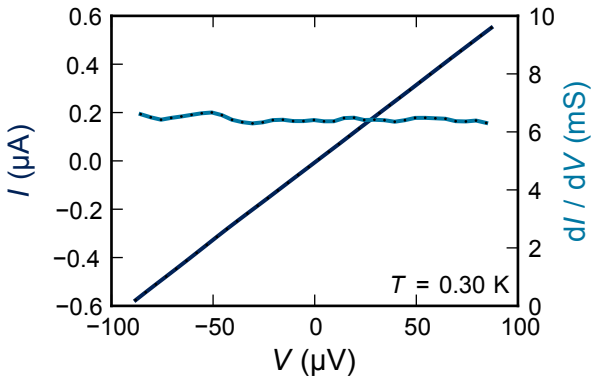

Fig. 3.1: Current-voltage-characteristic $I(V)$ and its first derivative $\mathrm{d}I(V)/\mathrm{d}V$ of an Au-$LaAlO_3$-$SrTiO_3$ tunnel junction, measured at 0.30 K. The voltage V is the voltage on the Au electrode, with respect to the LAO-STO 2DEL at ground potential $V = 0 =: V_{2DEL}$.

3.1. Tunneling on a microvolt scale: the superconducting gap

This section is about my tunneling experiments on Au-$LaAlO_3$-$SrTiO_3$ tunnel junctions at millikelvin temperatures, on a sub-millivolt voltage scale. On a microvolt scale, tunneling spectroscopy is not expected to yield interesting features on most any material. This is because for such small voltages the tunneling probability is determined by the density of states only and on a µeV energy scale, the density of states of any material is usually constant, to a very good approximation.

As shown in Figure 3.1, $LaAlO_3$-$SrTiO_3$ interfaces are no exception in this respect. At 300 mK the (4-wire) $I(V)$ characteristic of an Au-LAO-STO tunnel junction is strictly linear. Its derivative $\mathrm{d}I(V)\mathrm{d}V$, the differential conductance, which is a direct measure of the density of states, is nearly constant.

It is the superconducting state that makes µV-scale tunneling spectroscopy interesting. The critical temperature of the two samples investigated is about 100 mK, which equates to a thermal energy of $k_B T_c \sim 10\,\mu eV$. 10 µV therefore gives the tunneling voltage scale on which to expect the pairing energy, the energy gap of the two-dimensional superconducting state. At such voltages, the differential conductance, which is either measured directly with a standard (AC) lock-in method, or derived from DC $I(V)$ measurements numerically, can usually be interpreted directly as the density of states[68, 85]: On this energy scale, the tunnel-matrix $\mathcal{M}$ and the density of states of gold ϱ_{Au} are constant, and so is ϱ_{2DEL}—for normal conducting LAO-STO.

3.1.1. Temperature dependence of tunnel spectra

This changes substantially, when the sample is cooled below 300 mK. Figure 3.2 shows, how a gap in $\mathrm{d}I(V)/\mathrm{d}V$ develops at about 280 mK, and deepens upon further cooling. This gap is the signature of the two-dimensional superconducting state at the LAO-STO interface. It is only below approximately 150 mK, though, that the distinctive feature of a superconducting gap, its coherence peaks, are discernible.

The BCS-theory[86] predicts an energy gap Δ for the excitation of individual electrons from the superconducting ground state. The characteristic quasiparticle density

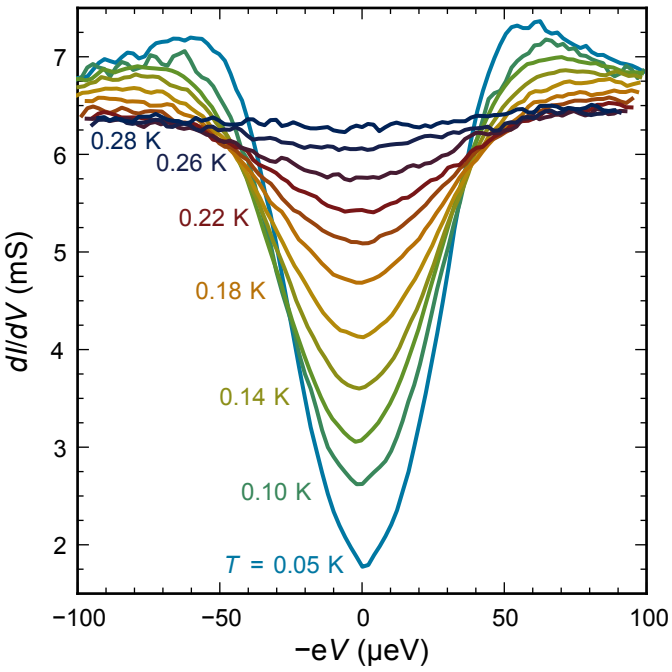

Fig. 3.2: Evolution of $\mathrm{d}I(V)/\mathrm{d}V$ tunnel-spectra as a function of temperature. The data were derived by differentiating numerically the average of sets of 4-wire $V(I)$ measurements on a 0.26 mm^2 large circular tunnel junction.

of states, with an energy gap of width 2Δ around the Fermi energy is:

$$\varrho(E) = \Re\frac{E}{\sqrt{E^2-\Delta^2}} \tag{3.1}$$

The expression is 0 for $|E| << \Delta$ and 1 for $|E| >> \Delta$. It is singular at $E = \pm\Delta$, the edges of the gap. At these edges, the states missing inside the energy gap collate. They form the so-called coherence peaks at $E = \pm\Delta$.

Obviously, the measured $\mathrm{d}I/\mathrm{d}V$ spectra do not feature any singularities. The peaks at $\approx \pm 50\,\mu\mathrm{eV}$ are not as sharp, and even at low temperatures the curves are not as box-shaped as the BCS-prediction. Instrumental broadening, which is estimated to be less than 5 µV in all the spectra shown[1], does only account for small parts of the overall broadening. Two effects have to be considered to develop the BCS gap-equation 3.1 into a model that fits the measured data reasonably well.

Finite lifetime effects In tunneling experiments on the strong-coupled superconductor $Pb_{0.9}Bi_{0.1}$, R. C. Dynes, V. Narayanamurti and J. P. Garno encountered a similar discrepancy[87]. They interpret the coherence-peak "broadening as due to finite-lifetime effects of the quasiparticles at the gap edge, and (...) analyze the data (...) by introducing lifetime effects into the density of excitations." They do this by adding an imaginary

[1] In DC-measurements the measured $V(I)$ data with a voltage resolution better than 2 µV was binned into an equally spaced V-grid by (re-)sampling the data with a Gaussian window of at most 5 µV FWHM. In AC-measurements the AC input current was adjusted prior to each measurement to keep the 4-wire AC voltage at the tunnel device below 3 µV (rms).

part $\mathrm{i}\Gamma$ to the energy $E \to E - \mathrm{i}\Gamma$,

$$\varrho(E,\Gamma) = \Re\frac{E - \mathrm{i}\Gamma}{\sqrt{(E-\mathrm{i}\Gamma)^2 - \Delta^2}}. \tag{3.2}$$

$\Gamma(E)$ measures the lifetime of quasiparticles at a specific energy inside the in-principle forbidden zone, inside the gap. $\Gamma(E)$ is not necessarily constant, but we will use only constant values throughout the fits and models in this section.

Fermi function thermal smearing The second mechanism which leads to smeared out tunneling measurements of sharp density-of-states features, is the energy distribution of electrons, the Fermi-distribution $f(E)$. For a given sample DOS $\varrho_\mathrm{s}(E)$ and a constant DOS inside the counter-electrode, the differential tunnel-conductance $\mathrm{d}I/\mathrm{d}V$ is

$$\frac{\mathrm{d}I}{\mathrm{d}V} \propto \int_{-\infty}^{\infty} \mathrm{d}E \frac{-\partial f(E+\mathrm{e}V)}{\partial E}\varrho_\mathrm{s}(E). \tag{3.3}$$

Tunnel-spectroscopy, in the sense of this formula, can be imagined as the mechanical scanning of a DOS-landscape $\varrho_\mathrm{s}(E)$ with a (blunt) tip, the shape of which is given by the derivative of the Fermi function $-\partial f/\partial E$. Only at very low temperatures, this "tip" becomes infinitely sharp, its $T \to 0$ limit is the Dirac δ-function. At moderate temperatures, when the thermal energy $\mathrm{k_B}T$ is comparable to or larger than the feature width (e.g. of the coherence-peaks) inside the DOS, the thermal smearing by the Fermi function is considerable. This obviously applies in the present case.

As a consequence, the measured $\mathrm{d}I/\mathrm{d}V$ tunnel spectra can not be interpreted directly as the interface density of states. Instead, Equation 3.3 with a suitable model for ϱ_s (e.g. Equation 3.2), has to be used, to fit the measured data and extract key parameters like the width of the superconducting gap Δ. Figure 3.3 demonstrates that the combination of Equation 3.2 and Equation 3.3 can give acceptable fit results. It also demonstrates the effect of the finite quasiparticle lifetime and the Fermi function thermal smearing. The former rearranges the density of states in that it redistributes spectral weight from the coherence peaks into the gap and softens the curves' appearance. The latter tends to stretch the curves horizontally and makes the $\mathrm{d}I/\mathrm{d}V$ gap-structure appear broader than the density-of-states gap, from which it originates. It should be noted that especially at low temperatures the fits deviate from the measured data. Fits assuming an inhomogeneous order-parameter or alternative order-parameter symmetries were tried and gave mixed results, which are subsumed in Appendix B. The basic lesson learned from these attempts is that Δ, the parameter which we are most interested in, does not depend much on the model employed. It is noteworthy that no background conductance enters the fits presented, as a constant positive background makes the fits fall off in quality. This means that apart from finite-lifetime effects the DOS is fully gapped around E_F and that apart from tunneling into the superconductor no significant parallel transport channels exist.

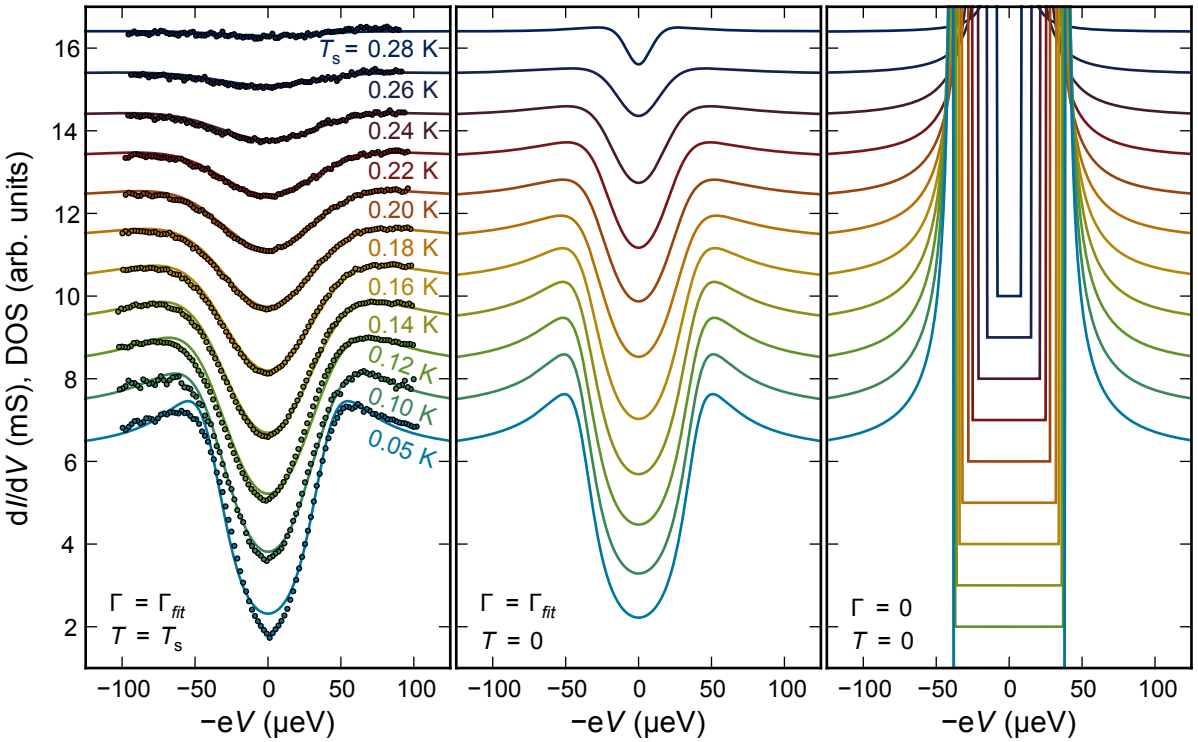

Fig. 3.3: Left panel: the temperature dependent $\mathrm{d}I(V)/\mathrm{d}V$ tunnel spectra of Figure 3.2 (circles) are fitted using Equation 3.3 (lines) with Δ, Γ as free parameters and T set to T_s, the measured sample temperature. The data are offset for clarity. Center: the (lifetime-broadened) quasiparticle DOS (Equation 3.2) corresponding to the fits. Right: the same DOS, but with the lifetime parameter Γ set to 0 (BCS-limit Equation 3.1).

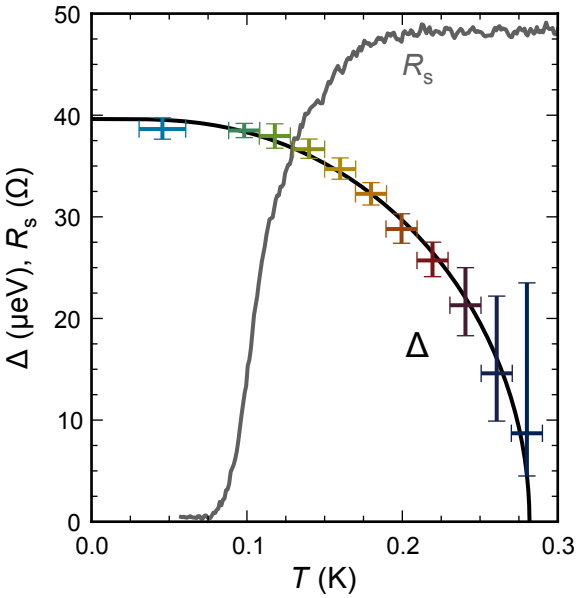

Fig. 3.4: Superconducting energy gap Δ and interface sheet resistance R_s as a function of temperature. The colored error-bars represent a 95 % confidence interval for the fit parameter Δ, as obtained from the fits shown in Figure 3.3. The solid black line through the error-bars is a best fit of $\Delta(T)$ based on the BCS theory.

3.1.2. Temperature dependence of the superconducting gap

Figure 3.4 gives the temperature dependence of the superconducting gap $\Delta(T)$ and contrasts it with the measured LAO-STO sheet resistance. When taken on its own right, the measured $\Delta(T)$ dependence is consistent with the basic BCS-predictions: $\Delta(T)$ converges to a constant value Δ_0 for small T ($T << T_c$); it vanishes when T approaches a critical temperature T_c. The ratio between $T_c = (0.29 \pm 0.01)$ K and $\Delta_0 = (40 \pm 4)$ μeV[2] equates to $\Delta_0/k_B T_c = 1.6 \pm 0.2$, which is close to the canonical BCS weak-coupling value of 1.76. Even the shape of $\Delta(T)$ fits the BCS-model nicely. The solid black curve in Figure 3.4 is a fit of the functional form

$$\Delta(T) = \delta \frac{k_B T_c}{e} \tanh\left[\frac{\pi}{\delta}\sqrt{c\left(\frac{T_c}{T} - 1\right)}\right], \tag{3.4}$$

with $\delta = 1.61$, $T_c = 281$ mK, $c = 0.61$ as the best fit parameters. Hence, the superconducting gap $\Delta(T)$ itself behaves regular. The comparison to the sheet resistance $R_s(T)$, however, has a surprising result: there are two clearly distinct critical temperatures.

In a three-dimensional BCS superconductor, the opening of a gap around the Fermi energy and the onset of ideal conductivity are two sides of one and the same coin, they happen at the very same critical temperature. The gap is a manifestation of the attractive force, by which the electrons are bound into Cooper pairs. The existence of Cooper pairs implies a macroscopic wave-function and a zero-resistance state.

The LAO-STO interface is obviously different in this regard: The superconducting gap begins to open when cooling through 280 mK. The sheet resistance R_s remains finite,

[2] The relatively large error estimate results from considering different weighting in the fit procedure and different models for the quasiparticle density of states.

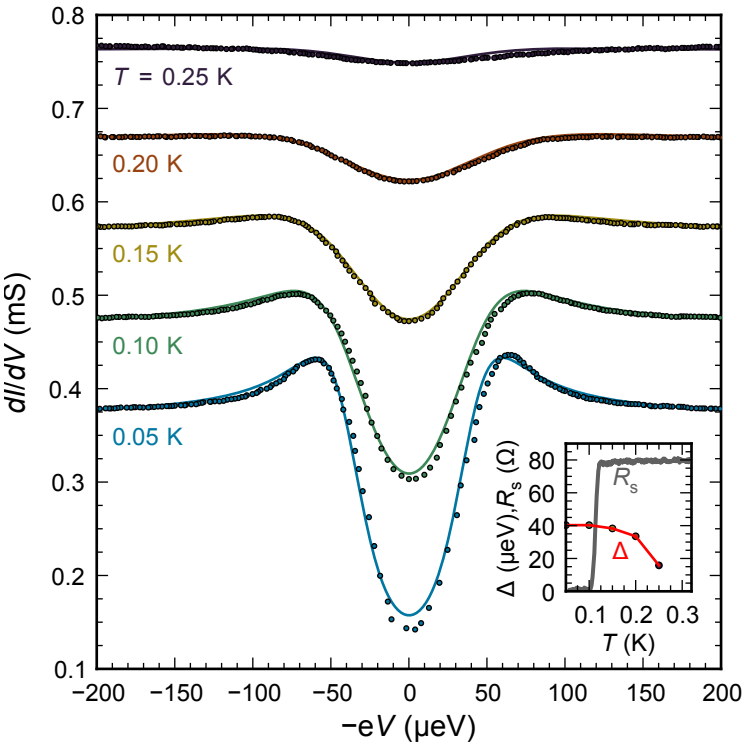

Fig. 3.5: Temperature dependence of differential tunneling conductance dI/dV characteristics of an LAO-STO tunnel device on sample T41. The curves have been offset by multiples of 0.1 mS from the 0.05 K curve. The points represent measured data, the solid lines are Dynes-fits, with life-time parameter Γ and gap-width Δ as fit parameters. The resulting temperature dependence $\Delta(T)$ is plotted in the inset, along with the sheet resistance $R_s(T)$, which has been measured in a different cool-down on a 4-wire contact configuration near to the tunnel device. See section 2.4.3 for details.

and constant, though, until at below approximately 180 mK it starts to decrease. Only at about 80 mK does R_s vanish completely. Consequently, there is a major discrepancy between the temperature at which the gap opens ($T_G = 0.28$ K) and the temperature, at which the resistance vanishes ($T_{BKT} = 0.08$ K). Very similar critical temperatures were found also in the second sample investigated, sample T41, the temperature dependent tunneling spectra of which are shown in Figure 3.5.

BKT transition The most natural explanation for the discrepancy between the two critical temperatures T_G and T_{BKT} lies in the two-dimensional nature of the superconducting state at the $LaAlO_3$-$SrTiO_3$ interface. In previous works[88, 89, 3] it has been established that the transition into the zero-resistance state is a Berezinsky-Kosterlitz-Thouless (BKT) transition. Therefore the lower critical temperature is named "T_{BKT}".

A BKT-transition is a special kind of phase transition in two-dimensional systems from a disordered phase at high temperatures to a low-temperature quasi-ordered phase. While Kosterlitz and Thouless themselves pointed out that "this type of phase transition cannot occur in a superconductor nor in a Heisenberg ferromagnet"[90], the "possibility of vortex-antivortex pair dissociation in two-dimensional superconductors"[91] was recognized by M.R. Beasley and others soon after. In a two-dimensional xy model, a vortex is a topologically stable configuration. Below T_{BKT}, two antiparallely oriented vortices are bound into a so called vortex-antivortex pair. Above T_{BKT}, they spontaneously dissociate into free vortices.

At temperatures between T_{BKT} and T_G Cooper pairs exist, but fluctuating vortices keep the electronic transport dissipative. Non-dissipative transport is only possible at

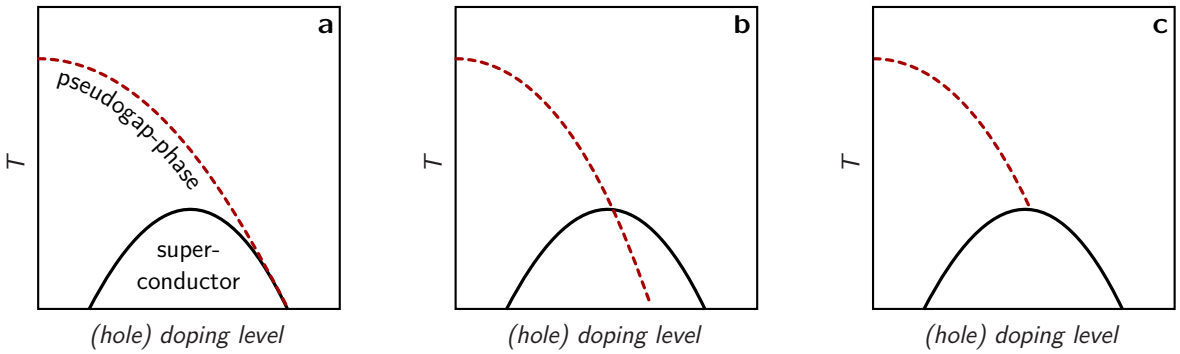

Fig. 3.6: Three possibilities for the phase diagram of the cuprates. The solid black line marks the superconducting transition temperature, the red dashed line is the pseudogap phase-line T^*. In most scenarios, the T^* line should be taken as a crossover, rather than a phase-transition. (adapted from Ref. [98])

$T < T_{\mathrm{BKT}}$, where the vortices are bound. Previously, transport measurements could only determine T_{BKT}. My tunnel devices allow to measure both T_{G} and T_{BKT}, independently. This might allow for unprecedented insights into the physics of two-dimensional superconductivity. As will be shown in the following, these insights might be very relevant to the understanding of high-temperature superconductivity.

Pseudogap Only three years after their discovery in 1986, cuprate high-temperature superconductors have been found to expose the same phenomenon of an energy gap at temperatures above the resistive critical temperature[69, 92, 93]. The phenomenon is commonly known as the *pseudogap*. While numerous experimental observations exist—recently also in ultra thin[94] or strongly disordered[95, 96] films of conventional superconductors and a correlated two-dimensional Fermi gas[97]—its physical origin is still debated[98–100]. Proposed explanations include pre-formed Cooper pairs, resonating valence bonds and short-range spin correlations.

One of the central questions regarding the pseudogap state is, if the temperature T_{G}, or T^*, as it is commonly called, is just a crossover temperature or corresponds to a phase transition. A related question concerns the detailed phase-diagram of the pseudogap-phase and how (and if) it relates to the superconducting state. Figure 3.6 sketches three possible configurations. The previously explained BKT-scenario is compatible to configuration a and b. If the BKT-scenario applies, a phase diagram like case (a) implies a purely two-dimensional superconductor. Case (b) implies a crossover from a two-dimensional BKT superconductor to a three dimensional one at the pseudogap-line.

While LAO-STO is not a cuprate—it does not even contain copper—the physics of both systems might be related. Phenomenologically, both have a pseudogap-phase, and the phase-diagrams of both feature a similar "superconducting dome"[88]. Microscopically, the CuO_2 planes, the essential structural element of the cuprates, are two-dimensional elecronic systems[101], in which BKT-physics might well apply[102].

My LAO-STO tunnel junctions might thus be a useful tool to study the physics of the pseudogap in particular, and high-temperature superconductivity in general. For such studies, the LAO-STO interface has a unique feature over cuprate superconductors: its doping level can be tuned continuously and widely via gate fields. A gate voltage, applied between the back (bottom) side of the substrate and the 2DEL, controls the charge carrier density at the interface[52] and with it its electronic ground state[88]. The technique is compatible with my tunnel devices, so tunneling spectroscopy across the complete LAO-STO phase-diagram is feasible.

With cuprates it is a big challenge already to fabricate reliable tunnel junctions. Gating them over a large doping range is another challenge[103] that can only be accomplished with electrolytes[104] or ionic liquids[105] in an electric double-layer transistor configuration[106]. Such configurations do, however, complicate tunneling experiments even more.

The LAO-STO interface, on the other hand, provides both reliable tunnel junctions, and a means to dope the superconductor (almost) all the way throughout the superconducting dome. The combination of both features will now be used to learn about the doping dependency of the superconducting (pseudo-) gap.

3.1.3. Doping (gate-voltage) dependency of the gap

The key to control the doping level, the electronic density at the LAO-STO interface is electrostatic gating using a back gate contact on the bottom of the $SrTiO_3$ substrate. I will briefly introduce the working mechanism, nomenclature and the caveats of back gate experiments and then present the tunneling results.

Working principle of back gating

The back gate configuration with a gate voltage applied between the 2DEL on the one side and a silver electrode on the opposite side of a $SrTiO_3$ substrate is akin to a parallel-plate capacitor. A voltage V_{bg} applied between the two plates causes an electric field $E = V_{\mathrm{bg}}/d$ across the $SrTiO_3$ dielectric with thickness d. At the same time, the charge on both plates is rearranged according to $\delta Q = C \times V_{\mathrm{bg}}$, where C is the capacitance of the capacitor configuration. V_{bg} consequently alters the charge carrier density n_{e} on both capacitor plates: $\frac{\delta Q}{A} = \delta n_{\mathrm{e}} \mathrm{e} = \frac{C}{A} V_{\mathrm{bg}}$, where e is the elementary charge, and A is the geometric area of the plates, i.e. the sample area of typically $5 \times 5\,\mathrm{mm}^2$.

For practical gate voltages $\sim 100\,\mathrm{V}$, assuming a relative dielectric constant of $\varepsilon_{\mathrm{STO}} = 1000$, δn_{e} is on the order of $10^{13}\mathrm{e}\,/\mathrm{cm}^2$, which is a negligible quantity compared to typical carrier densities of metals, but happens to be the typical density of mobile electrons at the LAO-STO interface.

For this reason the electric field-effect in a back-gate configuration is a practical tool to tune the charge carrier density at LAO-STO interfaces. The effectiveness of the back-gate approach has previously been demonstrated[52, 88, 107]. A positive gate voltage (with regard to the 2DEL at ground potential) enhances the electron density at the LAO-STO interface, a negative gate voltage depletes it. At a critical carrier density of

$0.5 - 1.5 \times 10^{13}$ /cm^2 (depending on sample and temperature) the interface undergoes a metal-insulator transition[10]. The gate voltage at which this transition sets in also depends on sample and temperature; typical values for our samples are -50 V to -100 V.

Caveats of back gating

Unfortunately, two effects complicate the interpretation of the gate voltage V_{bg} as a direct indicator for a reproducible charge carrier density: the electric field dependency of $SrTiO_3$'s dielectric constant $\varepsilon_{\mathrm{STO}}$[43], and a peculiar memory effect[52, 53]. The former makes $n_{\mathrm{e}}(V_{\mathrm{bg}})$ a strongly non-linear function, the latter implies time-effects and a certain non-reproducibility of a specific sample state $S(V_{\mathrm{bg}}, n_{\mathrm{e}})$. Field-focusing might be an additional issue, but is only expected at the sample edges.

n_e(V) non-linearity The $n_{\mathrm{e}}(V_{\mathrm{bg}})$ non-linearity due to $SrTiO_3$'s field-dependent dielectric constant can be accounted for, as $\varepsilon_{\mathrm{STO}}(V_{\mathrm{bg}})$ is a directly measurable quantity (e.g. using $C(V)$ measurements). So in cases, where n_{e} is not directly measurable, the change in charge carrier density δn_{e}, which V_{bg} has induced, can be evaluated simply by integrating the measured $C(V)$ curve: $\delta n_{\mathrm{e}} = A^{-1} \int_0^{V_{\mathrm{bg}}} C(V)\mathrm{d}V$.

It should be noted that $\varepsilon_{\mathrm{STO}}$ varies strongly with temperature[43], so the measured $C(V)$ curve can be used to evaluate $n_{\mathrm{e}}(V_{\mathrm{bg}})$ only at the temperature at which $C(V)$ was acquired.

Memory effect The memory effect is more difficult to deal with. At a fixed temperature, the charge-carrier density (as well as the mobility) does not depend directly and exclusively on V_{bg}, it depends on the V_{bg} prehistory as well. There are strategies to achieve quasi-reproducible gating results nevertheless, e.g. to always start gate sweeps at a large positive V_{bg}[88] or to keep V_{bg} below a certain positive threshold[53, 10]. The initial, as-grown state of an LAO-STO interface, however, is unique and can not easily be reproduced after the initial application of gate fields. This is akin to the initial magnetization curve in ferromagnetic hysteresis and can probably be ascribed to the interplay between several parameters governing the LAO-STO interface. The sample state is mainly determined by the charge-carrier density n_{e} and the momentary electric field $E \propto V_{\mathrm{bg}}$. Since the electric field fundamentally defines a number of parameters relevant to the LAO-STO interface, e.g. the local dielectric constant[43] or the spin-orbit coupling[108], it is considered as important to describe the electronic state, as the electron density n_{e}. Each one of both quantities, $n_{\mathrm{e}}(V_{\mathrm{bg}})$ and $E(V_{\mathrm{bg}})$ is, of course, reproducible on its own. Their combination $< n_{\mathrm{e}}, E > (V_{\mathrm{bg}})$, however, is not.

With this in mind, let me continue this section with a number of reproducible back-gated tunnel measurements, and only later on reveal some fascinating tunnel spectra, which have only been obtainable throughout the "initial polarization curve", the very first measurement session in which gate voltages have been applied to sample T41.

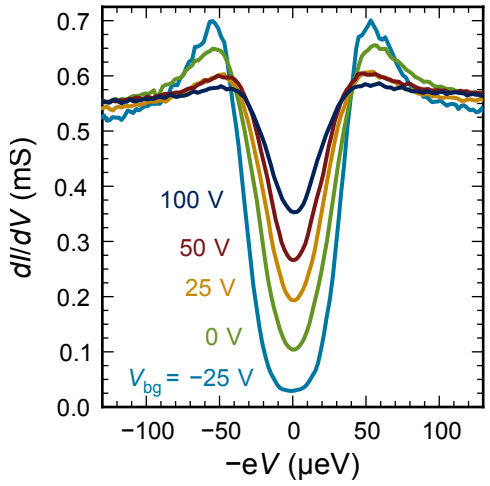

Fig. 3.7: Gate voltage V_{bg} dependence of dI/dV tunneling spectra, measured at about 50 mK. For positive gate-voltages, electrons accumulate at the interface.

Basic doping dependency of the superconducting gap

The basic effect of electrostatic doping on the superconducting gap is depicted in Figure 3.7. Positive V_{bg}, which increase the electron density, decrease the superconducting gap. Negative V_{bg}, which decrease the electron density, increase the superconducting gap. This fundamental result is easily visible from the tunnel spectra and is universal across all experiments made in the course of this research. For a quantitative analysis, fits using the previously discussed formulae (Equation 3.3 with 3.2) were engaged. This is shown in Figure 3.8, which presents the fit-results of the data shown in Figure 3.7 and of additional data sets. The fit results confirm the qualitative finding: With increasing electron doping, the superconducting gap Δ decreases continuously, whereas the lifetime broadening parameter Γ increases.

This doping dependency of Δ is another incompatibility of the two-dimensional superconducting state at LAO-STO interfaces with the BCS theory. The superconducting gap of a BCS superconductor is directly proportional to the critical temperature: $\Delta_{BCS} = 1.76\,k_B T_c$. Andrea Caviglia et al. have previously mapped the $T_c(n_e)$ and $T_c(V_{bg})$ phase diagram and found a dome-shaped curve with a single peak at $V_{bg} \approx 100$ V. Figure 3.9 shows this phase diagram, as reproduced from Ref. [88]. Indeed, the measured gate-voltage dependence of the critical current inside my tunnel devices is fully consistent with this result, provided I_c is directly proportional to T_c (as in Ginzburg-Landau theory[109]). In said measurement, which is presented in Figure 3.10, the critical current and tunnel spectra were measured back-to-back at each gate voltage. Owing to the local heating, which was imposed upon the sample by the relatively large currents needed for I_c-measurements and the electrical noise of the many instruments attached in that experiment, the sample temperature exceeded 100 mK, which explains the shallow tunnel spectra. The result is still a clear confirmation that the critical current (which most probably scales with the resistive critical temperature T_{BKT}), and the superconducting gap have opposite doping dependencies: The critical current tracks the critical temperature and increases with V_{bg}, the superconducting gap does the opposite, it monotonously decreases with increasing electron doping.

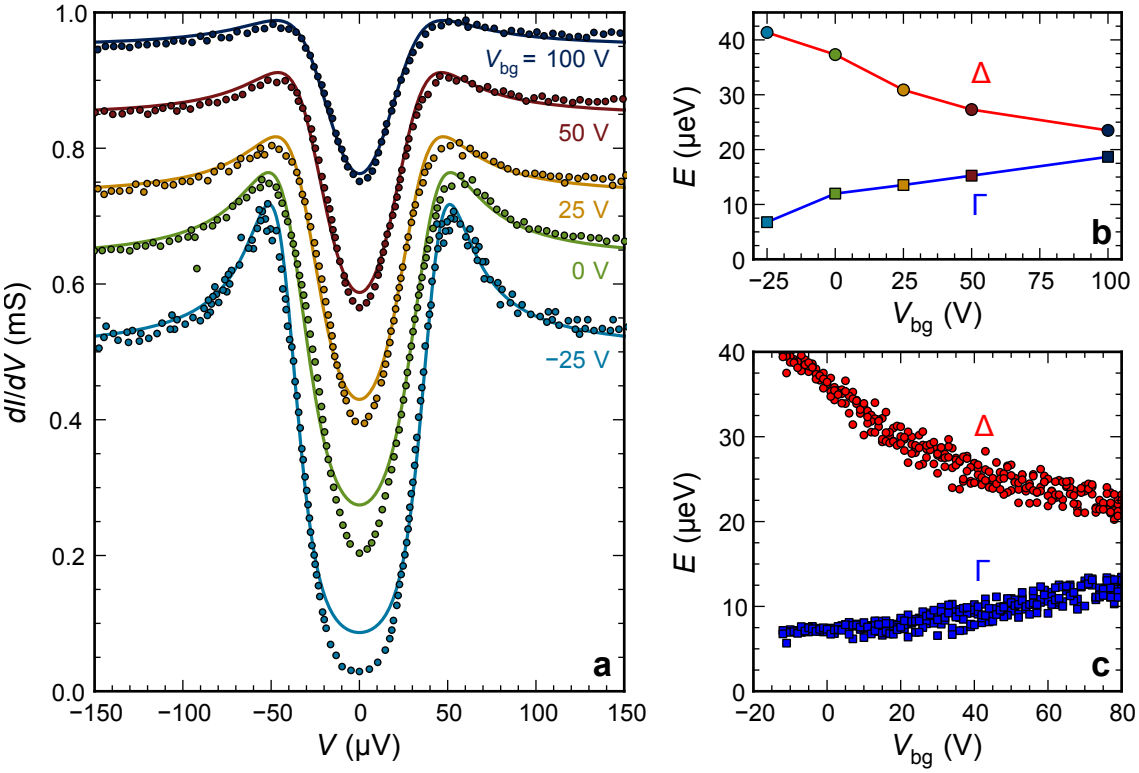

Fig. 3.8: a) The same tunnel spectra as in Figure 3.7 (circles), offset for clarity and with s-wave Dynes-fits (solid lines). The gap-width Δ and the lifetime-parameter Γ employed in the fits are plotted as a function of gate-voltage V_{bg} in **b)**. **c)** An analogous evaluation of a larger set of tunnel-spectra from another tunnel device. All measurements were performed at around 50 mK.

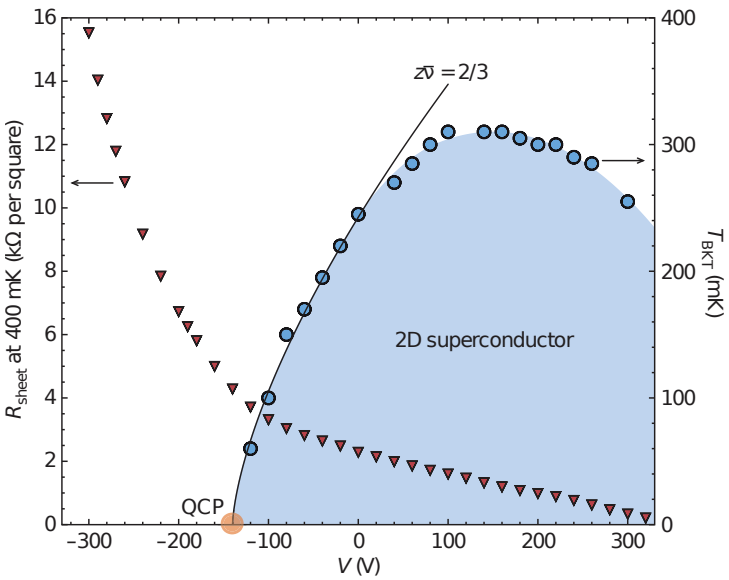

Fig. 3.9: Gate voltage $V\,(= V_{bg})$ dependence of the resistive critical temperature T_{BKT} (in blue) and sheet resistance measured at 400 mK (in red). For positive gate-voltages, electrons accumulate at the interface, which reduces the sheet resistance, but enhances T_{BKT}, until it gets maximal at around $V = 140$ V. The slope of $T_{BKT}(V)$ towards the quantum-critical-point (QCP) at $V_c = -140$ V is consistent with the scaling relation $T_{BKT} \propto (V - V_c)^{z\overline{\nu}}$, with $z\overline{\nu} = 2/3$. For details, see Ref. [88], from which this figure is reproduced.

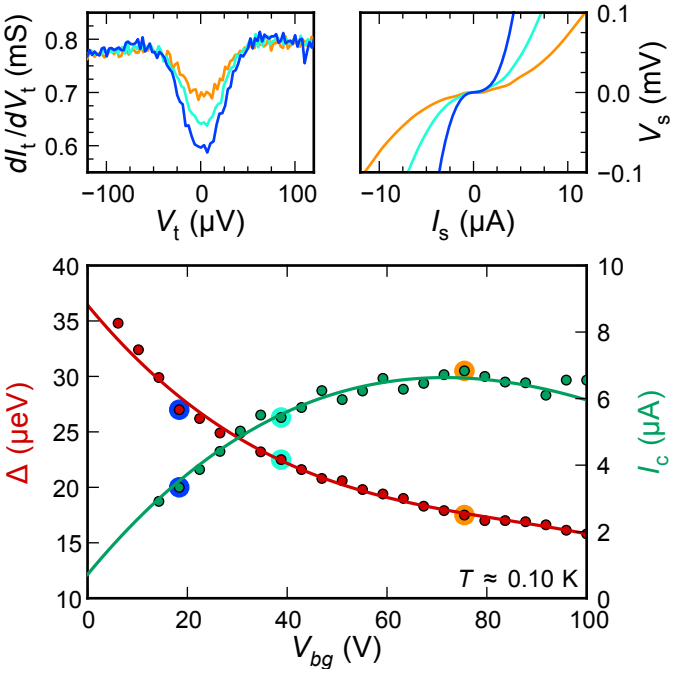

Fig. 3.10: Quasi-simultaneous measurement of tunnel-spectra dI_t/dV_t and 2-wire current-voltage characteristics along the interface $V_s(I_s)$ at a number of gate voltages V_{bg}, and $T \approx 0.10$ K. The upper panels exemplify 3 such measurement pairs, done at $V_{bg} = 19, 38$ and 76 V. To account for the cable- and contact resistances present in the 2-wire measurement, a linear function has been subtracted from the $V_s(I_s)$-data, to nullify the slope around $I_s = 0$. The lower panel presents, as a function of gate voltage, the value of the superconducting gap Δ obtained from fitting a larger set of dI_t/dV_t data with a Dynes-model, and the critical current I_c extracted from the corresponding $V_s(I_s)$ curves.

Similarity to pseudogap Fascinatingly, the very same behavior is known from the pseudogap phase of cuprate superconductors[99]. The same effect that hole-doping has in the cuprates, I have found for electron-doping at an LAO-STO interface. At this time, no definite phase diagram of the pseudogap line $T^*(n_e)$ in comparison to a direct measurement of $T_{BKT}(n_e)$ can be drawn, because with the present sample design no 4-wire measurements along the LAO-STO interface right inside the tunnel devices are possible, and the charge carrier density can not be determined accurately. Measurements with an improved sample design, which addresses these points, are underway and will be reported elsewhere. Along these lines, a collaboration with Kathrin Moler's Stanford group would be highly interesting, as Julie Bert and her colleagues from that group are able to deduce the superfluid density, the density of *superconducting* charge-carriers n_s from measurements of the local magnetic susceptibility at LAO-STO interfaces[107] with a scanning SQUID technique. Since their method is compatible with my tunnel devices, we could collaboratively measure the superconducting gap and n_s simultaneously to see how they are related.

In-gap features at initial application of gate voltages

The tunnel spectra presented so far have been reproduced many times, in different cryostats, with different instruments (AC- and DC-methods[3]), and on many different tunnel devices. Apart from a slight shift of $\Delta(V_{bg})$ on the V_{bg}-axis, due to the aforementioned memory effect, the qualitative and quantitative reproducibility of the doping

[3] All AC-results shown were verified to coincide with their simultaneously measured DC-counterpart. The same was not generally true for tunneling measurements near to or inside the insulating state ($V_{bg} \lessapprox -30$ V of LAO-STO interfaces, which are not shown here.

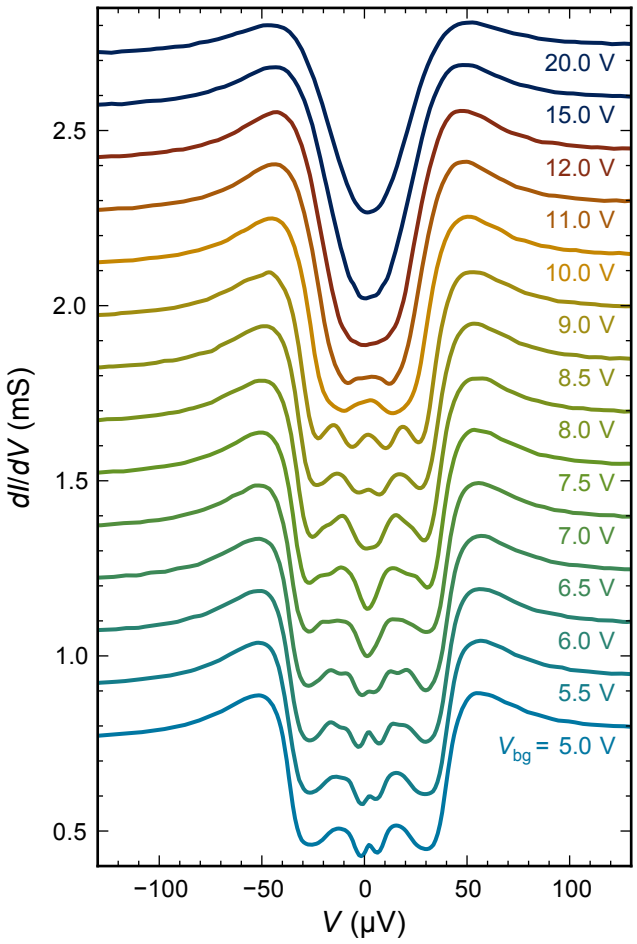

Fig. 3.11: Tunneling differential conductance spectra of a superconducting LAO-STO interface, measured at around 50 mK, at a number of gate voltages V_{bg}. For a clearer appearance, an artificial offset has been introduced between consecutive curves; the as-measured differential conductance of all curves coincides completely for $|V| > 120\,\mu V$.

dependent spectra is excellent.

As mentioned, the spectra we could measure in the very first cool-down session involving gate fields stood out in this regard. Figure 3.11 highlights a selection of gate-voltage dependent tunnel spectra that we have acquired in that session. They feature unique in-gap structure, only remotely comparable to other zero-bias anomalies, which have been reported in some cuprates or other systems with complex order parameters. Decreasing the electron doping level by decreasing V_{bg} from 20 V to 10 V, a peak emerges around zero bias and develops into a series of multiplets upon further decrease of V_{bg}. While for some gate voltages a zero bias conductance peak is found, for others the conductance has a minimum at zero bias. Similar features were obtainable on both of the two devices wire-bonded on sample T41 at that time. The measurement-technique used was a robust 4-wire DC-method with a Keithley 2400 or 6430 current source and a Keithley 2182A nanovoltmeter. The features were seen for both current-sweep directions and independently of the sweep-rate[4]. Appendix C presents further technical details regarding the measurement as well as the raw data including both traces.

[4]Of course, providing a suitable delay to account for the charging time of the relatively large capacitance of the junction, and a suitable integration time to achieve acceptable noise-levels.

These features, which we denote as in-gap states, along with their extreme sensitivity towards gate fields, are both tantalizing and hard to explain. Possible starting points are Andreev or Majorana bound states[110, 111] or unconventional superconducting order-parameters like in Sr_2RuO_4[112–114]. Besides their unique tunnel spectra[115, 116], Sr_2RuO_4 and LAO-STO interfaces have additional similarities: Both have coexisting magnetic and superconducting ordering[117, 14], both have the $R(T) \propto T^2$ characteristic of a Landau-Fermi liquid, and for both systems impurities (magnetic and non-magnetic) seem to influence their superconducting properties most sensitively[118].

In fact, a doping dependent spin-triplet component of the superconducting gap function of $LaAlO_3$-$SrTiO_3$ interfaces has previously been predicted[119]. It has also been proposed the LAO-STO interface could give rise to a finite-momentum superconducting state[120, 121] with intra- and inter-band pairing. Such a system could indeed feature peculiar sub-gap structure in its quasiparticle density of states[121].

Experimentally, the challenge at hand is to check the reproducibility of these features in additional samples and also to improve on the voltage resolution. The present data has an effective resolution of approximately 2 µV at best. The measured points of some of the spectra in Figure 3.11 and Appendix C indicate that this resolution is not sufficient to fully resolve the complex spectra in some situations. Like the mapping of a complete phase-diagram, this is currently ongoing work.

Replacing the Au tunneling-electrode with a (conventional) superconducting material would be another interesting research direction. The sharply peaked superconducting density of states of the conventional superconductor would allow for a superior resolution in the tunnel-spectra as compared to the normal conducting Au electrode, where the Fermi-function limits the energy resolution. In addition, the Josephson junction between the conventional superconductor and the LAO-STO interface could be used to directly probe for a finite momentum state[120]. Iridium might be a good candidate for replacing Au. The noble metal Ir has a critical temperature of 0.11 K[122], which can be tuned to above 3 K by alloying with tiny amounts of Yttrium[123]. A noble metal like Ir is preferable to non-noble metals in this case, because it is not expected to chemically interact with the $LaAlO_3$ and—most importantly—does presumably not affect the oxygen stoichiometry at the $LaAlO_3$-$SrTiO_3$ interface.

3.1.4. Summary

Using my tunnel devices at millikelvin temperatures in a microvolt voltage range, I have measured the superconducting energy gap of LAO-STO interfaces. In its (reproducible) ground state, the gap shape is compatible with an s-wave order-parameter with a gap-width of 2×40 µeV. Its temperature- and doping-dependence bear a striking similarity to the pseudogap-phase of the cuprates: The gap is present at temperatures well above the resistive critical temperature T_{BKT}, it shrinks monotonously with increasing electronic density, which was tuned via gate fields. The superconducting gap $\Delta(V_{\mathrm{bg}})$ therefore acts exactly opposite compared to the critical temperature $T_{\mathrm{BKT}}(V_{\mathrm{bg}})$[88], the critical current $I_{\mathrm{c}}(V_{\mathrm{bg}})$ and the superfluid density $n_{\mathrm{s}}(V_{\mathrm{bg}})$[107] of LAO-STO interfaces. It should be mentioned that the present research is clearly just a starting point for much

more extensive investigations, which are on their way. The developed tunnel devices (at least in their next-generation implementation) provide the unique opportunity to study the complete doping dependency of a two-dimensional superconductor and to combine high-resolution tunnel-spectroscopy with measurements of critical parameters and the electron- as well as the superfluid-density. Considering the two-dimensional nature of cuprate superconductors on the one hand, and the herein established analogies between the pseudogap phase of these systems and the LAO-STO interface on the other hand, the results to come could well become a precious contribution towards understanding high-T_c superconductivity[24].

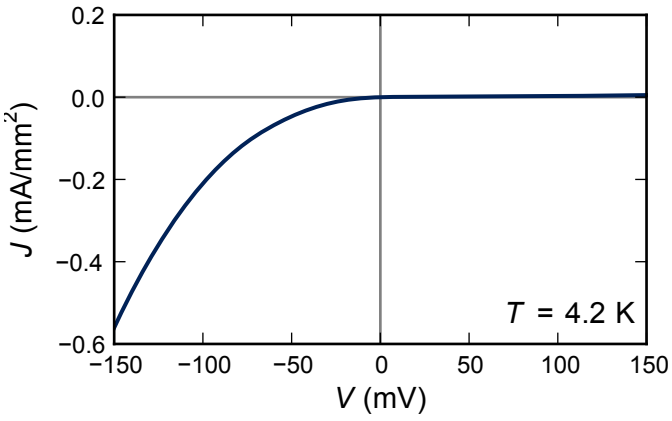

Fig. 3.12: Current-voltage characteristic of a typical Au-LAO-STO tunnel junction with a nominal LAO thickness of 4 uc, measured at a temperature of 4.2 K. The ratio between forward- and reverse-current at $|V| = 150$ mV is $J(\text{-}150\text{ mV})/J(150\text{ mV}) = 115$.

3.2. Tunneling on a millivolt scale: low chemical potential and LO phonons

In this section the tunneling voltage range is extended into the millivolt regime. The conduction-band structure near the Fermi-level of normal-conducting LAO-STO interfaces is explored. The spectral tunneling density of states (TDOS) is found to be far from constant on a meV scale, with a band edge right below the Fermi-level. The tunneling of electrons out of the interface into the Au electrode is found to be dominated by inelastic tunneling. This hinders spectroscopic access to the occupied part of the DOS, but allows for an accurate mapping of optical $SrTiO_3$ phonons.

3.2.1. I(V) asymmetry and conduction-band structure

In the millivolt range, at least at temperatures low enough to ensure that the tunneling resistance of the $LaAlO_3$ barrier is dominating over the in-plane resistance of the $LaAlO_3$-$SrTiO_3$ interface, the tunneling current is highly asymmetric with regard to the polarity of the tunnel voltage. As Figure 3.12 shows, the tunneling $I(V)$ characteristic of a typical Au-LAO-STO tunnel junction is diode-like: The tunnel rate (current) for electrons tunneling from the Au into the 2DEL at a negative voltage is about 100 times larger, than for electrons tunneling out of the 2DEL at a positive voltage of the same magnitude. In other words, electrons tunnel easily from the gold into the LAO-STO interface, but they hardly escape it.

The $I(V)$ asymmetry can be interpreted as a direct consequence of the band structure of the LAO-STO interface. At small tunnel voltages, the differential conductance $\mathrm{d}I(V)/\mathrm{d}V$ is a direct measure of the 2DEL tunneling density of states[68]. The millivolt regime represents an intermediate case, in which the effect of the tunnel-voltage on the tunnel-barrier might become relevant[124]. In scanning tunneling spectroscopy the normalized differential conductance NDC,

$$\mathrm{NDC}(V) = \frac{\mathrm{d}I/\mathrm{d}V}{I/V} = \frac{\mathrm{d}(\log I)}{\mathrm{d}(\log V)}, \tag{3.5}$$

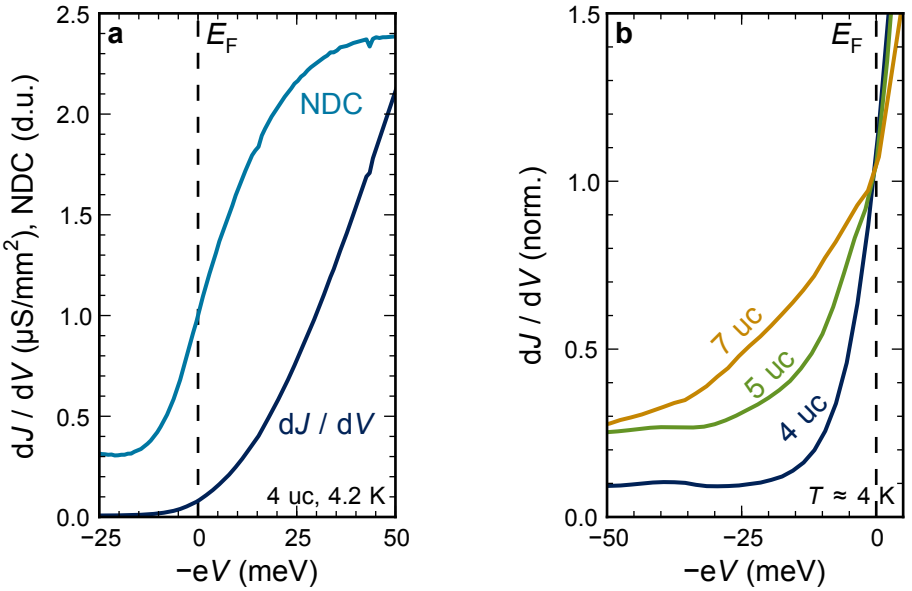

Fig. 3.13: Differential conductivity $\mathrm{d}J/\mathrm{d}V$ and normalized differential conductance $\mathrm{NDC}(V) = \mathrm{d}I/\mathrm{d}V/(I/V)$ of an Au-LAO-STO tunnel junction with 4 uc thick $LaAlO_3$, measured at 4.2 K (**a**). Fig. **b** compares the normalized $\mathrm{d}J/\mathrm{d}V$ characteristics of junctions with different LAO thickness. The data provide a measure of the density of electronic states at the LAO-STO interface. The x-axis therefore gives the energy of an electron, measured from the Fermi-level E_F. States *left* of E_F ($E < E_F$) are occupied states.

which approximately cancels barrier-effects[125, 126], is often used to measure the spectral DOS. The NDC normalizes the differential conductance $\mathrm{d}I/\mathrm{d}V$ by the absolute conductance I/V.

Figure 3.13a displays the differential and normalized differential conductivity of a 4 uc Au-LAO-STO tunnel junction, measured at 4.2 K. Note that the x-axis of this graph is reversed to reflect the energy $E = -\mathrm{e}V$ (e is the elementary charge, V the voltage on the top gold electrode) of an electron inside the 2DEL with respect to the electrochemical potential of the gold tunnel-electrode. $E = 0$ is the Fermi-level E_F inside the 2DEL. It is obvious that near the Fermi-level the DOS of the LAO-STO interface is by no means constant. It has a large positive slope. If the NDC is interpreted directly as the density of states, the Fermi-level appears just about 10 meV above an apparent band edge. Figure 3.13b compares the low-voltage tunneling characteristics of junctions with 4, 5, and 7 uc thick $LaAlO_3$ layers. The data have been normalized to $\mathrm{d}J/\mathrm{d}V|_{V=0} = 1$. A kink develops at E_F, which in direct interpretation of the data as the DOS can be ascribed to a sub-band whose onset shifts away from E_F, to lower energies with increasing $LaAlO_3$ thickness. In this picture, the measured low-energy DOS would be comprised of 3 bands:

1. A band that regardless of the LAO thickness is pinned at the Fermi-level.
2. A band whose band edge shifts from about $E_F - 10$ meV to $E_F - 30$ meV with increasing LAO thickness.

3. A band with a relatively small and flat TDOS. Its tunneling contribution is small, but grows relative to TDOS(E_F) with increasing LAO thickness.

The band edge of sub-band 3 would be well beyond −50 meV, it could not be observed directly in the tunneling data. As will be shown in the following, inelastic tunneling from bands 1 and 2 contributes heavily to the tunneling current in this regime of occupied states. Inelastic tunneling therefore obscures the minor elastic contribution of band 3 at $V \lessapprox -60$ meV.

The three enumerated bands can probably be ascribed to different Ti 3d derived sub-bands. The degeneracy of the Ti 3d orbitals is lifted due to the symmetry breaking at the interface. According to x-ray absorption spectroscopy by M. Salluzzo et al. [5] (on LAO-STO samples that I have grown) the d_{xy} orbitals are around 50 meV below the d_{xz} and d_{yz} orbitals. Recent results from photoelectron spectroscopy (also on samples grown by myself) and density-functional theory[21] give 300 meV as energy difference between the xy and the xz/yz bands; the Fermi-level was found only slightly above the band edge of the xz/yz bands.

Furthermore, the conduction band may be split at the Fermi surface due to the strong Rashba spin-orbit interaction at LAO-STO interfaces[108]. We therefore tentatively assign band 1 and 2 to the possibly split xz/yz bands, and band 3 to the xy band.

3.2.2. Phonon-assisted tunneling

A zoom into the low-current reverse-direction regime ($V > 0$ regime in Figure 3.12) reveals distinct steps in the current-voltage $I(V)$ characteristic, e.g. at around 40 mV, 60 mV and 100 mV. This $I(V)$ data is shown in Figure 3.14 along with the 1st and 2nd derivative $\mathrm{d}I/\mathrm{d}V$ and $\mathrm{d}^2I/\mathrm{d}V^2$, which elucidate these features further and uncover even more voltages with local non-linearities in the tunneling $I(V)$. Peaks or shoulders in $\mathrm{d}^2I/\mathrm{d}V^2$ can be found at 33 mV, 50 mV, 59 mV, 79 mV, 98 mV, 117 mV, 130 mV, 158 mV and 196 mV. Of these peaks, the ones at 33 mV, 59 mV and 98 mV clearly surpass the rest. The energies eV of the peak positions correspond to $SrTiO_3$ LO-phonons.

$SrTiO_3$ has 7 distinct optical phonon modes, of which four are transversal (TO) and four are longitudinal modes. Their dispersion and their phonon density of states has previously been investigated extensively[39, 127–137]. Two exceptionally thorough investigations are by H. Vogt[133], who analyses precise Hyper-Raman spectroscopy using a number of models and R.A. Cowley[137], who uses inelastic neutron scattering in conjunction with several theoretical models to investigate the $SrTiO_3$ phonons and their temperature dependence.

Table 3.1 lists the authors' results. Vogt tabulates the (zone-center $q = 0$) energies of the TO phonons as 10.9, 21.7, 33.0 and 67.6 meV. The LO-phonon energies are given as 19.8, 33.0, 58.8 and 98.6 meV.

Clearly, the latter three energies correspond exactly to the positions of the three largest peaks in the tunneling $\mathrm{d}^2I/\mathrm{d}V^2$. The LO phonon with the lowest energy (19.8 meV) does

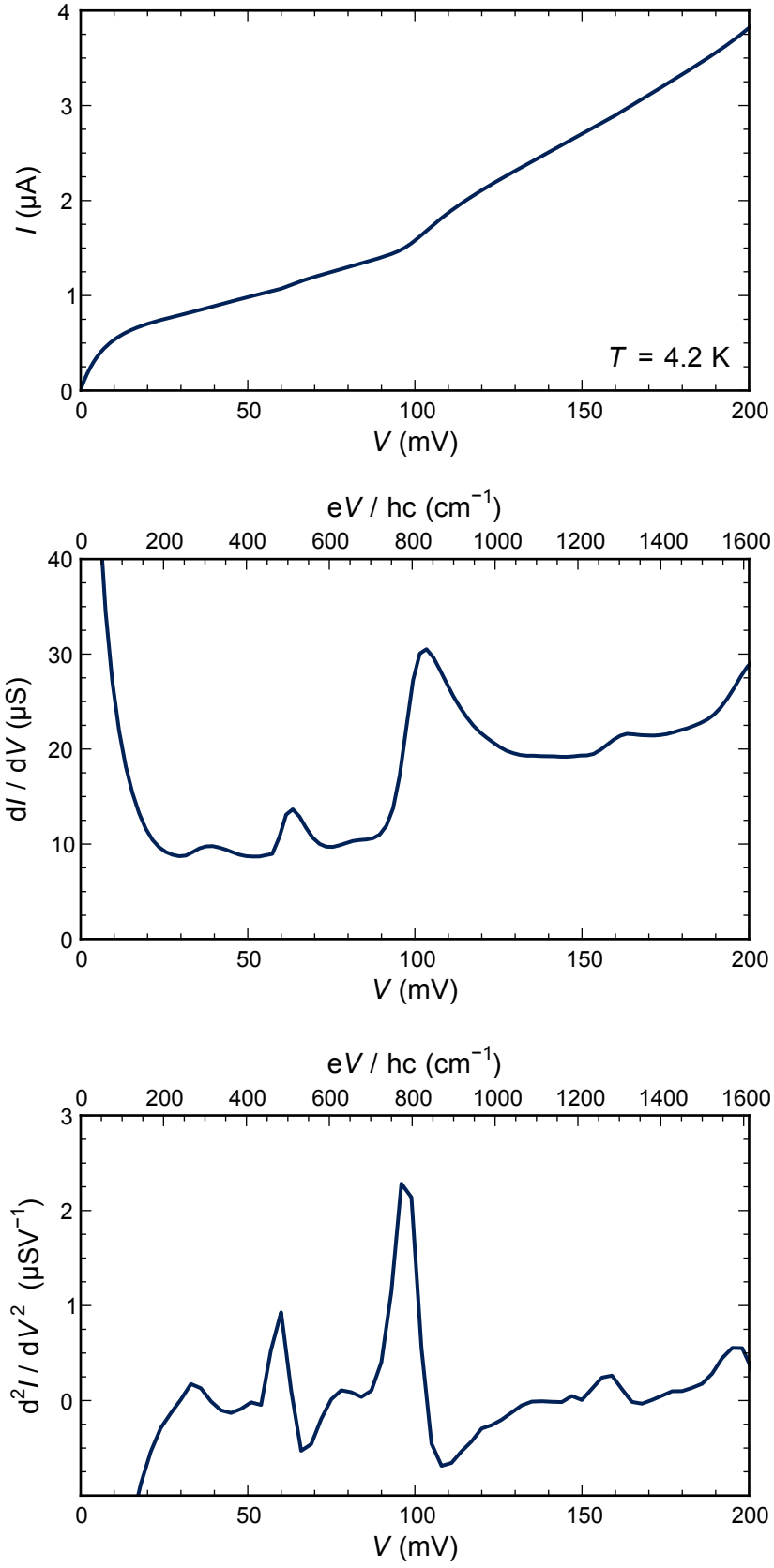

Fig. 3.14: Current-voltage $I(V)$ characteristic, and its first and second derivatives $\mathrm{d}I/\mathrm{d}V$ and $\mathrm{d}^2I/\mathrm{d}V^2$ of an Au - 4uc LAO - STO tunnel junction in its reverse direction (electrons tunneling out of the 2DEL, into the Au). The voltage V given on the lower axes is the voltage on the top Au electrode with respect to the 2DEL. The value eV/hc with e the elementary charge, h the Planck constant and c the speed of light, reflects the wavenumber corresponding to the electrostatic energy eV. The $I(V)$ measurement was done at $T = 4.2\,\mathrm{K}$, the derivatives were computed from that data numerically.
The $I(V)$ curve has visible steps at around 60 mV and 100 mV. It features even more, even smaller steps, which the many peaks in its derivative $\mathrm{d}I/\mathrm{d}V$ prove. The peaks in $\mathrm{d}^2I/\mathrm{d}V^2$ mark the energies of longitudinal optical phonons of $SrTiO_3$, which are the reason for the inelastic tunneling in this voltage range.

Tab. 3.1: Energies of zone-center $SrTiO_3$ longitudinal optical phonons. The columns labeled HRS (Hyper-Raman spectroscopy) and NS (Neutron spectroscopy) are reproduced from Refs. [133, 137]. The third column lists the peak-positions of d^2I/dV^2 tunneling data as shown in Figure 3.15. The numbers in parentheses are numbers derived indirectly from their respective experiment.

	E (meV)		
Mode	HRS (290 K)	NS (90 K)	this work (4 K)
LO1	(19.8)	21.1	(18.5)
LO2	33.0	32.9	33.5
LO3	58.8	-	59.4
LO4	98.6	-	98.1

not appear directly in the tunnel-data, it is hidden below the elastic tunneling signal. The peak in d^2I/dV^2 around 78 mV proves, though, that the phonon LO1 contributes to the inelastic tunneling, too. The peak originates from a two-phonon-process involving one LO1 and one LO3 phonon: $\hbar\omega_{LO3} + \hbar\omega_{LO1} = 59\,\text{meV} + 19\,\text{meV} = 78\,\text{meV}$. All of the remaining lower-intensity peaks in d^2I/dV^2 can be explained in that manner: The peaks at 78 mV (LO3+LO1), 158 mV (LO4+LO3) and 197 mV (2×LO4) as well as the shoulders at 52 mV (LO1+LO2), 119 mV (LO4+LO1) and 132 mV (LO4+LO2, 2×LO3), are all due to inelastic tunneling involving two phonons. In fact, with a loving eye, almost all of the combinations possible can be identified in the measured d^2I/dV^2 spectra. Figure 3.15 demonstrates that such spectra are useful for exact phonon-spectroscopy, since they are highly reproducible among samples and can be measured at extremely low temperatures. Low temperatures reduce the Fermi-function hermal smearing, which is inherent to tunneling spectroscopy, to a minimum. Table 3.1 compares the peak positions obtained from my tunneling d^2I/dV^2 data with the results of Cowley and Vogt.

The spectrum of a special $LaAlO_3$-$SrTi^{18}O_3$ sample, which I have prepared in collaboration with Christof W. Schneider (PSI, Villigen, Switzerland), is shown in Figure 3.16. Since this sample has, instead of a natural oxygen isotope distribution (99.76%^{16}O[138]), a large fraction of the heavier ^{18}O isotope, the phonon frequencies, at least for modes involving oxygen motion, should be shifted. The result that the highest phonon-mode is shifted by −3 meV, is consistent with results from Raman-spectroscopy done on similar samples at the PSI. It therefore proves that a sizable fraction of ^{18}O is present near the interface.

3.2.3. Formal description of inelastic tunneling

How does phonon-assisted, inelastic tunneling work? How does it influence the tunneling current? Figure 3.17 illustrates the basic principle, with the classic example of tunneling between two simple metals with an energy independent, constant density of states. As stated previously, the elastic tunneling current between two metallic electrodes depends on occupied states on one side facing unoccupied states on the other side of the barrier. Neglecting any barrier effects, the tunnel probability, which translates to a tunnel rate and thus a tunnel current, is given by the product (folding) of the occupied states of one

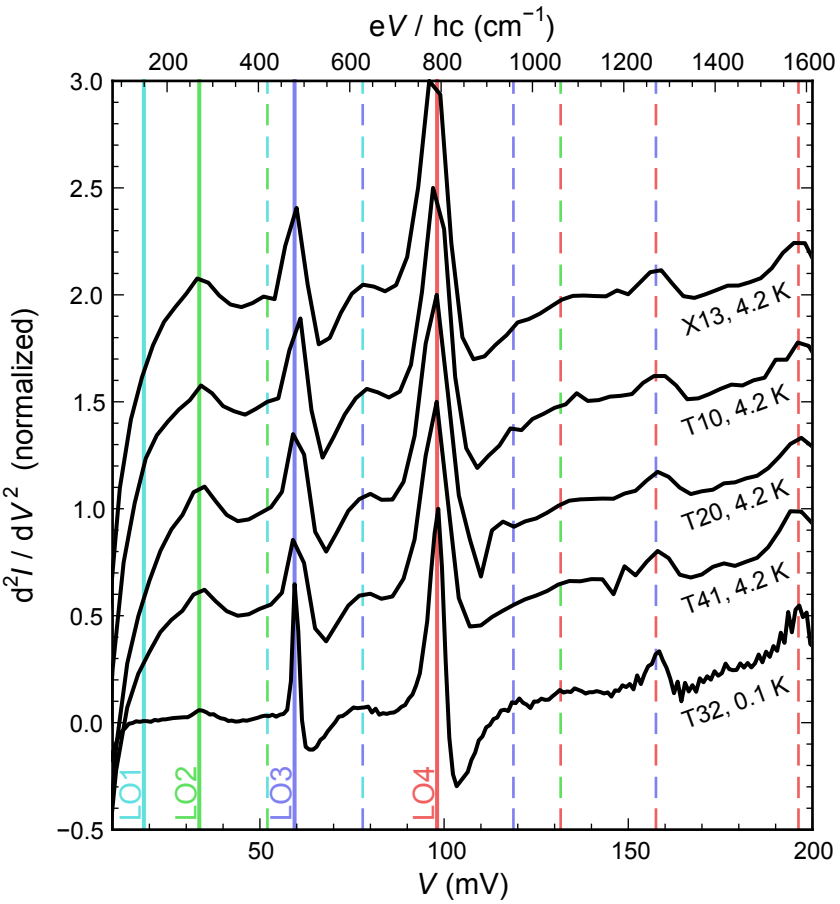

Fig. 3.15: Second derivatives of low-temperature inelastic tunneling $I(V)$ data from 5 different LAO-STO samples. The data have been normalized to a maximum of 1.0 and were offset from each other by 0.5 units. Every curve is labeled with the sample name and measurement temperature. Except of T32, which has a nominal LAO thickness of 5 uc, all other samples have 4 uc of LAO. The colored solid lines mark the energies of $SrTiO_3$ phonons as given in Table 3.1 ("this work"). Dashed lines mark sums and harmonics of these energies and adhere to the same color code.

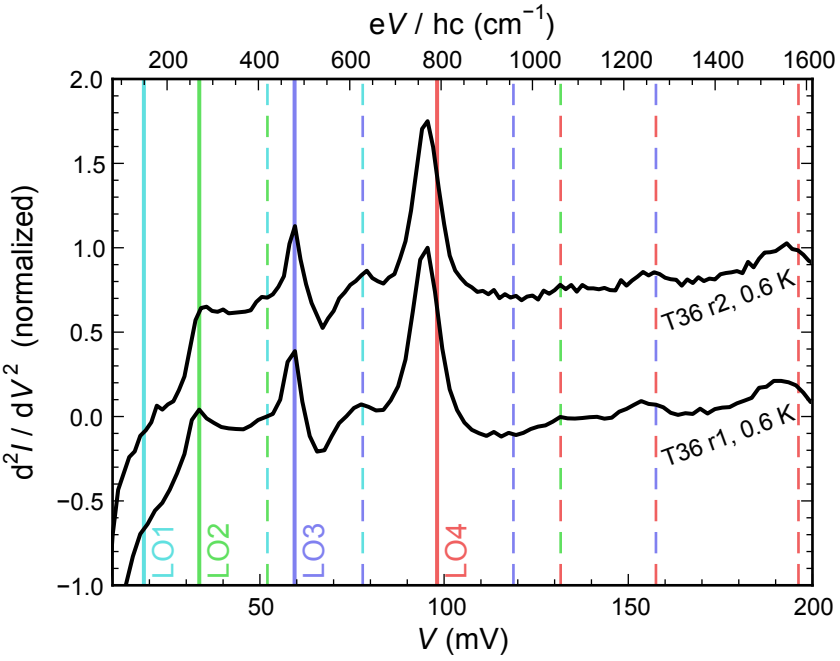

Fig. 3.16: Second derivatives of low-temperature inelastic tunneling $I(V)$ data from two tunnel devices on $LaAlO_3$-$SrTi^{18}O_3$ sample T36. The d^2I/dV^2 data have been normalized to a maximum of 1.0 and were offset from each other by 0.75 units. The colored lines mark $SrTi^{16}O_3$ phonon energies as identified in Figure 3.15. T36 is based on a $SrTi^{18}O_3$ substrate, as explained in the text.

electrode $\varrho_l(E)f(E)$ with the unoccupied states of the second electrode $\varrho_r(E+eV)(1-f(E+eV))$. $f(E)$ is the Fermi-distribution $f(E) = (1+\exp\frac{E}{\mathrm{k_B}T})^{-1}$, shifted by $\mathrm{e}V$ with respect to the Fermi-function on the right hand side, if a voltage V is applied to the right hand electrode. ϱ_l and ϱ_r are the densities of states of the respective electrodes left and right of the tunnel barrier. To obtain an expression for the elastic tunnel current (Equation 2.1), the current flowing in both directions, from and to both electrodes, has to be summed.

Whenever the voltage between the two electrodes is stepped up by an amount ΔV, the energy window in which occupied states on the one side face unoccupied states on the other side grows by an amount $\mathrm{e}\Delta V$. Consequently, every voltage step increases the tunnel-current by a fixed amount. The tunnel $I(V)$ characteristic between our model electrodes is linear, because each voltage step adds a new *channel* for elastic tunneling. For constant DOS ϱ_r, ϱ_l and $T = 0\,\mathrm{K}$, i.e. exchanging the Fermi-distribution $f(E)$ for a reversed Heaviside step function $\Theta(-E)$, this result is readily obtained from Equation 2.1:

$$
\begin{aligned}
I_e(V) &\propto \int_{-\infty}^{\infty} \mathrm{d}E \varrho_r(E)\varrho_l(E+eV)[f(E)-f(E+eV)]|\mathcal{M}|^2 \\
&\varrho_r, \varrho_l, |\mathcal{M}|^2 = const.; T = 0 \Rightarrow f(E) = \Theta(-E) \\
I_e(V) &\propto \varrho_r\varrho_l \int_{-\infty}^{\infty} \mathrm{d}E[\Theta(-E)-\Theta(-E-eV)] = \\
&= \varrho_r\varrho_l \int_{-\mathrm{e}V}^{0} \mathrm{d}E[\Theta(-E)-\Theta(-E-eV)] = \\
&= \varrho_r\varrho_l \int_{-\mathrm{e}V}^{0} \mathrm{d}E \\
I_e(V) &\propto \varrho_r\varrho_l\,\mathrm{e}V
\end{aligned}
$$

Inelastic tunneling provides an additional, alternative channel: Instead of tunneling elastically (from energy E to E) and conserving energy, an electron that can tunnel inelastically can also go from E to $E-\hbar\omega$, if it is able to give the energy difference $\hbar\omega$ to another quasiparticle, e.g. a phonon. Since this inelastic process involves at least two particles, it is usually less likely than the elastic single-particle path. Still, if an electron at an energy $E > \hbar\omega$ has the option to *either* go $E \to E$ or $E \to E-\hbar\omega$, this added option is another tunneling channel that each electron with $E > \hbar\omega$ has over every electron with $E < \hbar\omega$. Therefore, just as for $E < \hbar\omega$ the tunneling current increased by a fixed amount with each voltage step, for $E > \hbar\omega$ the current increases by a somewhat larger (but still fixed) amount with the same voltage step. The reason

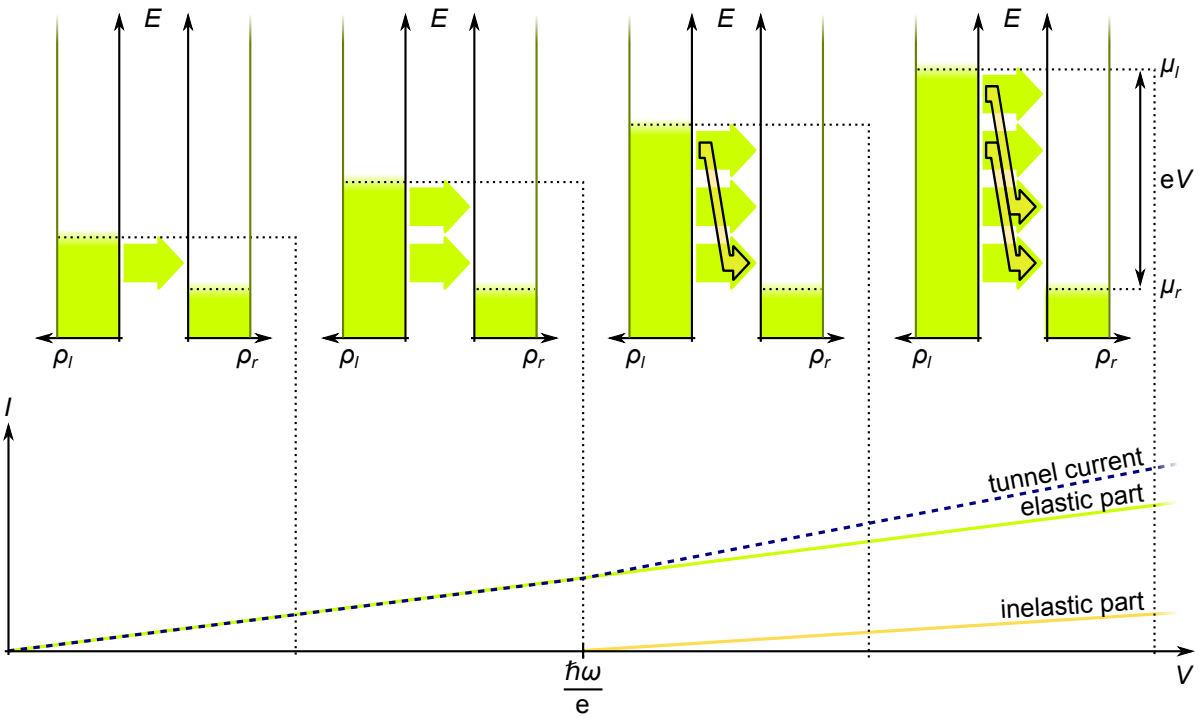

Fig. 3.17: Illustration of elastic and inelastic tunneling between two metals. The electrodes left and right of a tunnel barrier are represented by the graphs $\rho_l(E)$ and $\rho_r(E)$, which indicate their respective DOS (dark green solid line). Occupied states are represented by the bright green filling. A voltage V applied between the electrodes separates the electrochemical potentials μ_l, μ_r by an energy eV. Where occupied states on the left face empty states on the right, elastic tunnel currents flow, which are represented by green arrows. When eV exceeds the energy of an Einstein-phonon $\hbar\omega$, inelastic tunneling currents, represented by yellow arrows, are added. The $I(V)$ graph sketches the expected current-voltage characteristic with a kink at the voltage that corresponds to the phonon energy.

is that from $E = \hbar\omega$ each voltage step opens up not only an additional elastic, but also another (usually narrower) inelastic channel. In our model system, the tunneling $I(V)$ curve therefore has a kink at $\hbar\omega$, the energy of the inelastic excitation, which can be a phonon, plasmon, magnon, etc.—basically any quasiparticle that an electron can interact with.

This process can be modeled (see e.g. Refs. [139, 140]) in analogy to Equation 2.1, by introducing a probability density $P(\hbar\omega)$ of inelastic processes that an electron on the left hand side can interact with and lose energy $\hbar\omega$ before it tunnels to the right hand side. In the case of phonons, P closely resembles the phonon density of states.

$$I_i(V) \propto \int_{-\infty}^{\infty} \mathrm{d}E\, \varrho_l(E) f(E) \int_0^{\infty} \mathrm{d}(\hbar\omega) P(\hbar\omega) \varrho_r(E + \mathrm{e}V - \hbar\omega)[1 - f(E + \mathrm{e}V - \hbar\omega)] \quad (3.6)$$

Let $P(\hbar\omega)$ contain a single Einstein-phonon at energy $\hbar\omega_0$, with ϱ_l, ϱ_r constant at $T = 0$:

$$P(\hbar\omega) = \delta(\hbar\omega - \hbar\omega_0); \varrho_l, \varrho_r = const.; T = 0 \Rightarrow f(E) = \Theta(-E)$$

$$I_i(V) \propto \varrho_l \varrho_r \int_{-\infty}^{\infty} \mathrm{d}E\, \Theta(-E) \int_0^{\infty} \mathrm{d}(\hbar\omega) \delta(\hbar\omega - \hbar\omega_0)[1 - \Theta(-E - \mathrm{e}V + \hbar\omega)] =$$

$$= \varrho_l \varrho_r \int_{-\infty}^{\infty} \mathrm{d}E\, \Theta(-E)\Theta(E + \mathrm{e}V - \hbar\omega_0) =$$

$$= \varrho_l \varrho_r \int_{-\infty}^{0} \mathrm{d}E\, \Theta(E + \mathrm{e}V - \hbar\omega_0)$$

$$I_i(V) \propto \begin{cases} 0 & \forall\ \mathrm{e}V < \hbar\omega_0 \\ \varrho_l \varrho_r\ (\mathrm{e}V - \hbar\omega_0) & \forall\ \mathrm{e}V \geq \hbar\omega_0 \end{cases}$$

The inelastic tunneling current is $I_i = 0$ for $\mathrm{e}V < \hbar\omega_0$, and—as anticipated—linear with a positive slope for $\mathrm{e}V > \hbar\omega_0$. In sum with Equation 2.1 the result is exactly as anticipated: A linear $I(V)$ with a kink at $\hbar\omega_0$.

While this result is sound, it does not quite reflect what was measured in our Au-LAO-STO junctions: The results presented so far are different, in that it is not a kink, but a step in $I(V)$ at the phonon-frequencies. The simple model predicts a step in $\mathrm{d}I/\mathrm{d}V$ or a peak in $\mathrm{d}^2I/\mathrm{d}V^2$ at the phonon-frequencies, and this behavior is indeed found in many systems [71, 141, 142]. In thin Au-LAO-STO junctions, the peak is found already in $\mathrm{d}I/\mathrm{d}V$, not $\mathrm{d}^2I/\mathrm{d}V^2$; the step is in $I(V)$, not $\mathrm{d}I/\mathrm{d}V$.

3.2.4. Inelastic tunneling and LAO-STO band structure

Obviously, the simple model does not capture the situation in our Au-LAO-STO junctions. One striking difference is that one of the electrodes is not a simple metal. As we

have learned in the previous subsection, the 2DEL density of states around the Fermi-level is by no means constant. Instead, it has a steep positive slope, with the Fermi-level only a few meV above a band edge. The effect of this can be anticipated as illustrated in Figure 3.18. The basic difference between the simple model with constant $\varrho(E)$ on both sides of the barrier to the case of a large-curvature $\varrho_{\mathrm{2DEL}}(E)$ with its chemical potential only slightly above the conduction band edge is this: In the simple case, each voltage increase enlarged the energy window between the electrochemical potentials, in which occupied states on the one side faced unoccupied states on the other side (compare Figure 3.17). In principle, this situation is the same in LAO-STO with the essential difference, that the window in which occupied states in the 2DEL face empty states in the Au, is limited not by the difference in electrochemical potentials ($\propto$ applied voltage), but by the 2DEL band structure. This window spans the energy interval from the 2DEL's (highest) conduction band minimum up to the electrochemical potential (possible additional contributions of other bands are neglected at this point). This window is approximately constant, and independent of V. When a voltage increase does not enlarge this window, it does not add tunneling channels. Therefore, the tunneling rate and current are largely unaffected by the voltage. The $I(V)$ curve in this case is flat, until a new channel is added by another means; that is, until the energy eV is sufficient to excite a phonon $\hbar\omega_0$. At this point the tunnel current steps up. The step size, compared to the elastic current, is a measure of the electron-phonon coupling. Beyond $\hbar\omega_0$ the $I(V)$ characteristic is flat again, because—just as for e$V << \hbar\omega_0$—a voltage step does not add tunneling channels, since these are still limited by the narrow width of occupied states in the 2DEL.

In conclusion, the premise of a low chemical potential, only a few meV above the highest conduction band minimum, provides a natural explanation for the shape of the phonon peaks in the tunneling $\mathrm{d}I/\mathrm{d}V$ characteristics at positive voltages. The unique manner in which the phonons shape the tunnel spectra is, in turn, strong evidence for the correctness of the schematic band structure derived from the elastic tunneling data at negative voltages and around zero bias.

The band structure as seen by elastic tunneling was found to evolve with the LAO thickness: With increasing LAO thickness the xy-band with a flat DOS around E_{F} gained more spectral weight; the overall slope of the DOS around E_{F} flattened. The effect of this band structure evolution on the inelastic tunneling is shown in Figure 3.19, which plots the measured inelastic $J(V)$, $\mathrm{d}J/\mathrm{d}V$ and $\mathrm{d}^2J/\mathrm{d}V^2$ tunneling characteristics of Au-LAO-STO tunnel junctions with 4 uc, 5 uc, and 7 uc thick $LaAlO_3$ layers. Put simply, the inelastic tunneling characteristics evolve from the low chemical potential model (Figure 3.18) towards the simple metal–metal model (Figure 3.17). Whereas the $\mathrm{d}J/\mathrm{d}V$ of a 4 uc LAO-STO tunnel junction features mostly a peak around $V = 100\,\mathrm{mV}$, this structure becomes more and more step-like for thicker $LaAlO_3$ layers. Qualitatively, this behavior is in agreement with the LAO-thickness dependency of the low-energy band structure which I have derived from the elastic tunneling data. A quantitative analysis is difficult and computationally intensive, because the elastic, as well as 1st and 2nd

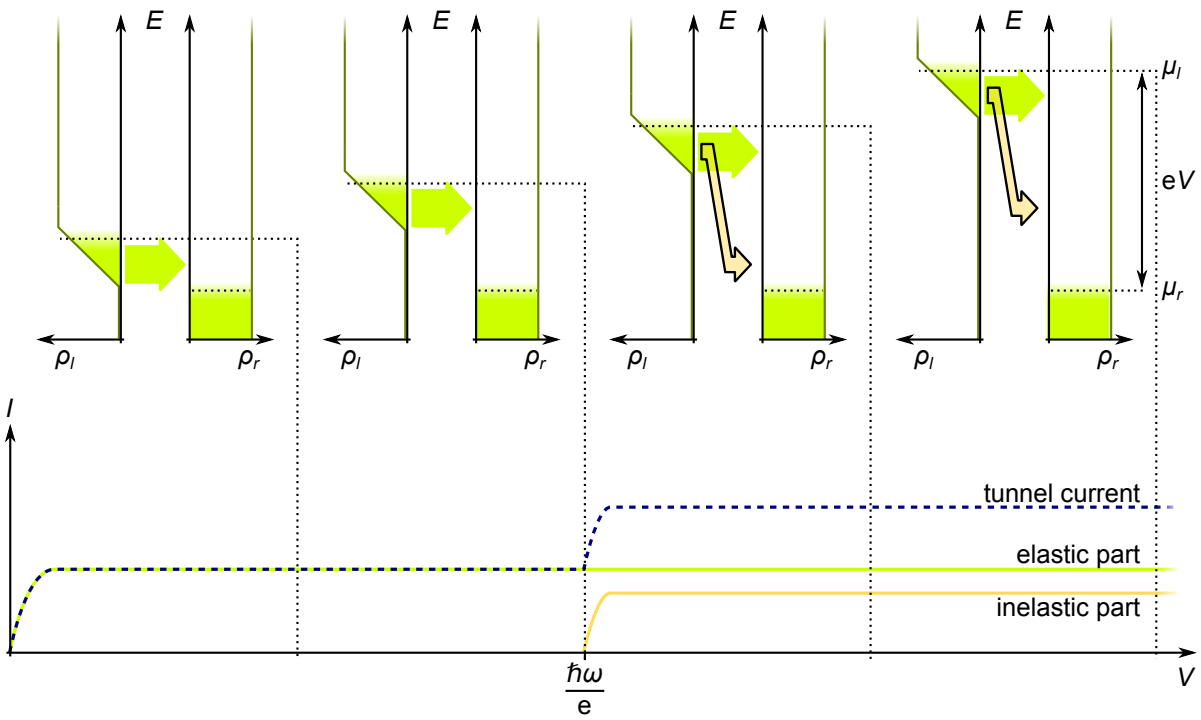

Fig. 3.18: Illustration of elastic and inelastic tunneling between a material with a sparsely populated band and a metal. In contrast to the example previously given in Figure 3.17, here, the tunnel current is limited not by the applied voltage, but by the low filling of the band on the left electrode.

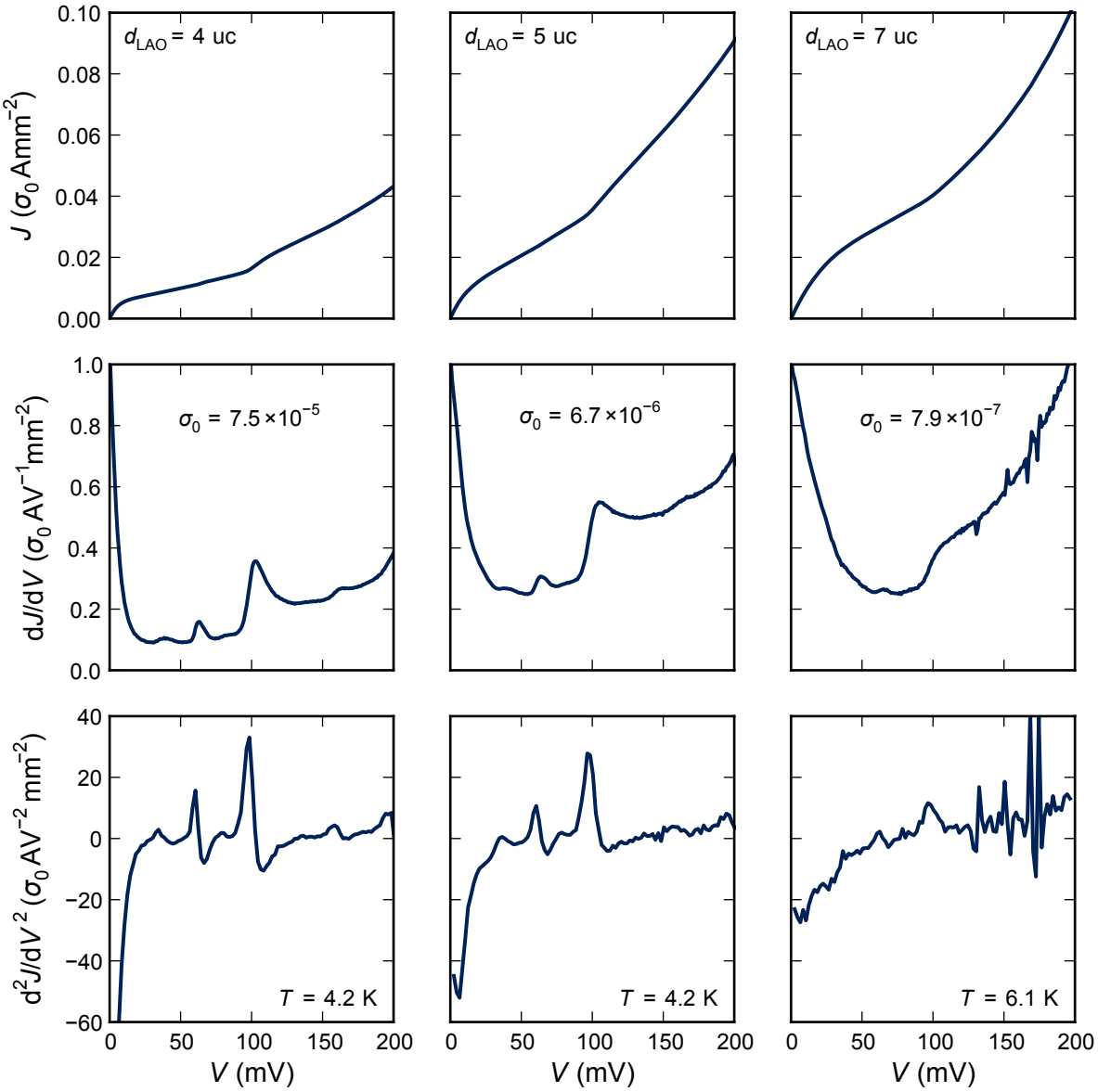

Fig. 3.19: Normalized tunnel current density J, and its 1st and 2nd derivative $\mathrm{d}J/\mathrm{d}V$ and $\mathrm{d}^2J/\mathrm{d}V^2$ of Au-LAO-STO tunnel junctions with different LAO thickness d_{LAO}. All data have been normalized to the zero-bias differential conductivity $\sigma_0 = \mathrm{d}J/\mathrm{d}V(V = 0)$. The $LaAlO_3$ thickness d_{LAO}, and the corresponding σ_0 and measurement temperature T are given in the upper, middle and lower corresponding graphs in the respective column.

order inelastic tunneling from 3 different bands with possibly different electron-phonon coupling per band and phonon mode must be taken into account. A good estimate of the electron-phonon coupling can already be obtained, though, by comparing the peaks at fundamental phonon-energies with the peaks at their respective first harmonic.

3.2.5. Summary and discussion

In summary, my Au-LAO-STO tunnel devices have provided insights into the low-energy density of states of $LaAlO_3$-$SrTiO_3$ interfaces and the phonon-spectrum of $SrTiO_3$.

Phonon spectroscopy For positive bias, inelastic tunneling of electrons was encountered, with the longitudinal optical phonons of $SrTiO_3$ as the dominant source of inelastic processes. The inelastic tunneling data can be used for robust and exact phonon-spectroscopy as well as for studying the coupling of electrons to the different phonon modes.

Low-energy band structure From the drastic $I(V)$ asymmetry and the manner in which $SrTiO_3$ optical phonons shape the inelastic tunneling, we have learned that the chemical potential inside the electronic system at the LAO-STO interface is situated only a few meV above a band edge. The $LaAlO_3$ thickness was found to directly affect the electronic structure at the LAO-STO interface. There has been previous theoretical[143] as well as experimental evidence[8] that this statement is not limited to the critical thickness for conductivity[52].

Recent results from resonant inelastic x-ray spectroscopy[8] (RIXS) and hard x-ray spectroscopy[58] (HAXPES) have clearly identified a density of (mostly localized) interface charge that grows beyond the Hall-value and saturates only at $d_{\mathrm{LAO}} > 6\,\mathrm{uc}$. Hence, a systematic increase of the Fermi-level with growing $LaAlO_3$ thickness was to be expected.

This increase can now be quantified. It is directly visible in the tunnel-spectra. The band edge shifts from -10 meV at an LAO thickness of 4 uc to -30 meV at an LAO thickness of 7 uc. This measured three-fold increase is compatible with the 3-4 times increase in (localized) charge carrier density found by the RIXS and HAXPES experiments[8]. The thickness dependence of elastic and inelastic tunneling at the LAO-STO interface therefore strongly supports the idea that the electronic reconstruction is not finished at $d_{\mathrm{LAO}} = 4\,\mathrm{uc}$; the electronic density at the interface continues to grow, even beyond 4 uc. Large fractions of this interface charge are not detectable in Hall-measurements, so not all of the sub-bands appear to contribute equally to electronic transport.

Implications on the superconducting state The main contribution to the tunneling density of states around E_{F} was tentatively ascribed to the Ti $3d_{xz}/3d_{yz}$ derived electronic bands at the $LaAlO_3$-$SrTiO_3$ interface. Consequently the superconducting gap, which was presented in the previous section, would in fact represent a band-gap not in the xy band, which is believed to host the high-mobility electron liquid[143], but in the xz/yz bands, which for their large effective mass are prone to localization[8].

3.3. Tunneling on a volt scale: barrier effects and interface resistivity

The concept of LAO-STO tunneling devices was largely inspired by the pioneering STM/STS experiments by Martin Breitschaft[9]. With his scanning probe microscope he was able to map the spectral density of (empty) states of the conducting interface between 4 uc of $LaAlO_3$ and TiO_2-terminated $SrTiO_3$ in an energy range of 0 to 2 eV. As presented in the previous sections, the goals behind the tunnel device concept could be achieved: the devices proved themselves in superconducting tunneling spectroscopy and in exploring the low-energy density of states of LAO-STO interfaces. This section is going to investigate if the devices can also be used to reproduce Martin's results and do tunneling spectroscopy on a 1 V scale.

3.3.1. Prerequisites

There are two potential obstacles. One is the shape of the potential barrier between the tunnel electrodes. The other is the resistivity of the $LaAlO_3$-$SrTiO_3$ interface itself, which can become a considerable hindrance to exact tunnel spectroscopy at high tunnel voltages.

Tunnel barrier effects

Tunneling spectroscopy can only give meaningful and easily interpretable information about the density of states, if the influence of the applied voltage on the tunnel barrier, i.e. on the barrier transmissivity, is more or less negligible. In *scanning* tunneling spectroscopy this prerequisite can usually be met by adjusting the tip-sample distance. Higher tunnel voltages require a larger barrier and therefore a larger distance between tip and sample. Martin Breitschaft successfully used this method to record tunnel spectra step-by-step over a wide voltage range[9]. In this regard, the rigid setup of my tunnel devices is a real drawback. The geometric arrangement of the tunnel junction is fixed during the sample growth. There is no way to enhance the tunnel barrier post-growth. Apart from choosing a different electrode material with a higher work-function, the only accessible option for adjustment of the tunnel barrier is to increase the thickness of the $LaAlO_3$ layer (or to insert an additional insulator). As proven in the previous section, however, this approach affects the electronic states at the LAO-STO interface. So from a sole consideration of tunnel barrier effects, it appears unlikely that tunneling spectroscopy on tunnel junctions with thin $LaAlO_3$ films can yield results that are comparable to that of Martin Breitschaft on a larger voltage scale.

Resistance of the 2DEL

An important aspect, which is specific to my tunnel junctions, is the resistance of the 2DEL. In conventional tunneling experiments with bulk conducting materials, the resistance of the tunnel *electrodes* is usually negligible when compared to the tunnel resistance

in *between* the electrodes. This is especially true in a scanning tunneling microscope, because the contact area between tip and sample is point-like. In other words: In a conventional tunneling experiment, the resistance of the tunnel junction is by far the highest resistance of the system. In this case, the contributions of the leads, the sample bulk and such are so minor, they can entirely be neglected, such that a 2-wire measurement of the tunnel resistance is perfectly acceptable.

In our LAO-STO tunnel junctions, before (after) an electron tunnels from the interface into the gold (or vice versa), it has to traverse the relatively high-ohmic 2DEL. The electrical resistance it encounters is the 2DEL sheet resistance R_s times the aspect ratio l/w of the pathway: $R_\mathrm{2DEL} = R_\mathrm{s}\, l/w$. Consequently, the 2DEL-resistance can be minimized by choosing a small aspect ratio. On the other hand, the tunneling current scales with the junction area $l \times w$: $I(V) = l \times w\, J(V)$, where $J_\mathrm{t}(V)$ is the voltage dependent tunneling current density, which for large V usually depends exponentially on V. The two equations can be combined to get a simple estimate of the voltage drop V_d that the tunneling current generates along the 2DEL:

$$V_\mathrm{d} < R_\mathrm{2DEL} I(V) = \frac{l}{w}\, R_\mathrm{s} J_\mathrm{t}(V)\, l \times w = R_\mathrm{s} l^2 J_\mathrm{t}(V) \tag{3.7}$$

Obviously, with the assumption that all of the tunneling current travels the complete depth of the junction, this is a rather crude upper estimate. The simple derivation is, however, adequate to stake out the spectroscopically accessible voltage range on the one hand, and to set out optimization strategies for enhancing this voltage range on the other hand.

Optimal temperature and device scaling

First, the voltage drop naturally depends on the sheet resistance R_2DEL. Exact spectroscopy therefore favors low temperatures, at which the 2DEL resistance is minimal. This fact is visualized in Figure 3.20, which shows the temperature dependency of tunneling $I(V)$-curves, which are broadened by the voltage drop along the LAO-STO interface beneath the tunnel electrode of a linear $w = 1.60$ mm wide, $l = 0.20$ mm deep tunnel device with 4 uc of $LaAlO_3$. For these measurements (see the figure inset for a schematic), a tunneling current to the junction's top-electrode was driven from one side of the junction. The voltage drop along the 2DEL beneath the tunnel electrode was measured as well as the voltage between the top-electrode and the other side of the junction, which was also used as a feedback signal to step the current. In an ideal scenario, in which the 2DEL resistance is small compared to the tunnel resistance, the voltages on both sides of the junction are identical. For all measurements presented in the previous sections, this was practically the case. For high voltages (or rather the resulting high currents) and high temperatures the 2DEL resistance makes the tunnel devices depart severely from that idealization.

Second, the voltage drop according to Equation 3.7 is independent of the junction width, but depends quadratically on the junction depth. It is therefore advisable to

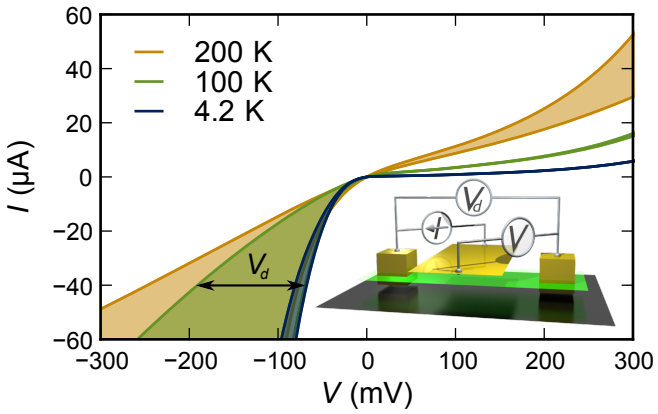

Fig. 3.20: Current-voltage $I(V)$ tunnel-characteristics of a 4 uc Au-LAO-STO tunnel junction, which is 1.60 mm wide and 0.20 mm deep, at three different temperatures. The horizontal width of the shaded areas demonstrates the voltage drop V_d along the 2DEL, due to its temperature dependent sheet resistance. The inset sketches the measurement setup, with the 2DEL depicted in green and the Au-contacts in gold/yellow.

design the junctions as thin as possible. Unfortunately, the approximately exponential shape of $J_t(V)$ implies, that the voltage drop goes exponentially with V, too: $V_d \propto \exp(V)$. Therefore, to extend the usable voltage range of a given junction by a fixed amount ΔV, its depth has to be scaled by a *factor* $\sqrt{\exp(\Delta V)} = \exp(\Delta V/2)$.

This, in turn, limits the extent to which device scaling can practically extend the spectroscopically accessible voltage range. In my experiments, tunnel electrodes with a depth down to approximately 10 µm have been used. Even with these thin devices, and at cryogenic temperatures, well-defined tunneling spectroscopy with 4 uc LAO samples was only possible for $|V| \lessapprox 0.5$ V.

LAO thickness scaling

An alternative approach to shrinking the depth of the tunnel junction is to limit the tunnel-current density by increasing the thickness of the tunnel barrier, i.e. to use thicker $LaAlO_3$ layers. This is reminiscent of the aforementioned method of adjusting the tip-sample distance in a scanning tunneling microscope. The method is very effective in limiting the current density J_t, because J_t decreases exponentially with the inverse barrier thickness. Experimentally I have found that each $LaAlO_3$ monolayer added to the tunnel barrier decreases J_t by about a factor of 12. Translated to the above-mentioned resistive restrictions, the addition of a single monolayer of $LaAlO_3$ increases the accessible voltage range by around 0.15 V. Hence, in order to do well-defined tunnel spectroscopy of the density of states of LAO-STO interfaces at voltages exceeding 1 V with solid-state tunnel devices, relatively thick (> 10 uc) $LaAlO_3$ layers are required. Of course, such devices yield very low (unmeasurable) tunnel currents at lower voltages. Clearly, a scanning tunneling microscope has a great advantage in this regard, as its tip-sample distance can be adjusted to accommodate different tunneling voltage ranges.

3.3.2. Results

Reproducible results from tunneling measurements at higher voltages are scarce. In particular, no unanimous confirmation of Martin Breitschaft's STM results could be achieved. Figure 3.21 presents the measured normalized differential conductance NDC =

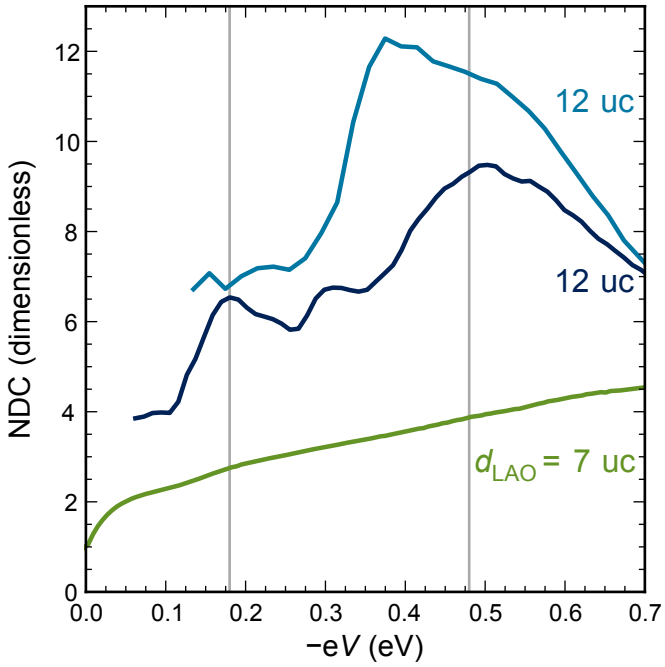

Fig. 3.21: Normalized differential conductance measured on three different tunnel junctions, on two different samples with either 12 uc (blue lines, measured at 30 K) or 7 uc (green line, measured at 20 K) of $LaAlO_3$.

$(\mathrm{d}I/\mathrm{d}V)/(I/V)$ of different junctions with either 7 or 12 uc thick $LaAlO_3$ layers. This data represents the measured density of unoccupied states of LAO-STO interfaces, the x-axis gives the energy $-eV$ of an electronic state at the interface with regard to the chemical potential of the gold-electrode. Common peaks can be found at about 0.15 to 0.25 eV and 0.4 to 0.6 eV. For the 12 uc sample, the peaks are not reproducible in detail among different junctions. The detailed shape even differs from one measurement to the next, on one and the same junction. The tunneling currents in that range are, however, very small: The curves shown were cut off at a current of 1 pA; at -0.2 V (0.2 eV), the current through a $0.1 \times 1.6\,\mathrm{mm}^2$ junction is just about 100 pA.

For the 7 uc sample, the tunneling currents are more than 4-5 orders of magnitude larger. The peaks in NDC(V) are more reproducible, but very faint. This suggests that sources outside the interface density of states (i.e. barrier-effects) affect the tunneling current dominantly.

While the normalized differential conductance spectra measured on the 12 uc junctions do not contradict the STM results, they are no clear confirmation either. In either experiment, the reproducibility of spectra in that voltage range was poor. Unfortunately, at higher voltages, for which the STM experiments gave sufficient data with good reproducibility, my tunnel junctions fail to deliver useful results. At tunnel-voltages of < -1 V on the gold-electrode, which corresponds to the targeted energy range > 1 eV, the electric field-effect increases the sheet-resistance of LAO-STO interfaces dramatically[2, 16]. A tunnel junction in this state is comparable to an n-channel MOSFET[5] biased below its threshold voltage. The subthreshold conduction of a MOSFET channel varies exponentially with the gate-voltage. This brings about a steep potential gradient along

[5] In fact, excellent FETs can be created utilizing LAO-STO interfaces as their drain-source channels. Appendix A gives an overview.

the 2DEL covered by the gold (gate) electrode. The tunnel voltage as well as the effective area of the tunnel junction become ill-defined as a consequence. This effect can be measured with capacitance-voltage spectroscopy[13] and was utilized in novel oxide-interface diodes[7]. Yet it severely limits the applicability of my tunneling devices at higher voltages.

3.3.3. Summary

The applicability of my tunnel devices for tunneling spectroscopy of the density of states of LAO-STO interfaces is limited by the sheet-resistance of the 2DEL in conjunction with the electric field-effect and tunnel barrier instabilities. Useful, reproducible spectra could only be obtained for voltages smaller than 1 V. Hence, my planar tunnel devices could not reach their original benchmark, namely to reproduce Martin Breitschaft's spectra, which he had obtained with scanning tunneling spectroscopy. Its point-like probe and the ability to adjust with the tip-sample distance the tunnel barrier to different voltage ranges makes an STM a much better suited instrument to study the density of states of LAO-STO interfaces at higher energies.

Modifications to the design of my tunnel devices, like more aggressive downscaling of the junction-depth, or the addition of a material with a low dielectric constant between the gold-electrode and $LaAlO_3$ could enable planar tunnel junctions to catch up in this respect. In their current implementation, however, planar tunnel junctions are not apt to reproduce Martin Breitschaft's pioneering tunneling spectroscopy.

3.4. Summarized results of tunneling experiments

I have designed, developed and fabricated planar solid-state tunnel junctions with the conducting interface between $LaAlO_3$ and $SrTiO_3$ as one tunnel electrode. A number of different materials were examined as a counter-electrode, of these materials, gold was found to be the most practical. The Au-$LaAlO_3$-$SrTiO_3$ tunnel devices have been investigated thoroughly, both structurally and electronically. They were put to use in very different voltage and temperature ranges.

1 Volt range The natural initial benchmark, to reproduce the tunnel-spectra previously obtained with scanning tunneling spectroscopy, could not be reached. For various reasons, the tunnel devices are not well-suited to tunneling spectroscopy on a 1 V voltage range. An STM has several advantages over my tunnel devices in that range.

Millivolt range For lower voltages, below about 500 mV, the tunnel devices become beneficial. Detailed information on the DOS of electrons as well as phonons could be gained in the millivolt range. The chemical potential of $LaAlO_3$-$SrTiO_3$ interfaces was found just a few meV above a band-edge. This finding is in agreement with predictions from density-functional theory as well recent ARPES results[21]. Referring to these results, the identified band-edge would belong to the Ti d_{xz}/d_{yz} bands. These bands also contribute the most to tunneling currents in the microvolt range.

Microvolt range At millikelvin temperatures, a gap develops in the measured tunnel-spectra. The gap, which is the signature of the two-dimensional superconducting state of LAO-STO interfaces, opens at about $T^* = 0.30\,\mathrm{K}$ and spans around $2 \times 40\,\mu\mathrm{eV}$ at 0.05 K. Like in the pseudogap-phase of high-temperature superconductors, the resistive critical temperature T_{BKT} is much smaller than T^*.

Using a back-gate to modulate the charge carrier density at the interface another analogy to the pseudogap-phase became apparent: the superconducting gap decreases monotonously with the electron doping level, i.e. the gap steadily increases, when the LAO-STO interface is depleted.

In summary, the developed tunnel junctions could not be used to reproduce previously published STM results. Instead, they revealed unique details about the near-Fermi-energy electronic structure, the electron-phonon coupling and the superconducting state of $LaAlO_3$-$SrTiO_3$ interfaces. These results are also summarized in a recent manuscript[24].

4. LAO-STO torque magnetometry

This chapter describes the direct experimental determination of the magnetic properties of LAO-STO interfaces by cantilever-based torque magnetometry. The experiments were enabled by a collaboration with Lu Li and Ray Ashoori at the Massachusetts Institute of Technology, Cambridge USA. Lu Li, who is an expert in torque magnetometry[66], has performed the measurements on samples which I have grown in Augsburg. This work has also been published in Nature Physics[14]. Parts of the text and the layout of the figures are copied from our publication.

Measuring the magnetization of a two-dimensional system requires extremely sensitive methods, because the magnetized volume and consequently the observable magnetic moment is extremely small. Moreover, the magnetic signal originating from an interface is often hidden in the orders of magnitude larger background from the surrounding bulk. A highly sensitive technique with an explicit selectivity for anisotropic media like interfaces is (cantilever-based) torque magnetometry. We have applied this technique to PLD-grown LAO-STO samples.

The working-principle of cantilever-based torque magnetometry has been explained in subsection 2.1.3. The sample growth has already been described in section 2.3. LAO-STO samples with 5 uc of $LaAlO_3$ and small Nb-contacts to the conducting interface have been investigated. Furthermore, 5 control samples have been measured: these were a TiO_2-terminated $SrTiO_3$ substrate, an as-bought $LaAlO_3$ substrate, 5 uc of $LaAlO_3$ grown on a $LaAlO_3$ substrate and two 0 uc LAO on STO samples. All n uc samples including the 0 uc samples were processed identically, including substrate preparation, a complete PLD heating- and cooling-cycle, contact preparation and wire-bonding as described in section 2.3. In contrast to the 5 uc samples, however, no laser pulse has entered the PLD chamber during the 0 uc $LaAlO_3$ "depositions".

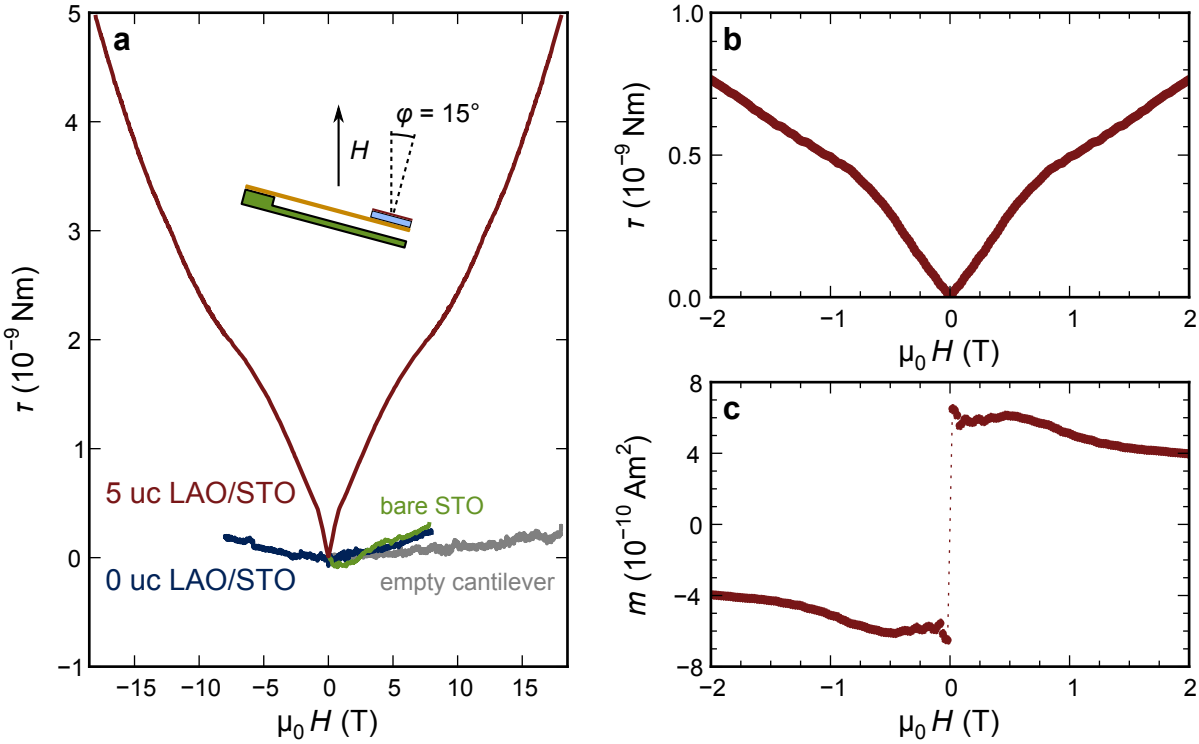

Fig. 4.1: Torque magnetometry of LAO-STO interfaces. **a)** The field dependence of the torque curves of various test samples (cantilever only, bare STO substrate and 0 uc sample) and a 5 uc LAO-STO sample, measured at $T = 300$ mK and tilt angle $\varphi = 15°$, the inset shows a schematic representation of the cantilever setup. **b)** Magnification of the low-field torque-data of the 5 uc sample. **c)** The magnetic moment $m(H) = \tau(H)/(\mu_0 H \cos\varphi)$ of the 5 uc sample, derived from the torque data in **b)**. (after [14])

4.1. Magnetometry results

The red curves in Figure 4.1 present the torque $\tau(H)$ and magnetic moment $m(H)$ of a 5 uc LAO-STO sample measured at $T = 300$ mK. The torque signal has a pronounced reversible curve with a sharp "cusp" at low field. This cusp is displayed clearly by Figure 4.1b, which zooms into this cusp. Figure 4.1c shows $m(H)$ determined from the $\tau(H)$ data. The V shape of the $\tau(H)$ curve centered at $H = 0$ yields a non-zero, H-independent m for $\mu_0 H$ up to 0.5 T. Close to $H = 0$, m jumps to 6×10^{-10} Am^2 = $2.6 \times 10^{14} \mu_B$ cm^{-2}, which corresponds to $0.4\,\mu_B$ per interface unit cell (assuming that the signal is generated by the single STO unit cell next to the interface). The values of m very close to zero field ($|\mu_0 H| \leq 5$ mT) are hard to determine, because the small H causes a large relative noise δm. At $|\mu_0 H| = 5$ mT, $\delta m \sim 4 \times 10^{10}$ Am^2, which is close to the magnitude of m. Starting at fields of order 1 T, m diminishes gradually at higher H, suggesting that an extra contribution appears in high fields. This high-field contribution was found to vary among different runs. The analysis below therefore focuses on the low-field behavior. To explore whether the torque signals originate from the LAO-STO interface, we performed control experiments using the reference samples described above.

Sizable torque signals were only observed from samples containing LAO-STO interfaces, the torque of which exceeds that of all background samples by two orders of magnitude. The negligible signals of the reference samples exclude several possible sources for the measured magnetic moment. These include the $SrTiO_3$ substrate, the $LaAlO_3$ film, the $LaAlO_3$ surface, the Nb contacts, the silver paste on the samples' back side as well as extrinsic, spurious contributions, which might have been introduced unintentionally during the sample growth. The most likely origin of the measured magnetic moment consequently is the LAO-STO interface.

4.1.1. Nature of the magnetic ordering, temperature dependence

The measured reversible $m(H)$ curves are consistent with superparamagnetism. In a superparamagnet ferromagnetic domains or clusters exist, but are so small, that their zero-field magnetic moment is controlled by thermal fluctuations. A superparamagnet features the large saturation magnetization of a ferromagnet, but has zero coercive field, i.e. it does not retain its magnetization, when the external field is removed.

Since thermal fluctuations are in direct competition with the magnetic ordering in a superparamagnet, a superparamagnetic magnetization curve has a characteristic temperature dependence, which is given by a Langevin function:

$$M(H) = \mathrm{M_s}(\coth \frac{\mu_0 \mu H}{\mathrm{k_B} T} - \frac{\mathrm{k_B} T}{\mu_0 \mu H}). \tag{4.1}$$

The equation expresses the magnetization M of a superparamagnet as a function of magnetic field H. M_s is the saturation magnetization, μ the magnetic moment of a single (super-)paramagnetic particle or cluster, T the temperature and $\mathrm{k_B}$ the Boltzmann constant. In Figure 4.2, the Langevin function is evaluated to give $M(H)$ and the corresponding magnetic torque curves $\tau(H) = \mu_0 H\, M(H)$ for selected values of T and μ. Figure 4.3 presents the measured temperature dependence of a 5 uc sample's $\tau(H)$ characteristics for comparison.

No significant temperature dependence of the $\tau(H)$ curves is observed between 0.3 K and 40 K, which sets a lower bound of $10^3 - 10^4 \mu_\mathrm{B}$ on the collective magnetic moment μ.

Besides with superparamagnetism, our measured $m(H)$ curves are also consistent with weak ferromagnetism: if the coercive field was < 5 mT, it would not be detectable by our experiment due to the large m noise at $|\mu_0 H| < 5$ mT. Although the two possibilities can not be distinguished by our data, both of them suggest a strong ferromagnetic-like coupling within domains.

4.1.2. Orientation of the magnetic moment

To determine the orientation of the magnetic moment, we made a series of torque measurements in which the sample tilt angle φ (as defined in the inset of Figure 4.1a) was

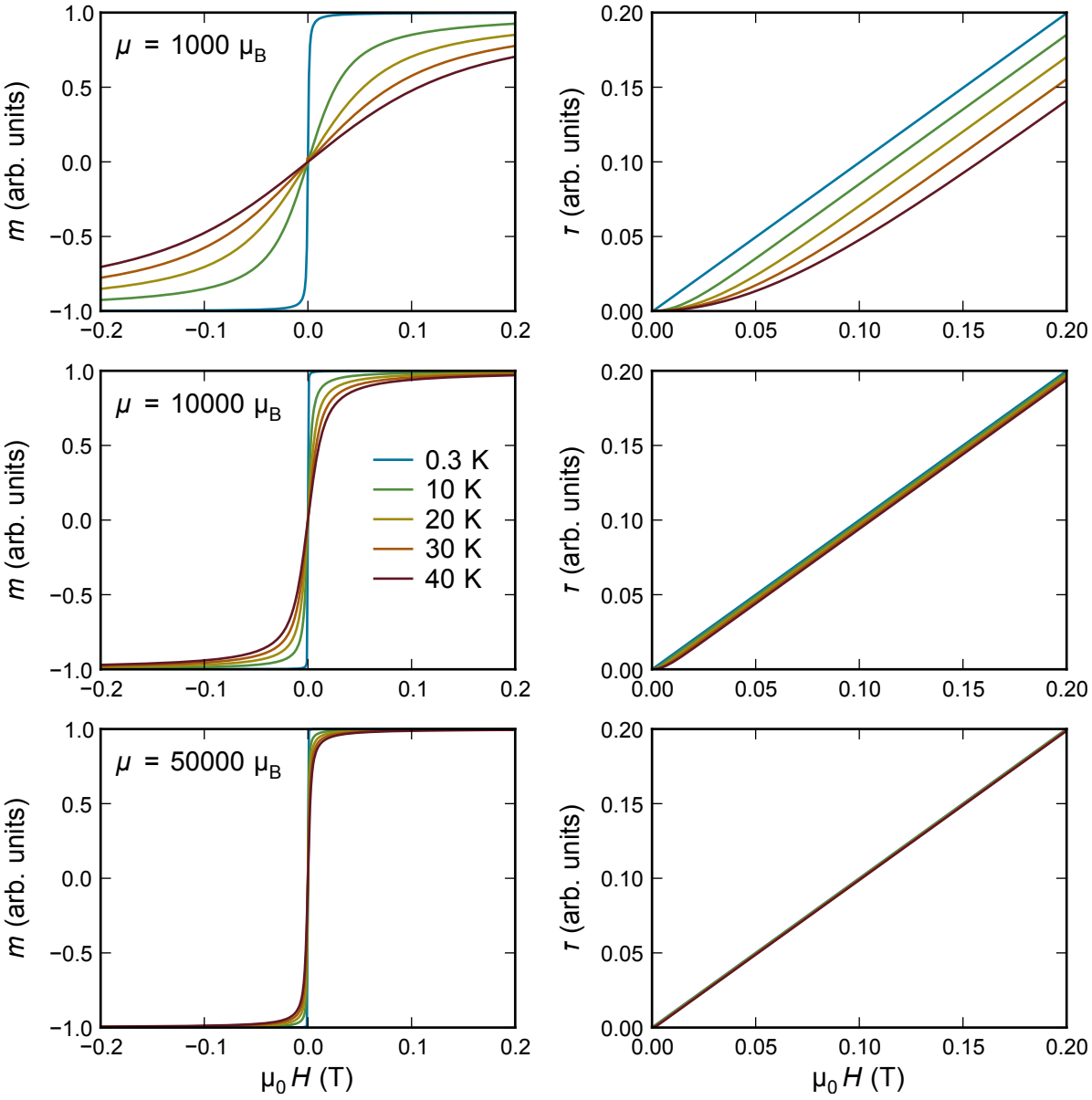

Fig. 4.2: Calculated magnetization $M(\mu_0 H)$ and magnetic torque $\tau(\mu_0 H)$ curves, according to the Langevin equation (Equation 4.1). The equation is evaluated for temperatures between 0.3 K and 40 K using different values for the collective magnetic moment μ of 10^3 (upper row), 10^4 (center row) and 5×10^4 (lower row) Bohr magnetons μ_B.

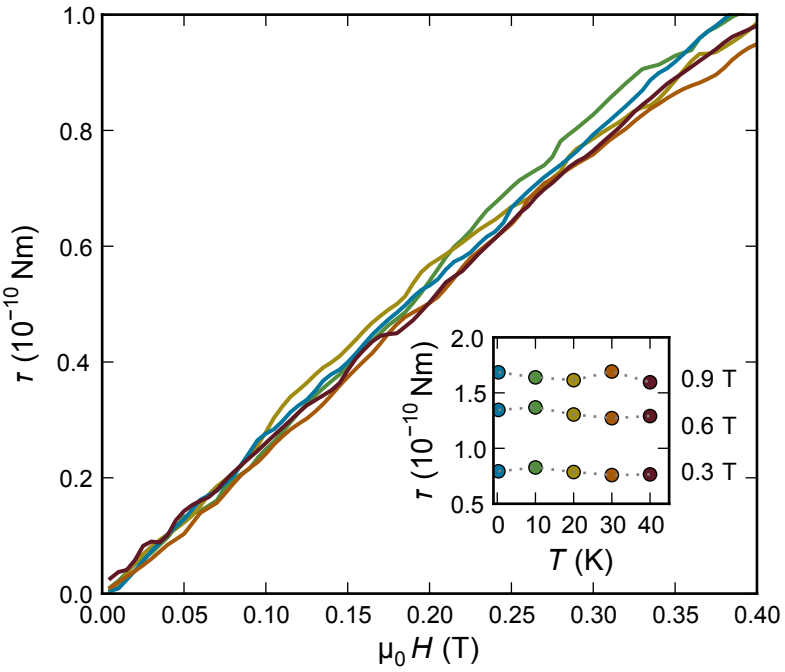

Fig. 4.3: Torque versus H curves of a 5 uc LAO-STO sample measured at selected temperatures between 300 mK and 40 K with a tilt angle of $\varphi \approx 49°$. The inset shows the temperature dependence of the magnetic torque at 0.3, 0.6 and 0.9 T using the same color code for temperature, as the $\tau(H)$ curves in the main graph.

varied. Because $\vec{\tau} = \mu_0 \vec{m} \times \vec{H} = \mu_0 m H_\perp$, where $H_\perp$ is the component of $\vec{H}$ perpendicular to $\vec{m}$, the orientation of the moments can be discerned by tracking the angular dependence of the torque signal. In a highly anisotropic system, m is determined by $H_\parallel$, the field component parallel to $\vec{m}$. Thus if $H_\parallel$ is large enough to saturate m, τ will increase as a sine function of the angle between $\vec{H}$ and $\vec{m}$. On the other hand, once $H_\parallel$ is insufficient to saturate m, τ will stop following the sine behavior.

The angle dependence shows that the saturation magnetic moment stays in the plane of the interface. We carried out low-field torque measurements at 300 mK at 30 different tilt angles. Figure 4.4 shows the $\tau(H)$ curves at several selected angles φ. As shown in Figure 4.4a, as φ changes from 15° to 94°, τ decreases monotonically and slowly approaches zero at $\varphi \approx 90°$, where $\vec{H}$ is almost parallel to $\vec{m}$. On the other hand, as φ varies between +15° and −10°, $\vec{H}$ is almost perpendicular to $\vec{m}$. $H_\parallel$ decreases and eventually changes to the opposite direction. The in-plane magnetic moment drops to zero once $H_\parallel$ is close to zero. As a result, the $\tau(H)$ curves swing from a positive saturation at $\varphi \approx 15°$ to a negative saturation at $\varphi \approx -10°$.

4.1.3. Summary

In summary, using torque magnetometry we have identified a ferromagnetic- or superparamagnetic-like magnetic ordering at LAO-STO interfaces. We have determined the saturation magnetic moment to be oriented in-plane with a magnitude of $0.3-0.4\,\mu_B$ per interface unit cell. The Curie-temperature is > 40 K. A tantalizing question is, whether the identified magnetic order can coexist with the two-dimensional superconductivity previously found at LAO-STO interfaces.

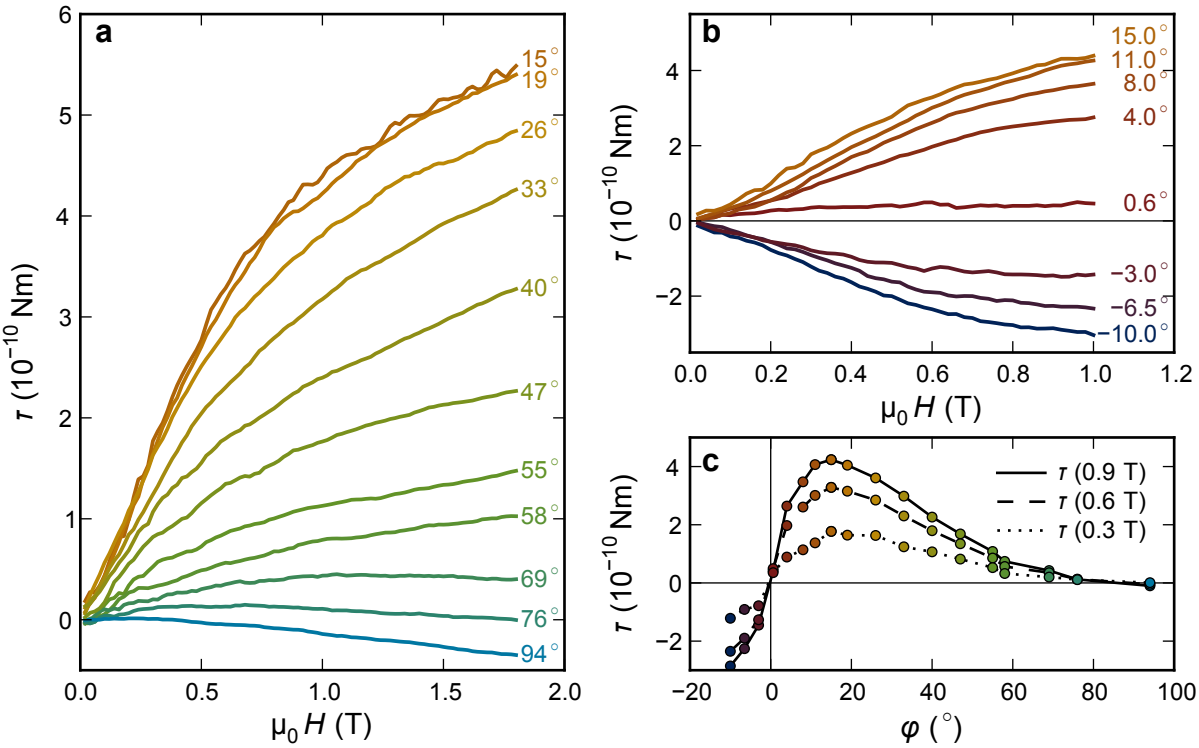

Fig. 4.4: Angular dependence of the interface magnetic torque τ measured at $T = 300$ mK, for tilt angle φ varying from 94° to 15° (**a**) and 15° to 10° (**b**). In **c)** the torque measured at 0.3, 0.6 and 0.9 T is plotted as a function of tilt angle φ.

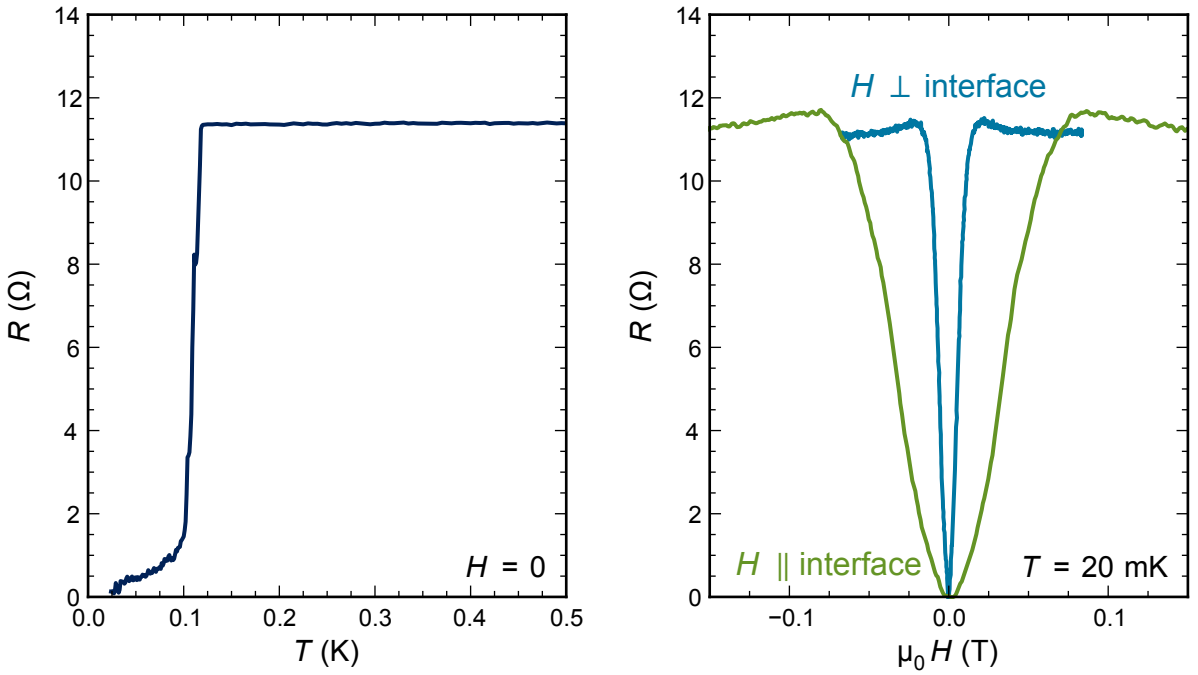

Fig. 4.5: 4-wire resistance of a 5 uc LAO-STO sample as a function of temperature T at $H = 0$ (left) and magnetic field at $T = 20$ mK (right). The critical temperature is about 120 mK. The critical field for H perpendicular to is much lower than for H parallel to the LAO-STO interface.

4.2. Coexistent superconductivity and magnetic order

To clarify the question of coexistence regarding the magnetic ordering and the superconducting state, we performed 4-wire transport measurements utilizing the ohmic Nb-contacts of one of the 5 uc LAO-STO samples. Figure 4.5 presents the temperature and magnetic field dependence of the electrical resistance R. The $R(T)$ data show a superconducting transition at $T_c \approx 120$ mK with a resistance foot extending to 25 mK. The critical magnetic field, which can be derived from the $R(H)$ data, is highly anisotropic with $\mu_0 H_{c\perp}$ (perpendicular to the interface) and $\mu_0 H_{c\parallel}$ (parallel to interface plane) on the order of 10 mT and 50 mT, respectively. This anisotropy has previously been reported[3]. It is a signature of the two-dimensional nature of the superconducting state at LAO-STO interfaces.

Figure 4.6 compares directly the resistance $R(H)$ and magnetization $m(H)$ measured on the very same sample. As can be seen, a finite magnetic moment m is recorded at $\mu_0 H_\perp = 5$ mT, whereas the sample resistance R does not reach the normal-state value until $\mu_0 H_\perp = 20$ mT. The magnetic ordering signal and the superconducting state are therefore found to coexist. Different authors have recently arrived at the same conclusion using diverse experimental techniques and LAO-STO samples grown in different institutions.[144–148] Whether the superconductivity and the magnetic signal originate from the same or separate electronic phases remains to be seen. The following section will discuss this question using our tunneling spectroscopy results.

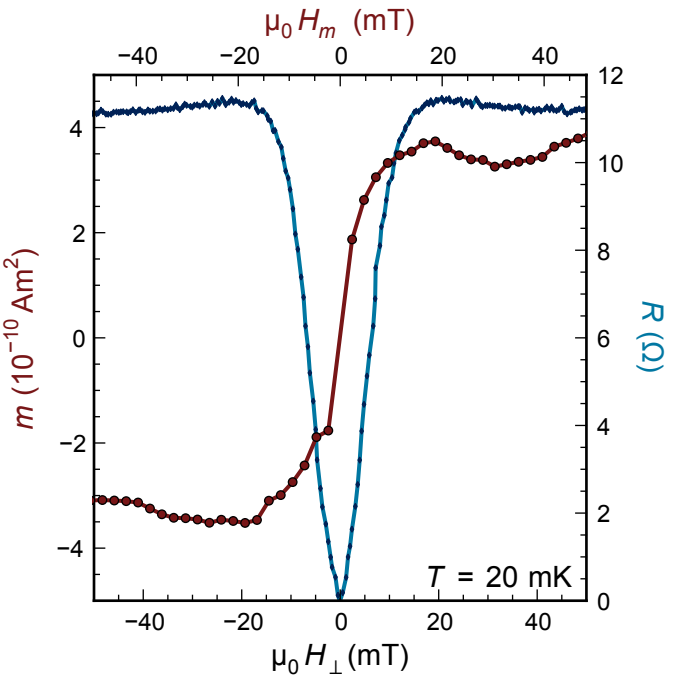

Fig. 4.6: 4-wire resistance and magnetization of a 5 uc LAO-STO sample as a function of the applied magnetic field component $H_\perp$ perpendicular to the LAO-STO interface (lower scale). Both measurements were done at $T = 20$ mK. For the torque magnetometry, the cantilever tilt angle was $\varphi = 15°$, so $H_\perp = H_m \cos 15°$, where H_m denotes the absolute magnitude of the applied magnetic field, which is given in the upper scale. For the $R(H)$ measurement the magnetic field was a priori oriented in perpendicular to the LAO-STO interface, so $H_\perp = H$.

4.3. Discussion of electronic phase separation

The key result of my tunneling spectroscopy with solid state planar tunnel devices is the measurement of the superconducting gap of $LaAlO_3$-$SrTiO_3$ interfaces, the temperature- and doping-dependence of which is akin to the pseudogap phase of high-T_c superconductors. In the superconducting state the measured quasiparticle density of states of $LaAlO_3$-$SrTiO_3$ interfaces is, apart from finite lifetime effects[87], fully gapped around E_F. In particular, the best fits to the acquired tunnel spectra were obtained assuming only a single tunneling channel into a superconducting state. No parallel tunneling channels, e.g. into normal-conducting domains, could be identified. This result has several consequences relevant to the coexistent superconducting and magnetic order and the question of electronic phase separation: Are the magnetic signal and the superconductivity created by the same or separate electronic phases?

The tunneling results are inconsistent with parallel normal-conducting and superconducting patches, distributed side-by-side along the interface plane. That is assuming both phases would contribute a comparable tunneling probability. If different phases are stacked in layers coplanar to the interface, with different phases in different $SrTiO_3$ layers, then the topmost layer with a tunneling density of states must be superconducting.

The tunneling results are consistent with a spatially homogeneous superconducting state in the TiO_2 layer nearest to the interface. They are consistent with localized magnetic moments, too, but only as long as those do not locally destroy superconductivity on sizable fractions of the tunneling interface area. Recent DFT-results[64] point to oxygen vacancies in either $LaAlO_{3-\delta}$ or $SrTiO_{3-\delta}$ layers near the interface as a possible origin of localized magnetic moments.

The superconducting and ferromagnetic phases could be associated with different electronic bands. If so, the non-superconducting spin-polarized band must be characterized by a small tunneling density of states that did not appear prominently in the tunnel spectra. Multiple sub-bands have indeed been identified in the measured tunnel spectra and were tentatively assigned to different Ti $3d$ orbitals, with major contributions of the d_{xz}/d_{yz} and negligible contributions of d_{xy} around E_F.

Our data are consistent with the idea that the same electron system forms a magnetically ordered, superconducting electron liquid. These two properties are usually considered to be mutually exclusive, but have been suggested to coexist in finite-momentum pairing states[149, 150]. Experimentally, coexisting magnetic and superconducting order have been found in very few systems, notably some heavy-fermion superconductors[151].

At LAO-STO interfaces the broken inversion symmetry and the Rashba spin-orbit interaction[108] might enable spin triplet superconductivity[119] and a Fulde-Ferrell-Larkin-Ovchinnikov (FFLO) finite-momentum pairing state[120, 121].

Our tunneling results provide hints to both of the proposed FFLO models by Michaeli et al. [120] and Loder et al. [121]: The main contribution to the tunneling spectra in the

microvolt range probably was from the Ti $3d_{xz}$ and $3d_{yz}$ sub-bands, which set in only a few mV below E_F. The superconducting gap has consequently developed in these bands. This would be in agreement to K. Michaeli, A. Potter and P. Lee[120]. The authors ascribe the main magnetic contribution to a non-superconducting, spin polarized $3d_{xy}$ band. This proposition is consistent with our measurements, if our assignment of the band-edge to the $3d_{xz}$ and $3d_{yz}$ sub-bands is correct. On the other hand, the peculiar zero-bias anomalies in the tunneling characteristics (see Figure 3.11) are reminiscent of the DOS derived by F. Loder, A. P. Kampf and T. Kopp[121, Fig. 3]. The authors predict different possible configurations of inter- and intra-band coupling that are controlled mainly by spin-orbit coupling and the in-plane magnetic field.

In conclusion, a single electronic phase that is responsible for both magnetism and superconductivity at LAO-STO interface is indeed possible and consistent with my tunneling spectroscopy results. On the other hand, certain configurations in which magnetism and superconductivity are generated by separate electronic phases are compatible with those results as well. Further experiments are needed. Torque magnetometry with a gated 2DEL (using, e.g., a back-gate or EDL) could be used to assess and compare the magnetism of itinerant and localized electrons. Spin-polarized tunneling with a ferromagnetic tunnel electrode could be used to measure the degree of spin-polarization in the different interface bands. Tunneling-spectroscopy in magnetic fields and/or with superconducting tunnel-electrodes instead of Au (Josephson-junctions) could give further experimental clues for clarifying the nature of the superconducting state. Such a Josephson-tunneling experiment in order to prove a finite-momentum superconducting state is discussed by Michaeli et al. [120].

5. Conclusions and outlook

The main part of this thesis has pursued two fundamental properties of $LaAlO_3$-$SrTiO_3$ interfaces: the magnetic ordering and energetic ordering (DOS) inside the 2-dimensional electron liquid. In both fields, robust results have been achieved.

Using cantilever-based torque magnetometry, we have uncovered a ferromagnetic- or superparamagnetic-like ordering at conducting $LaAlO_3$-$SrTiO_3$ interfaces. We have determined the saturation magnetic moment of $0.3 - 0.4\,\mu_B$ per interface unit cell to be oriented in-plane. The magnetic ordering was found to persist to elevated temperatures and coexist with the two-dimensional superconducting state.

The superconducting state and the low-energy band-structure on which the superconductivity is based have been characterized using tunneling spectroscopy. To make this possible, I have developed and implemented solid-state tunnel devices with *in-situ* deposited planar gold contacts as tunneling counter electrodes to the 2DEL. The device design and the key processing steps are quite generic and enable using other (e.g. superconducting or ferromagnetic) materials as well.

In the measured LAO-STO interface low-energy density of states at least two subbands with band-edges near the Fermi-level could be identified. They are sparsely populated: the band-edges are only about 10 meV below E_F at an $LaAlO_3$ thickness of $d_{LAO} = 4$ uc. This distance grows to about 30 meV at $d_{LAO} = 7$ uc, so the detailed relative arrangement of the sub-bands depends on the $LaAlO_3$ thickness. It will be interesting to investigate if any of the conduction sub-bands are spin-polarized. This should be possible using ferromagnetic or half-metallic tunneling electrodes (e.g. $La_{1-x}Sr_xMnO_3$[152]).

The two-dimensional superconducting state is accompanied by an energy gap in the DOS, which could be directly mapped with my devices. The gap opens at $T_c = 0.3$ K. Its width converges to about $2\Delta(T = 0) \approx 2 \times 40$ µeV at $T < 0.1$ K. Its shape and the ratio $\Delta(T = 0)/T_c \approx 1.6$ are consistent with a BCS weak-coupling s-wave superconductor.

My experiments have revealed striking similarities between the two-dimensional superconducting state at LAO-STO interfaces and the pseudogap phase of high-T_c superconductors. The energy-gap, which marks the condensation of electrons into Cooper pairs at $T < 0.3$ K, is independent of ideal conductivity, the suprafluid state of the condensate which sets in at $T < 0.1$ K. Moreover, the measured energy gap increases monotonously when the interface is depleted from charge carriers towards an insulating state.

A substantial amount of new information on the two-dimensional (super-) conducting LAO-STO interface has been gained throughout this thesis. The apparent similarities to

other two-dimensional superconductors (cuprates, Sr_2RuO_4) or heavy fermion superconductors extend the relevancy of this work. Still, the research set down is just a starting point. The developed tunnel devices with their unique field-effect doping capability offer possibilities over and above those demonstrated here. We are currently gathering a complete phase diagram of the superconducting gap as a function of doping, temperature and magnetic field. Simultaneously, the electron-phonon coupling can be studied by an analysis of the inelastic tunneling data. This way LAO-STO tunnel devices will provide unprecedented insights into the physics of two-dimensional superconductivity—insights which may well be relevant for the understanding of high-temperature superconductivity.

Tradition has it that a thesis ends with an outlook. The idea to learn from a $T_c = 300\,\mathrm{mK}$ superconductor how to design a $T_c = 300\,\mathrm{K}$ superconductor is a tempting one for sure. So is the possibility of tunable spin-triplet or finite-momentum superconductivity at the LAO-STO interface. The simultaneous magnetic order and strong spin orbit coupling might even enable Majorana physics[153, 154]. Without further research, though, these possibilities are mere speculation.

There are yet more direct, more practical applications for oxide-interfaces and the technology developed throughout this thesis. Completely analogous to how the tunnel junctions are fabricated I have built ultra-thin plate capacitors with the LAO-STO interface as one of the capacitor plates. It turned out that the strong electronic correlations present in the interface system give rise to a negative electronic compressibility that enhances the capacitance of such capacitors[155] well beyond their classical geometric capacitance. We have proven this effect for capacitors with relatively thick (10-12 uc) LAO layers[13]. Recently, we have proven the negative compressibility to be present at interfaces with ultra-thin LAO layers[17], too. This means that LAO-STO capacitors which combine ultra-thin LAO layers with high-κ dielectrics may achieve capacitances which exceed their (already large) geometric values multiple times. This effect could be used to integrate large on-chip capacitances, e.g. into analog integrated circuits, or to enhance the performance of field-effect transistors.

Formidable field-effect transistors using the LAO-STO interface as drain-source channels can indeed be built with only slight modifications to the thin-film processes used to make LAO-STO tunnel junctions. Our research towards all-oxide integrated digital circuits, which is subsumed in Appendix A, has recently yielded first self-oscillating integrated circuits—LAO-STO ring-oscillators[22].

Practical applications of our technology will obviously require further research. A big obstacle is that LAO-STO like oxide interfaces are complex to create. For a long time, pulsed laser deposition, a costly technique that does not scale to large wafers, was the only option to create conducting LAO-STO interfaces. In section D.2 I will show how molecular-beam epitaxy can be used instead. Moreover, in the same chapter D other material combinations including an alternative substrate will be presented that generate conducting interfaces comparable to LAO-STO.

In conclusion, LAO-STO is a material system that enables both a great research tool to studying basic science and a promising candidate for real-world electronic applications. If LAO-STO alone has brought such a wealth of fascinating and challenging physics, one can conjecture what the growing family of related interfaces will bring. In this spirit I am confident in concluding my thesis with an almost four year old quote from Stefan Thiel[67, p. 118] "that also for the following years it will remain thrilling in this field to analyze the fascinating physics of interfaces in oxides."

A. With OIFETs towards all-oxide integrated circuits

The $LaAlO_3$-$SrTiO_3$ interface is intrinsically well-suited to be used as the drain-source channel of a field-effect transistor (FET): the conducting interface has a modest charge carrier density and is embedded in high-κ dielectrics ($\varepsilon_{\mathrm{STO}} = 300, \varepsilon_{\mathrm{LAO}} = 24$).

The tunnel junctions which I have developed throughout this thesis required advanced film-growth techniques, *in-situ* processing and new patterning strategies. As a side project I have constantly been utilizing these advances to develop LAO-STO-based oxide interface field-effect transistors (OIFETs) further. I had implemented the first such devices during my diploma-thesis[2]. This first generation had amorphous gate-dielectrics and *ex-situ* sputtered Au gate electrodes. As a consequence of interface states and probably also improper oxidation of the amorphous dielectric gate creep on multiple time scales from seconds to hours was a major downside of these devices.

I have resolved these problems using *in-situ* processing and subtractive patterning of the gate-electrodes, as described for the tunnel devices in section 2.3. In addition, the ohmic source- and drain-contacts could be improved markedly by *in-situ* sputtering of optimized[156] contact materials like Ti or Nb into freshly ion-milled pits. The gate-stack has been optimized, too, by *epitaxial* growth of high-κ dielectrics like $SrTiO_3$ or $BaTiO_3$[157] directly on top of thin $LaAlO_3$ layers. Figure A.1 presents the FET characteristics of 3 different implementations of LAO-STO field-effect devices. Of these devices the YBCO-LAO-STO FET is a special case. The (electrically conducting) YBCO gate electrode was found to directly affect the electronic properties of the LAO-STO interface. It depletes the interface and shifts the critical LAO thickness to $\sim 7 - 8\,\mathrm{uc}$[1]. In other words, the gate material can be used to dope the LAO-STO channel and control the threshold voltage V_{th} of such FETs.

To demonstrate the capability of LAO-STO FETs to amplify voltages and to be used in digital integrated circuits we pursued ring-oscillators in which a number of OIFETs are interconnected in order to achieve self-sustained oscillation. Figure A.2 presents the basic building block of such ring-oscillators: a logic NOT gate, whose working-principle is comparable to that used in depletion-load NMOS logic. Our FETs are n-channel depletion-mode devices ($V_{\mathrm{th}} < 0$). This type of transistor is not very practical for designing NOT-gates. Conventional NMOS uses not depletion- but enhancement-mode FETs to drive its NOT-circuits. Enhancement-mode OIFETs could most likely be realized by varying the $LaAlO_3$ thickness in the gate-stack. We have not further developed such devices[7, 16], but could implement working ring-oscillators nevertheless.

The main flaw that a depletion-mode FET as a driver in our NOT-gate causes, is an offset voltage. Our NOT gates could often achieve large transconductance values, but

[1] Benjamin Förg has thoroughly investigated YBCO-LAO-STO heterostructures and field-effect transistors[16] in the course of his master-thesis[76], which I have supervised.

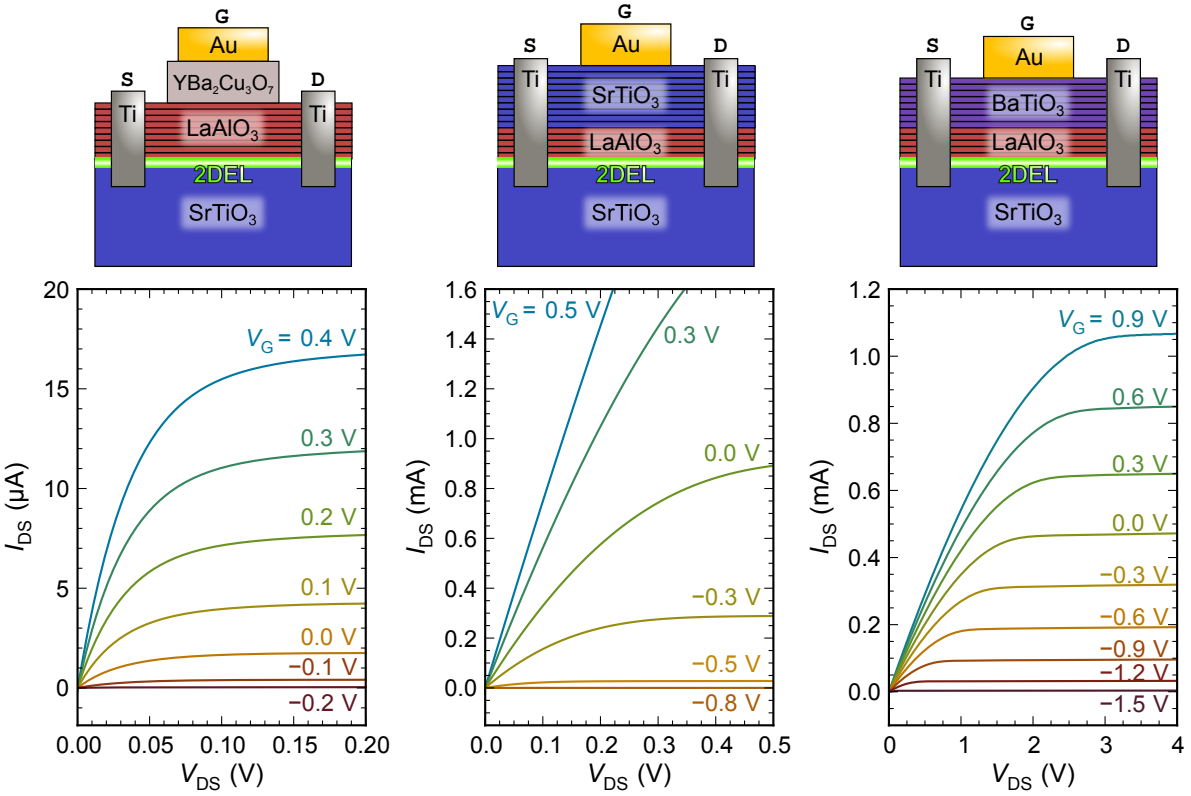

Fig. A.1: Room temperature FET-characteristics of different OIFET implementations utilizing LAO-STO interfaces as their active channel. The set-up of the respective transistor is sketched right above each graph. Left: $YBa_2Cu_3O_7$ (YBCO) gate on 9 uc $LaAlO_3$; center: Au gate on 10 uc $SrTiO_3$ on 5 uc $LaAlO_3$; right: Au gate on 8 uc $BaTiO_3$ on 5 uc $LaAlO_3$.

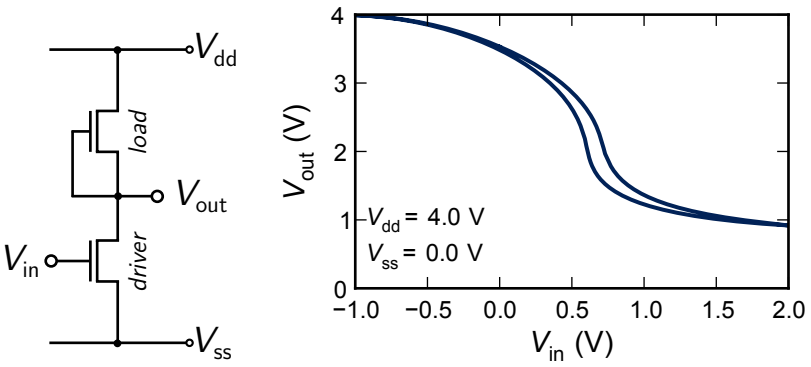

Fig. A.2: Schematic of logic NOT-gates using OIFETs (left) and typical transfer characteristic of an implementation using an Au-BTO-LAO gate stack (right).

their output would hardly swing below an offset voltage $V_{\text{off}} \sim V_{\text{dd}}/2$ (see Figure A.2 for an exemplary transfer characteristic). This offset prohibits the direct coupling of one NOT-gate to the next. In order to remove it a coupling stage is required in between any two NOT-stages. Figure A.3 documents our first successful attempt using external capacitors to couple the ring-oscillator stages. This design, which I have implemented together with Benjamin Förg, was using 8 YBCO-LAO-STO transistors in 3 oscillator stages and 1 output stage. My colleague Rainer Jany has improved the design towards monolithically integrated coupling stages. He has recently achieved a fully integrated LAO-STO ring-oscillator with no need for any external components[22]. Instead of capacitive coupling he used on-chip voltage dividers and an additional negative supply voltage. He employed Au-BTO-LAO-STO transistors[2], for these can operate at higher supply voltages than the YBCO-LAO-STO FETs. Details regarding Rainer's design will be available in his doctoral thesis.

Both implementations worked and demonstrated self-sustained oscillation at room temperature. Their oscillation frequencies were around 66 kHz for the capacitively coupled and 1.5 kHz for the resistively coupled design. In both cases the RC charging-time of the gate capacitance was the limiting factor. Research to shrink the FET dimensions in order to drastically reduce those time-constants is underway. Using advanced e-beam lithography, Carsten Woltmann (Max-Planck-Institute, Stuttgart) has achieved first promising results (see Figure A.4). It will be interesting to explore the scaling limitations of this OIFET technology. As there is no need for chemical doping (neither for the channel nor drain and source) the functionality of LAO-STO transistors could still be usable and well-defined on a unit cell level (0.4 nm). The possibility to integrate ultra-high-κ materials and ferroelectrica into the gate-stack promises high switching speeds at low power consumption. Moreover, we have found that the correlated nature of the LAO-STO 2DEL leads to a negative compressibility[17] when the system is depleted. This way the gate capacitance is markedly enhanced beyond its classical geometric value[13].

Conducting LAO-STO interfaces are optically transparent and can be implemented on silicon[158]. As shown in section D.4, conducting oxide interfaces can also be realized on substrates other than $SrTiO_3$, with lower dielectric losses.

Oxide interface field-effect transistors may soon rival the performance of conventional semiconductor-based FETs. Yet the demonstrated correlation effects of the 2DEL and the possibility to (epitaxially) integrate piezoelectric, ferroelectric, multiferroic and memristive elements promises unprecedented functionality and novel applications beyond binary logic and CMOS technology.

[2]The Au-BTO-LAO-STO FETs have initially been developed by Georg Pfanzelt[157] and were further investigated and improved as part of Rainer Jany's phD thesis

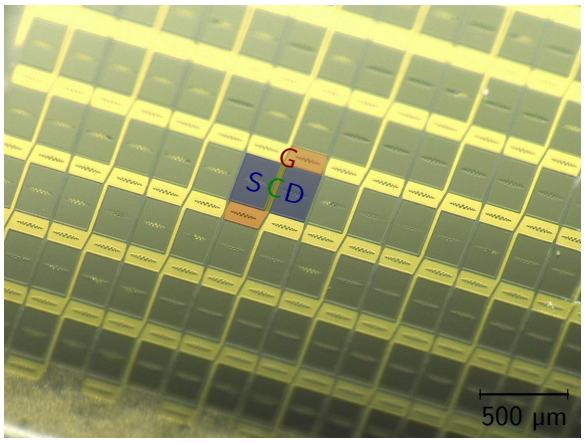

a Microscopic image of an OIFET array. The source and drain (Ti-pads), channel, and gate (Au on YBCO) of one exemplary FET source are colorized.

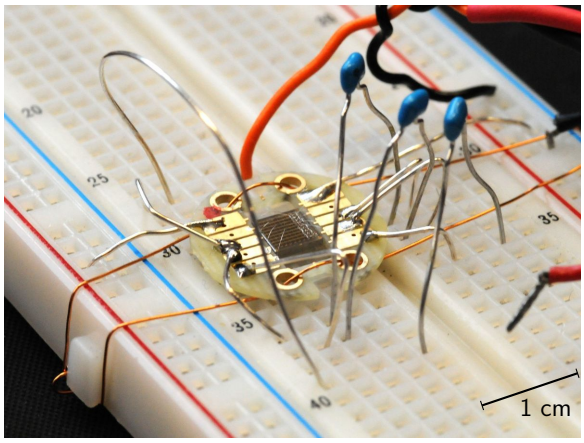

b Photo of ring-oscillator circuit using wire-bonded FETs from the chip shown in **a**. Individual NOT-gates are coupled via the 3 ceramic capacitors (blue).

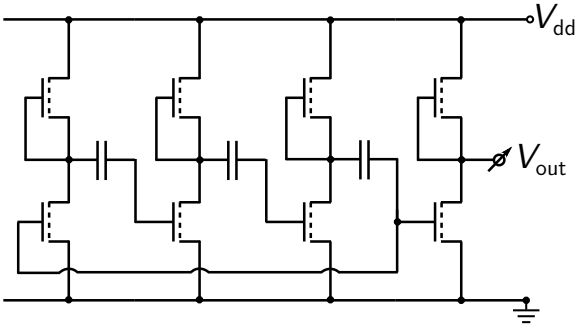

c Schematic of the capacitively coupled ring-oscillator circuit

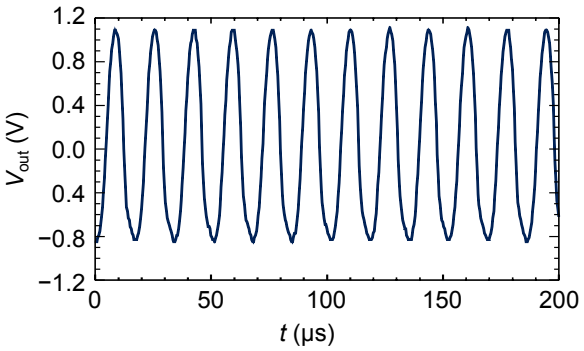

d Ring oscillator output signal V_{out} oscillating at a frequency of 66 kHz.

Fig. A.3: Illustration of a working ring-oscillator based on YBCO-LAO-STO FETs. The individual FETs shown in **a** have been interconnected using wire-bonds and coupling capacitors as shown in **b** according to the schematic shown in **c**. At an operating voltage $V_{dd} = 2.3\,\text{V}$ the ring-oscillator generated an oscillating output signal (**d**) with a frequency of $f = 66\,\text{kHz}$, and a peak-to-peak amplitude of 2.0 V, which was sampled by an AC-coupled oscilloscope.

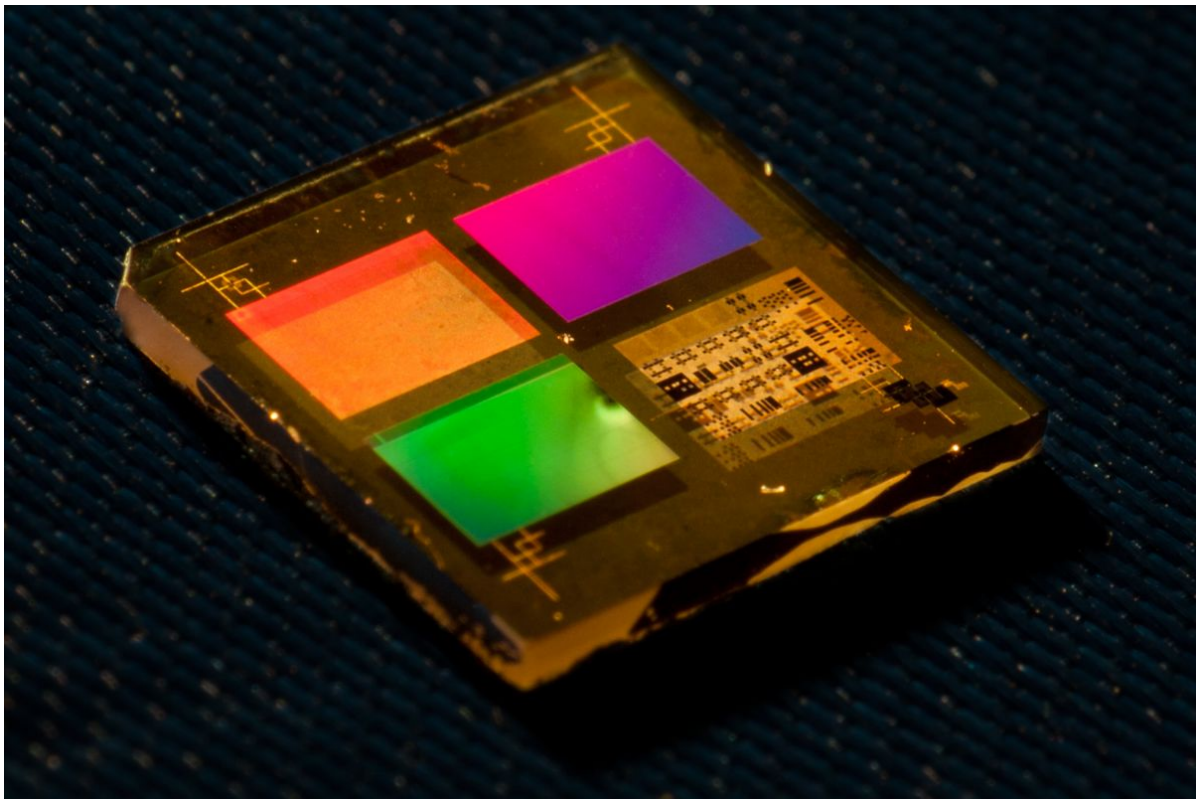

Fig. A.4: Photo of e-beam lithographically patterned arrays of OIFETs with gate-lengths down to 100 nm. The dimensions of the chip are $10 \times 10 \times 1\ \mathrm{mm}^3$. (Photo by C. Müller and C. Woltmann, Max-Planck-Institute for Solid State Research, Stuttgart)

B. Nature of the superconducting state – fits to the tunnel-spectra

To learn about the nature of the LAO/STO interface-superconductivity and to extract from the measured tunnel-spectra key parameters describing the superconducting state, we attempted to fit our data with standard models for the superconducting quasiparticle density of states.

Fits We used the quasiparticle finite-lifetime broadened DOS, which was first introduced by Dynes, Narayanamurti and Garno in reference [87]:

$$\varrho(E,\Gamma) = \Re\frac{E - i\Gamma}{\sqrt{(E - i\Gamma)^2 - \Delta^2}}, \tag{B.1}$$

Γ is a measure of the quasiparticle life-time, Δ is the magnitude of the superconducting gap and E is the energy, measured from the chemical potential inside the superconductor. From Equation B.1, the differential conductance between a metal with constant DOS and the superconductor with a density of states $\varrho(E,\Gamma)$ is derived:

$$\frac{\mathrm{d}I}{\mathrm{d}V} = G_0 + G_1 \int_{-\infty}^{\infty} \mathrm{d}E \frac{-\partial f(E + \mathrm{e}V)}{\partial E} \varrho_{\mathrm{s}}(E). \tag{B.2}$$

G_0 is conventionally a small ($<< G_1$) *positive* constant meant to incorporate measurement errors like leakage currents. Figure B.1 shows a typical measured $dI(V)/dV$ tunneling characteristic at 50 mK, a temperature well below the superconducting transition. The solid lines in figure B.1 show three best-fits with different models, of which only one is acceptably close to the measured data-points. Neither a pure s-wave nor an s+d-wave spectral DOS fit the data well. Nice fits are obtained only, when G_0 is allowed to become *negative* ($G_0 \approx -0.5G_1$), as is demonstrated by the red curve labeled "shifted s". Since we cannot attribute physical meaning to a negative conductance correction, we fixed G_0 to zero for the fits used to evaluate the temperature- and gate-voltage dependence of the gap shown in section 3.1. As the s-wave and the s+d-wave fits are almost equally good, we used the simpler s-wave fit.

Another possibility to obtain very good fits (at least as good as the "shifted s" model) to the data is to introduce the imaginary lifetime constant $i\Gamma$ into the order parameter Δ, instead of the energy E. Whereas this procedure has been discussed to result in "the correct formula for the lifetime broadened superconducting density of states" by Božidar Mitrović and Lee A. Rozema[159], it is not widely accepted to be actually physically correct. Note that there are further possible interpretations for a complex order parameter. In any case, the results for (the real part of) Δ are about 10-20 %

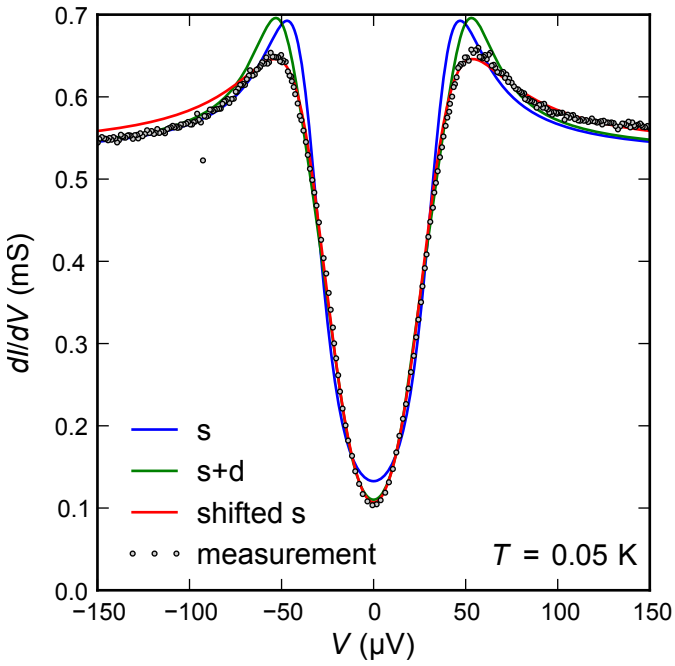

Fig. B.1: A prototypical dI/dV tunnel-spectrum of an LAO-STO interface (circles) measured at 50 mK using a standard AC-technique (details of measurement listed below). The solid lines represent best-fits to the measured data using different models, which are described in the text. The 4-wire measurement of the tunnel-conductance was done by sourcing a small AC-current I_{AC} added to a DC-current (bias) through the junction, and measuring the resulting DC- and AC-voltage at 2 independent terminals. The AC excitation and measurement was done using a Princeton Research (EG&G) 5210 lock-in amplifier: $I_{AC} = 0.25\,\text{nA} \Rightarrow V_{AC} < 3\,\mu\text{V}$, $f_{AC} = 133\,\text{Hz}$. A DC-current was added using a Keithley 6430 Sub-femtoamp Remote SourceMeter, the DC voltage was measured with a Keithley 2002 Multimeter (10× average over 2 powerline-cycles) and a Stanford Research 560 preamplifier (1000× gain, 1 Hz, 12 dB low-pass). Suitable measurement delays (DC: 1.5 s, AC: 3.0 s) were used to account for the time-constants of lock-in- and pre-amplifier.

lower than with the standard Dynes-fit (Equation B.1).

Order-parameter symmetry While a simple s-wave fit was used throughout this thesis to determine the magnitude of the superconducting gap Δ from measured tunnel-spectra, the correspondence between data and model is by no means perfect. In fact, a fit with a pure d-wave order parameter is of comparable quality, and d- or even p-wave superconducting states are well possible at $LaAlO_3$-$SrTiO_3$ interfaces[119, 160].

With the present tunneling data, which naturally lacks momentum resolution, no definite conclusion about the order-parameter symmetry can be drawn.

C. In-gap features in tunneling spectra

The tunneling spectra plotted in the following were obtained from a DC 4-wire $V(I)$-measurement of the tunnel conductance of a tunnel device on sample T41, at a sample temperature of 50 mK. A Keithley 6430 SMU was used as a current source and current meter. A Keithley 2182A Nanovoltmeter was used to measure the 4-wire voltage with a 5 power-line-cycle integration time. The derivative was done in the most straightforward manner by taking the pointwise direct difference between neighbouring points (centered differences). Filled circles denote the forward- open circles the backward-trace. The solid line is a cubic spline connecting the average of the traces.

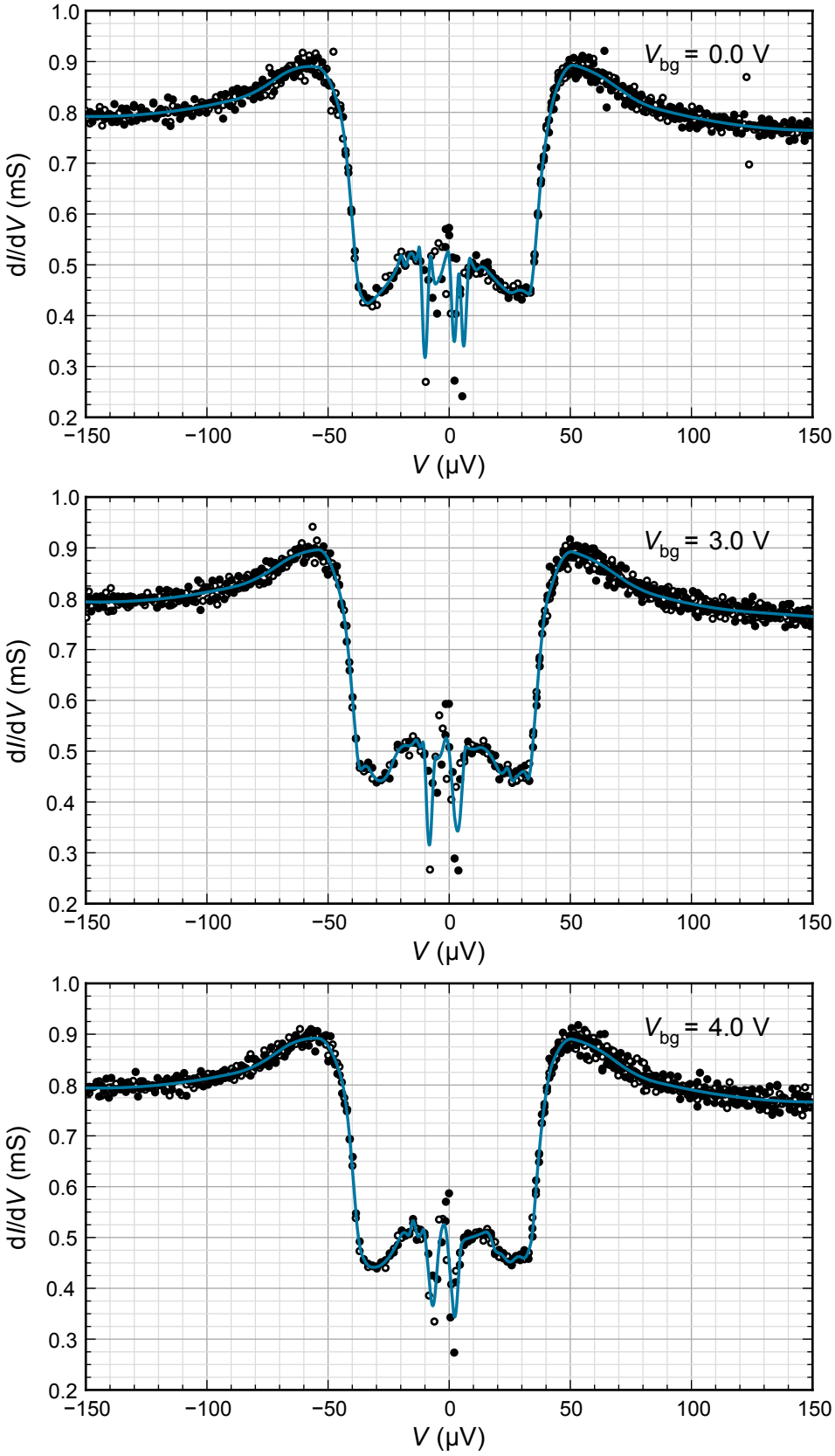

Fig. C.1: Tunnel spectra measured at $T = 50$ mK and varying gate voltage V_{bg}

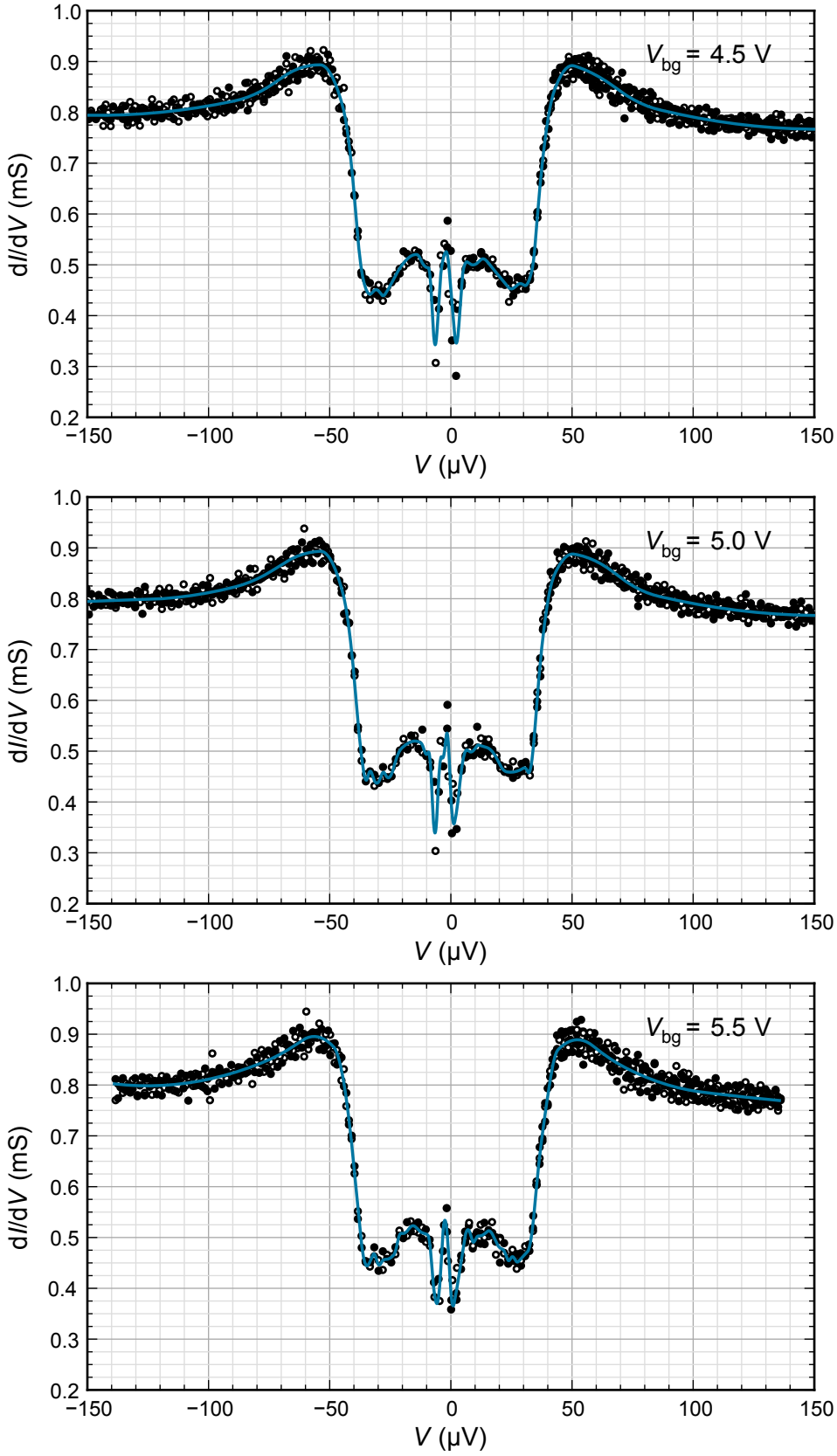

Fig. C.2: Tunnel spectra measured at $T = 50$ mK and varying gate voltage V_{bg}

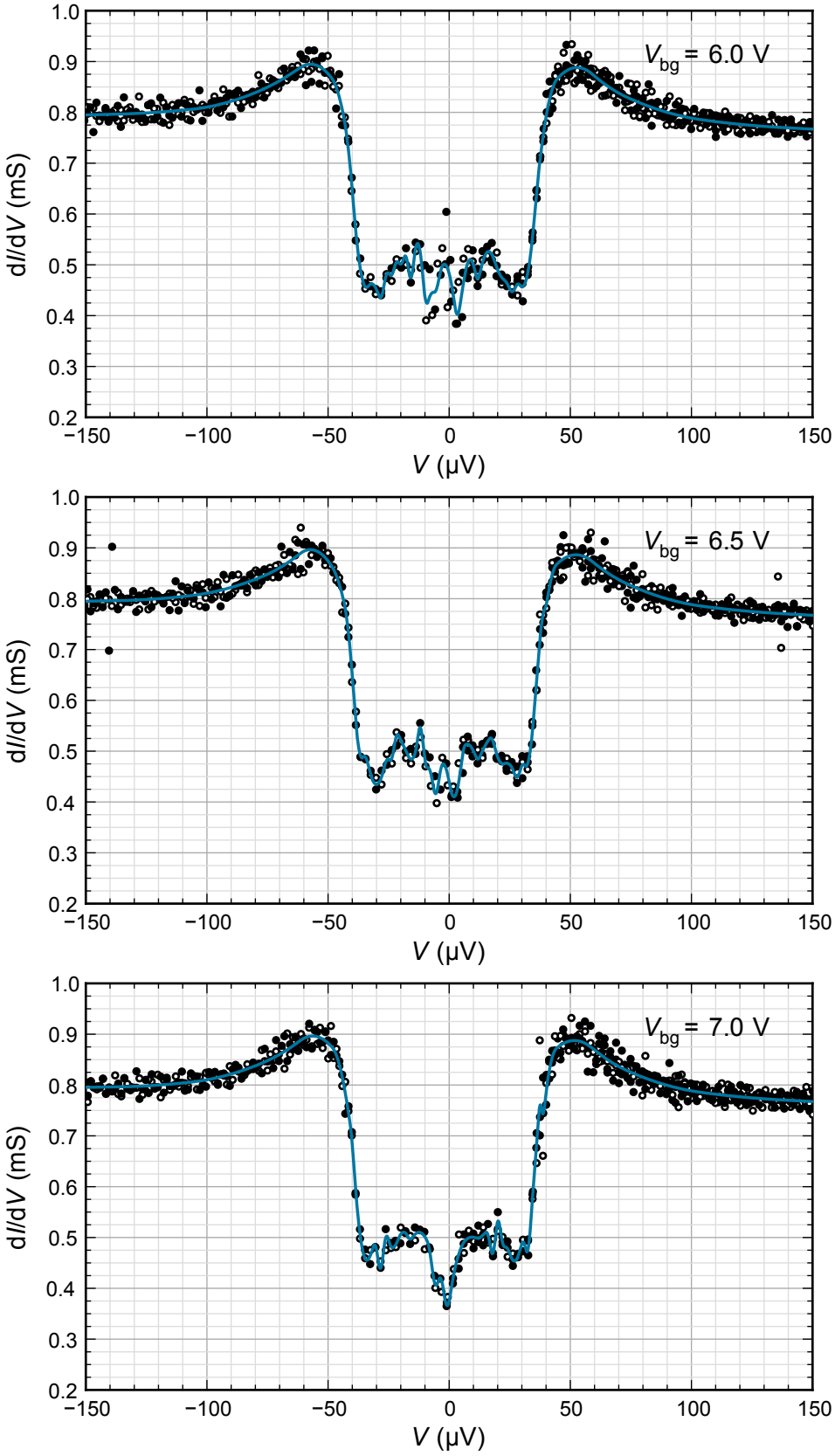

Fig. C.3: Tunnel spectra measured at $T = 50$ mK and varying gate voltage V_{bg}

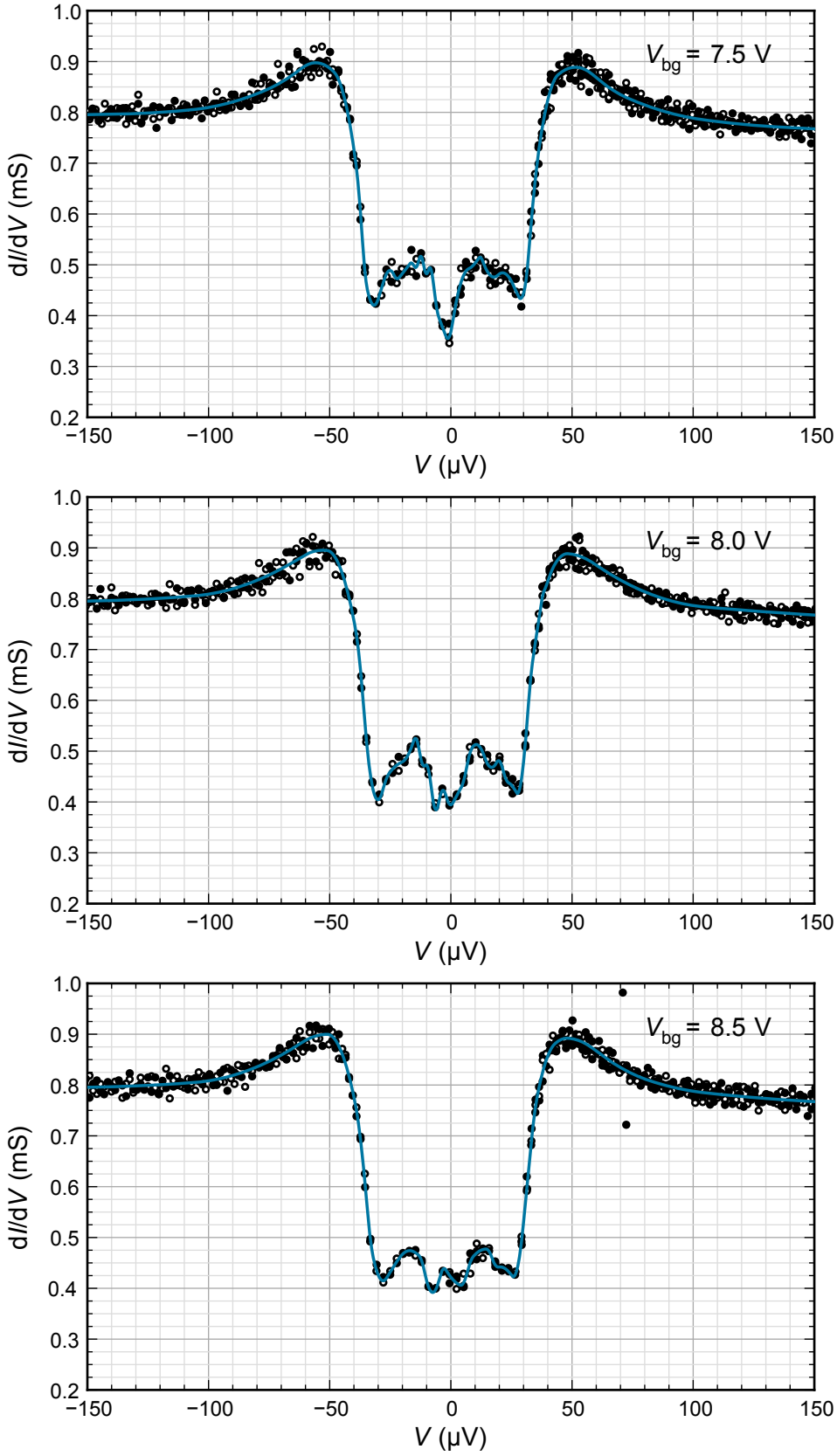

Fig. C.4: Tunnel spectra measured at $T = 50\,\mathrm{mK}$ and varying gate voltage V_{bg}

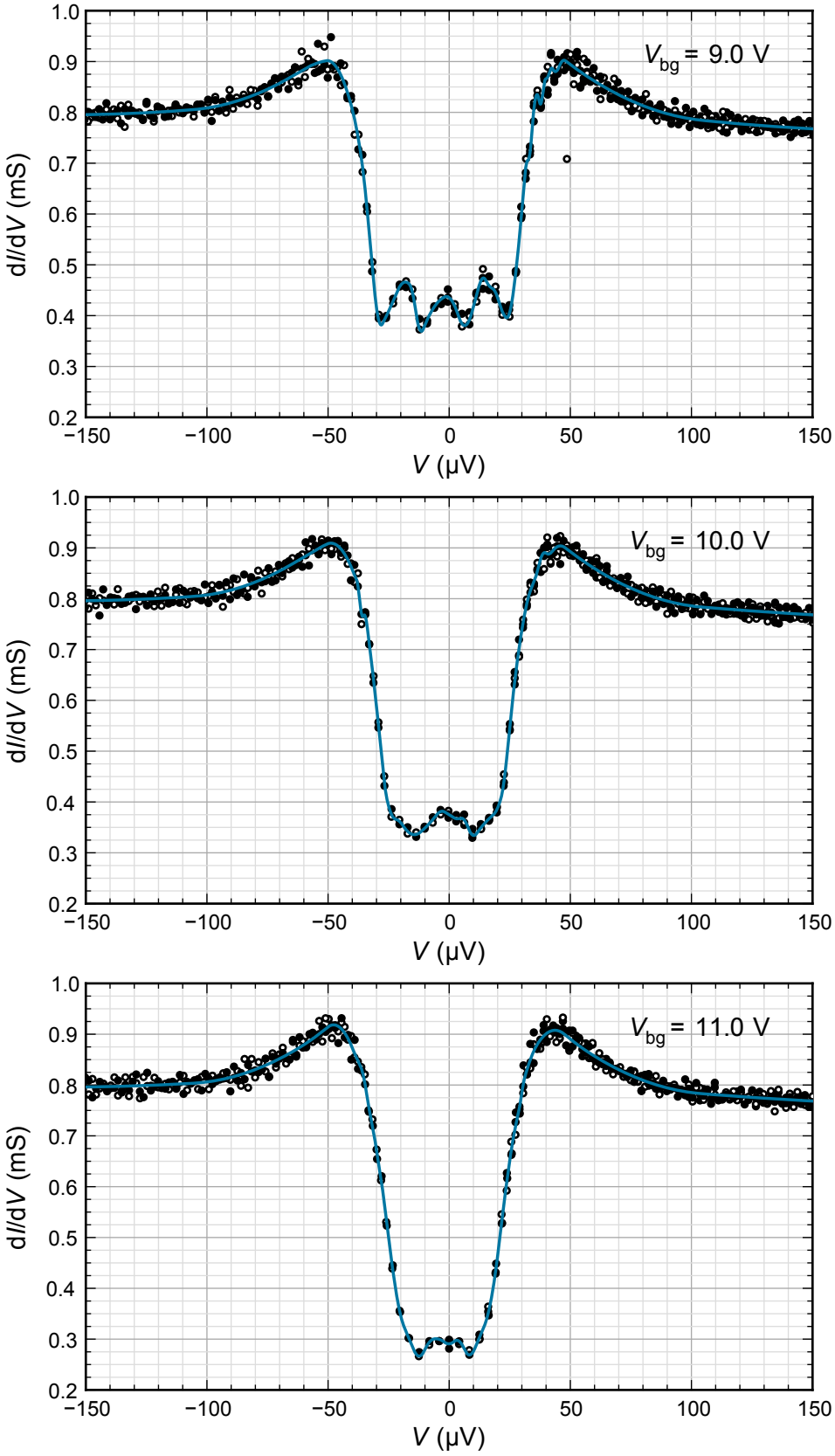

Fig. C.5: Tunnel spectra measured at $T = 50$ mK and varying gate voltage V_{bg}

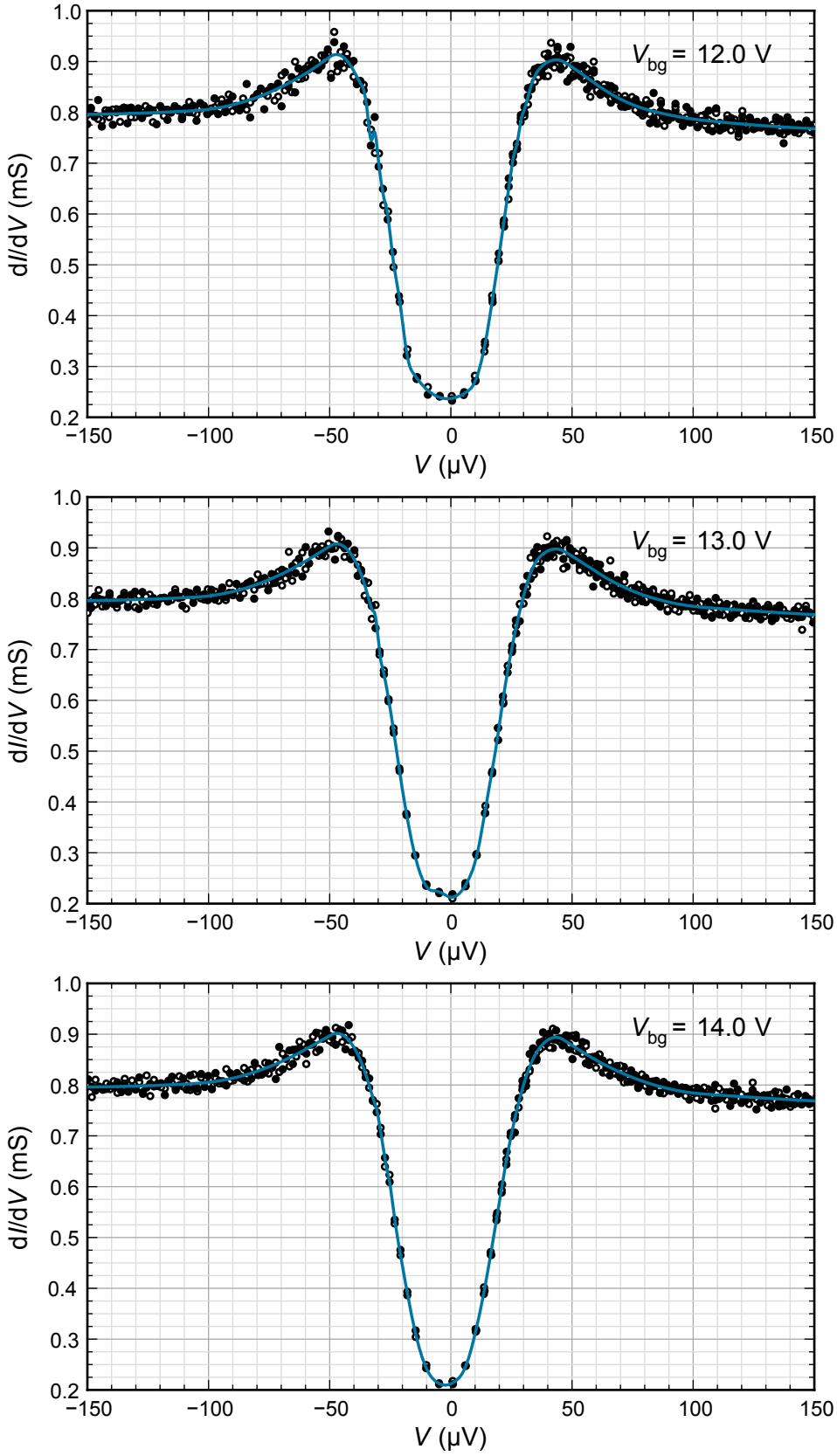

Fig. C.6: Tunnel spectra measured at $T = 50\,\mathrm{mK}$ and varying gate voltage V_{bg}

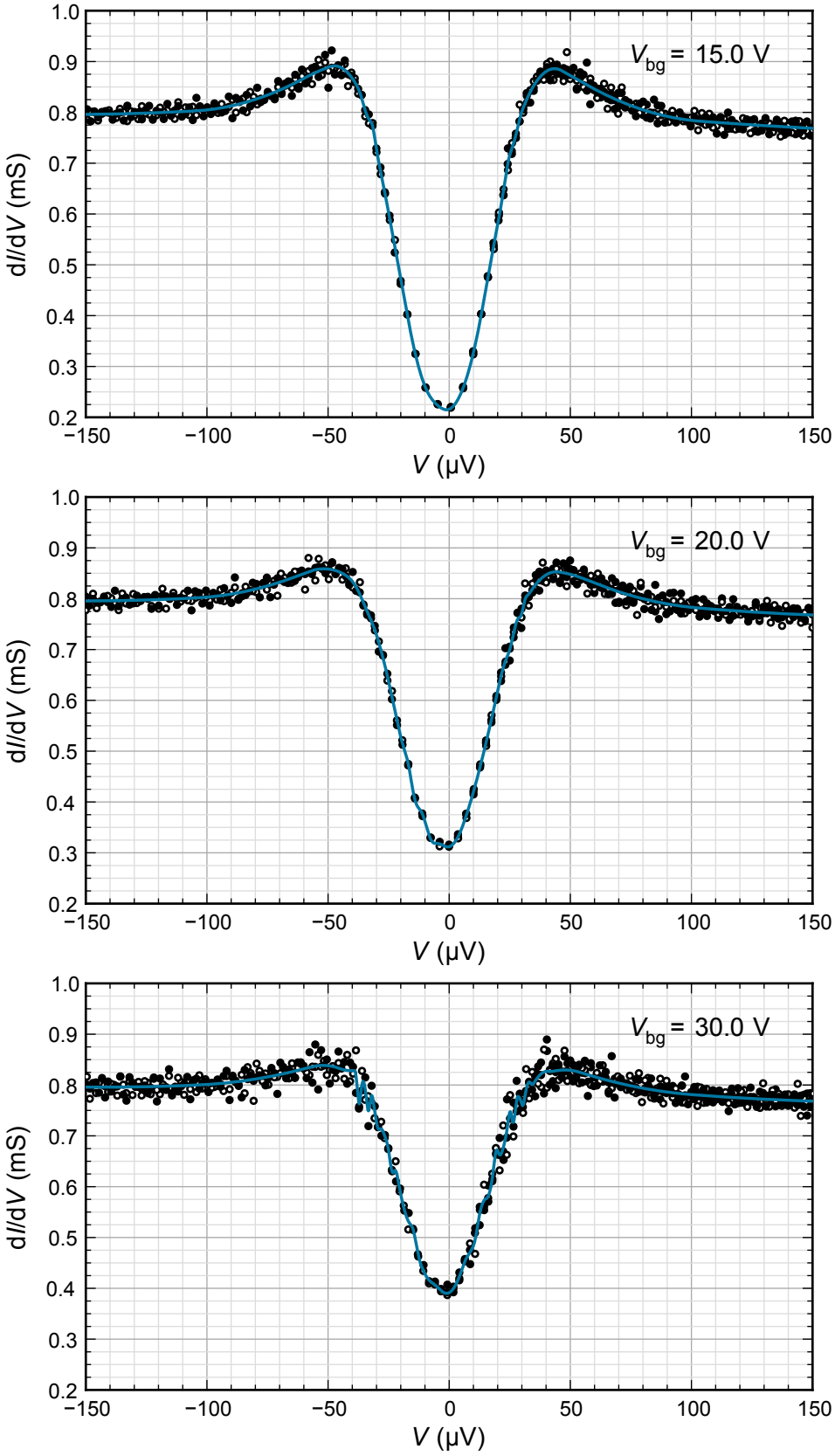

Fig. C.7: Tunnel spectra measured at $T = 50\,\mathrm{mK}$ and varying gate voltage V_{bg}

D. Alternative growth procedures; oxide interfaces related to LAO-STO

A good way of learning about a phenomenon and understanding its essence lies in experimenting with its recipe. Which of the ingredients, which of the processing steps are essential? Which ones are not? To tell unimportant ingredients from essential ones is a key ability in cooking as well as in experimental solid state physics. It enables us to understand, to generalize and to devise.

$LaAlO_3/SrTiO_3$, the conducting interface between two insulating oxides, has long been a scientific singularity: Not only was there just 1 known material combination; there was merely 1 working procedure for fabricating the conducting oxide interface: pulsed laser deposition of $LaAlO_3$ on a BHF-treated $SrTiO_3$ substrate.

In this chapter I will present experimental work that abstracts from this restricted recipe step-by-step. The thin-film ($LaAlO_3$-side) material, the $LaAlO_3$ growth procedure, the $SrTiO_3$ substrate preparation, and the substrate itself will all be varied. The transport properties of the resulting interfaces will be investigated.

The chapter opens with a literature survey and review of experimental reports about $LaAlO_3$ alternatives, i.e. conducting ABO_3-$SrTiO_3$ interfaces. Next, I report on a collaborative investigation of an alternative growth technique, molecular-beam epitaxy, for growing $LaAlO_3$-$SrTiO_3$ interfaces. This is followed by an investigation of an alternative, HF-free STO-termination procedure, before finally I present a conducting oxide interface on a substrate material other than $SrTiO_3$: the $LaAlO_3$-$CaTiO_3$ interface. The chapter closes with a discussion of the results and their implications on the understanding of the LAO-STO interface.

D.1. Conducting oxide interfaces without $LaAlO_3$

With the polar catastrophe as the dominant and widely accepted model explaining the high-mobility electron gas at the $LaAlO_3$-$SrTiO_3$ interface it was clear—at least in principle—how to systematically identify alternative materials for substituting the $LaAlO_3$. The material, let us call it ABO_3, had to feature similar polar AO^+ - BO_2^- sublayers that create the polar discontinuity, which triggers the electronic reconstruction. This sets a constraint on the chemical valency of the constituent elements. Natural additional boundary conditions are a close lattice match to $SrTiO_3$ ($a = 3.905$ Å), as well as the prerequisite that the material should be an insulator.

By now a number of LAO-substitutes have been reported that can generate conductivity similar to that found between $LaAlO_3$ and $SrTiO_3$. The validity of some of these reports has to be thoroughly checked, though, since the substrate material and thus the host of the conducting electron system is $SrTiO_3$; and an electronic reconstruction is not the only way to induce conductivity in $SrTiO_3$.

While it is a band-insulator in its pure, stoichiometric form, doping can make $SrTiO_3$ a semiconductor, metal, and superconductor. Effective ways to n-dope $SrTiO_3$ include chemical doping with metals like niobium or lanthanum or, even more accessible, oxygen vacancies.

Chemical doping can happen in thin-film deposition techniques involving high substrate temperatures or high-energy particles, like in sputtering or PLD, which can implant (target-) ions into the substrate.

Oxygen vacancies are easily created in $SrTiO_3$ in reducing atmospheres. Naturally, the ultra-high-vacuum (UHV) conditions that are commonly found in most physical-vapor-deposition techniques, especially in molecular-beam epitaxy, are reducing atmospheres for $SrTiO_3$ at least at elevated temperatures.

An additional point of concern is the substrate preparation employed to achieve a single-terminated substrate surface—an essential ingredient to any well-defined interface experiment. The chemical treatment used to remove SrO from the surface involves buffered hydrofluoric acid (BHF), which has been found to induce a large amount of defects, including oxygen vacancies, in surface-near regions of $SrTiO_3$ substrates.

All three of these caveats are met in all experimental work that this section is going to cite (this section does not include any of my own experimental work); and it is mainly for these three reasons that reports about conducting interfaces involving $SrTiO_3$ should be taken with a grain of salt. Early research on conducting LAO-STO interfaces has, in fact, been met with a lot of skepticism for just the same reasons. Today the concept of an electronic reconstruction driven by the polar discontinuity between $LaAlO_3$ and $SrTiO_3$ is widely accepted as the fundamental explanation for the observed conductivity at the interface between $LaAlO_3$ and TiO_2-terminated (100) $SrTiO_3$.

This paradigm shift is mainly thanks to three key experimental observations: Beside experimental results that directly support the polar catastrophe and an electronic reconstruction scenario.

1. *A conducting interface can be grown under conditions that do not reduce $SrTiO_3$.*

Moreover, the interface conductivity survives a high-pressure oxygen anneal. Both cases result in fully oxidized $SrTiO_3$, in which doping by oxygen vacancies can be excluded.

2. *The substrate termination matters: A conducting interface is found only when grown on TiO_2-terminated $SrTiO_3$. $LaAlO_3$ grown on SrO-terminated $SrTiO_3$ does not yield a conducting interface* (although the polar catastrophe scenario predicts a *p*-type interface in this case). In any way whatsoever the growth conditions or high-energy particles ablated from the target might dope the $SrTiO_3$ substrate surface: it is hard to imagine how a single SrO layer would change or hinder this doping to the point, that no conductance can be found, when under the same growth conditions, without the SrO layer, a conducting interface would readily form.

3. *A critical $LaAlO_3$ thickness was found. Only when the $LaAlO_3$ film exceeds this thickness, the conducting 2DEL is generated.* This result nicely fits the polar-catastrophe scenario, but is really hard to reconcile with the unintended $SrTiO_3$-doping scenario. This is because the difference between a conducting and an insulating sample is a mere unit cell of $LaAlO_3$. The growth-procedure of a 3 and a 4 unit-cell LAO-STO sample are almost exactly identical, the result is still two very different electronic states. Considering that the same critical thickness has been reproduced in more than a handful of institutions with different PLD (and MBE) systems, it becomes very clear that the conductance can not be caused by unintended doping, but is triggered by the additional electric potential of the 4th $LaAlO_3$ unit cell.

Every single one of these facts is hard to reconcile with the idea that the LAO-STO 2DEG is due to unintended substrate doping. Still another striking experimental observation, which should be added to the top of that list, will be presented in the next section. The present section will summarize and critically review experimental reports about materials that, like $LaAlO_3$, were found to create conductivity at their interface with $SrTiO_3$ (note that at the present time no reports about a similar conducting oxide-2DEG without $SrTiO_3$ exist). To exclude the enumerated pitfalls with unintended doping of $SrTiO_3$, all reports are checked for the three key points:

1. Oxygen pressure during growth and post-growth annealing,

2. Effect of substrate termination,

3. Critical thickness.

Only if all three points are adequately fulfilled, unintended doping as the source of conductivity can be excluded to the same level as in LAO-STO.

D.1.1. $LaVO_3$[161]: lanthanum vanadate, a Mott-insulator

The historically first report about a material that can generate an oxide-interface similar to LAO-STO came in 2007 from Y. Hotta, T. Susaki, and H. Y. Hwang. Harold Hwang had, together with Akira Ohtomo, discovered the conducting $LaAlO_3$-$SrTiO_3$ interface in 2004[25]. Whereas $LaAlO_3$ and $SrTiO_3$ are both band-insulators, $LaVO_3$ is a Mott-insulator[162]. Despite this difference, the $LaVO_3$-$SrTiO_3$ and the $LaAlO_3$-$SrTiO_3$ interface have a lot in common:

Critical thickness Only when five or more[161] monolayers of $LaVO_3$ are grown on Ti-terminated $SrTiO_3$, n-type conductivity arises with a carrier density of 10^{12} to 10^{14} /cm^2. Unlike in LAO-STO, the carrier density is not constant for $d > d_c$, but rises considerably with each added $LaVO_3$ monolayer, until, at a thickness of 10 unit cells the value saturates at around 1.5×10^{14} /cm^2. For a 10 uc $LaVO_3$-$SrTiO_3$ interface the charge carrier mobility is reported to be 2 cm^2/Vs and 20 cm^2/Vs at 280 K and 100 K, respectively. Interfaces with a lower $LaVO_3$ thickness are found to have a higher Hall-mobility of up to 200 cm^2/Vs at $T = 100$ K. At $T < 100$ K the measured $R(T)$-curves are non-monotonic with a minimum at around 50 K.

Effect of substrate termination The electronic properties of the $LaVO_3$-$SrTiO_3$ interface depend critically on the $SrTiO_3$ substrate termination. If the substrate termination is switched from TiO_2 to SrO, by inserting a single SrO or $SrVO_3$ unit cell before the $LaVO_3$ growth, the room-temperature sheet-resistance of the interface rises by an order of magnitude and diverges at lower temperatures–*the $p-$type interface is insulating.*

This result is especially striking if a unit cell of $SrVO_3$ is used to switch the substrate termination, since bulk $SrVO_3$ is a metal.[163]

In a later study[164], F. S. Razavi *et al.* have implemented an alleged random network of diodes utilizing the mixed termination of an untreated $SrTiO_3$ to result in a random network of p- and n-type $LaVO_3$-$SrTiO_3$ interfaces.

Oxygen pressure The $LaVO_3$ thin-films in the cited study were grown in an oxygen partial pressure of 1.3×10^{-6} mbar at a growth-temperature of 600 °C. No post-growth annealing was done. Both measures were mandatory to achieve stoichiometric $LaVO_3$, since at higher oxygen pressure $LaVO_4$ would have formed.[165]

With respect to maintaining a fully oxidized $SrTiO_3$ substrate and to exclude substrate doping via oxygen vacancies, the present growth conditions should be considered questionable. The critical thickness and the effect of substrate termination seem to rule out substrate conductivity due to oxygen deficient $SrTiO_3$. Nevertheless, at least at $T > 100$ K a finite resistivity was also found in p-type interfaces and in a 4 uc $LaVO_3$-$SrTiO_3$ interface (below the critical thickness of 5 uc). The temperature dependence of the resistance in these cases is semiconducting, which is to be expected from slightly reduced $SrTiO_3$. It should also be noted that reduced $LaVO_{3-\delta}$ is semiconducting in itself[166]. Consequently, a certain contribution of a reduced $SrTiO_{3-x}$ substrate

(or even the $LaVO_{3-\delta}$ film) to the measured conductance in all samples made at such growth-conditions is quite likely.

Electronic reconstruction or unintended doping? The PLD-conditions necessary to achieve $LaVO_3$ that grows layer-by-layer can not guarantee a fully oxidized $SrTiO_3$ substrate. So a minor contribution of reduced $SrTiO_3$ to the observed conductivity is likely present in all of the transport measurements. Still, the influence of the $LaVO_3$ thickness and the substrate termination on the electronic properties are so dramatic that unintended substrate doping alone is extremely unlikely to explain these effects. In summary, although not all of the three conditions are fulfilled completely, the $LaVO_3$-$SrTiO_3$ interface is almost certainly to be judged as another representative of LAO-STO-like conducting oxide-interfaces. An electronic reconstruction as the result of the polar discontinuity between the polar $LaVO_3$ and the non-polar $SrTiO_3$ is at present the most likely explanation of the observed interface conductance.

D.1.2. $LaGaO_3$[167]: lanthanum gallate, $LaAlO_3$'s nearest relative

Reports of a conducting interface at the $LaGaO_3$-$SrTiO_3$ interface were first orally presented by Fabio Miletto Granozio in 2009 and appeared in Applied Physics Letters in 2010[167]. $LaGaO_3$ could be considered the closest relative to $LaAlO_3$, since on a periodic table gallium (Ga) and aluminium (Al) lie adjacent in the same periodic group. Even in terms of the electronic properties of their interfaces to $SrTiO_3$ both materials are almost identical:

Critical thickness The $LaGaO_3$-$SrTiO_3$ interface exhibits a critical thickness behaviour that is identical to that found in $LaAlO_3$-$SrTiO_3$. At 4 uc, even the critical thickness itself is identical to LAO-STO. The authors hint at another similarity between $LaAlO_3$ and $LaGaO_3$ that might serve as an explanation for this coincidence: With $\varepsilon_r \approx 25$, the dielectric constant as "the principal parameter determining the polar layer response within the electronic reconstruction model" is equal in both materials[168]. The charge carrier density at the $LaGaO_3$-$SrTiO_3$ interface is $1 \times 10^{14} - 3 \times 10^{14}$ /cm^2 at room temperature and decreases slightly at low temperatures. The Hall mobility features the LAO-STO typical T^{-2} dependence at high temperature. It saturates to 10 - 100 cm^2/Vs at low temperatures.

Effect of substrate termination The effect of the substrate termination on the electronic properties of $LaGaO_3$-$SrTiO_3$ interfaces is not given explicitly, i.e. the p-type interface has not been realized purposely. The authors claim instead: "A proper surface preparation proved to be of paramount importance, since we could verify that an accidental inaccurate treatment on a batch of substrates, revealed by RHEED and attributed to partial double termination, resulted in the growth of insulating interfaces with room temperature resistance of about 4 - 8 MΩ." A theoretical study based on density functional theory predicts the GaO_2/SrO interface to be p-type with a gradual transition to n-type conductance on reduction of the oxygen content[169].

Oxide pressure On properly terminated substrates the $LaGaO_3$-$SrTiO_3$ interfaces exhibit sheet resistances of 20 - 30 kΩ at room temperature. This resistance value is almost independent of the oxygen partial pressure during growth, which was varied between 10^{-2} mbar and 10^{-4} mbar at a growth-temperature of 800 °C. The samples were cooled to room temperature in the same oxygen pressure employed for the deposition.

While these deposition parameters are unlikely to introduce a major amount of oxygen vacancies into the $SrTiO_3$, a minor substrate reduction can not be excluded, especially due to the missing post-annealing. The authors can, however, quantify this contribution, as a different oxide, $LaMnO_3$, grown on $SrTiO_3$ at otherwise identical conditions yielded a semiconducting $R(T)$ characteristic with $R_{\mathrm{sheet}} > 10\,\mathrm{M\Omega}$ for $T < 300\,\mathrm{K}$. The contribution of unintended substrate doping to the observed conductivity is therefore negligible. All the more noteworthy is that an $LaGaO_3$-$SrTiO_3$ sample grown at 10^{-4} mbar was found to be superconducting below a critical temperature of about $T_c = 150\,\mathrm{mK}$. This T_c is remarkably similar to that found in LAO-STO[3].

Electronic reconstruction or unintended doping? Just like in the $LaVO_3$ case, not all three conditions are fulfilled satisfactory: The samples did not receive any post-annealing in high-oxygen pressure and the effect of substrate termination on the electronic properties of $LaGaO_3$-$SrTiO_3$ interfaces was not checked properly. The presented evidence is nevertheless convincing and clear (almost) without ambiguity that the $LaGaO_3$-$SrTiO_3$ interface is yet another representative of LAO-STO-like conducting oxide-interfaces.

D.1.3. $DyScO_3$[170]: dysprosium scandate, a La-free oxide interface

Two publications about the $DyScO_3$-$SrTiO_3$ interface give opposite statements about its electronic properties: While Martina Luysberg and co-workers from the Research Center Jülich report[171] rather insulating behavior of $DyScO_3$-$SrTiO_3$ heterostructures grown by PLD on a 1-10 Ωcm silicon (100) wafer, D. F. Li, Yan Wang, and J. Y. Dai from The Hong Kong Polytechnic University have measured LAO-STO like electronic properties at $DyScO_3$-$SrTiO_3$ interfaces created by PLD on $SrTiO_3$ substrates.[170] Since the former approach, using a Si-substrate has several complications that are disconnected from the oxide-interface itself, I am going to focus on the latter, more traditional approach of using BHF-treated $SrTiO_3$ substrates.

$DyScO_3$ is the first material not containing La in this listing. It holds the same polarity as $LaAlO_3$. Its pseudocubic lattice constant of 3.944 Å matches that of $SrTiO_3$ quite closely. Based on these two facts Li *et al.* conclude, the $DyScO_3$-$SrTiO_3$ interface should have similar properties like LAO-STO, but with less defects thanks to the close lattice match. Their experimental observations can be summarized as follows.

Critical thickness The authors state in the beginning, to have grown $DyScO_3$ "thin films with different thicknesses and under different O_2 pressure conditions (PO_2) on TiO2-terminated STO single crystal substrate". In the remaining part of the paper they do nevertheless report on interfaces between 6 uc of $DyScO_3$ and $SrTiO_3$ only. No comment about a critical thickness for the reported conductivity is given.

Effect of substrate termination Only $DyScO_3$ films grown on Ti-site terminated $SrTiO_3$ have been investigated. No comment about the *p*-type interface is made.

Oxygen pressure The published temperature dependent magneto-transport data has been measured on samples grown at a substrate temperature of 750 °C, with the oxygen partial pressure at growths varying between 10^{-6} mbar and 10^{-3} mbar. After growth, the samples were annealed for 1 h at 400 °C in 10 mbar of oxygen[1]. Only for samples grown at 10^{-5} mbar or 10^{-6} mbar could metallic conductivity with Hall-mobilities up to 10^4 cm^2/Vs be found. A sample grown at 10^{-4} mbar had a non-monotonous $R(T)$-characteristic; samples grown at 10^{-3} mbar were insulating. The authors observed blue photo-luminescence in their samples, which proves that at least their low-pressure samples are oxygen deficient. Blue luminescence[172] is a well-known feature of reduced $SrTiO_3$ and has also been observed at oxygen deficient LAO-STO interfaces[173]. The observed conductivity is therefore quite clearly related to a reduced $SrTiO_3$ substrate.

Electronic reconstruction or unintended doping? The experiments of D. F. Li *et al.* are an example of an apparent LAO-STO like oxide interface that in the end turns out to be reduced $SrTiO_3$ only. Neither a critical thickness nor an effect of the substrate termination has been reported. Furthermore, the transport properties depend a lot on the growth conditions; metallic conductivity is found only if $DyScO_3$ is grown at low oxygen pressure. With additional evidence from other sources that claim the $DyScO_3$-$SrTiO_3$ interface to be insulating[171, 174], the reviewed report by Li *et al.* is quite definitely more about reduced $SrTiO_3$ than about an electronic reconstruction. Hence, $DyScO_3$-$SrTiO_3$ is not a member of the LAO-STO like conducting oxide-interfaces.

D.1.4. $GdTiO_3$[175]: gadolinium titanate, an MBE-grown interface

A special case in many regards is the report[175] about conductance in $GdTiO_3$-$SrTiO_3$ heterostructures by Pouya Moetakef and his co-workers from Susanne Stemmer's research group in Santa Barbara, USA. One peculiarity is the applied growth-technique, which in this case is a variant of MBE rather than PLD. Another peculiarity is the substrate used, which is not $SrTiO_3$, but $(LaAlO_3)_{0.3}(Sr_2AlTaO_6)_{0.7}$ (LSAT). On the (100) oriented LSAT substrate (no information about substrate termination is given) a $SrTiO_3$ film of variable thickness is grown by the group's unique hybrid MBE approach[176] with both gas and solid sources. On top of the $SrTiO_3$ film $GdTiO_3$ with a fixed thickness of 50 monolayers is grown. Interestingly, in the $GdTiO_3$-$SrTiO_3$ heterostructure only a single type of interface is structurally possible: since the B-site cation is Ti in both constituents, the only stable interface configuration is SrO-TiO_2-GdO.

Apart from electronic transport with high mobilities, the samples exhibit ferromagnetism comparable to that found in LAO-STO heterostructures[14].

[1] as a comparison: our standard LAO-STO samples are cooled in 400 mbar of oxygen, with 1 h long annealing steps at 600° and 400-450°.

Critical thickness In this special case the concept of a critical thickness for electronic transport is literally turned around: The $GdTiO_3$ layer has a fixed thickness, the $SrTiO_3$ thickness is varied instead. As a function of $SrTiO_3$ thickness the report indeed finds a critical behavior, comparable to that in $LaAlO_3$-$SrTiO_3$. The conductance of $GdTiO_3$-$SrTiO_3$ heterostructures with thick (≥ 20 nm) $SrTiO_3$ is 1-2 orders of magnitude higher than with thin (≤ 5 nm) $SrTiO_3$ layers. Furthermore, heterostructures with only a single unit cell or less $SrTiO_3$ are insulating. In a follow-up publication[177] the same authors state that the interface properties do not depend on the $GdTiO_3$ thickness and that a repeated stacking of 4 nm $SrTiO_3$/0.8 nm $GdTiO_3$ is conducting.

Oxygen pressure The deposition parameters are such that $SrTiO_3$ becomes heavily reduced: the organic titanium tetra isopropoxide precursor used as a Ti source might provide some additional oxygen, but at 950° and 1.33×10^{-9} mbar oxygen vacancies are inevitable. Why is it that a polar reconstruction is still considered as the reason for the observed conductance? Beyond the "critical thickness" of 20 nm the measured conductance does not scale much further with the $SrTiO_3$ thickness. The charge carrier density in these samples equals $\sim 3.5 \times 10^{14}$ /cm^2, which closely corresponds to the half an electron per surface unit cell required to compensate for the polar discontinuity at the interface according to the "polar catastrophe" scenario[57].

Moreover, the sheet carrier concentration scales (partially) when the $GdTiO_3$-$SrTiO_3$ stack is repeatedly grown. "The total carrier sheet density is not proportional to the total Gd in the superlattice nor is it proportional to the Gd concentration. It is proportional to the number of interfaces."[177]

Electronic reconstruction or unintended doping? In the present case this question is particularly difficult to answer. On the one hand, the growth conditions are obviously leading to reduced $SrTiO_3$, which must be contributing to the conductance of the heterostructure. When judged strictly by the three measures applied in the previous subsections, unintended doping of the $SrTiO_3$ by oxygen vacancies is by far the most likely explanation for conductivity in this system. On the other hand, the measured charge carrier density does not scale with the $SrTiO_3$ thickness, but with number of $GdTiO_3$-$SrTiO_3$ interfaces inserted by repeated growth of that heterostructure. It is hard to make a definite decision in this special and interesting example.

D.1.5. Other related interface systems

$NdGaO_3$[178]

In oral presentations[179] and a recent preprint[178] Fabio Miletto Granozio has presented evidence for conductivity and superconductivity at $NdGaO_3$-$SrTiO_3$ interfaces. The observation of conductivity at $NdGaO_3$-$SrTiO_3$ interfaces has also been confirmed very recently by F. Gunkel and coworkers from Rainer Waser's group in Aachen[180].

A single layer of LaO, PrO or NdO, embedded in $SrTiO_3$[181]

H. W. Jang and co-workers have inserted single atomic layers of rare-earth oxides (RO) into (100) oriented $SrTiO_3$.[181] They find conducting electron gases with a mobile charge carrier density of $\sim 10^{13}$ /cm^2 when R is lanthanum (La), praseodymium (Pr) or neodymium (Nd). On the contrary, no conductivity is found when R is samarium (Sm) or yttrium (Y). This difference is attributed to electronic correlations that are controlled by the rare-earth ion and lattice strain (compressive strain increases from Y to La, with $YTiO_3$ and $SmTiO_3$ under biaxial tension).

$CaHfO_3$[182]

The interface between $CaHfO_3$ and $SrTiO_3$ was found to be metallic with a high Hall mobility up to 2000 cm^2/Vs by Keisuke Shibuya *et al.*[182]. This system is nevertheless not directly related to LAO-STO, as $CaHfO_3$ is not a polar material. Further on, the $CaHfO_3$ layers in this study were grown at room temperature and are amorphous. Since the measured conductance is related to the laser-fluency, whose primary impact is on the energy of ablated species as they impinge on the substrate, the conductance is attributed to oxygen vacancies created by high-energy collisions at the $SrTiO_3$ crystal surface. The low substrate temperature prohibits re-oxidization from the surrounding oxygen atmosphere.

$LaCrO_3$[183]

Scott Chambers and co-workers have investigated the $LaCrO_3$-$SrTiO_3$ (100) interface. In their MBE-grown heterostructures they found "potential gradients within the $LaCrO_3$ sufficient to trigger an electronic reconstruction"[183]. They were unable to detect conductance, though, which they attribute "to interfacial cation mixing combined with charge redistribution within CrO_2 layers, enabled by low-lying d states within $LaCrO_3$, which suppresses an electronic reconstruction." Two alternative, more mundane effects could have hindered electronic transport in these studies, though: Contacts that were prepared with a focused ion beam (FIB), and the $LaCrO_3$ stoichiometry. As even tiny doses of gallium-ions produced in an FIB drive LAO-STO samples insulating[67, p. 112], its quite likely that the same would happen to any related oxide interface. Since in an FIB accelerated gallium is used not only to etch into, but also to image the sample, a not properly protected sample (e.g. by photo-resist) will probably become high-ohmic or insulating throughout the region scanned before etching, that is at least around the contact regions in the case of the $LaCrO_3$-$SrTiO_3$ samples of S. A. Chambers *et al.* The $LaCrO_3$-stoichiometry might be another point of concern for interface conductivity, especially in MBE-grown films. This point will be elaborated on in the next section about MBE-grown LAO-STO interfaces.

D.1.6. Summary

This section has collected reports about conducting oxide interfaces that might be related to LAO-STO. Without exception it is $SrTiO_3$ on the substrate side of these interfaces. In most cases the heterostructures were grown by PLD. Regarding the nature of the observed conductance, the doping-sensitivity of $SrTiO_3$ has therefore to be taken into account. Consequently, of the presented systems only two, namely $LaVO_3$ and $LaGaO_3$, should be considered to be driven by an intrinsic electronic reconstruction similar to that in $LaAlO_3$-$SrTiO_3$, and not by extrinsic doping due to oxygen vacancies[2]. With a large, and quickly rising number of theoretical predictions[184–186] more material combinations to extend this class of oxide interfaces are likely to be found in the coming years. A very welcome addition, especially from the view-point of possible applications in integrated circuits, would be a high-mobility hole-gas at an oxide interface as is predicted[184] at the $AgTaO_3$-$SrTiO_3$ interface. The following section will present another important degree of freedom for such interfaces, which is both an important prerequisite for interface conductivity and a powerful tool to exclude unintended substrate doping as a source of mobile charge carriers.

[2] $NdGaO_3$-$SrTiO_3$ is another likely candidate system, but the results of U.S. di Uccio, F. Miletto Granozio *et al.* [178] have not yet been published in a peer-reviewed journal.

D.2. Conducting oxide interfaces by molecular-beam epitaxy: stoichiometry matters

As pointed out in the previous section, $LaAlO_3$-$SrTiO_3$ is not the only oxide interface generating a two-dimensional electron gas. Several related compounds have been identified that, when grown beyond a characteristic critical thickness, induce a metallic interface. In all of these experiments, though, two constants remain: substrate = BHF-treated STO, deposition technique = PLD. Alternative substrates or substrate preparations will be the subject of the following sections. This section is going to tackle the latter point: the deposition technique.

PLD vs MBE Pulsed laser deposition (PLD) has certainly proven itself to be a versatile and reliable technique that produces complex-oxides thin-films and superlattices of excellent quality. With the help of RHEED, the thin-film growth can be controlled precisely on a sub-unit-cell level. Atomically sharp heterointerfaces are routinely fabricated. Their level of perfection manifests itself in the very high electronic mobility recently achieved[81, 187] in $LaAlO_3$-$SrTiO_3$ interfaces. Nevertheless, PLD has certain weak-points, in which another thin-film growth technique, molecular-beam epitaxy (MBE), excels. Two of them are especially relevant to LAO-STO interfaces: The film growth kinetics and the scalability of the technique. The kinetic energy of particles inside the PLD-plume can reach up to several 100 eV. In principle this kinetic energy enables particles to penetrate into the substrate, which is a point of concern when the substrate is susceptible to doping. $SrTiO_3$ is known to possess a rich phase diagram, its electronic properties are very sensitive to doping. It can be n-doped, for example, by small amounts of oxygen vacancies or niobium, but also lanthanum. So the pulsed-laser-deposition of lanthanum aluminate might indeed n-dope the $SrTiO_3$ substrate. In this regard MBE is clearly superior: The kinetic energy inside the molecular beam equates to the thermal energy of the evaporated material, which is well below 1 eV. At such a low energy, unintended doping by ion-implantation is out of question.

A second advantage MBE has over PLD is scalability. With MBE much larger samples, wafers up to several inches in diameter, can be processed. Producing large wafers is of course of primary importance for the cost-effectiveness of technological applications. But for some scientific applications like neutron- or muon-diffraction large-scale homogeneous samples are desirable as well. PLD is relatively limited in this regard, mainly by the beam-diameter of available high-energy laser sources. Therefore, molecular-beam epitaxy finds much more widespread use in semiconductor industry, where it is routinely used to produce e.g. GaAs/GaAlAs heterostructures for optoelectronics or high-electron-mobility transistors for very high frequency operation. In fact, 2DEGs in III/V semiconductor heterostructures are by far the most widespread application of molecular-beam epitaxy. They have been key to the discovery of the quantum Hall effect and other fascinating phenomena. They have enabled socially important technological innovations especially in the field of high frequency and optical data transmission.

The perfection of MBE grown semiconductor interfaces allows for almost infinite elec-

tron mobilities ($> 10^6\,\mathrm{cm}^2/\mathrm{Vs}$); an electron's mean free path associated with such a high mobility approaches macroscopic length scales enabling ballistic transport in these systems.

It is natural to ask if MBE can also boost the mobility achievable in oxide interfaces. We have tackled this question in collaboration with Darrell G. Schlom's group at Penn State University, PA (now at Cornell University, NY): Maitri Warusawithana (now Assistant Professor at Florida State University) used the group's oxide-molecular-beam-epitaxy facilities to grow high-quality LAO thin-films on BHF-treated (TiO_2-terminated) STO substrates. In this section, I am going to present the challenges, surprises and achievements of this research. Our corresponding manuscript entitled "$La_{1-\delta}Al_{1+\delta}O_3$ stoichiometry found key to electron liquid formation at $LaAlO_3/SrTiO_3$ interfaces" is currently in review[20].

D.2.1. Previous work

Surprisingly little has been published on the topic of MBE made LAO-STO interfaces. C. Merckling and M. El Kazzi and coworkers in G. Hollinger's research group reported[188, 189] on structural data of $LaAlO_3$ films grown on $SrTiO_3$. The only report of conducting interfaces in MBE grown samples is from Charles H. Ahn's group in Yale[190]. One should keep in mind, though, that the MBE growth of complex oxides is a daunting task and still a relatively young field. Only a handful of research groups worldwide are successfully operating oxide MBEs. The foremost reason, why the MBE growth of oxides is challenging, are the ultra-high vacuum conditions necessary for the molecular beam to travel from the source to the substrate without too much scattering. In standard MBE growth conditions most oxides would reduce quickly. This is nowadays counteracted with an ozone atmosphere. The enhanced reactivity of O_3 with respect to O_2 allows for a much lower background pressure at the same level of oxidization.

A pioneer in the field of oxide-MBE is Prof. Darrell G. Schlom with his group at Cornell University, NY, USA. They are currently operating two Veeco Gen10 MBE chambers modified for the requirements of oxide epitaxy. There have been a multitude of successful cooperations between Augsburg and Cornell, some of which will also be the subject of the following sections.

The MBE made $LaAlO_3$-$SrTiO_3$ interfaces that this section is going to discuss have almost exclusively been grown by Maitri Warusawithana. The sample contacts and most of the electrical characterization were done in Augsburg, primarily by Stefan Thiel and myself.

Our first tries to create conducting $LaAlO_3$-$SrTiO_3$ interfaces by MBE date back to 2007. It took many attempts to figure out that only with the substrate positioned on a certain 'sweet-spot' on the MBE's substrate heater the grown LAO film would generate a conducting interface. This finding was consequently investigated systematically: 16 substrates, each $5\,\mathrm{mm} \times 5\,\mathrm{mm}$ in size, were glued—in a mosaic style—to adjacent places, distributed on the substrate heater (see D.1b). To exclude a systematic influence of the individual substrate quality, the order in which the substrates were put into place was randomized. Unlike usual practice during MBE depositions, the sample stage was not

rotated while La and Al were deposited from sources on opposite sides of the vacuum chamber. This procedure created an intended spread in stoichiometry across the samples. D.1c presents the sample arrangement on the substrate heater along with the condensed results of transport measurements we have done with all of the samples: In the three runs with overall 48 samples processed in this way, only a fraction of the samples exhibited a conductivity comparable to our PLD grown $LaAlO_3$-$SrTiO_3$ interfaces. The experiment demonstrates a direct correlation between the composition of the LAO film and the electronic properties of the underlying interface: *stoichiometry matters!*

D.2.2. Large composition spread samples

To reproduce this finding and to improve the resolution of the experiment with regard to the $LaAlO_3$ composition (stoichiometry), the experiment was modified in the following way:

Experimental setup

Sample preparation Instead of many small substrates, a single large (10 mm × 25 mm) substrate was coated in the previously described manner. Overall 12 samples have been grown in that way, with different LAO thicknesses and different "biasing" of stoichiometry. The large specimen were then further processed in Augsburg, where I made ion-milled contacts using a lithographic mask designed in the group of Prof. James N. Eckstein, University of Illinois, USA. Figure D.2 shows photos of such samples in which the contact arrangement with 25 adjacent 4-wire measurement bridges (in two rows) is visible.

Contact design The main concept behind the contact design was probably to optimize the number of measurement points per sample length unit. Each measurement bridge comprises a pair of long-legged current contacts and two flanking voltage contacts. In this arrangement, depicted in D.2c, the current is to flow primarily in the narrow space centered in between the voltage contacts. This way only a very narrow region, with approximately homogeneous sheet resistance, is probed by each bridge. It should be noted that it is not entirely straightforward to quantitatively relate a 2-wire or 4-wire resistance measured in that configuration to the sheet-resistance of the interface region probed. If the contact resistance between the Au/Ti contacts and the 2DEG was negligible, the 2-point resistance measurable between the current contacts alone should be about 10 times the sheet resistance, as the aspect ratio of the current path between the contacts is at least 400 µm : 40 µm = 10. The 4-point resistance is more difficult to interpret, as the equipotential lines outside of the central current path can not be easily derived.

Cabling and instrumentation The size of the sample and the large count of contacts prohibited utilizing our normal sample probes. An automated wafer prober would have

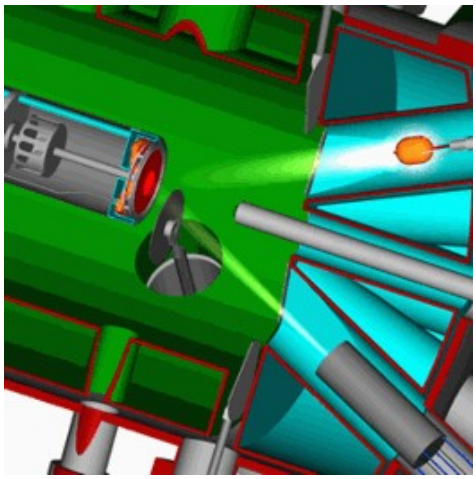

a Schematic of MBE system with central heated sample stage (red), and 2 sources on the right (blue)

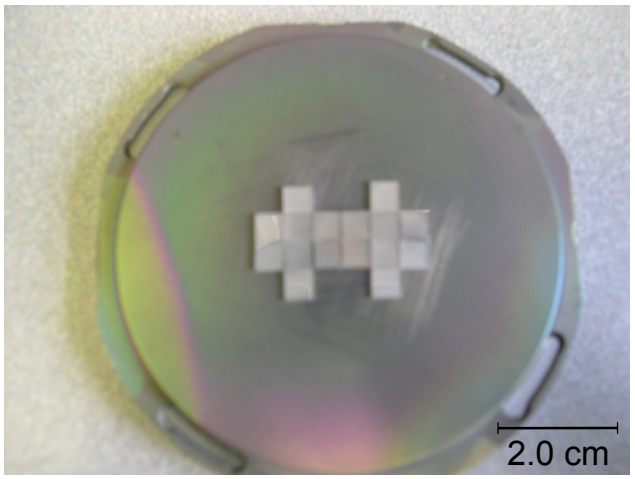

b Photo of sample stage used for MBE depositions, holding a mosaic of 16 LAO-STO samples

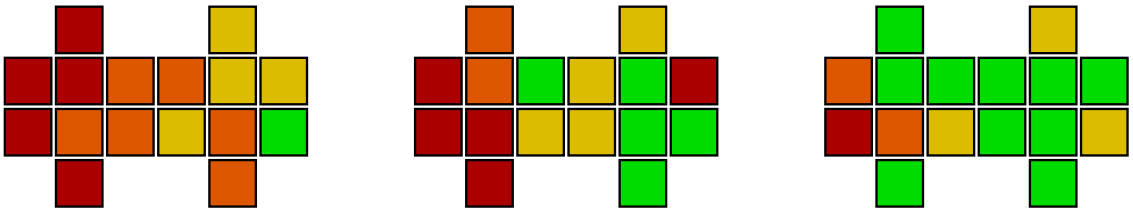

c Color-coded results of 3 mosaic experiments: red = insulating, orange = only photoconducting, yellow = semiconducting (conducting only at elevated temperature), green = conducting at all T

Fig. D.1: Illustration of the first MBE mosaic growth experiments: 16 samples, attached to the MBE sample holder in a mosaic, as photographed in (b) (courtesy of M. Warusawithana), were grown simultaneously by shuttered MBE growth. As illustrated in (a) (image courtesy of Andreas Schmehl), the lanthanum and aluminum sources are positioned on different sides of the sample holder. Therefore, the La/Al ratio varies among the samples. The electronic transport properties of the resulting interfaces between the 8 uc $La_{1-\delta}Al_{1+\delta}O_3$ film and the TiO_2 terminated $SrTiO_3$ substrates vary, too. The results of three different mosaic growths with regard to the samples' transport properties is summarized in (c).

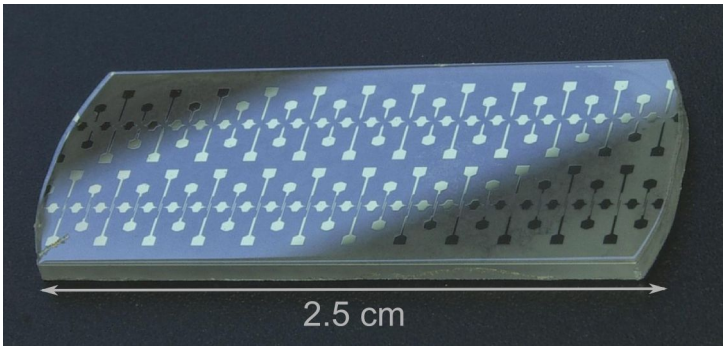

a Long composition spread sample with finished contacts

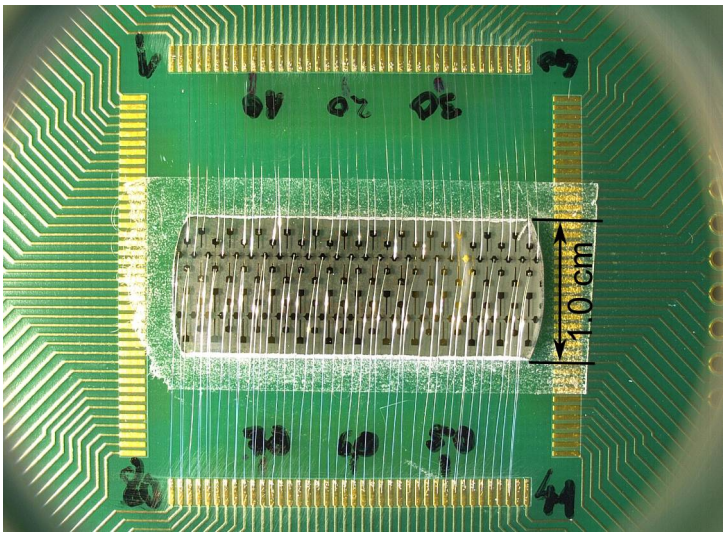

b Sample wire-bonded to a printed circuit board

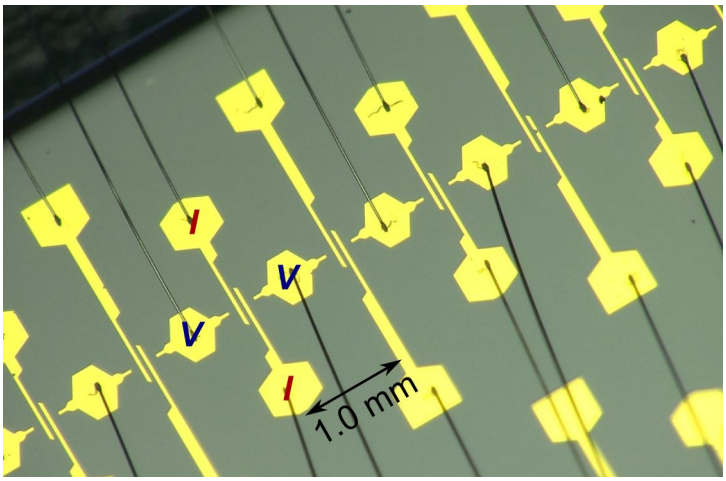

c Wire-bonded 4-wire measurement bridges; the letters indicate the current (I) and voltage (V) contacts.

Fig. D.2: Photographs of large (25 mm $\times$ 10 mm), MBE grown LAO-STO composition spread samples, with contacts made by sputtering Ti and Au into ion-milled pits defined by photo-lithography.

been the most practical tool for this research - our own technique involved more manual intervention.

Each sample was mounted on a printed circuit board (PCB), its 80 contacts were wire-bonded to the board's copper traces, as shown in D.2b. To shield the sample from light, the PCB with the bonded sample was mounted in a plastic box. Electrical connections to the PCB were fed through to the outside via D-Sub connectors. For each measurement bridge the corresponding pins (on the outside of the box) were manually connected to measurement equipment which usually consisted of a current source and a voltage meter, usually a Keithley 2400 source measure unit (SMU) and a Keithley 2001 multimeter. For measuring very high resistances $> 1\,\mathrm{G}\Omega$ appropriate instruments were employed: A Keithley 2636A high-impedance ($> 10^{14}\,\Omega$) SMU was used along with a Keithley 6514 electrometer.

With the described setup, measurements could solely be made at room temperature practically. Only at a later stage, selected portions of the samples were cut out and prepared separately to be measured in proper cryostats and in magnetic fields.

First results of resistance measurements

The first 3 samples investigated in that way (M420, M421, M422) had 8 unit cells of $LaAlO_3$. The nominal composition ratio of La/Al at the sample center was 1.0, 0.94 and 0.88. So the majority of the samples' real estate had more Al than La. The composition spread across the whole of each sample was estimated to be 20 %. The 3 samples consequently span an overlapping stoichiometry range from 22 % Al rich to 10 % La rich or $0.78 < \mathrm{La/Al} < 1.10$. Figure D.3 shows the result of the first resistance measurements on these samples. Clearly, the green, conducting part of all samples is on their Al rich right-hand side, suggesting that the formation of a 2DEG at the $LaAlO_3$-$SrTiO_3$ interface is much more tolerant to excess Al than it is to excess La in the $La_{1-\delta}Al_{1+\delta}O_3$ film.

Two oddities or irregularities regarding the results shown in Figure D.3 should be mentioned: The insulating island in the center of M420 and the overall relatively high resistance of M421. A possible reason for the former is either a non-monotonous relation between stoichiometry and conductivity or a non-monotonous spatial variance of stoichiometry along the sample. The latter reason will later be corroborated by an actual measurement of the spatial stoichiometry distribution. Both irregularities could also be due to a variation of the substrate quality or the substrate termination. From AFM images I have made on different spots of all samples prior to the contact preparation, no systematic connection between surface morphology and electronic properties could be drawn, though: All AFM images taken revealed a more or less perfect step-and-terrace structure with minor additional features (see Appendix E). On the one hand there were conducting as well as insulating areas found with a perfectly nice AFM image. On the other hand AFM images with precipitates or minor etch-pits were found in conducting as well as in insulating areas. So unfortunately the only conclusion one can draw, is that the surface morphology is not a clear indicator for the interface conductivity.

The qualitative result of the first resistance measurements is very clear, though: While a conducting LAO-STO interface can bear much excess Al, it is not nearly as tolerant

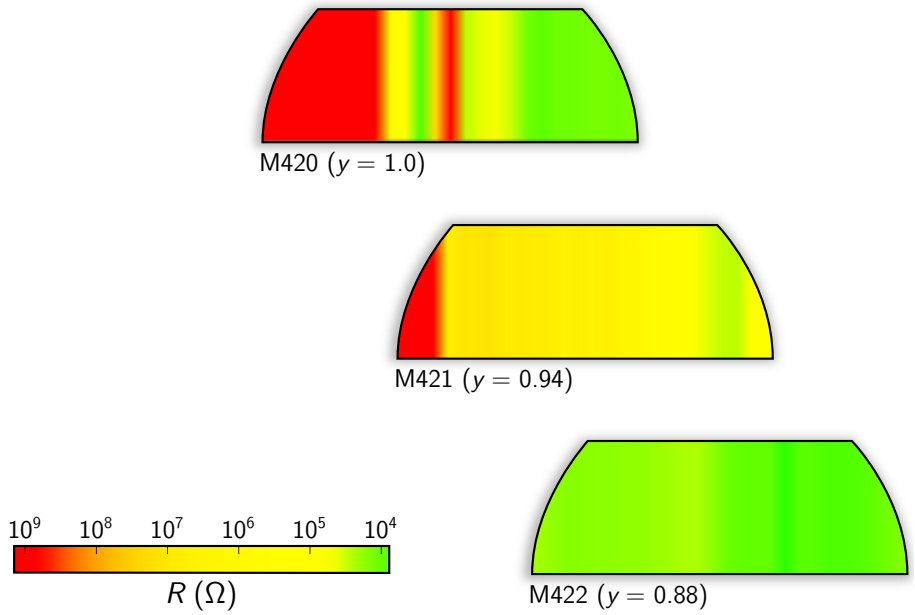

Fig. D.3: Color-code representation of the (interpolated) resistance measured on individual measurement-bridges along the first three large, MBE-grown LAO-STO samples. The composition of the $La_{1-\delta}Al_{1+\delta}O_3$ film varies, with a decreasing La/Al ratio from left to right along each sample. The parameter y, which is given in parenthesis after the sample name, represents the estimated nominal ratio of La/Al at the center of the sample. The 4-point resistivity measurements were done with the samples in darkness for at least 16 h.

to excess La. A more fundamental result should be mentioned as well: We have established a reliable and reproducible way to create large conducting LAO-STO interfaces by molecular-beam epitaxy. With only a slight modification of the process (enabling the sample stage rotation during deposition) we could cover an entire 1" wafer with a conducting LAO-STO 2DEG—a milestone for the technological advancement of oxide electronics. With a size of 25 mm × 10 mm, sample M422 is probably hosting the world's largest $LaAlO_3$-$SrTiO_3$ 2DEG so far.

D.2.3. Quantitative determination of $LaAlO_3$ stoichiometry by RBS

At this point it is obvious that the cation stoichiometry is at least as important to the electronic properties of a $La_{1-\delta}Al_{1+\delta}O_3$-$SrTiO_3$ interface as the LAO thickness. To quantify this statement, a quantitative measure of the film composition is required.

Rutherford Backscattering The method of choice for this kind of experimental question is Rutherford Backscattering Spectrometry (RBS). With RBS the structure and composition of materials can be determined by measuring the backscattering of a beam of high energy ions (usually alpha particles) impinging on a sample. From the scattering angle and energy loss of a backscattered ion the type of element with which the ion collided can, in principle, be determined. In an RBS experiment, there are two distinct processes for a He^+-ion to lose energy: Scattering events with sample nuclei and small-angle scattering with sample electrons. The former process gives sharp, discrete, element-specific peaks in the $N(E)$ profile recorded in a typical RBS experiment, where $N(E)$ is the count of detected scattered particles with energy E. The energy loss associated with the latter process is much lower. Multiple events thereof lead to a broadening of the elemental peaks, which rises with the number of collisions. The peak-width therefore depends sensitively on the probing depth.

Special RBS samples This probing depth dependent peak-broadening prohibits the direct application of RBS on a standard LAO-STO sample: Due to the thinness of the $LaAlO_3$ layer with respect to the thick substrate, the strontium and titanium peaks of the substrate surpass the lanthanum and aluminium peak by orders of magnitude. Due to the high probing depth, the substrate peaks are furthermore broadened considerable, with the result that the La and Al peaks of the film are completely buried in the substrate signal.

To circumvent this effect and get a proper measurement of our film composition nevertheless, we employed different substrates and thicker $La_{1-\delta}Al_{1+\delta}O_3$ films on specially structured companion samples. These companion samples consisted of approximately 400 Å of $La_{1-\delta}Al_{1+\delta}O_3$ on an approximately 500 Å thick $SrTiO_3$ buffer layer grown on a (100) MgO substrate. The purpose of the intermediate $SrTiO_3$ film was to lower the energy of the alpha particles as they penetrated through the intermediate film before being scattered off the substrate. This moved the substrate magnesium peak to sufficiently lower energies such that the aluminum peak was clearly separated from the magnesium peak. For each LAO-STO device sample I have patterned and measured, a

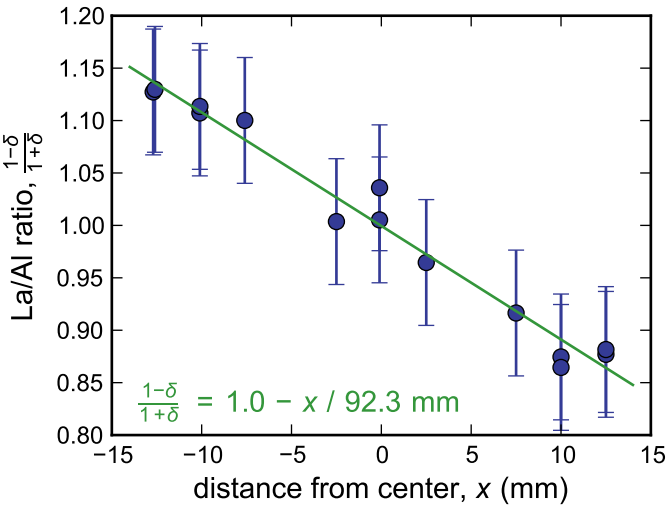

Fig. D.4: La/Al composition spread across two MBE grown $La_{1-\delta}Al_{1+\delta}O_3$ films, measured with Rutherford Backscattering Spectrometry. The linear relationship between La/Al ratio and position, derived from this data, is shown as a green line. The errorbars cumulatively represent the RBS counting error (1.0 %), the spatial (mis-)determination of the RBS measurement spot position (2.0 %), the drift in source fluxes between consecutive growths (2.0 %) and the device (mis-)placement from center of sample (1.2 %).

companion sample was grown right afterwards at identical growth conditions. From the RBS spectrum, by peak integration, an accurate measurement of the La/Al ratio at the center of the companion device sample was determined.

To obtain the spatial variation of the La/Al ratio across the $La_{1-\delta}Al_{1+\delta}O_3$ films grown on the long (100) $SrTiO_3$ crystals, two separate RBS calibration samples were grown, which also spanned the spatial extent of the long LAO-STO samples. These RBS calibration samples were structured similar to the companion RBS samples. RBS data was measured as a function of position on both of these two calibration growths. From the spatially resolved RBS measurements it was observed that, for our system, the variation in the La/Al ratio was mostly along the left-to-right (x) direction. To obtain the relative spatial variation of the La/Al ratio, $(1-\delta)/(1+\delta)$, along the x-direction for any sample, the La/Al ratio at the center of each of the calibration RBS samples was scaled to $(1-\delta)/(1+\delta) = 1.00$. This data (see Figure D.4) which provides the spatial variation of the La/Al ratio across a sample along the x-direction, together with the data from the companion RBS sample which provides the absolute La/Al ratio at a given point of the sample, makes it possible to accurately determine the La/Al ratio, $(1-\delta)/(1+\delta)$ at any point of the long $La_{1-\delta}Al_{1+\delta}O_3$-$SrTiO_3$ samples.

While the x-dependence of $(1-\delta)/(1+\delta)$, which is shown in Figure D.4, can be well approximated with a linear function, on closer inspection the data appears non-linear and even non-monotonic. Disregarding the error-bars, a local maximum of $(1-\delta)/(1+\delta)$ around $x = 0$ mm can be recognized. Coming from negative x, the La/Al ratio first approaches 1.0 from above at $x \approx$ -2 mm, but spikes around $x \approx 0$. If this was not a measurement error, but reflected the true stoichiometry along the MBE samples, this would explain the insulating island around the center of M420 and a number of additional samples: In this case the local maxima would be caused by the non-monotonic $\delta(x)$ dependence of the La/Al ratio.

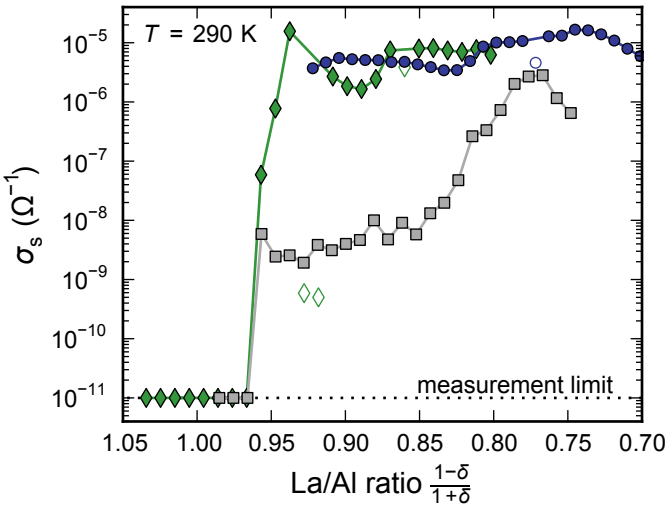

Fig. D.5: Local sheet conductance σ_s at MBE made LAO-STO interfaces on 3 different samples as a function of local stoichiometry $(1-\delta)/(1+\delta)$ of the MBE grown, 8 uc thick $La_{1-\delta}Al_{1+\delta}O_3$ films. The La/Al ratio (stoichiometry) was derived from RBS measurements. The sheet conductance represented by filled symbols was derived from 4-wire measurements for all data points above the measurement limit. In cases, in which the 4-point resistance could not be unambiguously measured, a 2-point resistance was measured instead. These cases are marked with open symbols.

D.2.4. Result: no conductivity in stoichiometric LAO-STO

With the results from the RBS measurements, which were done by W. Zander and J. Schubert at the Research Centre Jülich, Germany, we can put together a direct mapping between the local stoichiometry and conductivity of the investigated MBE samples. This is done in Figure D.5. As can be seen, the steep crossover from insulating to conducting behavior is measured at a La/Al ratio of 0.97 ± 0.03, consistently across the samples. A La/Al ratio $\leq 0.97 \pm 0.03$ is found to be a necessary condition for obtaining a 2-DEL at the interface between $LaAlO_3$ and $SrTiO_3$. Consequently, a stoichiometric LAO-STO interface is insulating, even though the $LaAlO_3$ layer is more than 4 uc thick.

This surprising result has a lot of important implications and begs several exciting questions of which one of the foremost probably asks for the stoichiometry of $LaAlO_3$-$SrTiO_3$ interfaces grown by PLD. The common understanding of how pulsed laser deposition works, is that it transfers material from the target onto the substrate preserving the original target stoichiometry also in the film to a large extent. Our $LaAlO_3$ target is single crystalline, suggesting a near-perfect stoichiometry, which should in consequence be found in PLD grown films, too.

Stoichiometry of PLD grown $LaAlO_3$ To determine the actual composition of our PLD grown $LaAlO_3$ films, we prepared in our PLD system, using our standard parameters for the $LaAlO_3$ film growth, a sample for RBS measurements similar to the previously described MBE-grown RBS samples. This sample was also measured by RBS in Jülich, alongside the MBE samples. The measured La/Al ratio in the PLD grown $La_{1-\delta}Al_{1+\delta}O_3$ film is 0.88 ± 0.02. On the one hand this value is rather surprising, considering the aforementioned general property of the PLD process. On closer inspection, though, it is obvious that different elemental species in a PLD plasma plume have dif-

ferent kinetic energy and different scattering cross-sections.[3] Also the vapor pressure of different molecules on the hot substrate surface differ which leads to different evaporation rates. On the other hand, a La/Al ratio in our PLD grown $La_{1-\delta}Al_{1+\delta}O_3$ films of < 0.95 was to be expected from a comparison of the transport properties of PLD and MBE grown LAO-STO interfaces. Provided that the stoichiometry-dependence we have derived from MBE-samples applies universally, it is indeed a fascinating coincident, that numerous other institutions have grown the same non-stoichiometric $La_{1-\delta}Al_{1+\delta}O_3$ films, reproducing Akira Ohtomo's and Stefan Thiel's original results.

On the contrary, our result that an aluminum surplus is a requirement for conductance at LAO-STO interfaces, provides an explanation, why sputtered $LaAlO_3$ has not yet generated conducting oxide 2DEGs: Sputtering seems to promote a lanthanum surplus; the sputtered $La_{1-\delta}Al_{1+\delta}O_3$ films grown by I. M. Dildar *et al.* are lanthanum rich with a La/Al ratio of 1.07.[192]

D.2.5. Carrier density and mobility of MBE samples

The initial goal of this research was to implement the growth of high-quality $LaAlO_3$-$SrTiO_3$ interfaces by molecular-beam epitaxy with the hope to gain an enhanced mobility due to the possibly higher crystalline perfection of MBE grown $LaAlO_3$ films. To make sure that the large MBE samples have transport properties similar to that of PLD samples, magneto-transport measurements at low temperatures are indispensable. As the large sample size is incompatible with most cryostat systems, and the previously described contact-arrangement does not allow a quantitative analysis of transport measurements, the samples had to be modified.

Sample preparation for Hall-measurements Figure D.6 outlines the way in which the samples were sliced and patterned to facilitate temperature dependent magneto-transport measurements: Samples were first halved parallel to the long edge. One half was patterned with contacts for room-temperature measurements, similar to the procedure previously described. The other half was sliced into three 5 mm × 8 mm pieces. Each of these pieces was again sub-divided into 4 electrically separated individual devices by cutting the sample surface perpendicular to the long edge with a wire-saw, approximately 200 µm deep (see Figure D.6). The approximately 1.6 mm × 5 mm big slices were oriented with their short edge parallel to the stoichiometry gradient. The stoichiometry and therefore also the electronic properties of each 1.6 mm × 5 mm slice should therefore be quite homogeneous.

Using photo-lithography and our usual contact preparation with ion-milling and sputtering, contacts to the LAO-STO interface were prepared around the edges of each device.

[3] This effect has been investigated by T. C. Droubay and coworkers[191]. The result of their research is that more lanthanum than aluminum is deposited on the substrate. Their deposition parameters, however, include a high oxygen pressure of 0.013 mbar, an uncommonly large laser spot of 1 mm × 10 mm and their target was neither scanned nor rotated. LAO-STO interfaces grown at such high oxygen pressure do not exhibit a high-mobility 2DEG[59].

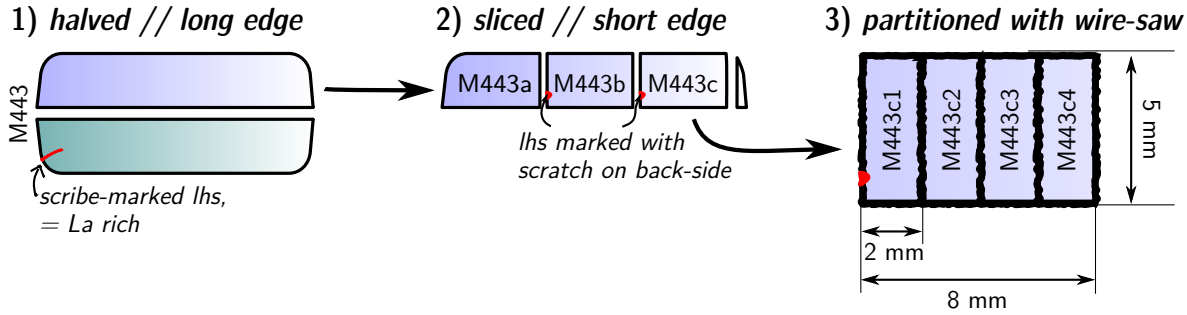

a Schematic illustration of sample preparation for Hall-measurements with exemplary naming scheme for sample M443.

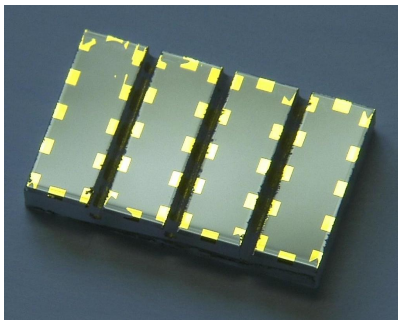

b Partitioned subsample M443c, with ion-milled Au/Ti contacts

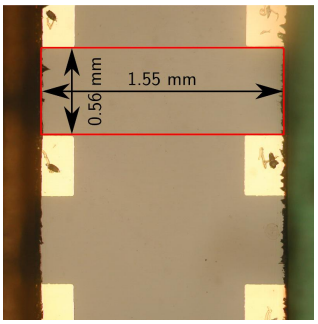

c Single device M443c4 on subsample M443c

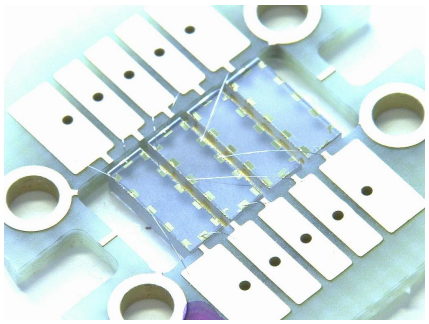

d M443c mounted and wire-bonded in sample-holder

Fig. D.6: Illustration of the way in which, starting from a large 25 mm × 10 mm MBE-grown LAO-STO sample, smaller 8 mm × 5 mm subsamples are made; each with four individual partitions/devices with ion-milled and sputtered Au/Ti contacts at their edges.

The result of this procedure were multiple thin slices of MBE grown LAO-STO interfaces with contacts compatible with the van-der-Pauw technique[193]. This way, the charge carrier density and Hall-mobility of our MBE samples could be accurately determined.

Hall-measurement results Figure D.7 summarizes the results of temperature dependent magneto-transport measurements on two of those slices with an approximate La/Al ratio of 0.95-0.9. Their charge carrier densities were $n_s = 0.8 - 0.9 \times 10^{13}$ /cm^2 for $T >$ 100 K, but would drop considerably below 100 K. Whereas n_s is noticeably lower than in a typical PLD sample, the drop below 100 K is typical for LAO-STO interfaces.[67, 194] The charge carrier mobility μ in the investigated slices is noticeably higher than that in our standard PLD samples, where μ hardly approaches 1000 cm^2/Vs[52]. The measured MBE value of around 6600 cm^2/Vs at $T = 4$ K is on par with the highest mobility reached by Andrea Caviglia *et al.* by excessively optimizing their PLD growth parameters; it is high enough for observing quantum conductance oscillations.[187]

The investigated samples featured another peculiarity of LAO-STO interfaces, a hysteretic $R(T)$-behavior: When warming up LAO-STO interfaces from 4 K to room tem-

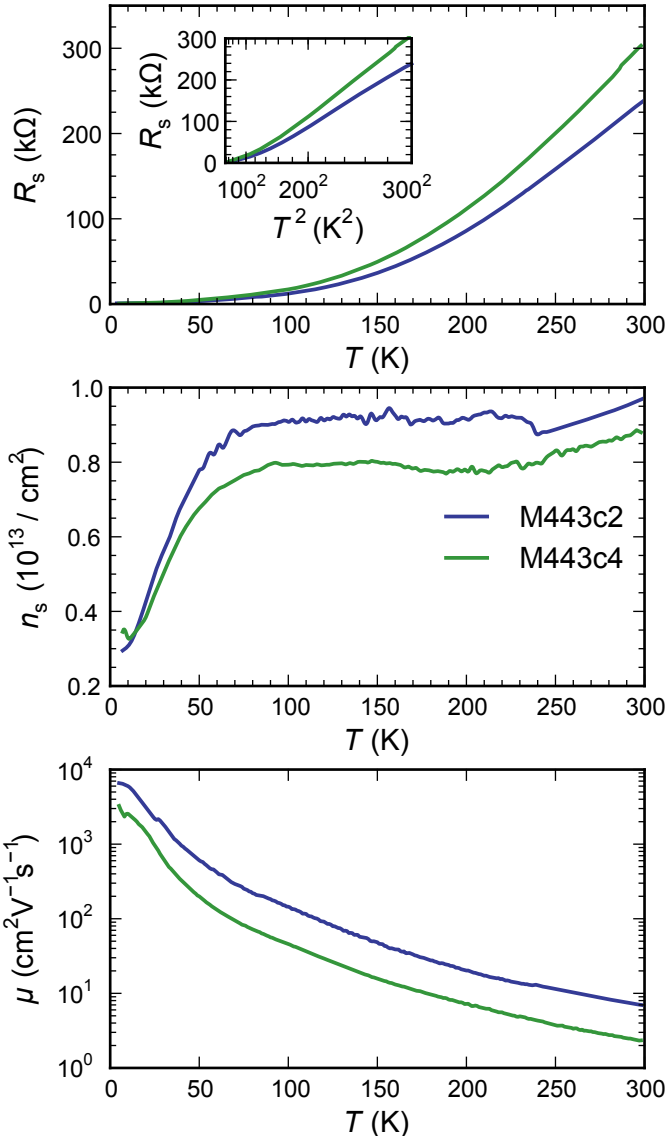

Fig. D.7: Temperature dependence of sheet resistance R_s, charge carrier density n_s and Hall-mobility μ, measured on two different devices (with different La/Al ratio) on a piece of MBE-grown LAO-STO sample M443, with a $LaAlO_3$ thickness of 8 uc. The sheet resistance is proportional to T^2 as is demonstrated by inset in the topmost graph, where R_s is plotted against T^2. The carrier density in both samples is $< 10^{13}$ /cm^2 and displays the LAO-STO-typical drop at $T < 100$ K. At the lowest temperatures probed (4 K), mobility exceeds 1000 cm^2/Vs in both slices, with sample M443c2 approaching 6600 cm^2/Vs.

perature one often observes local maxima or humps in $R(T)$ that were previously absent when the sample was first cooled. I have also found such features in the investigated MBE samples, even more pronounced than in usual PLD made samples. A magneto-transport analysis of these features, which traces their origin to thermally activated charge-carriers can be found in Appendix F.

The presented measurements were just a starting point, a prove of concept for the described preparation and measurement technique. Experiments with the sliced samples were continued by Priyashree Roy, Jonathan Ludwig and others at the National High Magnetic Field Laboratory of Florida State University. Among other things they found an interesting relation between $La_{1-\delta}Al_{1+\delta}O_3$ stoichiometry, charge carrier density and superconducting transition temperature.

D.2.6. Summary and conclusions

We have proven that conducting $LaAlO_3$-$SrTiO_3$ interfaces can be realized by a technique other than pulsed laser deposition. By purposely growing non-stoichiometric, aluminum rich $La_{1-\delta}Al_{1+\delta}O_3$ films on Ti-terminated $SrTiO_3$ substrates, we were able to create conducting oxide 2DEGs of unprecedented size and with sizable electron mobilities. Surprisingly we found no conductivity beneath stoichiometric or lanthanum-rich $LaAlO_3$ films, even if their thickness surpassed the critical value of 4 uc.

The critical thickness of 4 uc, previously found for PLD made LAO-STO interfaces[52], could be reproduced also in MBE samples, if the stoichiometry is taken as fixed to a La/Al ratio of 0.91, the value measured in our PLD samples. The complete phase-space spanned by $La_{1-\delta}Al_{1+\delta}O_3$-thickness and -stoichiometry was not presented, as it requires additional research.

The finding that conducting $LaAlO_3$-$SrTiO_3$ interfaces can be made by molecular-beam epitaxy, and how their properties depend sensitively on the $LaAlO_3$ composition has several important implications. Most importantly it excludes most (if not all) of the proposed extrinsic causes of conductivity in $LaAlO_3$ on TiO_2-terminated (100) $SrTiO_3$ samples:

1. *Oxygen vacancies in the $SrTiO_3$ due to substrate preparation (termination[195]) or insufficiently oxidizing conditions during heating, growth and cooling[173, 196–198]:* All of those conditions would have reduced the entire sample. They would not have selected regions with a special $LaAlO_3$ stoichiometry.

2. *Bombardment of the $SrTiO_3$ by energetic species during growth leading to oxygen vacancies[182, 199–201]:* As described in this section's introduction, MBE affords a gentle means of film growth utilizing only thermal beams of neutral species, including the purified ozone beam used as the oxidant, with energies well below 1 eV.

3. *Chemical intermixing of lanthanum from the $LaAlO_3$ with the $SrTiO_3$ to make La-doped $SrTiO_3$[202, 203]:* Conductance is found in the aluminum rich, not the

lanthanum rich regions of the sample. Diffusion of La into the substrate would be expected to be more pronounced in the La rich regions. These are, however, found to be insulating.

With the strong correlation between $LaAlO_3$ stoichiometry and electrical properties we have discovered an important prerequisite for the applicability of new deposition techniques like sputtering or chemical vapor deposition for conducting oxide interfaces. Almost certainly will the scope of of this finding extend to the aforementioned $LaAlO_3$ alternatives found, as well as on those not yet found. It might well be that the class of $LaAlO_3$-$SrTiO_3$ like oxide 2DEGs will broaden considerably, once the cation stoichiometry can properly be taken account of. A proper theoretical understanding of the microscopical mechanism relating $LaAlO_3$ defects to free charge carriers at the interface would be highly desirable in this regard. Density functional calculations on non-stoichiometric $La_{1-\delta}Al_{1+\delta}O_3$-$SrTiO_3$ heterostructures by Stephen Hellberg[20] suggest that different kinds of defects are formed depending on whether the La/Al ratio is smaller or larger than 1. For La-rich samples, charged cation vacancies form at the interface. These vacancies can compensate the polar discontinuity, inhibiting an electronic reconstruction and the emergence of mobile electrons at the $LaAlO_3$-$SrTiO_3$ interface. This is not the case for Al-rich $La_{1-\delta}Al_{1+\delta}O_3$-$SrTiO_3$. Here, the excess Al can substitute La. This substitution does not result in any net charge and hence does not interfere with the polar discontinuity and electronic reconstruction.

D.3. HF-free termination-process for high-quality LAO-STO interfaces

The starting point for each and every $LaAlO_3$-$SrTiO_3$ sample grown in our PLD is a high-quality substrate with the right surface termination. The $SrTiO_3$ crystal can be thought of as stacked layers of SrO and TiO_2, alternating along the [001] crystal direction. The (100) surface of a polished substrate, as it can be bought from vendors like CrysTec, Surfacenet or Shinkosha, will usually comprise a mix of both species. Only a TiO_2-terminated $SrTiO_3$ substrate, though, can generate the conducting electron system[25], when at least 4 unit cells[52] of $LaAlO_3$ are grown on its TiO_2 surface. Thus, the natural prerequisite for any conducting $LaAlO_3$-$SrTiO_3$ sample is to prepare the $SrTiO_3$ substrate surface according to a well-proven recipe: the so-called "Twente-Etch". The main ingredients to this recipe are:

1. **10 minutes in H_2O** (bidest.), in ultrasonic bath: In water, any strontium on the crystal surface reacts to strontium hydroxide: $SrO + H_2O \longrightarrow Sr(OH)_2$

2. **30 seconds in HF**, in ultrasonic bath: The strontium hydroxide is very slightly soluble in water. To remove it from the surface completely, a buffered hydrofluoric acid ("BHF" or "buffered oxide etch": 87.5% NH_4F, 12.5% HF) is used.

3. **7 hours in O_2 at 950 °C**: After thoroughly rinsing the substrates in water to wash off the BHF, they are loaded into a tube furnace, where in a steady flow of oxygen they are heated to 950 °C. This process cleans and heals the substrate surface.

This 3-step process was first published in 1998 by Gertjan Koster and his coworkers[36] from the University of Twente in the Netherlands (thus the colloquial naming "Twente-Etch"). It is a refinement of Masashi Kawasaki's original recipe[35], which involved only steps 2-3. The Twente-Etch has been used almost exclusively to achieve high-quality single-terminated $SrTiO_3$ substrates, surely for more than a thousand substrates in our labs alone.

The HF-etching involved is not without flaws, though. Apart from the harm that fluoric acid poses to the environment and human health, it also alters the $SrTiO_3$-crystal's chemical composition to a certain extend. Using surface sensitive X-ray spectroscopy, Götz Berner and his colleagues from Ralf Claessen's group in Würzburg found traces of fluorine in some of our $LaAlO_3$-$SrTiO_3$ samples (private communications). A recent publication by Scott Chambers *et al.* [204] state that "on average $\approx$ 13% of the O anions in the surface layer are replaced by F, but that F does not occupy O sites in deeper layers." The authors suggest to replace the HF-etching with a boil in deionized water. The sample treatment in this report is slightly different from our standard recipe, though, which might be the reason for the much higher level of fluorine doping found by Chambers *et al.* HF-etching has also been found to produce a high-density of point-defects mostly in the form of oxygen vacancies near the $SrTiO_3$ surface.[195]

In this section I will present a different procedure to achieve high-quality single-terminated $SrTiO_3$-substrates and explore, whether such substrates can be used to obtain fluorine-free conducting $LaAlO_3$-$SrTiO_3$ interfaces.

D.3.1. The Arkansas-Etch

The Arkansas-Etch is a $SrTiO_3$ termination procedure that yields a terminating TiO_2 layer at the substrate surface. It was first published in by M. Kareev and coworkers in 2008[205]. The procedure was found to produce less defects than the venerable Twente-Etch[195]. The main point of difference between Twente- and Arkansas-Etch is the acid used to remove the strontium hydroxide. Instead of BHF, the Arkansas-Etch uses a solution of chloric and nitric acid HCl:HNO_3 3:1 also called "aqua regia". The recipe I used, was slightly modified from the published[205] one:

1. 25 minutes in H_2O, in ultrasonic bath,
2. 12 minutes in HCl/HNO_3 (3:1), in ultrasonic bath,
3. rinse with H_2O, anneal in O_2 for 7h at 950 °C.

It should be noted, that the substrates have been left in water for almost twice as long as in our Twente-Etch recipe. Also the 12 minutes etching time in aqua regia is much longer than the 30 seconds our substrates usually spend in HF. Prolonged etches often result in visible defects on the substrate surface. The natural defects present on any real-world crystal surface are weak points, easily attacked and removed by the etch. Therefore, prolonged etching is a useful tool to make crystal defects visible to surface probes like AFM or even optical microscopy.

D.3.2. Surface morphology of Arkansas-etched substrates

AFM images of a $SrTiO_3$ substrate surface treated with the Arkansas-Etch are shown in Figure D.8. The unit-cell high steps-and-terraces observed indicate that the substrate is indeed single-terminated. No precipitates or other impurities have been observed. On the contrary, the HCl:HNO_3 etching has created many etch-pits ($\approx 10^7$ /cm^2), preferentially located at step edges. The pits are quadratic, roughly 0.1 µm × 0.1 µm wide and approximately 10 $SrTiO_3$ unit cells (3-4 nm) deep. The etch-pit areal density is a measure of the surface dislocation density. The measured number of 10^7 /cm^2 is quite typical for Verneuill-grown $SrTiO_3$ crystals.

D.3.3. RHEED-controlled $LaAlO_3$ film growth

To test if a conducting $LaAlO_3$-$SrTiO_3$ interface can be created on a $SrTiO_3$ substrate terminated by the Arkansas-Etch, 4 $LaAlO_3$ monolayers have been PLD-grown with our standard recipe. As usual the $LaAlO_3$ growth was monitored with reflection high energy electron diffraction (RHEED). The observed RHEED-pattern is identical to that of HF-etched $SrTiO_3$ substrates. As Figure D.9 shows, the intensity of the main diffraction

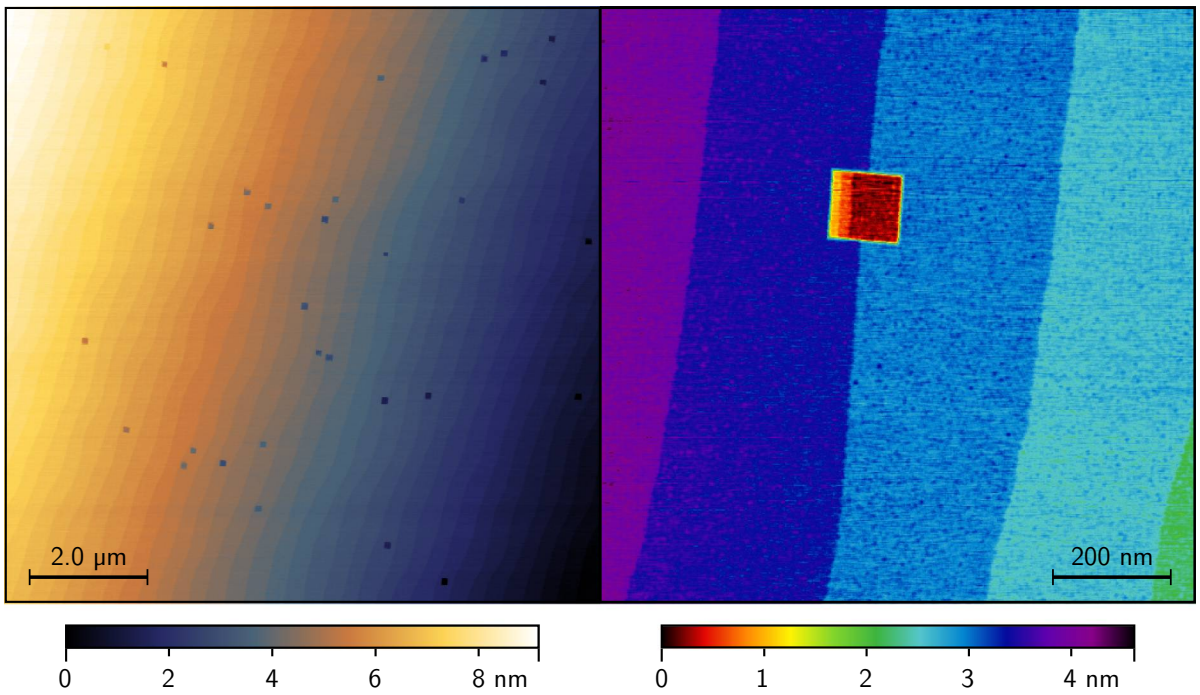

Fig. D.8: AFM topographic images of a $SrTiO_3$ substrate treated with the Arkansas-Etch. A step-and-terrace like structure with 0.2 - 0.3 µm wide terraces and 0.4 nm high steps is observed. The surface is speckled with 0.1 µm × 0.1 µm wide, ≈ 3 nm deep etch-pits.

spot oscillated over 4 periods during the $LaAlO_3$ film growth, with a period of about 20 shots, indicating nice layer-by-layer growth of 4 monolayers of $LaAlO_3$.

D.3.4. Electronic properties of HF-free $LaAlO_3$-$SrTiO_3$ interfaces

To measure the sample's sheet-resistance, the Van-der-Pauw method[193] had to be employed, since the grown $LaAlO_3$-$SrTiO_3$ interface is unpatterned. Therefore Al-wire-bonds were cold-welded to the edges of the sample surface. Although this contact-method is not as elegant as recessed contact plugs made by ion-milling and sputtering, the resulting contacts are more than adequate for 4-wire measurements and more point-like than lithographically defined contacts. Another advantage over photolithographically defined contacts is, that the surface is not exposed to water or chemicals, which might alter the electronic properties of the LAO-STO interface[206].

Figure D.10 shows the measured temperature dependence of the sheet-resistance. The interface between $LaAlO_3$ and an Arkansas-etched $SrTiO_3$ substrate is very similar to standard $LaAlO_3$-$SrTiO_3$ samples. Its sheet resistance is 68 kΩ at 290 K and 0.14 kΩ at 4 K. The temperature coefficient is always positive (metallic), the $R_s(T)$-curve is parabolic, a well-known feature of $LaAlO_3$-$SrTiO_3$, commonly attributed to electron-electron interactions as the scattering mechanism dominating the resistivity ("Fermi-liquid behavior"). In comparison to standard $LaAlO_3$-$SrTiO_3$ samples the resistance of the Arkansas-etched sample is a bit higher at elevated temperatures, but somewhat

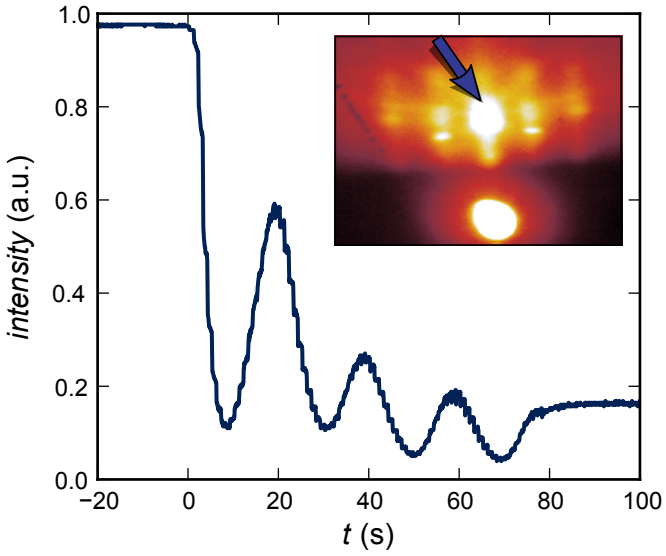

Fig. D.9: Normalized RHEED intensity during growth of 4 monolayers of $LaAlO_3$ on an Arkansas-etched $SrTiO_3$ substrate. The deposition started at $t = 0\,s$ and ended after 79 shots at $t = 78\,s$. The plotted intensity is the peak intensity of the main diffraction spot indicated by an arrow in the inset RHEED image. The image shown is the diffraction pattern after the finished film-growth.

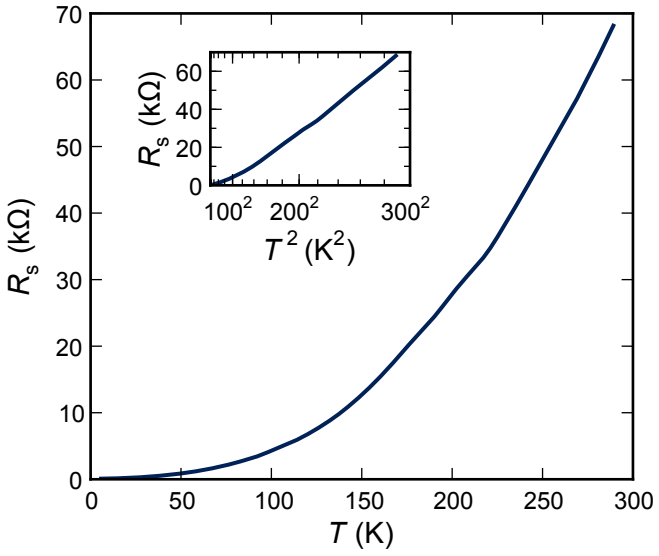

Fig. D.10: Sheet resistance R_s measured as a function of temperature in a Van-der-Pauw configuration on a sample of 4 uc $LaAlO_3$ on an Arkansas-etched $SrTiO_3$ substrate. The sheet resistance is proportional to T^2 as is demonstrated by the inset, where R_s is plotted against T^2.

lower at cryogenic temperatures. As the spread in charge carrier density and mobility is quite large among our usual $LaAlO_3$-$SrTiO_3$ samples, a fair comparison would require a larger sample set to gather statistics. Still, two conclusions can safely be drawn from this experiment:

First, the Arkansas-Etch provides a viable method for obtaining single-terminated, fluorine-free $SrTiO_3$ substrates on which a conducting $LaAlO_3$-$SrTiO_3$ interface can be realized. This also means that neither the specific influence of the HF-etching on the substrate nor fluorine itself is a necessary ingredient to the conducting interface between insulators.

Second, etch-pits on the sample-surface are apparently no worse than other types of dislocations. It is only at dislocations, that holes are etched into the substrate. So depending on the type and duration of the etching, either a surface dislocation stays untouched, or is exchanged for an etch-pit. Either of both might pose a scattering center to the interface electronic system. At low temperatures, the sheet-resistance of the Arkansas-etched sample, although speckled with etch-pits, is equal or lower than the sheet-resistance of samples not etched long enough to remove the dislocations. This is an indication, that at low temperatures, the scattering cross section of $SrTiO_3$ surface defects is larger than that of an etch-pit. See [207] and [67] for a more detailed study of the impact, which dislocations have on the $LaAlO_3$-$SrTiO_3$ interface transport properties.

	$SrTiO_3$	$CaTiO_3$	$LaAlO_3$
cubic lattice constant (Å)	3.905	3.82	3.790
bandgap (eV)	3.2	3.6	5.6
rel. permittivity (300 K)	300	170	24.0
rel. permittivity (4 K)	$> 10^4$	330	23.7

Tab. D.1: Comparison of selected structural and electronic properties of $SrTiO_3$, $CaTiO_3$ and $LaAlO_3$. Data from [27, 30, 33, 34, 42, 44, 209–211].

D.4. A conducting interface on an insulator that is not $SrTiO_3$: the $LaAlO_3$-$CaTiO_3$ interface

In the previous sections I have shown that the $LaAlO_3$-$SrTiO_3$ interface is not a singular entity, but belongs to a broader class of polar oxide interfaces. As special and peculiar as this physical phenomenon had seemed in the beginning, most of its constituents can be varied. By now the emergence of a conducting interface between two insulators has been observed with $LaAlO_3$ grown on $SrTiO_3$ by pulsed-laser- and molecular-beam-epitaxy; active research to achieve the same with sputtering is on its way[192]. It has been shown that the interface between $LaVO_3$[161], $LaGaO_3$[167] or $NdGaO_3$[178] and $SrTiO_3$ generates an electron system quite similar to the $LaAlO_3$-$SrTiO_3$ interface. So neither lanthanum nor aluminium (but the polar nature of the AlO_2 and LaO sublayers) are essential ingredients to the observed phenomenon. I have shown that the HF-based etching process commonly used to prepare a single-terminated $SrTiO_3$ substrate surface can safely be replaced by a different recipe, which is not involving fluorine. Yet, for all of these experiments, the same substrate material has been used: $SrTiO_3$. The aim of this section is to show that a conducting interface can be realized on a substrate other than $SrTiO_3$, namely $CaTiO_3$, a mineral known as "Perovskite", which lends its name to the rich class of materials which have the same type of crystal structure.

D.4.1. Material properties of $CaTiO_3$ (perovskite)

In many aspects, $CaTiO_3$ is very similar to $SrTiO_3$. Both are perovskites with similar lattice constants. Both are band-insulators with approximately similar bandgaps. And both are incipient ferroelectrics with a relatively high dielectric constant[208, 209]. subsection D.4.1 compares several key properties of $CaTiO_3$ and $SrTiO_3$ found in literature. It should be noted that $CaTiO_3$'s lattice constant is almost identical to that of $LaAlO_3$: The lattice mismatch between the two materials is only 0.5 %. Its lattice constant made $LaAlO_3$ a popular substrate for epitaxial thin-film growth of many interesting materials, in particular high-temperature superconductors like $YBa_2Cu_3O_7$. In this sense, $CaTiO_3$ could be a popular substrate material as well. And although tried recipes for $CaTiO_3$ single crystal growth exist[212, 213], $CaTiO_3$ substrates are not available commercially. A possible reason, why $CaTiO_3$ has not become a popular substrate material, might be its inherent tendency to twinning. Despite its mineral name, Perovskite does not have the ideal cubic perovskite structure, it is orthorhombic; its pseudo-cubic unit cell, containing one $CaTiO_3$ formula unit, is distorted by a shear of 48' to give a true orthorhombic cell of $a = 5.37, b = 7.64, c = 5.44$ Å[210]. Figure D.11 depicts the relation

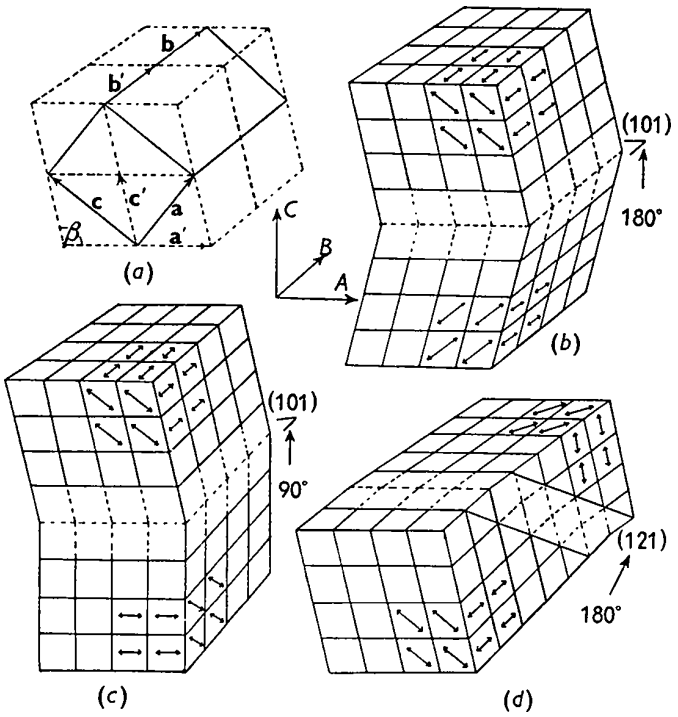

Fig. D.11: (a) Orthorhombic unit cell of $CaTiO_3$ (full-line) in relation to sheared pseudo-cubic primitive cells (broken line). (b) Most common form of twinning, by rotation about normal to (101) with composition plane (101). (c) Twinning by rotation of 90° about normal to (101) with composition plane (101). (d) Twinning by rotation of 180° about normal to (121) with composition plane (121). Copied from [210]

between the pseudo-cubic and orthorhombic unit cells as well as the types of twinning observed by H. F. Kay and P. C. Bailey.

Ironically, $CaTiO_3$ twin boundaries have also triggered a renewed interest in the material in recent years: It has been found that $CaTiO_3$ twin boundaries are ferrielectric[214, 215] and that they represent sinks for oxygen vacancies[216]. If similar domain boundaries could be engineered, they could possibly be used as a novel type of ferroelectric memory, which is remotely comparable to IBM's race-track memory[217, 218].

D.4.2. Characterization of $CaTiO_3$ substrates

A small batch of 5 substrates, each $5 \times 5 \times 0.5\,\mathrm{mm}^3$ in size, could be obtained from Darrell G. Schlom. The substrates were (001) oriented and polished by CrysTec GmbH, Berlin (the same company that provides us with high-quality $SrTiO_3$ substrates). As Figure D.12 shows, the quality of the $CaTiO_3$ substrates at hand, at least when judged from a purely optical viewpoint, is in no way comparable to that of commercially available $SrTiO_3$, $LaAlO_3$ or $DyScO_3$ substrates. The substrates received were transparent with a light pink color. Major portions of the samples had cracks and fractures preferably on their non-polished back sides. In addition different forms of twinning, mostly of a lamellar type, could be observed. Nevertheless each of the five substrates had regions of at least $1\,\mathrm{mm}^2$ with a quality sufficient for the interface experiments envisioned. X-ray investigations with the Laue-technique further approved this finding. The relative dielectric constant of one of the substrates was measured with an LCR-meter (Hewlett-Packard HP4284A) at $f = 1\,\mathrm{kHz}$ and determined to be 160 at 300 K and 270 at 5 K, which is about 10 % lower than the literature values cited in subsection D.4.1. The

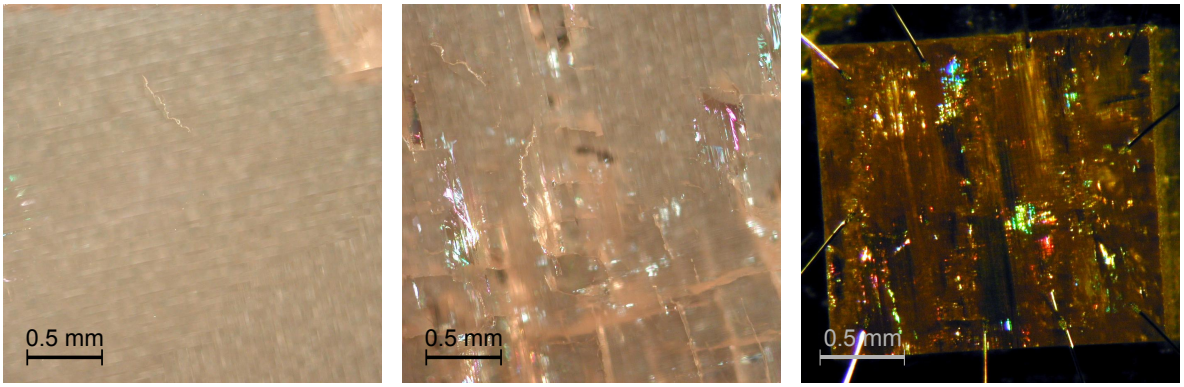

a high-quality region: twin-boundaries, minor cracks

b low-quality region: major cracks and fractures

c conchoidal fractures on wire-bonded $CaTiO_3$

Fig. D.12: Optical micrographs of $CaTiO_3$ substrates. Apart from twinning, cracks and conchoidal fractures characterize large parts of the substrates.

difference is within the experimental error margin.

Reduction

A major complication for experiments involving the conducting $LaAlO_3$-$SrTiO_3$ interface is the rich phase diagram of $SrTiO_3$ itself: Its electronic properties can be widely tuned by doping the crystal with oxygen vacancies[219]. Already with a slight reduction, metallic behavior emerges in bulk $SrTiO_{3-x}$. In addition, reduced $SrTiO_3$ is superconducting with a $T_c(n)$ phase diagram[47, 220] quite similar to that reported for the $LaAlO_3$-$SrTiO_3$ interface[221].

At the temperatures necessary for epitaxial growth of $LaAlO_3$, $SrTiO_3$ can reduce and thus become conducting, effectively shunting the conducting $LaAlO_3$-$SrTiO_3$ interface. Thus, care must be taken to maintain a sufficient oxygen background pressure before, during and after the deposition process or generally whenever $SrTiO_3$ is heated above about 300 °C.

In this regard, $CaTiO_3$ was found to be much less delicate, which could be related to the ability of $CaTiO_3$ twin-walls to trap oxygen vacancies. On the one hand, the conductivity of $CaTiO_3$ is not nearly as sensitive to its oxygen content, no superconducting phase of $CaTiO_{3-x}$ has been reported, yet. On the other hand, $CaTiO_3$ is much harder to reduce than $SrTiO_3$: Various attempts with different furnaces and under different atmospheric conditions did not result in a visibly (dark color) or measurably (electrically conducting) reduced $CaTiO_{3-x}$ crystal. The only successful way to create black $CaTiO_3$ with high electric conductance and a metallic $R(T)$-characteristic involved a high-vacuum, high-temperature molybdenum furnace at 1400 °C. After this treatment, the substrate was completely coated by a metal, presumably Mo (molybdenum), that had evaporated from the heating elements. To remove the metal coating, the substrate was ground on all faces until a shiny black surface appeared. The black crystal

was found to have metallic conductance with a charge carrier density and mobility of $1.29 \times 10^{20}\,\mathrm{cm}^{-3}$ and $10.7\,\mathrm{cm}^2/\mathrm{Vs}$ at a temperature of 4 K. Whether the conductance was due to oxygen vacancies or Mo-doping has not been investigated. The most important result is that in all other experiments, at high temperatures up to 1200 °C, even in a reducing Ar:H_2 atmosphere for more than 20 h, $CaTiO_3$ did not reduce into a conducting state. Consequently both planned processing steps, substrate termination (HF-etching and annealing at 950 °C in O_2) and PLD-growth of $LaAlO_3$ (at $\approx 800\,°C$) are absolutely safe with regard to a possible sample reduction.

Termination control

A necessity for a well defined $LaAlO_3$-$CaTiO_3$ interface is a single-terminated substrate. Due to the very small number of available substrates a detailed set of experiments to figure out optimal parameters for etching and annealing could not be carried out. The natural first try was the well established HF-based "Twente-Etch", which has also been described in the previous section D.3. Chemically, Ca and Sr are relatively similar. Both react with water exothermically to their respective hydroxides, which are in turn soluble in acid, but hardly so in water (aqueous solubility at 20°C: 0.14 mol/L $Sr(OH)_2$, 0.023 mol/L $Ca(OH)_2$[222, 223]). Consequently, the Twente-etch should work analogously for $CaTiO_3$ and $SrTiO_3$: Ca on the substrate surface reacts with water to $Ca(OH)_2$, which is then dissolved in buffered fluoric acid. The resulting surface of each substrate was investigated by atomic force microscopy (AFM). A typical AFM-image of a $CaTiO_3$ surface after the termination process is shown in Figure D.13. A clean step-and-terrace structure (miscut angle $0.09 \pm 0.02°$) was observed on each of the substrates with a step-height equivalent to the length of the $CaTiO_3$ pseudo-cubic unit-cell. On closer inspection, though, a narrow intermediate step of roughly half that height could be identified at many of the step-edges. No etch-pits were observed, which indicates a high substrate-quality with a low density of (clustered) surface dislocations. Since no information on the thermal stability of the single-terminated surface is available, each of the substrates was prepared at most 2 days before the pulsed laser deposition of $LaAlO_3$.

D.4.3. Epitaxial growth of $LaAlO_3$ on $CaTiO_3$

The $LaAlO_3$ film-growth was initially carried out completely analogue to our standard $LaAlO_3$-$SrTiO_3$ recipe (see [67] for details): Pulses at a repetition rate of 1 Hz at a laser energy of 450 mJ onto a single-crystalline $LaAlO_3$ target in an oxygen atmosphere of 1×10^{-4} mbar. The standard cooling sequence with annealing steps at 600 °C and 450 °C in 400 mbar of oxygen was done only for the first two samples. For the other samples the oxygen-pressure during cooling and deposition was varied.

RHEED In every deposition the $LaAlO_3$ film growth was monitored with reflection high-energy electron diffraction (RHEED). Figure D.14 documents the typical development of the diffraction pattern. Owing to the similar crystal structure, the RHEED-image of $CaTiO_3$ is very similar to that of $SrTiO_3$. The smaller lattice constant of

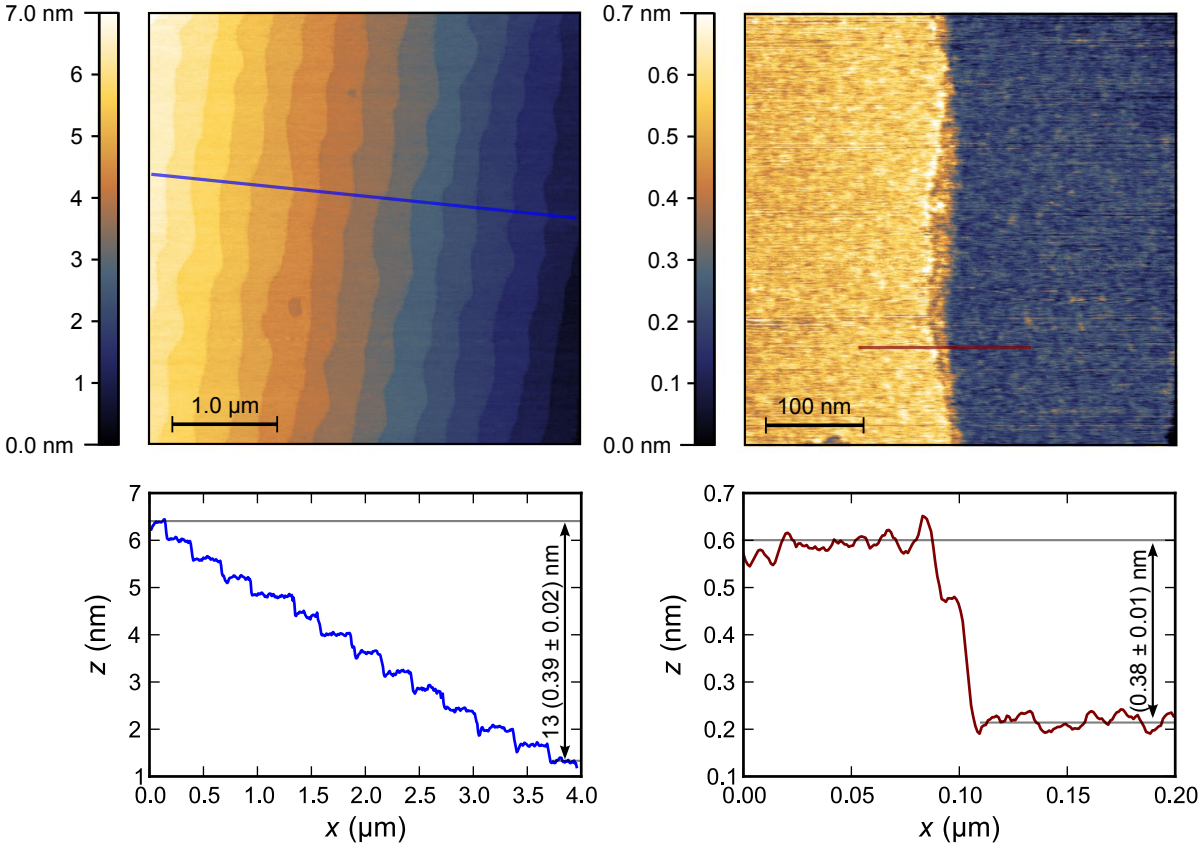

Fig. D.13: AFM topographic images of a $CaTiO_3$ substrate surface after the termination process. The images and cross sections (positions marked by colored lines) reveal a clean surface with a clear step-and-terrace structure with ≈ 300 nm wide terraces and unit-cell high steps ($c'_{CTO} = 0.38$ nm). On a smaller scale, most of the steps feature a narrow, 5-15 nm wide intermediate step with roughly half of the height of a full $CaTiO_3$ unit cell.

$CaTiO_3$ results in a small, but measurable increase of the peak to peak distance. Unlike high-quality $SrTiO_3$, the diffraction peaks created by the present $CaTiO_3$ substrates would fan out into double- or triple-peaks quite often. This effect is caused by twinning which creates either a slightly uneven surface or simultaneous diffraction by regions slightly tilted around the surface normal with respect to each other.

During the $LaAlO_3$ growth the peak intensity oscillated with a period of 15-18 laser pulses, indicating layer-by-layer growth. The intensity oscillation amplitude was somewhat smaller, but comparable with a usual $LaAlO_3$ deposition on $SrTiO_3$. In addition to the intensity statistics gathered in elliptic areas around the diffraction peaks, line-profiles through the (00)-peak were also sampled. These line-profiles can be used to measure the peak's sharpness by its *full width at half maximum* (FWHM). Like the peak intensity, its FWHM reacts sensitively (but conversely) on the partial material coverage during epitaxial growth. Unlike the peak intensity, the FWHM is independent of the overall scale of the peak. Hence, the FWHM does not scale when the incident beam current is increased. Only its signal-to-noise ratio is improved. This makes the FWHM-analysis a valuable tool to a-posteriori verify the number of unit cells grown during a PLD-session, especially if the intensity graph was noisy or ambiguous.

STEM/EELS To get a direct measure of the structural perfection of the $LaAlO_3$-$CaTiO_3$ samples produced, one sample (ct7, 20 uc $LaAlO_3$, RHEED-signal in Figure D.14) was prepared for scanning transmission electron microscopy (STEM) with an additional capping layer of amorphous $CaTiO_3$, deposited by PLD at room temperature. The finished sample was cut into two halves, each with a size of $\approx 2 \times 5 \times 0.5\,\mathrm{mm}^3$. One half was sent to Dr. Lena Fitting, a leading expert in high-resolution STEM on oxides, for detailed investigations. I equipped the other half-sample with contacts and have characterized it by electronic transport measurements. The STEM results are summarized in Figure D.15 and D.16. The Z-contrast STEM image (high-angle annular dark-field) in Figure D.15 shows a well ordered crystal structure inside the $CaTiO_3$ substrate as well as in the $LaAlO_3$ film. The interface between substrate and film is not perfectly sharp: Intermixing of Ca and La is visible in the 1-2 monolayers nearest to the interface. Compared to our $LaAlO_3$-$SrTiO_3$ samples, intermixing is notably enhanced. A probable reason for the enhanced diffusivity is the smaller ion-radius and mass of the Ca^{2+} ion as compared to Sr^{2+}.

By analysing the energy loss of detected electrons (EELS), the distribution of chemical elements and their valency can be mapped across the specimen. The EELS results confirm an intermixing of La and Ca in a 1-2 uc wide region at the interface. In addition, Ti atoms diffuse into the first 2 uc of the $LaAlO_3$ film. From fits of reference data to the measured EELS-spectra a slightly reduced Ti-valency at the $LaAlO_3$-$CaTiO_3$ interface could be deduced. The best fit to the measured data were obtained assuming a ratio of $Ti^{3+}/Ti^{4+} = 0.05$. The elemental intermixing at the interface creates a complex solid solution containing $LaTiO_3$ which can, depending on the exact (and hard to control) stoichiometry, be metallic[50], even when it is just a single unit cell thick[51]. A few distributed $LaTiO_3$ unit cells could thus account for the measured Ti-valency.

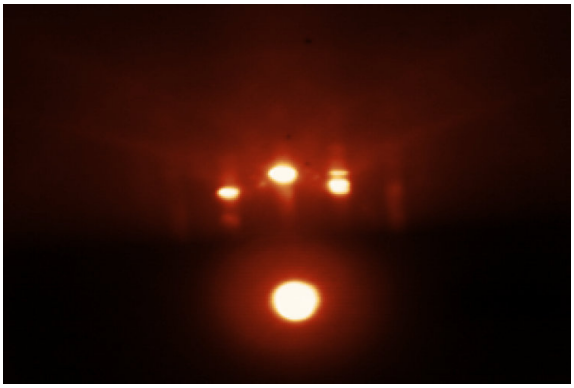

a RHEED diffraction pattern of $CaTiO_3$ substrate

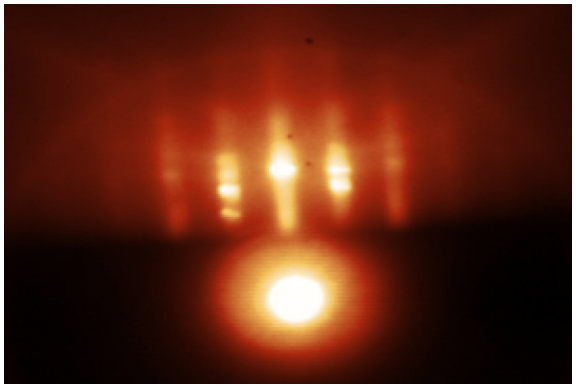

b RHEED pattern of $LaAlO_3$ film grown on $CaTiO_3$

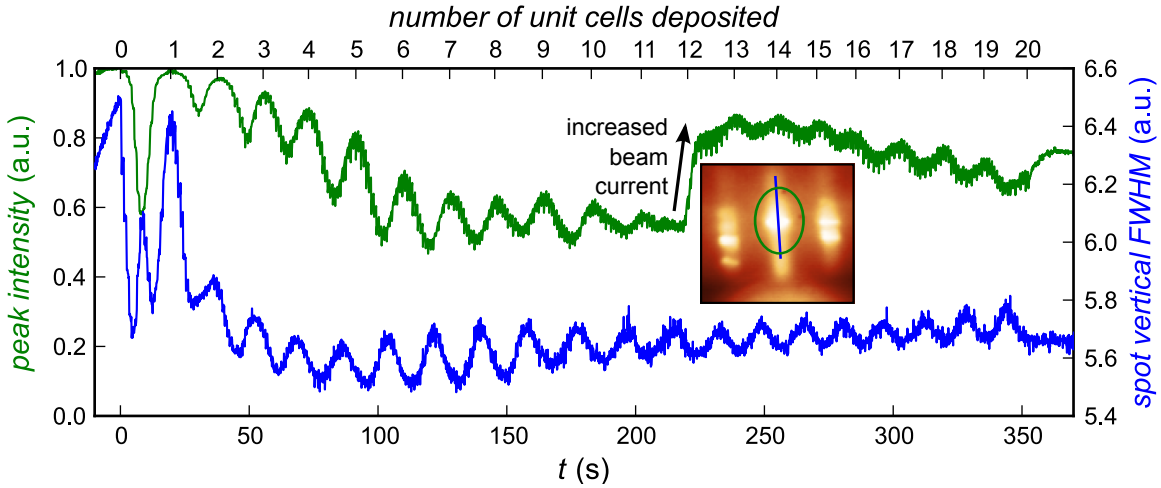

c variation of RHEED signal during $LaAlO_3$ growth on $CaTiO_3$ substrate

Fig. D.14: RHEED-analysis of $LaAlO_3$ growth on a TiO_2-terminated $CaTiO_3$ substrate. The diffraction patterns before and after the deposition indicate a clean, single crystalline surface with only slight double-spots due to twinning. The maximum intensity and vertical full-width at half-maximum of the main (00) diffraction peak (measured inside the green ellipse and along the blue line drawn into the graph's inset, respectively) change with each laser pulse ($f_{\text{pulse}} = 1$ Hz, first shot at $t = 0$ s) and oscillate with a period of ≈ 17 shots/uc. In the present deposition 20 uc of $LaAlO_3$ were grown in a layer-by-layer growth-mode. Note that the intensity of the incident electron-beam was increased at $t = 220$ s, which directly affects the maximum intensity, but not the FWHM.

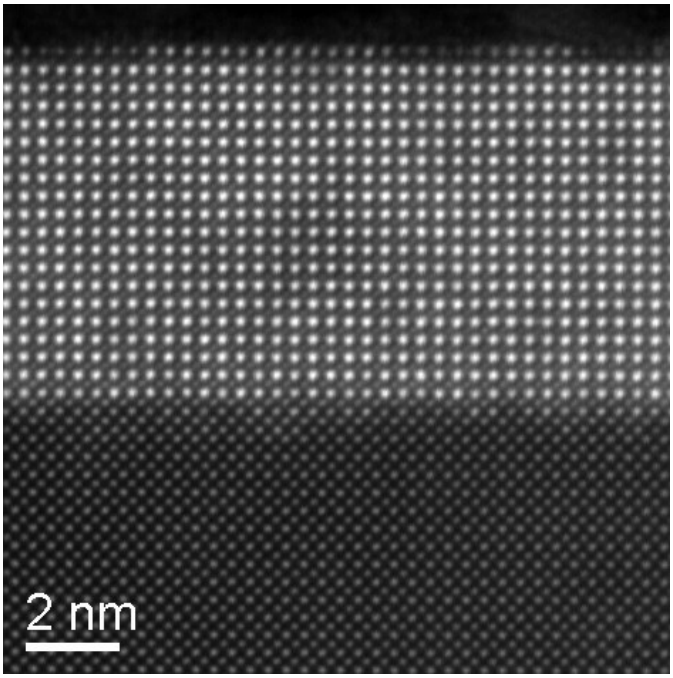

Fig. D.15: STEM (*Z*-contrast, high-angle annular dark-field) cross-section, perpendicular to (100) direction of a $LaAlO_3$ thin film on a $CaTiO_3$ substrate. The nominal thickness of the $LaAlO_3$ film (as counted from the RHEED-oscillations plotted in D.14c) is 20 uc. A part of the La atoms, appearing brightest in this viewgraph, intermix with Ca at the $LaAlO_3$-$CaTiO_3$ interface. (Microscopy by L. Fitting Kourkoutis, Cornell)

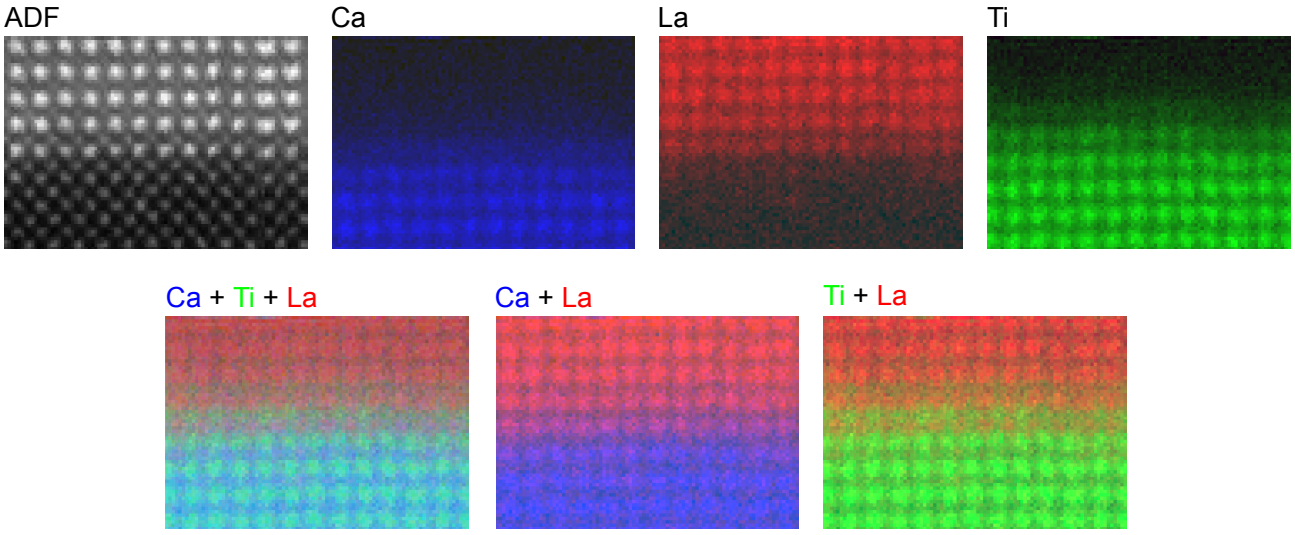

Fig. D.16: Annular dark-field (ADF) and chemical (EELS) analysis of a $LaAlO_3$-$CaTiO_3$ interface. In a 1-2 uc wide region at the interface Ca and La intermix. Ti atoms are detected in the first 2 $LaAlO_3$ unit cells. (Microscopy by L. Fitting Kourkoutis, Cornell)

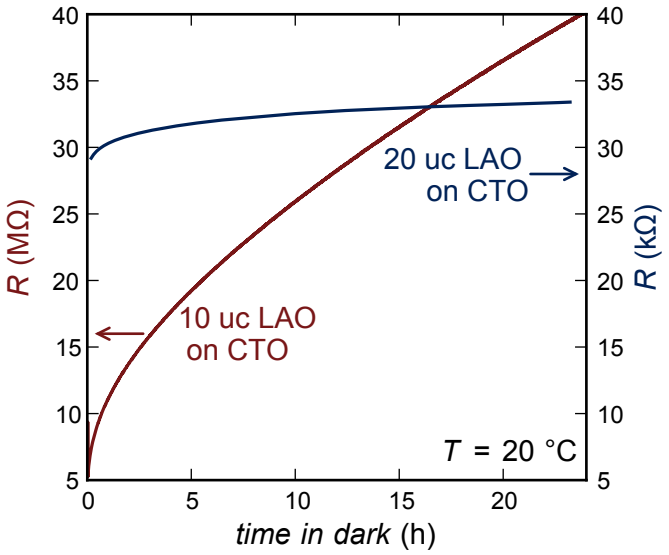

Fig. D.17: Transient photoconductance of $LaAlO_3$-$CaTiO_3$ interfaces with 10 uc and 20 uc $LaAlO_3$, measured at room-temperature (mind the different scales). The resistance of the 10 uc sample increases approximately linearly with time. Its initial value is more than three orders of magnitude higher than that of the 20 uc sample. The resistance of the 20 uc sample also increases with time, but converges to a stable value of $\approx 34\,\mathrm{k\Omega}$.

D.4.4. Electronic transport properties of $LaAlO_3$-$CaTiO_3$ interfaces

Overall five $LaAlO_3$-$CaTiO_3$ samples have been grown using the substrates previously described in this section. The samples differed in the thickness of their $LaAlO_3$ layers and their growth conditions. The relevant growth parameters are summarized at the end of this section, in Table D.2. This table also contains the summarized results of electric transport measurements done on all samples. As will be shown, several of the electronic properties of $LaAlO_3$-$CaTiO_3$ samples are comparable to that of the $LaAlO_3$-$SrTiO_3$ system.

Photoconductance

A long-known, but poorly investigated[224] feature of LAO-STO is a transient light-induced conductance, which decays in the darkness. The typical decay time constants depend on the $LaAlO_3$ thickness and the sample-preparation, but are typically very high: a few hours for a sample of 3 uc LAO to weeks or months for samples with thicker LAO layer. We have found a similar effect in $LaAlO_3$-$CaTiO_3$ samples. Figure D.17 compares the photoconductance of a 10 uc $LaAlO_3$-$CaTiO_3$ sample to that of a 20 uc $LaAlO_3$-$CaTiO_3$ sample. The 10 uc sample is characterized by a high sheet resistance of several MΩ, rising approximately linear with time, when the sample is in the dark. The resistance of the 20 uc $LaAlO_3$ on $CaTiO_3$ sample is more than 2 orders of magnitude lower and much more stable: During a 24 h measurement period, the resistance has risen by less than 15% from 29 kΩ to 33.5 kΩ. The transient photoconductance can be very well described by a stretched exponential decay:

$$G_{10\mathrm{uc}}(t) = 0.39\,\mu\mathrm{S} \times \exp\left(-(t/1.5\,\mathrm{h})^{0.21}\right) \quad \text{(D.1)}$$

$$G_{20\mathrm{uc}}(t) = 28.7\,\mu\mathrm{S} + 6.8\,\mu\mathrm{S} \times \exp\left(-(t/5.5\,\mathrm{h})^{0.42}\right) \quad \text{(D.2)}$$

A decay-law of that type can be deduced from a normal exponential decay $\propto \exp(-t/t_\mathrm{h})$ by assuming instead of a single sharply defined half-life t_h a probability distribution P of half-value periods or decay rates $\lambda = 1/t_\mathrm{h}$:

$$\exp(-(\lambda t)^\beta) = \int_0^\infty P(s,\beta)\exp\left(-s\lambda t\right)\mathrm{ds}$$

A relaxation behavior of that type is therefore naturally interpreted as the relaxation of a system containing many independently relaxing species, each of which decays exponentially in time with a specific fixed relaxation rate[225].

As Equation D.2 suggests, the observed $R(t)$ behavior can be interpreted in terms of two independent conduction channels; one is stable (time independent), the other is transient, albeit with a large decay time of several hours. For the 20 uc sample both channels exist in parallel, but the transient one decays in time. The 10 uc sample lacks the stable channel, only the transient one contributes to the electric transport. Consequently, after a sufficiently long period in darkness, the 10 uc sample becomes insulating, its conductance approaches 0. Qualitatively this behavior is similar to $LaAlO_3$-$SrTiO_3$: For LAO-STO samples with a $LaAlO_3$ layer thinner than 4 uc, any conductance is induced by light[4] and transient, while thicker $LaAlO_3$ layers create a stable, non-volatile conduction channel. Nevertheless, also in conducting $LaAlO_3$-$SrTiO_3$ samples a light-sensitive, transient conductance component is observed.

Temperature dependence of resistance

Besides its transient behavior, the temperature dependence of the electrical resistivity is a characteristic feature for any electronic system—it is a fingerprint of the electronic scattering processes. The temperature dependent sheet resistance measured on several $LaAlO_3$-$CaTiO_3$ samples is shown in Figure D.18. Measurements between 4 K and room-temperature were done in a bath- or flow-cryostat. Sample ct3 has additionally been measured down to $T = 60$ mK in a dilution refrigerator.

Our standard $LaAlO_3$-$SrTiO_3$ samples are characterized by a monotonously rising, parabolic $R(T)$-curve and a transition into a superconducting state at $T \approx$ 100-200 mK. In contrast, all $LaAlO_3$-$CaTiO_3$ samples investigated had a non-monotonous $R(T)$-characteristic with a single minimum at $T_\mathrm{min} =$ 30-80 K.[5] For $T > T_\mathrm{min}$, the resistance is a relatively linear function of temperature with a ratio $R(300\,\mathrm{K})/R(T_\mathrm{min})$ of 4.0 (samples ct3, ct7) to 5.75 (sample ct2). The analogous ratio for LAO-STO is much larger: $R(300\,\mathrm{K})/R(4\,\mathrm{K}) \approx 100$.

For $T < T_\mathrm{min}$, the resistance rises exponentially upon further cooling and diverges when approaching 0 K. No signs of superconductivity were found, the ground state of the $LaAlO_3$-$CaTiO_3$ interface is insulating. The apparent settling of the resistance for $T < 250$ mK is likely due to the device resistance approaching the limits of the

[4] in a sample with $\gtrapprox 3$ uc $LaAlO_3$ on $SrTiO_3$, an electric-field effect[52] can also create conductivity

[5] The photoconducting 10 uc sample ct1, after 24h in darkness, had a resistance minimum at $T \approx$ 150 K.

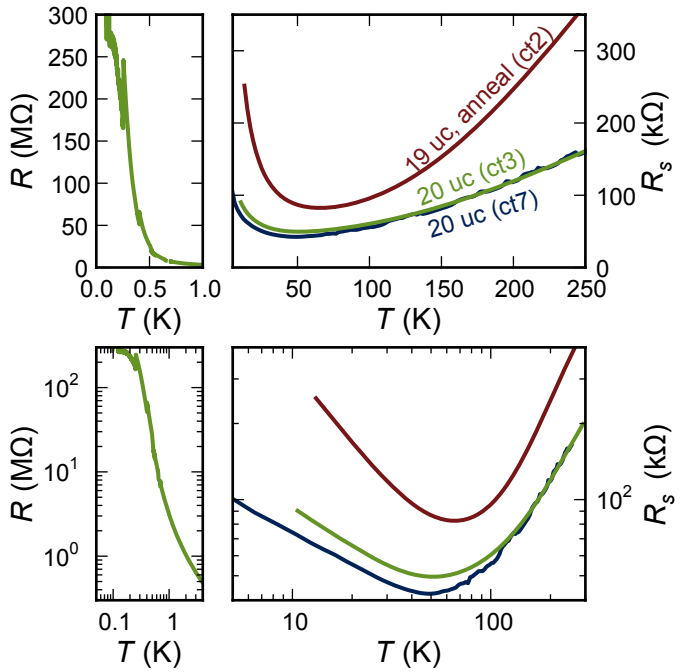

Fig. D.18: Temperature dependence of the sheet resistance of 3 different $LaAlO_3$-$CaTiO_3$ samples. For sample ct3 the sheet resistance can not be derived from the measured resistance. The curve shown has instead been scaled to match the resistance of ct7 at $T = 250\,\mathrm{K}$. The data for $T > 4\,\mathrm{K}$ have been measured in a bath- or flow-cryostat. For ct3 additional measurements down to 60 mK were made by Stefano Gariglio in a dilution cryostat in Geneva/Switzerland, below 150 mK the resistance was too high to be measured with the equipment available.

instrumentation used.

Either of two mechanisms are commonly used to explain a diverging resistance for $T \to 0$: thermally activated transport or the Kondo-Effect.

Kondo-Effect The Kondo-Effect, named after Jun Kondo, who formulated his theory in 1964[60], is based on charge carriers scattering at magnetic impurities. Mobile electrons interact with localized spins bound to the impurities. This creates a charged cloud of electrons surrounding every impurity atom. With decreasing temperature that cloud grows ever larger, while the screening length inside the electron system shrinks. The effective cross section of the Kondo scattering mechanism thus diverges when T sinks below a characteristic temperature $\mathrm{T_K}$ and approaches 0. In effect, the electrical resistance diverges logarithmically:

$$R \propto \log(\mathrm{T_K}/T)$$

This effect was first observed in 1934[226] by W. J. de Haas, J. H. de Boer and G. J. van de Berg in gold, doped with tiny amounts of iron. The Kondo-Effect was also reported for LAO-STO interfaces grown under high oxygen pressure[59].

Thermally activated transport The most basic example of thermally activated transport is that of an intrinsic semiconductor, in which the mobile charge carriers are thermally activated. In an (intrinsic) semiconductor, the Fermi-Energy is below the conduction band minimum. Thermal energy is needed to excite electrons into the conduction band, where they are mobile and contribute to the electric conductance. In an intrinsic

semiconductor, the number of conduction electrons n, which approximately determines its conductivity $\sigma = 1/R$, depends exponentially on temperature T:

$$\sigma \propto n \propto \exp(-\Delta/\mathrm{k_B}T)$$

where Δ is the band gap or, more general, the energy difference between the conduction band and the highest occupied valence state; $\mathrm{k_B}$ is the Boltzmann constant.

The charge carrier density can be measured directly in Hall-measurements. This way, on the 20 uc $LaAlO_3$-$CaTiO_3$ sample ct7 the charge carrier density n_s was found to be maximal at the resistance-minimum:

$$\begin{aligned} n_\mathrm{s,max} &= 2.9 \times 10^{13}\ /\mathrm{cm}^2 \quad @ \quad T = 38\ \mathrm{K} \\ n_\mathrm{s} &= 1.6 \times 10^{13}\ /\mathrm{cm}^2 \quad @ \quad T = 10\ \mathrm{K} \end{aligned}$$

It is thus quite likely, that thermally activated charge carriers are the reason for the low-temperature divergence of resistance. Beside semiconductivity, more examples of activated transport exist, most notably the class of variable range hopping conductance phenomena, which will be explained below.

An Arrhenius plot of the low-temperature $R(T)$ characteristic of sample ct3 is shown in Figure D.19. The data for $T < 4\,\mathrm{K}$, which is shown in the graph, is most specific to determine, which mechanism creates the low-temperature resistance increase. In the Arrhenius ($\log R$ vs $1/T$) plot, the measured data is approximately linear with a positive slope. A Kondo-like $R(T)$ curve would appear much more concave in this plot. The fit model of choice is therefore of the activated transport type:

$$R_\xi = a_0 \exp\left(\frac{a_1}{T}\right)^\xi$$

with a_0 and a_1 as fit parameters. The clear result of the analysis presented in Figure D.19 is, that an exponent of $\xi = \frac{2}{3}$ fits the measured data best.

Variable range hopping The best fit to the low-temperature data is the function $R \propto \exp((5.3\,\mathrm{K}/T)^{2/3})$. This function can be identified as a variant of the Mott variable range hopping model[227].

Mott variable range hopping models electronic transport by charge carriers in localized states[228], that can hop between sites by tunneling or by thermal excitation. Electrical transport by variable range hopping is normally found in strongly disordered electronic systems like organic semiconductors.

At first sight, a transport mechanism of this kind is not expected from a 2D electron gas. A possible explanation, why electric transport in $LaAlO_3$-$CaTiO_3$ samples could still be limited by a hopping or tunneling mechanism are the twin-boundaries of $CaTiO_3$.

Influence of twinning It has been shown that already small-angle (2°) grain boundaries have a major impact on the conductivity of LAO-STO interfaces[207]. The published

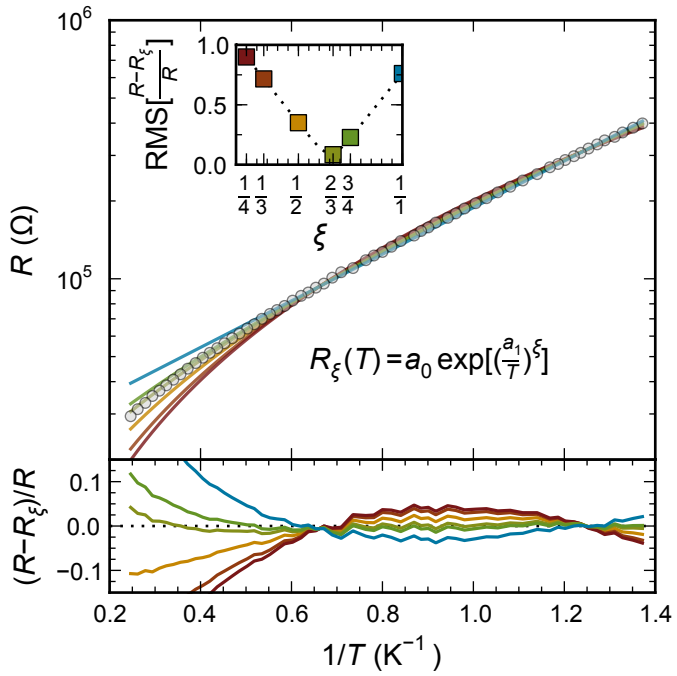

Fig. D.19: Low T temperature dependence of resistance of 20 uc LAO-CTO sample ct3 (circles) in an Arrhenius plot (main, upper panel), fitted with several models of activated transport (solid lines) $R \propto \exp\left(\frac{a_1}{T}\right)^{\xi}$. The relative difference between fits and measured data is plotted in the lower panel. The summed root mean square (RMS) of the differences of each individual best-fit, as a measure of the overall fit quality, is plotted in the inset as a function of the fit exponent ξ. The best fit is achieved for an exponent of $\xi = \frac{2}{3}$. The color code used to highlight distinguished ξ values with filled squares in the inset is also used consistently in the other panels of this figure.

$R(T)$ measurements across such artificially introduced grain boundaries are comparable to the case of the LAO-CTO interfaces investigated here, with a minimum at $T \approx 40$ K.

The differently oriented micro-twins of the $CaTiO_3$ substrate create grain boundaries of a different character. They can be visualized by optical microscopy with polarized light (using crossed Nicols), because differently oriented twin-domains have different directions of extinction. In D.20b the twinning of a $CaTiO_3$ substrate can be recognized as dark and bright stripes. The typical width of these stripes is 20-200 µm. Several publications, however, claim that $CaTiO_3$ micro-twins build a fine-grained substructure of even smaller dimensions[210]. I have made multiple attempts to contact only a single grain or achieve transport-measurements with a current-path that may not pass a twin-boundary. This is challenging, since neither our wire-bonder nor our mask-aligner feature the optical means to discern twin-domains. Two such attempts are documented in Figure D.20. In all attempts, though, the shape of the resulting $R(T)$-curve, including the position of $T_{\min}$, the temperature at which R is minimal, was largely unaffected by any special choice of contact arrangement. It is important to note, though, that this result does not rule out an influence of twin-boundaries on the transport properties of LAO-CTO interfaces completely, as the measured contact configurations might still have had twin-boundaries in their current paths.

Photodoping at low temperatures The only way in which a qualitative change of the $R(T)$-characteristic of LAO-CTO interfaces could be accomplished was by creating photo-excited charge carriers with light. Figure D.21 presents the result of an experiment in which a sample was illuminated for a few minutes during a cool-down, which changed the resistivity dramatically. In this experiment, a 4-probe $R(T)$ measurement was carried

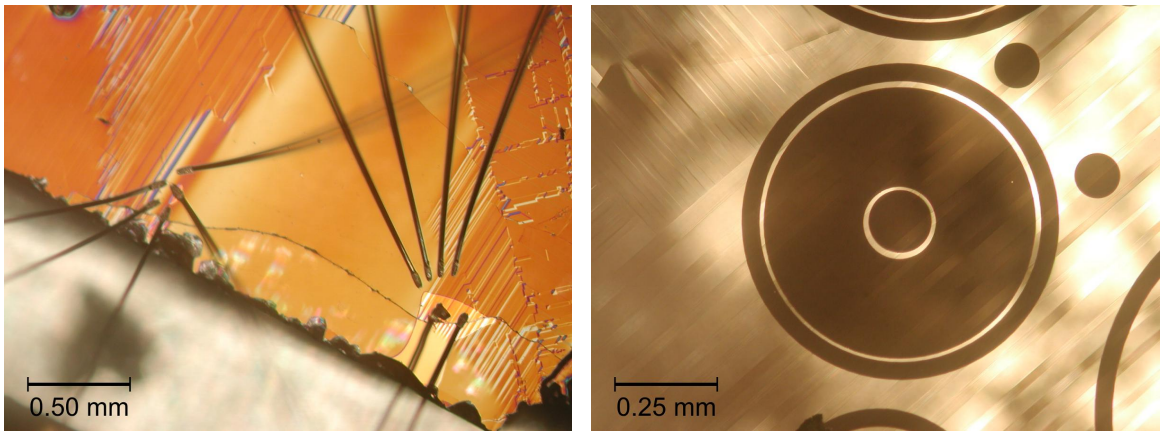

a Twinning and cracks on sample ct7b and two sets of wire bonds contacting individual twin-domains.

b Twinning on sample ct11, with metallic circular or ring shaped contacts (dark).

Fig. D.20: Photographs highlighting the twin-domains of two different LAO-CTO samples and contact arrangements made in an attempt to contact single twin-domains. Differential interference contrast (Nomarski) microscopy was used in (a). The two sets of wire-bonds were carefully placed to contact only a single domain. For sample ct11 in (b), ring-shaped electrodes with a spacing of 20 µm were used in an attempt to create a possible current path that is not crossing a twin-boundary. Here, the use of a crossed polarizer-analyzer pair ("crossed Nicols") creates an optical contrast between twin-domains.

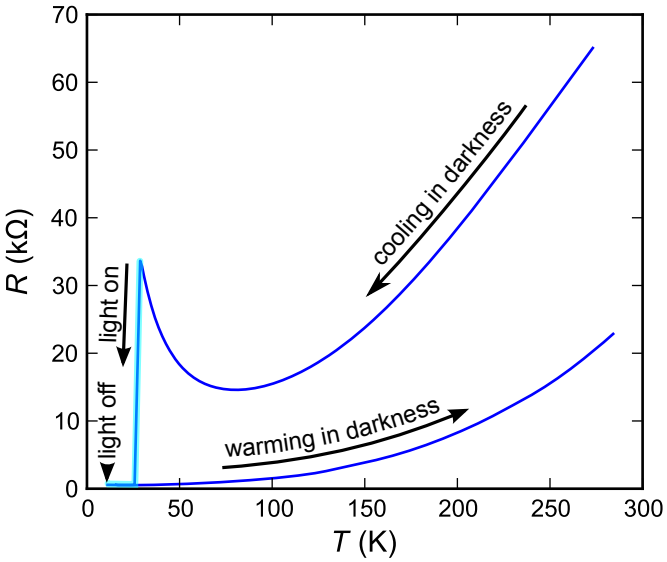

Fig. D.21: 4-probe $R(T)$ measurement cycle of $LaAlO_3$-$CaTiO_3$ sample ct2. The initial cool-down (duration $\approx$ 2 h) was in darkness. Passing T = 28 K the sample was illuminated with white light from a Xe-lamp, causing a drop in resistance by almost 2 orders of magnitude. After an intermediate temperature sweep to 270 K (not shown) and back to 15 K, light was switched off. The resistance did not increase back to its original (dark) value. During the subsequent warming (in darkness) the sample resistance remained relatively low, the resulting $R(T)$ curve is almost monotonic with only a slight minimum at 25 K.

out with a 19 uc LAO-CTO sample (ct2) in a flow-cryostat with optically transparent windows through which the light of a Xe short-bow lamp can be shone onto the sample. Before the cool-down, the sample was left in darkness for several hours. Moreover, during the initial cool-down, all cryostat windows were covered, so initially the sample cooled in darkness. The resulting $R(T)$ curve is thus identical to the ones previously shown: It features a marked minimum at 80 K, the resistance diverges when T is lowered further. At T = 28 K the sample was illuminated with bright white light from the Xe-lamp. Immediately the sample resistance dropped from 34 kΩ to 0.6 kΩ. A temperature cycle to 270 K and back to 15 K, with the Xe-light on, yielded a completely monotonic, parabolic $R(T)$-curve. Surprisingly, when afterwards the light was switched off at 15 K, the resistance, instead of jumping back to its initial dark-value of 34 kΩ, remained low: It increased from 0.5 kΩ to 0.6 kΩ only. The $R(T)$-curve consecutively measured when warming the sample to room temperature in darkness (plotted in Figure D.21) is nearly identical to the previously recorded $R(T)$-measurement in light (not shown).

Comparison to $LaTiO_3$ A different approach to explain the peculiar temperature dependence of the LAO-CTO sheet resistance is a comparison to $LaTiO_{3-x}$ films. EELS measurements on our LAO-CTO samples have already testified a Ti-valency comparable to that in $LaTiO_{3-x}$ in a narrow, approximately 2 uc thick layer at the LAO-CTO interface. And indeed, in films with a certain composition[229] or fractional unit cells of $LaTiO_3$ embedded in $SrTiO_3$[230] a temperature dependency qualitatively similar to the $R(T)$ curves of our LAO-CTO samples has been found. Therefore it would be tempting to attribute the observed conductivity to the formation of $LaTiO_3$ due to the apparent intermixing of Ti and Ca at the $LaAlO_3$-$CaTiO_3$ interface. The way in which the electronic properties of the interface depend on the $LaAlO_3$ layer thickness, however, can not be easily explained by the intermixing hypothesis. The intermixing of La and Ca

at the interface is most likely happening during deposition of the first few unit cells of $LaAlO_3$ onto the $CaTiO_3$ substrate. It is unlikely that the deposition of, say, the tenth $LaAlO_3$ unit cell has an impact on the atomic distribution at the interface, ten unit cells beneath the surface. If the formation of $LaTiO_3$ at the interface was responsible for the observed conductivity, the interface should retain its conductivity, even if some of the covering $LaAlO_3$ layers are removed.

Critical $LaAlO_3$ thickness

There is a critical dependency of the electronic properties of $LaAlO_3$-$CaTiO_3$ interfaces on the thickness of the grown $LaAlO_3$ film:

- Samples with 0 or 8 unit cells of $LaAlO_3$ are insulating.
- Samples with 10 uc of $LaAlO_3$ are semi-conducting: transient photo-conductance at room-temperature, negative temperature coefficient for $T \lessapprox 150\,\mathrm{K}$.
- Samples with 19 or 20 uc of $LaAlO_3$ are conducting: much lower resistance than 10 uc samples, non-volatile conductance, positive temperature coefficient for $T >$ 30-80 K.

The size of the sample set was limited by the small number of available substrates. To gather additional information on the critical thickness behavior of $LaAlO_3$-$CaTiO_3$ interfaces and to test the intermixing hypothesis, the grown $LaAlO_3$ layer of two samples was later reduced by Ar-ion-milling. On the two samples ct3 and ct11, both with an initial $LaAlO_3$ coverage of 20 uc, regions to etch were defined with photo-resist. In multiple short exposures, fractions of the $LaAlO_3$ film were etched away. The resulting film-thickness was measured by scanning the edges of the etched regions with a calibrated atomic force microscope (AFM). Some $LaAlO_3$ steps were too shallow to be accurately measured by AFM. In these cases the etch-depth was determined by measuring the approximately 10× deeper impact of the Ar-ion-beam exposure on a nearby Ti-contact, which was also covered partially with photo-resist. The etching rates of Ti and $LaAlO_3$ (and their ratio) could be measured in etches with a longer exposure. The result of the $LaAlO_3$ thickness evaluation on shallow steps by a co-measurement at the Ti-contact coincided nicely (to within ±0.5 uc) with values calculated by multiplying the measured etching rates and exposure-times. AFM images and a more detailed description of this co-etching method can be found in Appendix G.

The $R(T)$-characteristics and transient photo-conductance of the etched regions was found to be completely analogous to the previous data. The conductance characteristics of both the as-grown and the etched $LaAlO_3$-$CaTiO_3$ samples are compiled in Figure D.22. As can be seen, the data-points obtained from ion-milled samples complement (and reproduce) the previously measured data nicely:

- Samples with less than 10 uc of $LaAlO_3$ are insulating.

- Samples with 10 ± 1 uc of $LaAlO_3$ are semi-conducting: transient photo-conductance at room-temperature, negative temperature coefficient.
- Samples with 12 or more unit cells of $LaAlO_3$ are conducting: much lower resistance than 10 uc case, non-volatile conductance, positive temperature coefficient for $T >$ 60-100 K.

It should be noted, that irradiating a sample with an ion-beam does not only remove material from the surface. The bombardment has an influence on sub-surface regions, too. Local heating and ions with high kinetic energy can alter the sample bulk chemically and physically down to a characteristic penetration-depth[231]. Therefore, even if only, say, 10 of 20 unit cells of $LaAlO_3$ have been etched off a sample, its interface might have been influenced by the ion-bombardment. In this light, the etched samples reproducing the previous results might just be a coincident, and not connected to a critical $LaAlO_3$ thickness at all. This issue could be solved by repeating similar etching experiments with an ion-beam with a different kinetic energy. This way, the penetration profile of the beam would be different. If, regardless of the beam energy, the same critical $LaAlO_3$ thickness was found, that would be a clear indication that the $LaAlO_3$ thickness, and not intermixing is the deciding factor controlling the interface conductivity. TEM/EELS investigations of thinner as-grown samples and samples irradiated with an ion-beam would also help in this regard.

D.4.5. Summary

I have shown that heterostructures of the band-insulators $LaAlO_3$ and $CaTiO_3$ can give rise to a conducting electron system with a charge carrier density of $\sim 10^{13}$ /cm^2. Stable (light-independent) conductivity was found in samples with more than 10 uc of $LaAlO_3$ only. The mobility and temperature dependence of the electrical resistance of the investigated $LaAlO_3$-$CaTiO_3$ interfaces is comparable to that of $LaAlO_3$-$SrTiO_3$ interfaces with a high dislocation density[207]. Although no definite conclusion about the origin of the itinerant electrons can be drawn from the experiments presented in this section, the most likely interpretation is that an electronic reconstruction similar to that found at the interface between $LaAlO_3$ and $SrTiO_3$ is also happening at the $LaAlO_3$-$CaTiO_3$ interface. The experiments were limited by the quality and number of $CaTiO_3$ substrates available. With better substrates or with $CaTiO_3$ thin-films grown on different substrates, the $LaAlO_3$-$CaTiO_3$ system is an ideal starting-point to studying the role of the substrate in oxide-interface 2DEGs.

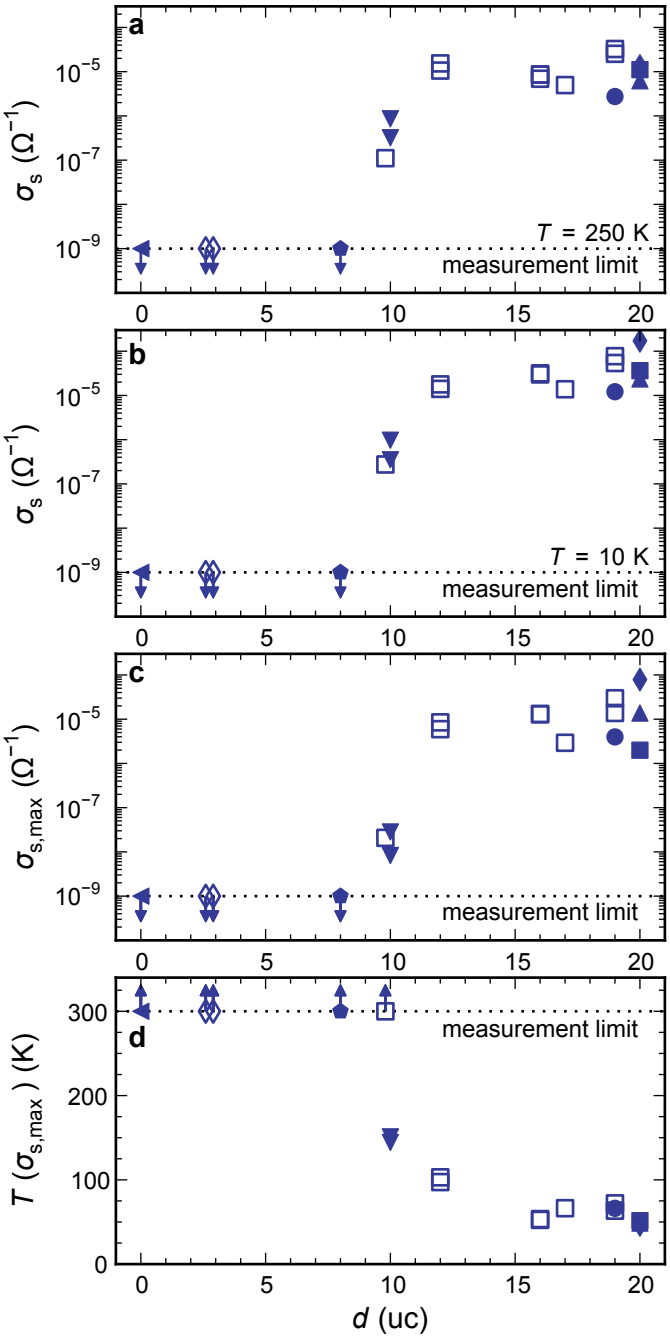

Fig. D.22: Influence of the $LaAlO_3$ thickness (given in number of unit cells) on the sheet conductance of $LaAlO_3$-$CaTiO_3$ interfaces. Differently shaped symbols refer to different samples. The samples' growth conditions with a reference to the symbols used here are given in Table D.2. Closed symbols: as-grown samples; open symbols: Part of the topmost $LaAlO_3$ layers removed by ion-milling. For all but the 0 uc datapoint the accuracy of the given $LaAlO_3$ thickness is ± 1 uc. Graphs **(a)** and **(b)** give the sheet conductance at 250 K and 10 K, respectively. In **(c)** $\sigma_{s,max}$, the maximum of $\sigma_s(T)$ is shown; the temperature at which $\sigma_s(T)$ is maximal is shown in **(d)**.

Tab. D.2: Growth conditions of investigated $LaAlO_3$-$CaTiO_3$ samples and basic characteristic of measured conductance ($-$: insulating, $+$: conducting, $\pm$: only photo-conductance). The given $LaAlO_3$ thickness is obtained by counting RHEED-oscillations. p_{O_2} is the oxygen pressure measured inside the PLD vacuum chamber. A tilde ($\sim$) indicates identical p_{O_2} during growth and cool-down. All samples have been grown at $T = 775 \pm 10\,^{\circ}\mathrm{C}$. The laser fluence was $\approx 1\,\mathrm{J/cm^2}$, the pulse frequency 1 Hz. The symbols next to the sample names correspond to the symbols used in Figure D.22.

sample name	ct0 ◁	ct15 ◇	ct1 ▽	ct2 ○	ct3 □	ct7 △	ct11 ⬠
$LaAlO_3$ layers grown	0	8	10	19	20	20	20
p_{O_2}, growth ($\times 10^{-5}$ mbar)	-	11.0	8.5	8.7	5.8	6.1	9.8
p_{O_2}, cool-down (mbar)	-	400	400	400	$\sim$	$\sim$	400
annealed	-	+	+	+	-	-	+
conducting	-	-	$\pm$	+	+	+	+

D.5. Chapter summary and discussion

In a first step we have shown that conducting $LaAlO_3$-$SrTiO_3$ interfaces with transport properties similar or even superior to that of standard LAO-STO, can be realized with different experimental methods. HCl:HNO_3-treated STO can be used instead of HF-treated STO. MBE can be used instead of PLD. Both methods are promising trails to further improve the quality of $LaAlO_3$-$SrTiO_3$ interfaces. Along the way we have learned that a slight $LaAlO_3$ cation off-stoichiometry is a key prerequisite for the conducting interface to emerge. This knowledge is an important input both for theory and to enable further thin-film growth techniques to create conducting oxide interfaces. Furthermore, the basic properties of $LaAlO_3$-$SrTiO_3$ interfaces are independent of the experimental methods used to produce the heterostructures. This defeats the idea, that extrinsic side-effects of the processing may be vital to the observed interface phenomena.

Material wise, conducting oxide interfaces with LAO-STO-like transport properties, but with thin-films other than $LaAlO_3$ and a substrate other than $SrTiO_3$ have been demonstrated. Consequently, LAO-STO can be understood as a representative of a broader class of conducting oxide interfaces. What are the similarities and dissimilarities among the different interfaces?

$LaXO_3$-$SrTiO_3$ Only two interfaces with comparable properties to $LaAlO_3$-$SrTiO_3$ have been identified[6]: $LaVO_3$-$SrTiO_3$[161] and $LaGaO_3$-$SrTiO_3$[167]. In particular, the $LaGaO_3$-$SrTiO_3$ and $LaAlO_3$-$SrTiO_3$ interfaces are characterized by the same critical thickness $d_c = 4\,\mathrm{uc}$, which could be linked to their nearly identical dielectric constants (see Reinle-Schmitt et al. [232] for a recent systematic study of the correlation between the critical thickness and dielectric constant).

Both $LaVO_3$ and $LaGaO_3$ share with $LaAlO_3$ the same basic ingredient to an electronic reconstruction: charged $(LaO)^+$ and $(XO_2)^-$ sub-layers. This could be seen as a confirmation for the electronic reconstruction scenario as an explanation for the itinerant electrons at the interface between polar- and non-polar oxides. On the other hand, other polar materials like $LaCrO_3$[183] were found not to generate conducting interfaces with $SrTiO_3$. Further material combinations may likely have been investigated, but have probably not been published if they did not feature conducting interfaces.

The picture is complicated by our finding that a slight cation off-stoichiometry in $LaAlO_3$ is required for the conducting $LaAlO_3$-$SrTiO_3$ interface to emerge. This widens the parameter space to scan for further related oxide interfaces and mandates modifications to the simple polar-catastrophe scenario. In conclusion, the search for LAO-STO-like interfaces with alternative thin-film materials has not delivered deeper insights into the nature of these interfaces. More research is necessary towards a coherent picture of polar oxide interfaces and their physical basis.

[6] According to very recent publications[178, 180] a third system, $NdGaO_3$-$SrTiO_3$, should be added to this list.

$LaAlO_3$-$CaTiO_3$ $CaTiO_3$ and $SrTiO_3$ are similar in many aspects. Most importantly, both were prepared to exhibit a TiO_2 surface. In this respect, both interfaces, $LaAlO_3$-$CaTiO_3$ and $LaAlO_3$-$SrTiO_3$, share the same host for itinerant electrons: Ti $3d$ derived bands. Yet the two interfaces were found to exhibit very different low-temperature $R(T)$-characteristics: Whereas LAO-STO behaves metallic and superconducts at $T < 200\,\mathrm{mK}$, LAO-CTO's resistivity diverges as $R(T) \propto \exp((5\,\mathrm{K}/T)^{2/3})$.

The most striking dissimilarity between bulk $CaTiO_3$ and $SrTiO_3$ lies in their dielectric properties. At room-temperature, the dielectric susceptibility of $SrTiO_3$ is about 50 % higher than in $CaTiO_3$. At cryogenic temperatures the discrepancy is much more drastic: the dielectric constant of $SrTiO_3$ rises beyond 10^4 at 4 K[42], whereas the dielectric constant of $CaTiO_3$ settles at about 330[209]. A high dielectric constant implies a lower screening length. Charged dislocations and electron–electron interactions are thus much more effectively screened in $SrTiO_3$ than in $CaTiO_3$, especially at low temperatures. The different dielectric properties of $SrTiO_3$ and $CaTiO_3$ may consequently be responsible for the different $R(T)$-characteristics of LAO-STO and LAO-CTO interfaces.

According to Reinle-Schmitt et al. [232] the dielectric constant of the polar $LaAlO_3$ film (and not the non-polar substrate) determines the critical thickness of a polar oxide interface. Still, the critical thickness of ~ 10 uc for LAO-CTO differs significantly from the well known 4 uc for LAO-STO. Apparently, the non-polar substrate plays an important role for the electronic reconstruction that is not sufficiently captured by current models.

In conclusion, the $LaAlO_3$-$CaTiO_3$ interface is a welcome addition to the family of conducting oxide interfaces. It is the first such interface on a substrate other than $SrTiO_3$, which highlights the generic nature of electronically reconstructed conducting oxide interfaces. The similarities and dissimilarities between LAO-CTO and LAO-STO with respect to their normal- and superconducting properties might enable a deeper understanding of the physics behind these two-dimensional systems.

E. AFM images of MBE-grown LAO-STO samples

The initial MBE-grown LAO-STO samples have been characterized in an atomic force microscope. The following figures present the surface morphology of the initial samples. For each of the large samples, images were acquired on the left- and right-hand-side and in the middle (only mid and right for M422). The orientation is like in figure D.3.

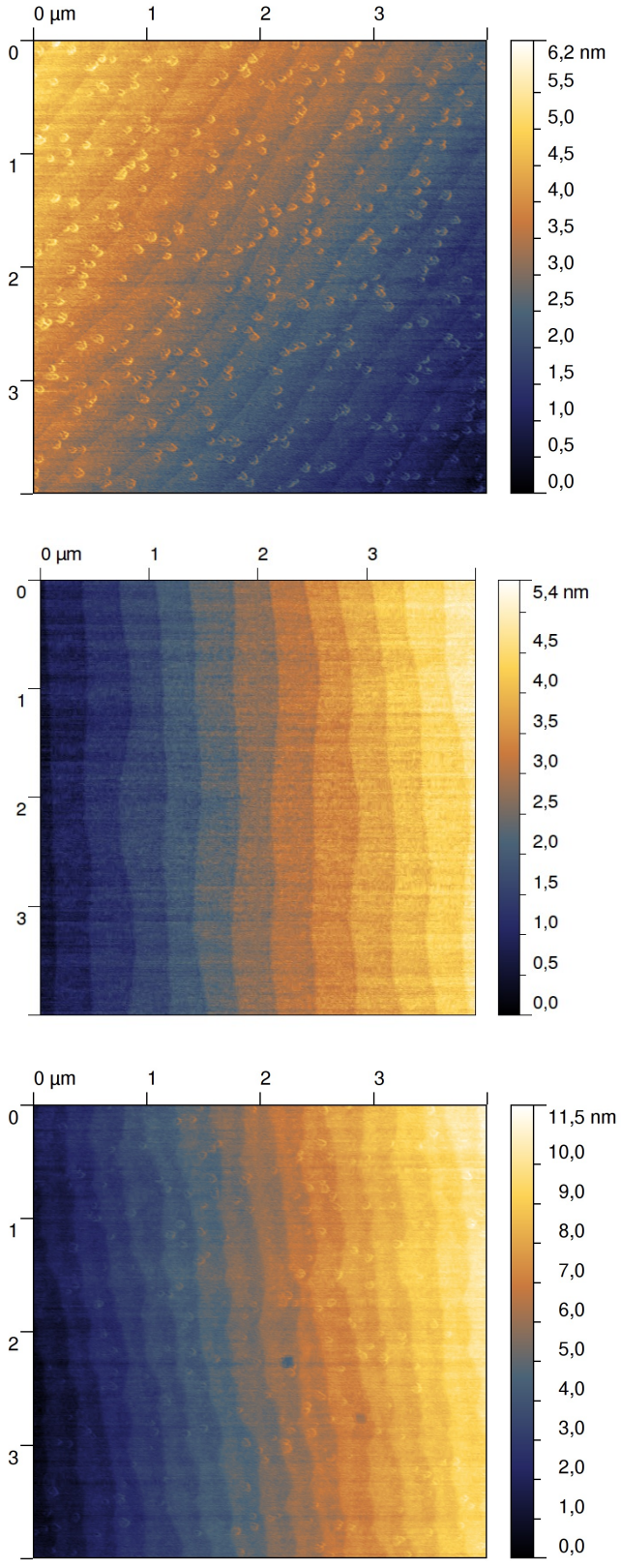

Fig. E.1: Atomic force microscopic images of the surface topography of MBE grown 8 uc LAO on STO sample M420

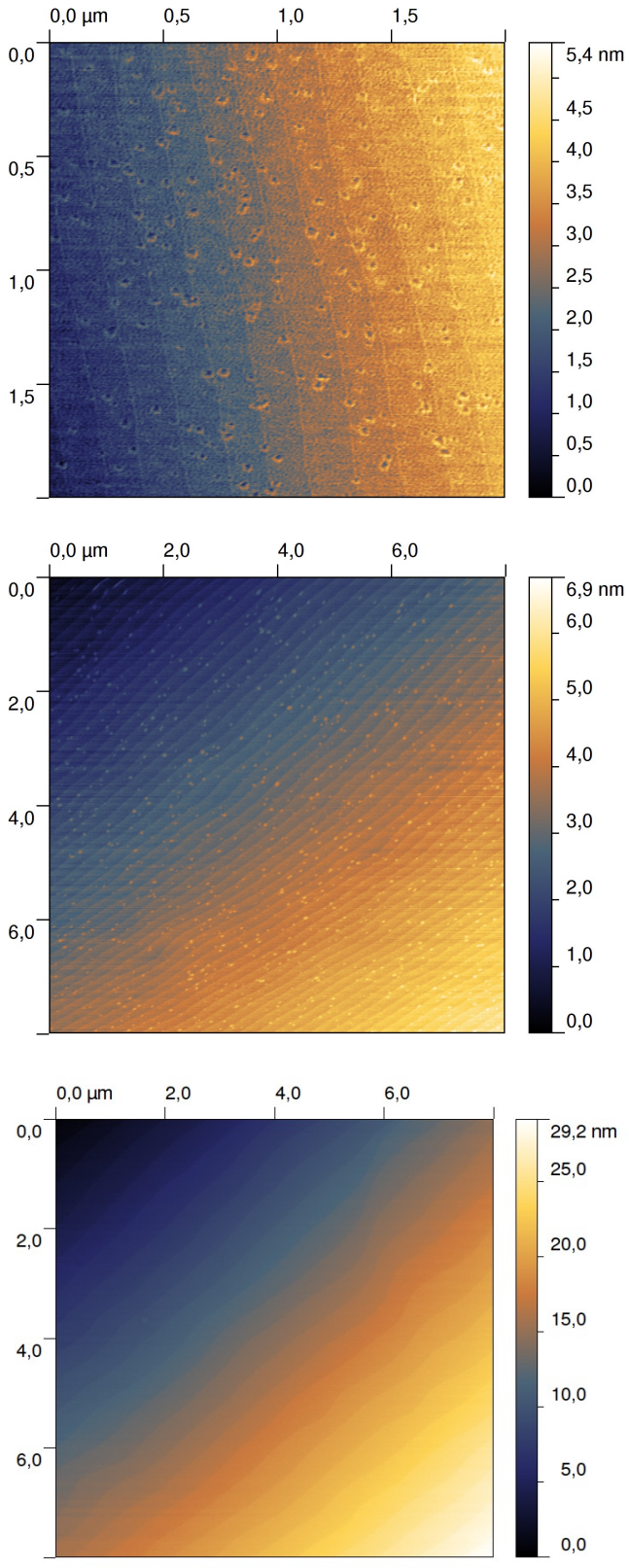

Fig. E.2: Atomic force microscopic images of the surface topography of MBE grown 8 uc LAO on STO sample M421

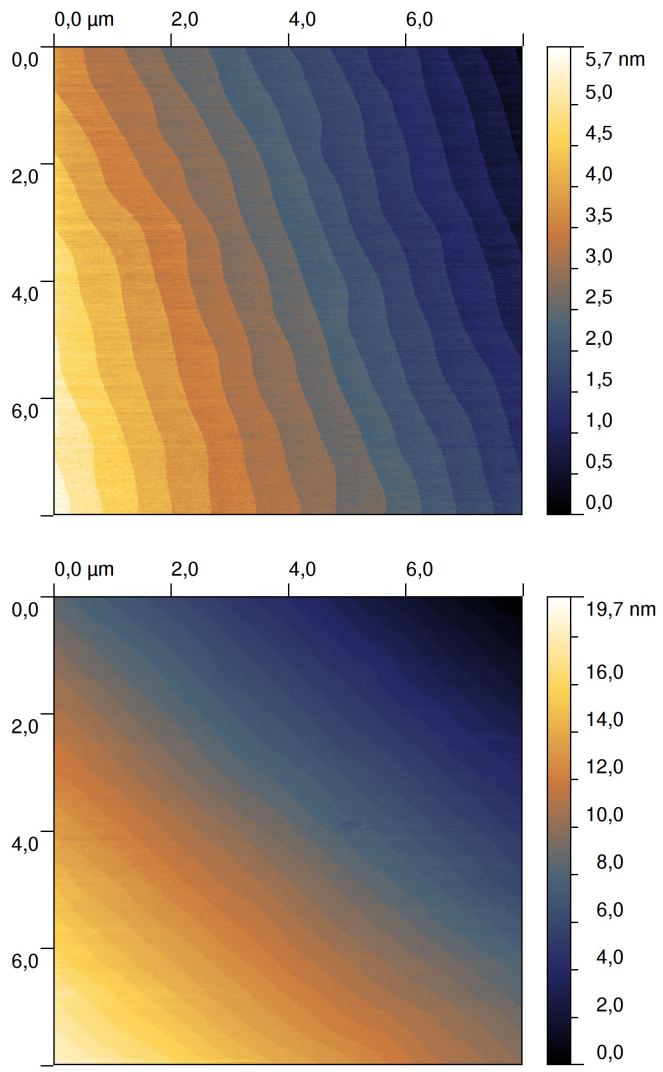

Fig. E.3: Atomic force microscopic images of the surface topography of MBE grown 8 uc LAO on STO sample M422

F. Hysteretic magnetotransport on MBE-grown LAO-STO samples

The magneto-transport properties of the investigated MBE-grown LAO-STO interfaces showed a pronounced hysteresis with regard to temperature sweeps. As shown in the main text, smooth, convex $R(T)$ curves were measured on cooling cycles. $R(T)$ curves measured during heating cycles, though, had pronounced humps and wiggles. Similar effects, albeit usually less pronounced, have also been seen and previously reported on PLD-grown LAO-STO samples[233, 234].

Using Hall-measurements, I have resolved these $R(T)$-anomalies into mobility μ and charge carrier density n_s contributions. The results are shown in figure F.1. The sample has been kept in the dark for $> 12\,\mathrm{h}$ before the measurement started.

The warming $n_\mathrm{s}(T)$ characteristic steps up markedly at around 90, 200, and 250 K. At the same temperatures $\mu(T)$ steps down. While it is tempting to attribute this effect to hypothetical structural transitions at these temperatures, there is no direct proof for such transitions, apart from the well-known antiferrodistortive phase transition of $SrTiO_3$ at 105 K[235] and minor elastic anomalies at $T < 100\,\mathrm{K}$[236]. Moreover, the time-constant with which electrons become trapped upon cooling through, e.g., 90 K is orders of magnitude larger than the time-constant with which the same electrons are released upon heating.

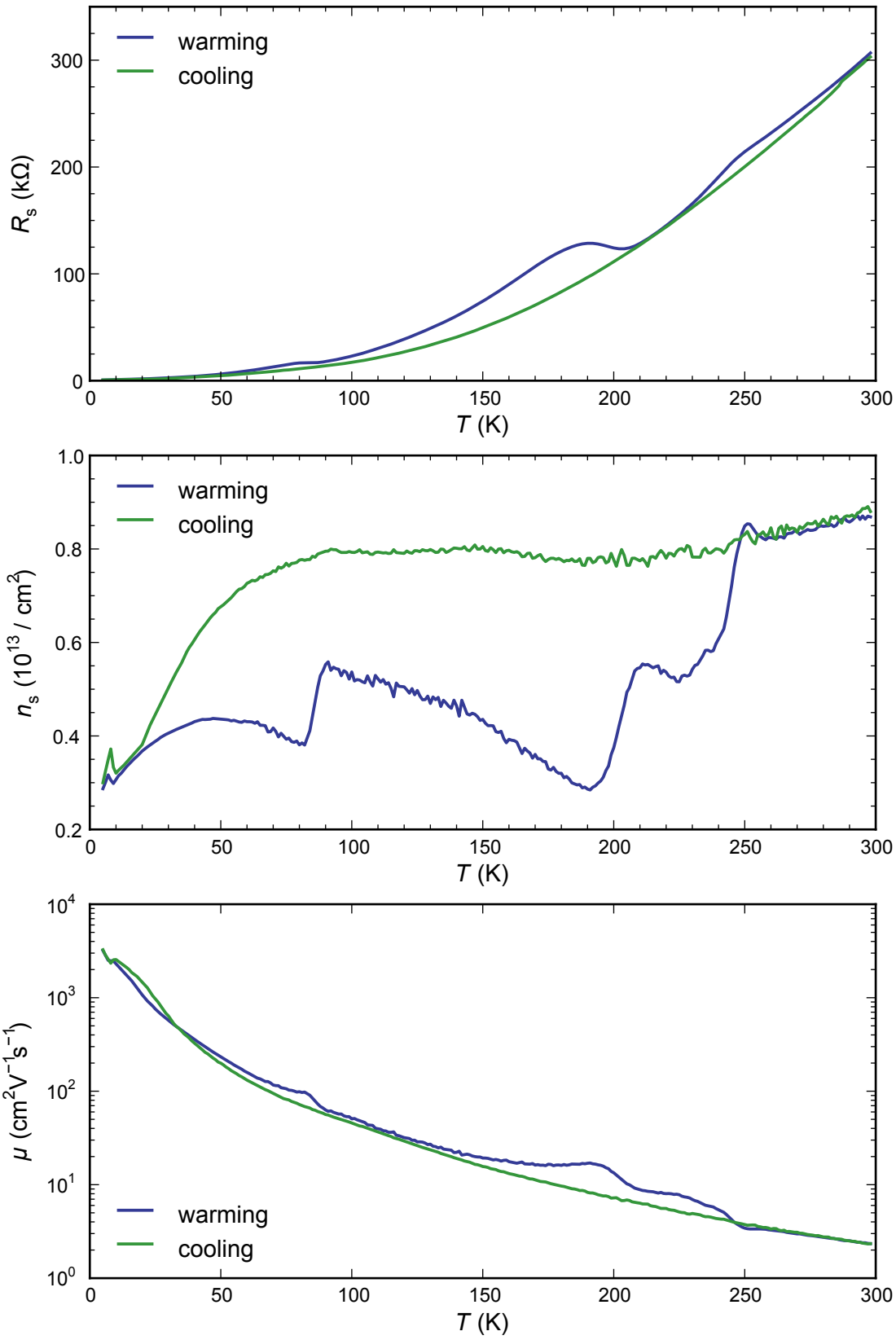

Fig. F.1: Hysteretic Magnetotransport on MBE-grown 8 uc LAO-STO sample

G. Co-etching to determine shallow etch steps

To figure out the critical thickness for conductivity at the $LaAlO_3/CaTiO_3$ interface, Ar-ion-milling was employed to reduce the $LaAlO_3$ thickness of two samples after growth. These samples were initially grown to a thickness of 20 uc $LaAlO_3$, as determined from counting RHEED oscillations.

The accuracy, with which the $LaAlO_3$ etch-depth of each ion-beam exposure can be determined, is crucial for this experiment. Step-heights on the order of a few nanometers can be measured with an atomic force microscope (AFM). Shallow steps, of 1 nm or below, can not be measured easily, though: The limitation is usually not the z-resolution of the AFM, it is the sample roughness, or noise. Adsorbates left from chemical treatments, moisture or air, create considerable roughness on a nanometer scale. This is demonstrated in Fig. G.1, which shows the partially ion-etched surfaces of $LaAlO_3$ and Ti after two separate exposures. The Ti is a recessed contact plug, which extends about 40 nm deep into the sample.

The longer exposure (33 s) created steps of 34 nm and 3 nm in the Ti and $LaAlO_3$, respectively. Obviously, the etching rate of Ti is about $10\times$ larger than that of $LaAlO_3$. This discrepancy can be utilized, to extract the $LaAlO_3$ etch-depth in shorter etches, even if the $LaAlO_3$ etch-edge is hidden in noise, as is the case in the right column of Fig. G.1. Here, after an etching-time of 12 s, no clear step is discernable in the $LaAlO_3$. Still, the Ti contact was clearly etched off by an easily measurable margin of 13.2 nm.

For technical reasons, the individual etching-rate for a given material in a given ion-mill system is often spatially inhomogeneous and might change over time or from exposure to exposure. The ratio between two etching-rates, on the contrary, is rather constant and highly reproducible. From the measured Ti etch-depth, the etch-depth inside the surrounding $LaAlO_3$ can therefore be deduced with a high level of accuracy. Much higher than, e.g. a simple inter- or extrapolation based on the exposure time and previously measured $LaAlO_3$ etching rates, only.

The main advantage of the co-etching technique lies obviously in the local nature of the measurement, both in space and time. This way it excludes the two most serious error sources: spatially varying etching-rates, because of an inhomogeneous ion-beam, and exposure to exposure parameter drift mainly due to filament aging. In addition, the co-etching technique does not rely on any measurement of the actual exposure time.

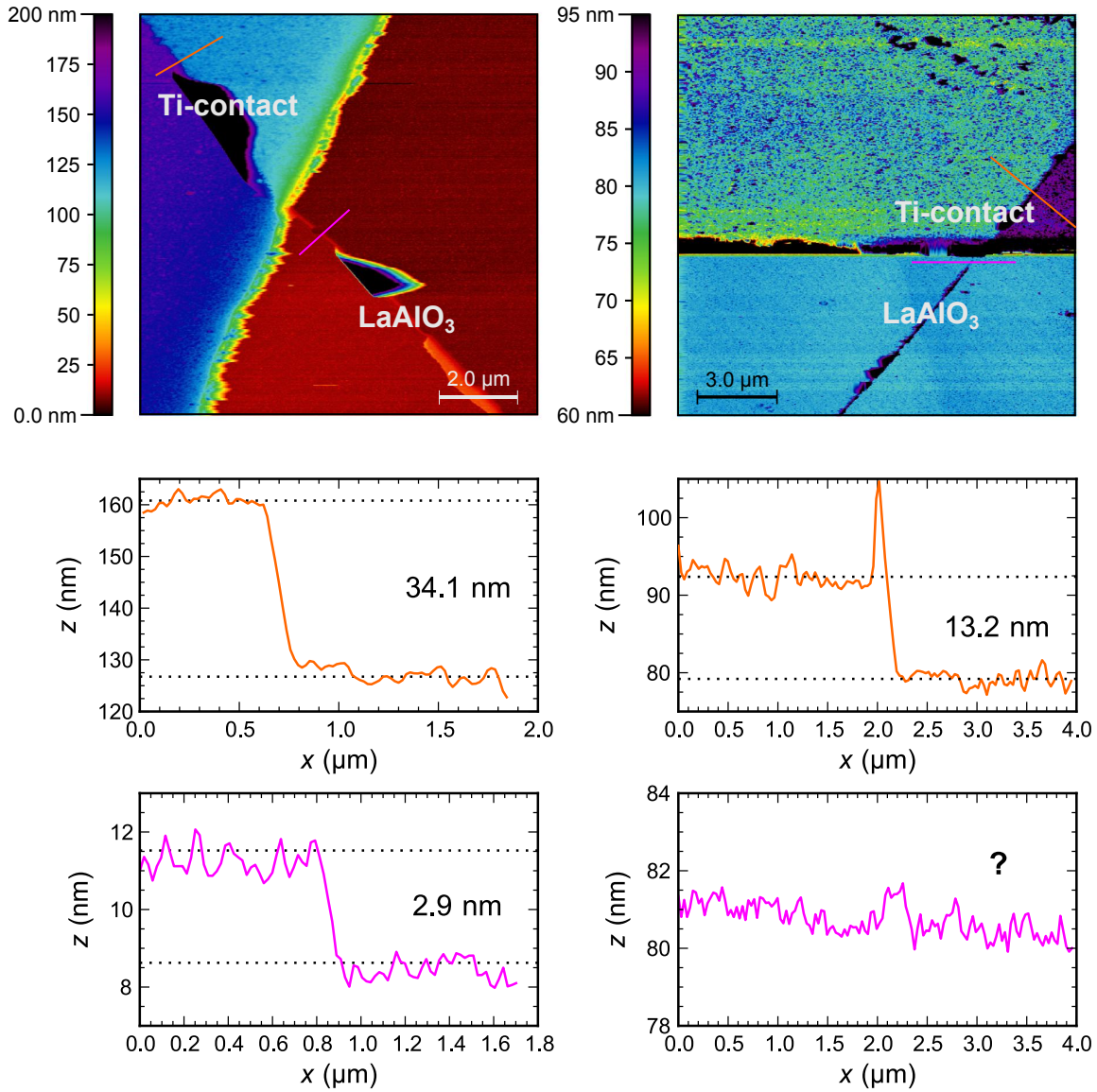

Fig. G.1: AFM topographic maps of etched $LaAlO_3$ near a co-etched Ti-contact (top panels) and corresponding cross-sections (lower panels), which allow measuring the etch-depth. For the image (and cross-sections) in the left column, the beam-exposure (etching-time) was 33 s. For the image (and cross-sections) in the right column, the exposure was 12 s. The upper graphs (orange lines) give the etch-depth for the Ti-contacts. This depth is roughly 10 times the etch-depth of the $LaAlO_3$, given by the purple curves in the bottom graphs. Note, that each of the cross-sections is averaged over 10 adjacent lines centered around the correspondingly colored lines drawn into the AFM images.

H. Curriculum vitae

Name:	Christoph Richter
Geburtstag:	25.2.1981
Geburtsort:	Frankfurt an der Oder
Familienstand:	Verheiratet

Schule

1987-1991	21. Polytechnische Oberschule "Jean-Pierre Timbaud", Frankfurt/Oder
1991-2000	Hertzhaimer-Gymnasium Trostberg
Juni 2000	Abschluss: Allgemeine Hochschulreife (Abitur)

Zivildienst

2000-2001	Betreuung und Pflege geistig behinderter Menschen in einem Wohnheim der Lebenshilfe Traunstein eV

Studium

2001-2006	Physikstudium an der Universität Augsburg
2006-2007	Diplomarbeit mit Thema "Untersuchung des Feldeffekts an $LaAlO_3/SrTiO_3$-Heterostrukturen", betreut von Prof. Dr. Jochen Mannhart
Februar 2008	Abschluss: Diplom-Physiker (Univ.)

Promotion

2008-2011	Zentrum für Elektronische Korrelationen und Magnetismus (EKM) der Universität Augsburg
2011-2012	Max Planck Institut für Festkörperforschung, Stuttgart
2013-	Zentrum für Elektronische Korrelationen und Magnetismus (EKM) der Universität Augsburg
Februar 2013	Abschluss: Doktor der Naturwissenschaften

H.1. List of publications

1. Christof W. Schneider, S. Thiel, G. Hammerl, Christoph Richter, and J. Mannhart. "Microlithography of electron gases formed at interfaces in oxide heterostructures". *Applied Physics Letters*, 89(12):122101, 2006. ISSN 00036951. doi: 10.1063/1.2354422. URL http://link.aip.org/link/APPLAB/v89/i12/p122101/s1&Agg=doi

2. Christoph Richter. "Untersuchung des Feldeffektes an $SrTiO_3$/$LaAlO_3$-Heterostrukturen". Diplomarbeit, Institut für Physik, Augsburg, Germany, 2007. URL http://www.student.uni-augsburg.de/~richtech/Dipla-Online.pdf

3. N. Reyren, S. Thiel, A. D. Caviglia, L. Fitting Kourkoutis, G. Hammerl, Christoph Richter, C. W. Schneider, T. Kopp, A.-S. Rüetschi, D. Jaccard, M. Gabay, D. A. Muller, J.-M. Triscone, and J. Mannhart. "Superconducting Interfaces Between Insulating Oxides". *Science*, 317(5842):1196–1199, August 2007. ISSN 0036-8075, 1095-9203. doi: 10.1126/science.1146006. URL http://www.sciencemag.org/content/317/5842/1196

4. Andreas Schmehl, V. Vaithyanathan, A. Herrnberger, S. Thiel, Christoph Richter, M. Liberati, T. Heeg, M. Röckerath, L. Fitting Kourkoutis, S. Mühlbauer, P. Böni, D.A. Muller, Y. Barash, J. Schubert, Y. Idzerda, J. Mannhart, and D.G. Schlom. "Epitaxial integration of the highly spin-polarized ferromagnetic semiconductor EuO with silicon and GaN". *Nature Materials*, 6(11):882–887, 2007. ISSN 1476-1122. doi: 10.1038/nmat2012. URL http://www.nature.com/nmat/journal/v6/n11/full/nmat2012.html

5. Marco Salluzzo, J. Cezar, N. Brookes, V. Bisogni, G. De Luca, Christoph Richter, S. Thiel, J. Mannhart, M. Huijben, A. Brinkman, G. Rijnders, and G. Ghiringhelli. "Orbital Reconstruction and the Two-Dimensional Electron Gas at the $LaAlO_3$/$SrTiO_3$ Interface". *Physical Review Letters*, 102(16), April 2009. ISSN 0031-9007, 1079-7114. doi: 10.1103/PhysRevLett.102.166804. URL http://link.aps.org/doi/10.1103/PhysRevLett.102.166804

6. A. Savoia, D. Paparo, P. Perna, Z. Ristic, M. Salluzzo, F. Miletto Granozio, U. Scotti di Uccio, Christoph Richter, S. Thiel, J. Mannhart, and L. Marrucci. "Polar catastrophe and electronic reconstructions at the $LaAlO_3$/$SrTiO_3$ interface: Evidence from optical second harmonic generation". *Physical Review B*, 80(7):075110, August 2009. doi: 10.1103/PhysRevB.80.075110. URL http://link.aps.org/doi/10.1103/PhysRevB.80.075110

7. Martin Breitschaft, V. Tinkl, N. Pavlenko, S. Paetel, Christoph Richter, J. R. Kirtley, Y. C. Liao, G. Hammerl, V. Eyert, T. Kopp, and J. Mannhart. "Two-dimensional electron liquid state at $LaAlO_3$-$SrTiO_3$ interfaces". *Physical Review B*, 81(15):153414, April 2010. doi: 10.1103/PhysRevB.81.153414. URL http://link.aps.org/doi/10.1103/PhysRevB.81.153414

8. Rainer Jany, M. Breitschaft, G. Hammerl, A. Horsche, Christoph Richter, S. Paetel, J. Mannhart, N. Stucki, N. Reyren, S. Gariglio, P. Zubko, A. D. Caviglia, and J.-M. Triscone. "Diodes with breakdown voltages enhanced by the metal-insulator transition of $LaAlO_3$-$SrTiO_3$ interfaces". *Applied Physics Letters*, 96(18):183504, May 2010. ISSN 00036951. doi: 10.1063/1.3428433. URL `http://apl.aip.org/resource/1/applab/v96/i18/p183504_s1`

9. Götz Berner, S. Glawion, J. Walde, F. Pfaff, H. Hollmark, L.-C. Duda, S. Paetel, Christoph Richter, J. Mannhart, M. Sing, and R. Claessen. "$LaAlO_3$/$SrTiO_3$ oxide heterostructures studied by resonant inelastic x-ray scattering". *Physical Review B*, 82(24):241405, December 2010. doi: 10.1103/PhysRevB.82.241405. URL `http://link.aps.org/doi/10.1103/PhysRevB.82.241405`

10. Zoran Ristic, R. Di Capua, G. M. De Luca, F. Chiarella, G. Ghiringhelli, J. C. Cezar, N. B. Brookes, Christoph Richter, J. Mannhart, and M. Salluzzo. "Nanoscale modulation of the density of states at the conducting interface between $LaAlO_3$ and $SrTiO_3$ band insulators". *EPL (Europhysics Letters)*, 93(1):17004, January 2011. ISSN 0295-5075, 1286-4854. doi: 10.1209/0295-5075/93/17004. URL `http://iopscience.iop.org/0295-5075/93/1/17004/`

11. Y.C. Liao, T. Kopp, Christoph Richter, A. Rosch, and J. Mannhart. "Metal-insulator transition of the $LaAlO_3$-$SrTiO_3$ interface electron system". *Physical Review B*, 83(7), February 2011. ISSN 1098-0121, 1550-235X. doi: 10.1103/PhysRevB.83.075402. URL `http://link.aps.org/doi/10.1103/PhysRevB.83.075402`

12. Andrea Rubano, M. Fiebig, D. Paparo, A. Marino, D. Maccariello, U. Scotti di Uccio, F. Miletto Granozio, L. Marrucci, Christoph Richter, S. Paetel, and J. Mannhart. "Spectral and spatial distribution of polarization at the $LaAlO_3$/$SrTiO_3$ interface". *Physical Review B*, 83(15):155405, April 2011. doi: 10.1103/PhysRevB.83.155405. URL `http://link.aps.org/doi/10.1103/PhysRevB.83.155405`

13. Lu Li, Christoph Richter, S. Paetel, T. Kopp, J. Mannhart, and R. C. Ashoori. "Very Large Capacitance Enhancement in a Two-Dimensional Electron System". *Science*, 332(6031):825–828, May 2011. ISSN 0036-8075, 1095-9203. doi: 10.1126/science.1204168. URL `http://www.sciencemag.org/content/332/6031/825`

14. Lu Li, Christoph Richter, J. Mannhart, and R. C. Ashoori. "Coexistence of magnetic order and two-dimensional superconductivity at $LaAlO_3$/$SrTiO_3$ interfaces". *Nature Physics*, 7(10):762–766, 2011. ISSN 1745-2473. doi: 10.1038/nphys2080. URL `http://www.nature.com/nphys/journal/v7/n10/full/nphys2080.html`

15. Cyril Stephanos, Martin Breitschaft, Rainer Jany, Birgit Kiessig, Stefan Paetel, Christoph Richter, and Jochen Mannhart. "Writing Nanowires with Large Conductivity Ratios in $LaAlO_3$/$SrTiO_3$ Interfaces". *Journal of the Physical Society of Japan*, 81(6):064703, 2012. doi: 10.1143/JPSJ.81.064703. URL `http://jpsj.ipap.jp/link?JPSJ/81/064703/`

16. Benjamin Förg, Christoph Richter, and Jochen Mannhart. "Field-effect devices utilizing $LaAlO_3$-$SrTiO_3$ interfaces". *Applied Physics Letters*, 100(5):053506, 2012. doi: 10.1063/1.3682102. URL http://link.aip.org/link/?APL/100/053506/1

17. Veronika Tinkl, M. Breitschaft, Christoph Richter, and J. Mannhart. "Large negative electronic compressibility of $LaAlO_3$-$SrTiO_3$ interfaces with ultrathin $LaAlO_3$ layers". *Physical Review B*, 86(7), August 2012. ISSN 1098-0121, 1550-235X. doi: 10.1103/PhysRevB.86.075116. URL http://link.aps.org/doi/10.1103/PhysRevB.86.075116

18. T. Günter, A. Rubano, D. Paparo, M. Lilienblum, L. Marrucci, F. Miletto Granozio, U. Scotti di Uccio, R. Jany, C. Richter, J. Mannhart, and M. Fiebig. "Spatial inhomogeneities at the $LaAlO_3/SrTiO_3$ interface: Evidence from second harmonic generation". *Physical Review B*, 86(23):235418, December 2012. doi: 10.1103/PhysRevB.86.235418. URL http://link.aps.org/doi/10.1103/PhysRevB.86.235418

19. Matthias Rössle, K. W. Kim, A. Dubroka, P. Marsik, C. N. Wang, R. Jany, Christoph Richter, J. Mannhart, C. W. Schneider, A. Frano, P. Wochner, Y. Lu, B. Keimer, D.K. Shukla, J. Strempfer, and C. Bernhard. "Electric-field-induced pyroelectric order and localization of the confined electrons in $LaAlO_3/SrTiO_3$ heterostructures". accepted at Phys. Rev. Lett., 2013. URL http://arxiv.org/abs/1209.4739

20. Maitri P. Warusawithana, Christoph Richter, J. A. Mundy, P. Roy, J. Ludwig, S. Paetel, T. Heeg, A. A. Pawlicki, Lena Fitting Kourkoutis, M. Zheng, B. Mulcahy, W. Zander, J. Schubert, J. N. Eckstein, D. A. Muller, C. S. Hellberg, J. Mannhart, and D. G. Schlom. "$La_{1-\delta}Al_{1+\delta}O_3$ stoichiometry found key to electron liquid formation at $LaAlO_3/SrTiO_3$ interfaces". submitted to Nature Communications, 2013. URL http://arxiv.org/abs/1303.5352

21. Götz Berner, M. Sing, H. Fujiwara, A. Yasui, Y. Saitoh, A. Yamasaki, Y. Nishitani, A. Sekiyama, N. Pavlenko, T. Kopp, Christoph Richter, J. Mannhart, S. Suga, and R. Claessen. "Direct k-space mapping of the $LaAlO_3/SrTiO_3$ interface". in review at Phys. Rev. Lett., 2013. URL http://arxiv.org/abs/1301.2824

22. Rainer Jany, Christoph Richter, C. Woltmann, G. Pfanzelt, B. Förg, J. Weis, M. Rommel, T. Reindl, U. Waizmann, J. Mundy, D.A. Muller, H. Boschker, and J. Mannhart. "Monolithically Integrated Circuits from Functional Oxides". in review at Nature Materials, 2013

23. Beena Kalisky, E.M. Spanton, H. Noad, J.R. Kirtley, K.C. Nowack, C. Bell, H.K. Sato, M. Hosoda, Y. Xie, Y. Hikita, C. Woltmann, G. Pfanzelt, R. Jany, Christoph Richter, H.Y. Hwang, J. Mannhart, and K.A. Moler. "Locally enhanced conductivity due to tetragonal domain structure in $LaAlO_3/SrTiO_3$ heterointerfaces". submitted to Nature Materials, 2013

24. Christoph Richter, H. Boschker, W. Dietsche, R. Jany, T. Kopp, F. Loder, L. Fitting Kourkoutis, D.A. Muller, J.R. Kirtley, C.W. Schneider, and J. Mannhart. "High-T_c-Superconductor-like Gap Behavior of a Non-Cuprate 2-D Interface Superconductor". submitted to Nature, 2013

Bibliography

[1] Christof W. Schneider, S. Thiel, G. Hammerl, Christoph Richter, and J. Mannhart. "Microlithography of electron gases formed at interfaces in oxide heterostructures". *Applied Physics Letters*, 89(12):122101, 2006. ISSN 00036951. doi: 10.1063/1.2354422. URL http://link.aip.org/link/APPLAB/v89/i12/p122101/s1&Agg=doi.

[2] Christoph Richter. "Untersuchung des Feldeffektes an $SrTiO_3$/$LaAlO_3$-Heterostrukturen". Diplomarbeit, Institut für Physik, Augsburg, Germany, 2007. URL http://www.student.uni-augsburg.de/~richtech/Dipla-Online.pdf.

[3] N. Reyren, S. Thiel, A. D. Caviglia, L. Fitting Kourkoutis, G. Hammerl, Christoph Richter, C. W. Schneider, T. Kopp, A.-S. Rüetschi, D. Jaccard, M. Gabay, D. A. Muller, J.-M. Triscone, and J. Mannhart. "Superconducting Interfaces Between Insulating Oxides". *Science*, 317(5842): 1196–1199, August 2007. ISSN 0036-8075, 1095-9203. doi: 10.1126/science.1146006. URL http://www.sciencemag.org/content/317/5842/1196.

[4] Andreas Schmehl, V. Vaithyanathan, A. Herrnberger, S. Thiel, Christoph Richter, M. Liberati, T. Heeg, M. Röckerath, L. Fitting Kourkoutis, S. Mühlbauer, P. Böni, D.A. Muller, Y. Barash, J. Schubert, Y. Idzerda, J. Mannhart, and D.G. Schlom. "Epitaxial integration of the highly spin-polarized ferromagnetic semiconductor EuO with silicon and GaN". *Nature Materials*, 6 (11):882–887, 2007. ISSN 1476-1122. doi: 10.1038/nmat2012. URL http://www.nature.com/nmat/journal/v6/n11/full/nmat2012.html.

[5] Marco Salluzzo, J. Cezar, N. Brookes, V. Bisogni, G. De Luca, Christoph Richter, S. Thiel, J. Mannhart, M. Huijben, A. Brinkman, G. Rijnders, and G. Ghiringhelli. "Orbital Reconstruction and the Two-Dimensional Electron Gas at the $LaAlO_3$/$SrTiO_3$ Interface". *Physical Review Letters*, 102(16), April 2009. ISSN 0031-9007, 1079-7114. doi: 10.1103/PhysRevLett.102.166804. URL http://link.aps.org/doi/10.1103/PhysRevLett.102.166804.

[6] A. Savoia, D. Paparo, P. Perna, Z. Ristic, M. Salluzzo, F. Miletto Granozio, U. Scotti di Uccio, Christoph Richter, S. Thiel, J. Mannhart, and L. Marrucci. "Polar catastrophe and electronic reconstructions at the $LaAlO_3$/$SrTiO_3$ interface: Evidence from optical second harmonic generation". *Physical Review B*, 80(7):075110, August 2009. doi: 10.1103/PhysRevB.80.075110. URL http://link.aps.org/doi/10.1103/PhysRevB.80.075110.

[7] Rainer Jany, M. Breitschaft, G. Hammerl, A. Horsche, Christoph Richter, S. Paetel, J. Mannhart, N. Stucki, N. Reyren, S. Gariglio, P. Zubko, A. D. Caviglia, and J.-M. Triscone. "Diodes with breakdown voltages enhanced by the metal-insulator transition of $LaAlO_3$-$SrTiO_3$ interfaces". *Applied Physics Letters*, 96(18):183504, May 2010. ISSN 00036951. doi: 10.1063/1.3428433. URL http://apl.aip.org/resource/1/applab/v96/i18/p183504_s1.

[8] Götz Berner, S. Glawion, J. Walde, F. Pfaff, H. Hollmark, L.-C. Duda, S. Paetel, Christoph Richter, J. Mannhart, M. Sing, and R. Claessen. "$LaAlO_3$/$SrTiO_3$ oxide heterostructures studied by resonant inelastic x-ray scattering". *Physical Review B*, 82(24):241405, December 2010. doi: 10.1103/PhysRevB.82.241405. URL http://link.aps.org/doi/10.1103/PhysRevB.82.241405.

[9] Martin Breitschaft, V. Tinkl, N. Pavlenko, S. Paetel, Christoph Richter, J. R. Kirtley, Y. C. Liao, G. Hammerl, V. Eyert, T. Kopp, and J. Mannhart. "Two-dimensional electron liquid state at $LaAlO_3$-$SrTiO_3$ interfaces". *Physical Review B*, 81(15):153414, April 2010. doi: 10.1103/PhysRevB.81.153414. URL http://link.aps.org/doi/10.1103/PhysRevB.81.153414.

[10] Y.C. Liao, T. Kopp, Christoph Richter, A. Rosch, and J. Mannhart. "Metal-insulator transition of the $LaAlO_3$-$SrTiO_3$ interface electron system". *Physical Review B*, 83(7), February 2011. ISSN 1098-0121, 1550-235X. doi: 10.1103/PhysRevB.83.075402. URL http://link.aps.org/doi/10.1103/PhysRevB.83.075402.

[11] Zoran Ristic, R. Di Capua, G. M. De Luca, F. Chiarella, G. Ghiringhelli, J. C. Cezar, N. B. Brookes, Christoph Richter, J. Mannhart, and M. Salluzzo. "Nanoscale modulation of the density of states at the conducting interface between $LaAlO_3$ and $SrTiO_3$ band insulators". *EPL (Europhysics Letters)*, 93(1):17004, January 2011. ISSN 0295-5075, 1286-4854. doi: 10.1209/0295-5075/93/17004. URL http://iopscience.iop.org/0295-5075/93/1/17004/.

[12] Andrea Rubano, M. Fiebig, D. Paparo, A. Marino, D. Maccariello, U. Scotti di Uccio, F. Miletto Granozio, L. Marrucci, Christoph Richter, S. Paetel, and J. Mannhart. "Spectral and spatial distribution of polarization at the $LaAlO_3$/$SrTiO_3$ interface". *Physical Review B*, 83 (15):155405, April 2011. doi: 10.1103/PhysRevB.83.155405. URL http://link.aps.org/doi/10.1103/PhysRevB.83.155405.

[13] Lu Li, Christoph Richter, S. Paetel, T. Kopp, J. Mannhart, and R. C. Ashoori. "Very Large Capacitance Enhancement in a Two-Dimensional Electron System". *Science*, 332(6031):825–828, May 2011. ISSN 0036-8075, 1095-9203. doi: 10.1126/science.1204168. URL http://www.sciencemag.org/content/332/6031/825.

[14] Lu Li, Christoph Richter, J. Mannhart, and R. C. Ashoori. "Coexistence of magnetic order and two-dimensional superconductivity at $LaAlO_3$/$SrTiO_3$ interfaces". *Nature Physics*, 7(10):762–766, 2011. ISSN 1745-2473. doi: 10.1038/nphys2080. URL http://www.nature.com/nphys/journal/v7/n10/full/nphys2080.html.

[15] Cyril Stephanos, Martin Breitschaft, Rainer Jany, Birgit Kiessig, Stefan Paetel, Christoph Richter, and Jochen Mannhart. "Writing Nanowires with Large Conductivity Ratios in $LaAlO_3$/$SrTiO_3$ Interfaces". *Journal of the Physical Society of Japan*, 81(6):064703, 2012. doi: 10.1143/JPSJ.81.064703. URL http://jpsj.ipap.jp/link?JPSJ/81/064703/.

[16] Benjamin Förg, Christoph Richter, and Jochen Mannhart. "Field-effect devices utilizing $LaAlO_3$-$SrTiO_3$ interfaces". *Applied Physics Letters*, 100(5):053506, 2012. doi: 10.1063/1.3682102. URL http://link.aip.org/link/?APL/100/053506/1.

[17] Veronika Tinkl, M. Breitschaft, Christoph Richter, and J. Mannhart. "Large negative electronic compressibility of $LaAlO_3$-$SrTiO_3$ interfaces with ultrathin $LaAlO_3$ layers". *Physical Review B*, 86(7), August 2012. ISSN 1098-0121, 1550-235X. doi: 10.1103/PhysRevB.86.075116. URL http://link.aps.org/doi/10.1103/PhysRevB.86.075116.

[18] T. Günter, A. Rubano, D. Paparo, M. Lilienblum, L. Marrucci, F. Miletto Granozio, U. Scotti di Uccio, R. Jany, C. Richter, J. Mannhart, and M. Fiebig. "Spatial inhomogeneities at the $LaAlO_3$/$SrTiO_3$ interface: Evidence from second harmonic generation". *Physical Review B*, 86 (23):235418, December 2012. doi: 10.1103/PhysRevB.86.235418. URL http://link.aps.org/doi/10.1103/PhysRevB.86.235418.

[19] Matthias Rössle, K. W. Kim, A. Dubroka, P. Marsik, C. N. Wang, R. Jany, Christoph Richter, J. Mannhart, C. W. Schneider, A. Frano, P. Wochner, Y. Lu, B. Keimer, D.K. Shukla, J. Strempfer, and C. Bernhard. "Electric-field-induced pyroelectric order and localization of the confined electrons in $LaAlO_3$/$SrTiO_3$ heterostructures". accepted at Phys. Rev. Lett., 2013. URL http://arxiv.org/abs/1209.4739.

[20] Maitri P. Warusawithana, Christoph Richter, J. A. Mundy, P. Roy, J. Ludwig, S. Paetel, T. Heeg, A. A. Pawlicki, Lena Fitting Kourkoutis, M. Zheng, B. Mulcahy, W. Zander, J. Schubert, J. N. Eckstein, D. A. Muller, C. S. Hellberg, J. Mannhart, and D. G. Schlom. "$La_{1-\delta}Al_{1+\delta}O_3$ stoichiometry found key to electron liquid formation at $LaAlO_3/SrTiO_3$ interfaces". submitted to Nature Communications, 2013. URL http://arxiv.org/abs/1303.5352.

[21] Götz Berner, M. Sing, H. Fujiwara, A. Yasui, Y. Saitoh, A. Yamasaki, Y. Nishitani, A. Sekiyama, N. Pavlenko, T. Kopp, Christoph Richter, J. Mannhart, S. Suga, and R. Claessen. "Direct k-space mapping of the $LaAlO_3/SrTiO_3$ interface". in review at Phys. Rev. Lett., 2013. URL http://arxiv.org/abs/1301.2824.

[22] Rainer Jany, Christoph Richter, C. Woltmann, G. Pfanzelt, B. Förg, J. Weis, M. Rommel, T. Reindl, U. Waizmann, J. Mundy, D.A. Muller, H. Boschker, and J. Mannhart. "Monolithically Integrated Circuits from Functional Oxides". in review at Nature Materials, 2013.

[23] Beena Kalisky, E.M. Spanton, H. Noad, J.R. Kirtley, K.C. Nowack, C. Bell, H.K. Sato, M. Hosoda, Y. Xie, Y. Hikita, C. Woltmann, G. Pfanzelt, R. Jany, Christoph Richter, H.Y. Hwang, J. Mannhart, and K.A. Moler. "Locally enhanced conductivity due to tetragonal domain structure in $LaAlO_3/SrTiO_3$ heterointerfaces". submitted to Nature Materials, 2013.

[24] Christoph Richter, H. Boschker, W. Dietsche, R. Jany, T. Kopp, F. Loder, L. Fitting Kourkoutis, D.A. Muller, J.R. Kirtley, C.W. Schneider, and J. Mannhart. "High-T_c-Superconductor-like Gap Behavior of a Non-Cuprate 2-D Interface Superconductor". submitted to Nature, 2013.

[25] A. Ohtomo and H. Y. Hwang. "A high-mobility electron gas at the $LaAlO_3/SrTiO_3$ heterointerface". *Nature*, 427(6973):423–426, 2004. doi: 10.1038/nature02308. URL http://www.nature.com/nature/journal/v427/n6973/full/nature02308.html.

[26] H.P.J. Wijn. "5.5.2 $RAlO_3$ compounds". In H.P.J. Wijn, editor, *Perovskites II, Oxides with Corundum, Ilmenite and Amorphous Structures*, volume 27F3, pages 8–22. Springer-Verlag, Berlin/Heidelberg, 1994. ISBN 3-540-57770-X. URL http://www.springermaterials.com/index/chapterdoi/10.1007/10465197_4.

[27] S. Geller and V. B. Bala. "Crystallographic studies of perovskite-like compounds. II. Rare earth alluminates". *Acta Crystallographica*, 9(12):1019–1025, December 1956. ISSN 0365-110X. doi: 10.1107/S0365110X56002965. URL http://scripts.iucr.org/cgi-bin/paper?S0365110X56002965.

[28] R. W Simon, C. E Platt, A. E Lee, G. S Lee, K. P Daly, M. S Wire, J. A Luine, and M. Urbanik. "Low-loss substrate for epitaxial growth of high-temperature superconductor thin films". *Applied Physics Letters*, 53(26):2677–2679, December 1988. ISSN 00036951. doi: 10.1063/1.100543. URL http://apl.aip.org/resource/1/applab/v53/i26/p2677_s1.

[29] Wen-Huang Yang, De-Sen Hou, Cong-Zhou Li, Hui Fan, and Hui Yun Zhang. "$LaAlO_3$ single crystal substrate for epitaxial superconducting thin films". *Solid State Communications*, 75(5): 421 – 424, 1990. ISSN 0038-1098. doi: 10.1016/0038-1098(90)90593-Z. URL http://www.sciencedirect.com/science/article/pii/003810989090593Z.

[30] Seung-Gu Lim, Stas Kriventsov, Thomas N. Jackson, J. H. Haeni, D. G. Schlom, A. M. Balbashov, R. Uecker, P. Reiche, J. L. Freeouf, and G. Lucovsky. "Dielectric functions and optical bandgaps of high-K dielectrics for metal-oxide-semiconductor field-effect transistors by far ultraviolet spectroscopic ellipsometry". *Journal of Applied Physics*, 91(7):4500–4505, April 2002. ISSN 00218979. doi: 10.1063/1.1456246. URL http://jap.aip.org/resource/1/japiau/v91/i7/p4500_s1.

[31] Tuong Lan Nguyen, Masayuki Dokiya, Shaorong Wang, Hiroaki Tagawa, and Takuya Hashimoto. "The effect of oxygen vacancy on the oxide ion mobility in $LaAlO_3$-based oxides". *Solid State Ionics*, 130(3–4):229–241, May 2000. ISSN 0167-2738. doi: 10.1016/S0167-2738(00)00640-8. URL http://www.sciencedirect.com/science/article/pii/S0167273800006408.

[32] H Park. "Oxygen permeation in Sr- and Mg-doped $LaAlO_3$ and Gd-doped CeO_2 at high temperature". *Solid State Ionics*, 175(1-4):399–403, November 2004. ISSN 01672738. doi: 10.1016/j.ssi.2004.03.048. URL http://linkinghub.elsevier.com/retrieve/pii/S0167-2738(04)00703-9.

[33] J. Krupka, R.G. Geyer, M. Kuhn, and J.H. Hinken. "Dielectric properties of single crystals of Al_2O_3 , $LaAlO_3$, $NdGaO_3$, $SrTiO_3$, and MgO at cryogenic temperatures". *IEEE Transactions on Microwave Theory and Techniques*, 42(10):1886 –1890, October 1994. ISSN 0018-9480. doi: 10.1109/22.320769. URL http://dx.doi.org/10.1109/22.320769.

[34] J.G. Bednorz and H.J. Scheel. "Flame-fusion growth of $SrTiO_3$". *Journal of Crystal Growth*, 41(1):5–12, November 1977. ISSN 0022-0248. doi: 10.1016/0022-0248(77)90088-4. URL http://www.sciencedirect.com/science/article/pii/0022024877900884.

[35] Masashi Kawasaki, Kazuhiro Takahashi, Tatsuro Maeda, Ryuta Tsuchiya, Makoto Shinohara, Osamu Ishiyama, Takuzo Yonezawa, Mamoru Yoshimoto, and Hideomi Koinuma. "Atomic Control of the SrTiO3 Crystal Surface". *Science*, 266(5190):1540–1542, 1994. doi: 10.1126/science.266.5190.1540. URL http://www.sciencemag.org/cgi/content/abstract/266/5190/1540.

[36] Gertjan Koster, Boike L. Kropman, Guus J. H. M. Rijnders, Dave H. A. Blank, and Horst Rogalla. "Quasi-ideal strontium titanate crystal surfaces through formation of strontium hydroxide". *Applied Physics Letters*, 73(20):2920–2922, 1998. doi: 10.1063/1.122630. URL http://link.aip.org/link/?APL/73/2920/1.

[37] H. P. R. Frederikse and George A. Candela. "Magnetic Susceptibility of Insulating and Semiconducting Strontium Titanate". *Physical Review*, 147(2):583–584, July 1966. doi: 10.1103/PhysRev.147.583. URL http://link.aps.org/doi/10.1103/PhysRev.147.583.

[38] J. H. Haeni, P. Irvin, W. Chang, R. Uecker, P. Reiche, Y. L. Li, S. Choudhury, W. Tian, M. E. Hawley, B. Craigo, A. K. Tagantsev, X. Q. Pan, S. K. Streiffer, L. Q. Chen, S. W. Kirchoefer, J. Levy, and D. G. Schlom. "Room-temperature ferroelectricity in strained $SrTiO_3$". *Nature*, 430(7001):758–761, August 2004. ISSN 0028-0836, 1476-4679. doi: 10.1038/nature02773. URL http://www.nature.com/doifinder/10.1038/nature02773.

[39] D. A. Tenne, A. K. Farrar, C. M. Brooks, T. Heeg, J. Schubert, H. W. Jang, C. W. Bark, C. M. Folkman, C. B. Eom, and D. G. Schlom. "Ferroelectricity in nonstoichiometric $SrTiO_3$ films studied by ultraviolet Raman spectroscopy". *Applied Physics Letters*, 97(14):142901, 2010. ISSN 00036951. doi: 10.1063/1.3499273. URL http://link.aip.org/link/?APL/97/142901/1.

[40] J. G. Bednorz and K. A. Müller. "$Sr_{1-x}Ca_xTiO_3$: An XY Quantum Ferroelectric with Transition to Randomness". *Physical Review Letters*, 52(25):2289–2292, June 1984. doi: 10.1103/PhysRevLett.52.2289. URL http://link.aps.org/doi/10.1103/PhysRevLett.52.2289.

[41] M. Itoh, R. Wang, Y. Inaguma, T. Yamaguchi, Y-J. Shan, and T. Nakamura. "Ferroelectricity Induced by Oxygen Isotope Exchange in Strontium Titanate Perovskite". *Physical Review Letters*, 82(17):3540–3543, April 1999. doi: 10.1103/PhysRevLett.82.3540. URL http://link.aps.org/doi/10.1103/PhysRevLett.82.3540.

[42] K. A. Müller and H. Burkard. "$SrTiO_3$: An intrinsic quantum paraelectric below 4 K". *Phys. Rev. B*, 19:3593–3602, Apr 1979. doi: 10.1103/PhysRevB.19.3593. URL http://link.aps.org/doi/10.1103/PhysRevB.19.3593.

[43] H.-M. Christen, J. Mannhart, E. J. Williams, and Ch. Gerber. "Dielectric properties of sputtered $SrTiO_3$ films". *Physical Review B*, 49(17):12095–12104, May 1994. doi: 10.1103/PhysRevB.49.12095. URL http://link.aps.org/doi/10.1103/PhysRevB.49.12095.

[44] H.A. Weakliem, W.J. Burke, and V. Korsun. "Optical Properties of $SrTiO_3$ and $LiNbO_3$". *R.C.A. Review*, 36:149–162, Mar 1975.

[45] Wikipedia. "Zinc oxide — Wikipedia, The Free Encyclopedia", 2012. URL http://en.wikipedia.org/w/index.php?title=Zinc_oxide&oldid=515418586. [Online; accessed 10-October-2012].

[46] J. F. Schooley, W. R. Hosler, and M. L. Cohen. "Superconductivity in Semiconducting $SrTiO_3$". *Physical Review Letters*, 12(17):474–475, 1964. URL http://link.aps.org/doi/10.1103/PhysRevLett.12.474.

[47] C. S. Koonce, Marvin L. Cohen, J. F. Schooley, W. R. Hosler, and E. R. Pfeiffer. "Superconducting Transition Temperatures of Semiconducting $SrTiO_3$". *Phys. Rev.*, 163:380–390, Nov 1967. doi: 10.1103/PhysRev.163.380. URL http://link.aps.org/doi/10.1103/PhysRev.163.380.

[48] K. Ueno, S. Nakamura, H. Shimotani, A. Ohtomo, N. Kimura, T. Nojima, H. Aoki, Y. Iwasa, and M. Kawasaki. "Electric-field-induced superconductivity in an insulator". *Nature Materials*, 7(11):855–858, 2008. ISSN 1476-1122. doi: 10.1038/nmat2298. URL http://www.nature.com/nmat/journal/v7/n11/full/nmat2298.html.

[49] S. Gariglio, J. W. Seo, J. Fompeyrine, J.-P. Locquet, and J.-M. Triscone. "Transport properties in doped Mott insulator epitaxial $La_{1-y}TiO_{3+\delta}$ thin films". *Physical Review B*, 63(16):161103, April 2001. doi: 10.1103/PhysRevB.63.161103. URL http://link.aps.org/doi/10.1103/PhysRevB.63.161103.

[50] A. Schmehl, F. Lichtenberg, H. Bielefeldt, J. Mannhart, and D. G. Schlom. "Transport properties of $LaTiO_{3+x}$ films and heterostructures". *Applied Physics Letters*, 82(18):3077, 2003. ISSN 00036951. doi: 10.1063/1.1572960. URL http://link.aip.org/link/APPLAB/v82/i18/p3077/s1&Agg=doi.

[51] R. Ohtsuka, M. Matvejeff, K. Nishio, R. Takahashi, and M. Lippmaa. "Transport properties of $LaTiO_3/SrTiO_3$ heterostructures". *Applied Physics Letters*, 96(19):192111, 2010. doi: 10.1063/1.3430006. URL http://link.aip.org/link/?APL/96/192111/1.

[52] S. Thiel, G. Hammerl, A. Schmehl, C. W. Schneider, and J. Mannhart. "Tunable Quasi-Two-Dimensional Electron Gases in Oxide Heterostructures". *Science*, 313(5795):1942–1945, 2006. doi: 10.1126/science.1131091. URL http://www.sciencemag.org/cgi/content/abstract/313/5795/1942.

[53] J. Biscaras, S. Hurand, C. Feuillet-Palma, A. Rastogi, R. C. Budhani, N. Reyren, E. Lesne, D. LeBoeuf, C. Proust, J. Lesueur, and N. Bergeal. "Irreversibility and time relaxation in electrostatic doping of oxide interfaces". *arXiv:1206.1198*, June 2012. URL http://arxiv.org/abs/1206.1198.

[54] Inc. Google. "Google-Scholar search for publications citing "A high-mobility electron gas at the $LaAlO_3/SrTiO_3$ heterointerface" by A. Ohtomo and H.Y. Hwang". http://scholar.google.de/scholar?cites=6529374616583591416, 2012. URL http://scholar.google.de/scholar?cites=6529374616583591416.

[55] R. Hesper, L. H. Tjeng, A. Heeres, and G. A. Sawatzky. "Photoemission evidence of electronic stabilization of polar surfaces in K_3C_{60}". *Phys. Rev. B*, 62(23):16046–16055, Dec 2000. doi: 10.1103/PhysRevB.62.16046. URL http://prb.aps.org/abstract/PRB/v62/i23/p16046_1.

[56] Satoshi Okamoto and Andrew J. Millis. "Electronic reconstruction at an interface between a Mott insulator and a band insulator". *Nature*, 428(6983):630–633, 2004. doi: 10.1038/nature02450. URL http://dx.doi.org/10.1038/nature02450.

[57] Naoyuki Nakagawa, Harold Y. Hwang, and David A. Muller. "Why some interfaces cannot be sharp". *Nature Materials*, 5(3):204–209, 2006. ISSN 1476-1122. doi: 10.1038/nmat1569. URL http://www.nature.com/nmat/journal/v5/n3/full/nmat1569.html.

[58] M. Sing, G. Berner, K. Goß, A. Müller, A. Ruff, A. Wetscherek, S. Thiel, J. Mannhart, S. A. Pauli, C. W. Schneider, P. R. Willmott, M. Gorgoi, F. Schäfers, and R. Claessen. "Profiling the Interface Electron Gas of $LaAlO_3/SrTiO_3$ Heterostructures with Hard X-Ray Photoelectron Spectroscopy". *Physical Review Letters*, 102(17):176805, April 2009. doi: 10.1103/PhysRevLett.102.176805. URL http://link.aps.org/doi/10.1103/PhysRevLett.102.176805.

[59] A. Brinkman, M. Huijben, M. van Zalk, J. Huijben, U. Zeitler, J. C. Maan, W. G. van der Wiel, G. Rijnders, D. H. A. Blank, and H. Hilgenkamp. "Magnetic effects at the interface between non-magnetic oxides". *Nature Materials*, 6(7):493–496, 2007. doi: 10.1038/nmat1931. URL http://dx.doi.org/10.1038/nmat1931.

[60] Jun Kondo. "Resistance Minimum in Dilute Magnetic Alloys". *Progress of Theoretical Physics*, 32(1):37–49, July 1964. ISSN 0033-068X. doi: 10.1143/PTP.32.37. URL http://ptp.ipap.jp/link?PTP/32/37/.

[61] Mark Huijben, Alexander Brinkman, Gertjan Koster, Guus Rijnders, Hans Hilgenkamp, and Dave H.A. Blank. "Structure-Property Relation of $SrTiO_3/LaAlO_3$ Interfaces". *Advanced Materials*, 21(17):1665–1677, 2009. doi: 10.1002/adma.200801448. URL http://doc.utwente.nl/72410/.

[62] Karolina Janicka, Julian P. Velev, and Evgeny Y. Tsymbal. "Magnetism of $LaAlO_3/SrTiO_3$ superlattices". *Journal of Applied Physics*, 103(7), APR 1 2008. ISSN 0021-8979. doi: {10.1063/1.2829244}. URL http://jap.aip.org/resource/1/japiau/v103/i7/p07B508_s1. 52nd Annual Conference on Magnetism and Magnetic Materials, Tampa, FL, NOV 05-09, 2007.

[63] Zhicheng Zhong and Paul J. Kelly. "Electronic-structure-induced reconstruction and magnetic ordering at the $LaAlO_3|SrTiO_3$ interface". *EPL (Europhysics Letters)*, 84(2):27001, October 2008. ISSN 0295-5075, 1286-4854. doi: 10.1209/0295-5075/84/27001. URL http://iopscience.iop.org/0295-5075/84/27001.

[64] N. Pavlenko, T. Kopp, E. Y. Tsymbal, G. A. Sawatzky, and J. Mannhart. "Magnetic and superconducting phases at the $LaAlO_3/SrTiO_3$ interface: The role of interfacial Ti 3d electrons". *Physical Review B*, 85(2):020407, January 2012. doi: 10.1103/PhysRevB.85.020407. URL http://link.aps.org/doi/10.1103/PhysRevB.85.020407.

[65] Quantum Design, Inc. "Magnetic Property Measurement System (MPMS)", 2012. URL http://www.qdusa.com/products/mpms.html.

[66] Lu Li. *Torque Magnetometry in Unconventional Superconductors*. PhD thesis, Princeton University, Princeton, NJ, 2008. URL https://www.princeton.edu/physics/graduate-program/theses/theses-from-2008/L.Luthesis.pdf.

[67] Stefan Patrick Thiel. *Study of Interface Properties in $LaAlO_3/SrTiO_3$ Heterostructures*. PhD thesis, Universität Augsburg, Universitätsstr. 22, 86159 Augsburg, 2009. URL http://opus.bibliothek.uni-augsburg.de/opus4/files/1264/Thesis_Thiel.pdf.

[68] Ivar Giaever. "Energy Gap in Superconductors Measured by Electron Tunneling". *Physical Review Letters*, 5(4):147–148, August 1960. doi: 10.1103/PhysRevLett.5.147. URL http://link.aps.org/doi/10.1103/PhysRevLett.5.147.

[69] C. Renner, B. Revaz, J. Y. Genoud, K. Kadowaki, and Ø Fischer. "Pseudogap Precursor of the Superconducting Gap in Under-and Overdoped $Bi_2Sr_2CaCu_2O_8 + \delta$". *Physical review letters*, 80 (1):149–152, 1998. URL http://link.aps.org/doi/10.1103/PhysRevLett.80.149.

[70] Guneeta Singh-Bhalla, Christopher Bell, Jayakanth Ravichandran, Wolter Siemons, Yasuyuki Hikita, Sayeef Salahuddin, Arthur F. Hebard, Harold Y. Hwang, and Ramamoorthy Ramesh. "Built-in and induced polarization across $LaAlO_3/SrTiO_3$ heterojunctions". *Nature Physics*, 7 (1):80–86, 2011. ISSN 1745-2473. doi: 10.1038/nphys1814. URL http://www.nature.com/nphys/journal/v7/n1/full/nphys1814.html.

[71] E. L. Wolf. *Principles of electron tunneling spectroscopy*. Oxford University Press, July 1985. ISBN 9780195034172.

[72] G. B. Mahan. *Many-Particle Physics*. Plenum Press, New York, 1993.

[73] J. Bardeen. "Tunnelling from a many-particle point of view". *Physical Review Letters*, 6(2):57–59, 1961. URL http://link.aps.org/doi/10.1103/PhysRevLett.6.57.

[74] A. D. Gottlieb and L. Wesoloski. "Bardeen's tunnelling theory as applied to scanning tunnelling microscopy: a technical guide to the traditional interpretation". *Nanotechnology*, 17(8):R57, 2006. URL http://iopscience.iop.org/0957-4484/17/8/R01.

[75] Martin Breitschaft. *Elektronische Charakterisierung von $LaAlO_3$-$SrTiO_3$-Grenzflächen mittels Rastertunnelspektroskopie*. PhD thesis, Universität Augsburg, Augsburg, 2011. URL http://opus.bibliothek.uni-augsburg.de/opus4/frontdoor/index/index/docId/1474.

[76] Förg, Benjamin. "Oxidische Feldeffekttransistoren mit Drain-Source-Kanälen aus zweidimensionalen Elektronensystemen". Masterarbeit, Institut für Physik, Augsburg, March 2012. URL http://pc210ep6.physik.uni-augsburg.de/LitDBPDF/3068-Masterarbeit_I.pdf.

[77] C. W. Schneider, M. Esposito, I. Marozau, K. Conder, M. Doebeli, Yi Hu, M. Mallepell, A. Wokaun, and T. Lippert. "The origin of oxygen in oxide thin films: Role of the substrate". *Applied Physics Letters*, 97(19):192107, November 2010. ISSN 00036951. doi: 10.1063/1.3515849. URL http://apl.aip.org/resource/1/applab/v97/i19/p192107_s1.

[78] F. C. Frank and J. H. van der Merwe. "One-Dimensional Dislocations. I. Static Theory". *Proceedings of the Royal Society of London. Series A. Mathematical and Physical Sciences*, 198 (1053):205–216, August 1949. ISSN 1364-5021, 1471-2946. doi: 10.1098/rspa.1949.0095. URL http://rspa.royalsocietypublishing.org/content/198/1053/205.

[79] H. M. Christen and G. Eres. "Recent advances in pulsed-laser deposition of complex oxides". *Journal of Physics: Condensed Matter*, 20(26):264005, July 2008. ISSN 0953-8984, 1361-648X. doi: 10.1088/0953-8984/20/26/264005. URL http://iopscience.iop.org/0953-8984/20/26/264005.

[80] AIR LIQUIDE Deutschland GmbH. "Air Liquide - Sauerstoff N60 - Unser Gas", 2012. URL http://www.airliquide.de/loesungen/produkte/gase/gasekatalog/stoffe/sauerstoffn60.html.

[81] M. Huijben, G. Koster, H. J. A. Molegraaf, M. K. Kruize, S. Wenderich, J. E. Kleibeuker, A. McCollam, V. K. Guduru, A. Brinkman, H. Hilgenkamp, U. Zeitler, J. C. Maan, D. H. A. Blank, and G. Rijnders. "High mobility interface electron gas by defect scavenging in a modulation doped oxide heterostructure". *arXiv:1008.1896*, August 2010. URL http://arxiv.org/abs/1008.1896.

[82] A. McCollam, S. Wenderich, M. K. Kruize, V. K. Guduru, H. J. A. Molegraaf, M. Huijben, G. Koster, D. H. A. Blank, G. Rijnders, A. Brinkman, H. Hilgenkamp, U. Zeitler, and J. C. Maan. "Quantum oscillations and subband properties of the two-dimensional electron gas at the $LaAlO_3/SrTiO_3$ interface". *arXiv:1207.7003*, July 2012. URL http://arxiv.org/abs/1207.7003.

[83] R. Pentcheva, M. Huijben, K. Otte, W. E. Pickett, J. E. Kleibeuker, J. Huijben, H. Boschker, D. Kockmann, W. Siemons, G. Koster, H. J. W. Zandvliet, G. Rijnders, D. H. A. Blank, H. Hilgenkamp, and A. Brinkman. "Parallel Electron-Hole Bilayer Conductivity from Electronic Interface Reconstruction". *Physical Review Letters*, 104(16):166804, April 2010. doi: 10.1103/PhysRevLett.104.166804. URL http://link.aps.org/doi/10.1103/PhysRevLett.104.166804.

[84] Rémi Arras, Victor G. Ruiz, Warren E. Pickett, and Rossitza Pentcheva. "Tuning the two-dimensional electron gas at the $LaAlO_3/SrTiO_3(001)$ interface by metallic contacts". *Physical Review B*, 85(12):125404, March 2012. doi: 10.1103/PhysRevB.85.125404. URL http://link.aps.org/doi/10.1103/PhysRevB.85.125404.

[85] Ivar Giaever. "Electron tunneling and superconductivity". *Reviews of Modern Physics*, 46(2):245–250, April 1974. doi: 10.1103/RevModPhys.46.245. URL http://link.aps.org/doi/10.1103/RevModPhys.46.245.

[86] J. Bardeen, L. N. Cooper, and J. R. Schrieffer. "Theory of Superconductivity". *Physical Review*, 108(5):1175–1204, December 1957. doi: 10.1103/PhysRev.108.1175. URL http://link.aps.org/doi/10.1103/PhysRev.108.1175.

[87] R. C. Dynes, V. Narayanamurti, and J. P. Garno. "Direct Measurement of Quasiparticle-Lifetime Broadening in a Strong-Coupled Superconductor". *Physical Review Letters*, 41(21):1509–1512, November 1978. doi: 10.1103/PhysRevLett.41.1509. URL http://link.aps.org/doi/10.1103/PhysRevLett.41.1509.

[88] A. D. Caviglia, S. Gariglio, N. Reyren, D. Jaccard, T. Schneider, M. Gabay, S. Thiel, G. Hammerl, J. Mannhart, and J.-M. Triscone. "Electric field control of the $LaAlO_3/SrTiO_3$ interface ground state". *Nature*, 456(7222):624–627, December 2008. ISSN 0028-0836. doi: 10.1038/nature07576. URL http://www.nature.com/nature/journal/v456/n7222/full/nature07576.html.

[89] T. Schneider, A. Caviglia, S. Gariglio, N. Reyren, and J.-M. Triscone. "Electrostatically-tuned superconductor-metal-insulator quantum transition at the $LaAlO_3/SrTiO_3$ interface". *Physical Review B*, 79(18), May 2009. ISSN 1098-0121, 1550-235X. doi: 10.1103/PhysRevB.79.184502. URL http://link.aps.org/doi/10.1103/PhysRevB.79.184502.

[90] J M Kosterlitz and D J Thouless. "Ordering, metastability and phase transitions in two-dimensional systems". *Journal of Physics C: Solid State Physics*, 6(7):1181–1203, April 1973. ISSN 0022-3719. doi: 10.1088/0022-3719/6/7/010. URL http://iopscience.iop.org/0022-3719/6/7/010.

[91] M. R. Beasley, J. E. Mooij, and T. P. Orlando. "Possibility of Vortex-Antivortex Pair Dissociation in Two-Dimensional Superconductors". *Physical Review Letters*, 42(17):1165–1168, April 1979.

doi: 10.1103/PhysRevLett.42.1165. URL http://link.aps.org/doi/10.1103/PhysRevLett.42.1165.

[92] W. W. Warren, R. E. Walstedt, G. F. Brennert, R. J. Cava, R. Tycko, R. F. Bell, and G. Dabbagh. "Cu spin dynamics and superconducting precursor effects in planes above T_c in $YBa_2Cu_3O_{6.7}$". *Physical Review Letters*, 62(10):1193–1196, March 1989. doi: 10.1103/PhysRevLett.62.1193. URL http://link.aps.org/doi/10.1103/PhysRevLett.62.1193.

[93] Tom Timusk and Bryan Statt. "The pseudogap in high-temperature superconductors: an experimental survey". *Reports on Progress in Physics*, 62(1):61, 1999. doi: http://dx.doi.org/10.1088/0034-4885/62/1/002. URL http://stacks.iop.org/0034-4885/62/i=1/a=002.

[94] Benjamin Sacépé, Claude Chapelier, Tatyana I. Baturina, Valerii M. Vinokur, Mikhail R. Baklanov, and Marc Sanquer. "Pseudogap in a thin film of a conventional superconductor". *Nature Communications*, 1:140, 2010. doi: 10.1038/ncomms1140. URL http://dx.doi.org/10.1038/ncomms1140.

[95] X. T. Wu and R. Ikeda. "Pseudogap phase in strongly disordered conventional superconductors". *Phys. Rev. B*, 83(10):104517, Mar 2011. doi: 10.1103/PhysRevB.83.104517. URL http://prb.aps.org/abstract/PRB/v83/i10/e104517.

[96] Mintu Mondal, Anand Kamlapure, Madhavi Chand, Garima Saraswat, Sanjeev Kumar, John Jesudasan, L. Benfatto, Vikram Tripathi, and Pratap Raychaudhuri. "Phase Fluctuations in a Strongly Disordered *s*-Wave NbN Superconductor Close to the Metal-Insulator Transition". *Phys. Rev. Lett.*, 106(4):047001, Jan 2011. doi: 10.1103/PhysRevLett.106.047001. URL http://prl.aps.org/abstract/PRL/v106/i4/e047001.

[97] Michael Feld, Bernd Fröhlich, Enrico Vogt, Marco Koschorreck, and Michael Köhl. "Observation of a pairing pseudogap in a two-dimensional Fermi gas". *Nature*, 480(7375):75–78, December 2011. ISSN 0028-0836. doi: 10.1038/nature10627. URL http://www.nature.com/nature/journal/v480/n7375/full/nature10627.html?WT.ec_id=NATURE-20111201.

[98] M. R. Norman, D. Pines, and C. Kallin. "The pseudogap: friend or foe of high T_c?". *Advances in Physics*, 54(8):715–733, December 2005. ISSN 0001-8732, 1460-6976. doi: 10.1080/00018730500459906. URL http://www.tandfonline.com/doi/abs/10.1080/00018730500459906.

[99] S Hüfner, M A Hossain, A Damascelli, and G A Sawatzky. "Two gaps make a high-temperature superconductor?". *Reports on Progress in Physics*, 71(6):062501, June 2008. ISSN 0034-4885, 1361-6633. doi: 10.1088/0034-4885/71/6/062501. URL http://iopscience.iop.org/0034-4885/71/6/062501.

[100] Chandra Varma. "High-temperature superconductivity: Mind the pseudogap". *Nature*, 468 (7321):184–185, November 2010. ISSN 0028-0836. doi: 10.1038/468184a. URL http://www.nature.com/nature/journal/v468/n7321/full/468184a.html.

[101] P. W. Anderson. "The resonating valence bond state in La_2CuO_4 and superconductivity". *science*, 235(4793):1196–1198, 1987. URL http://www.sciencemag.org/content/235/4793/1196.short.

[102] T Schneider. "On the occurrence of Berezinskii-Kosterlitz-Thouless behavior in highly anisotropic cuprate superconductors". *Europhysics Letters (EPL)*, 78(4):47003, May 2007. ISSN 0295-5075, 1286-4854. doi: 10.1209/0295-5075/78/47003. URL http://stacks.iop.org/0295-5075/78/i=4/a=47003?key=crossref.1930104a1f128d6548248ee0adfd5278.

[103] J. Mannhart, J. G. Bednorz, K. A. Müller, and D. G. Schlom. "Electric field effect on superconducting $YBa_2Cu_3O_{7-\delta}$ films". *Zeitschrift für Physik B Condensed Matter*, 83(3):307–311, 1991. ISSN 0722-3277. doi: 10.1007/BF01313398. URL http://www.springerlink.com/content/nr6017254007458g/abstract/.

[104] Anoop Singh Dhoot, Stuart C. Wimbush, Tim Benseman, Judith L. MacManus-Driscoll, J. R. Cooper, and Richard Henry Friend. "Increased T_c in Electrolyte-Gated Cuprates". *Advanced Materials*, 22(23):2529–2533, 2010. ISSN 1521-4095. doi: 10.1002/adma.200904024. URL http://dx.doi.org/10.1002/adma.200904024.

[105] Xiang Leng, Javier Garcia-Barriocanal, Boyi Yang, Yeonbae Lee, J. Kinney, and A. M. Goldman. "Indications of an Electronic Phase Transition in Two-Dimensional Superconducting $YBa_2Cu_3O_{7-x}$ Thin Films Induced by Electrostatic Doping". *Phys. Rev. Lett.*, 108:067004, Feb 2012. doi: 10.1103/PhysRevLett.108.067004. URL http://link.aps.org/doi/10.1103/PhysRevLett.108.067004.

[106] A. T. Bollinger, G. Dubuis, J. Yoon, D. Pavuna, J. Misewich, and I. Božović. "Superconductor–insulator transition in $La_{2-x}Sr_xCuO_4$ at the pair quantum resistance". *Nature*, 472 (7344):458–460, April 2011. ISSN 0028-0836, 1476-4687. doi: 10.1038/nature09998. URL http://www.nature.com/doifinder/10.1038/nature09998.

[107] Julie A. Bert, Katja C. Nowack, Beena Kalisky, Hilary Noad, John R. Kirtley, Chris Bell, Hiroki K. Sato, Masayuki Hosoda, Yasayuki Hikita, Harold Y. Hwang, and Kathryn A. Moler. "Measurements of the gate tuned superfluid density in superconducting $LaAlO_3/SrTiO_3$". *arXiv:1205.4064*, May 2012. URL http://arxiv.org/abs/1205.4064.

[108] A. D. Caviglia, M. Gabay, S. Gariglio, N. Reyren, C. Cancellieri, and J.-M. Triscone. "Tunable Rashba Spin-Orbit Interaction at Oxide Interfaces". *Physical Review Letters*, 104(12):126803, March 2010. doi: 10.1103/PhysRevLett.104.126803. URL http://link.aps.org/doi/10.1103/PhysRevLett.104.126803.

[109] Mikhael Yu. Kupriyanov and V. F. Lukichev. "Temperature Dependence of Pair-breaking Current in Superconductors". *Fiz. Nizk. Temp.*, 6(4):445–453, 1980.

[110] Satoshi Fujimoto. "Topological order and non-Abelian statistics in noncentrosymmetric s-wave superconductors". *Phys. Rev. B*, 77:220501, Jun 2008. doi: 10.1103/PhysRevB.77.220501. URL http://link.aps.org/doi/10.1103/PhysRevB.77.220501.

[111] K. Flensberg. "Tunneling characteristics of a chain of Majorana bound states". *Physical Review B*, 82(18):180516, 2010. URL http://prb.aps.org/abstract/PRB/v82/i18/e180516.

[112] Y. Maeno, H. Hashimoto, K. Yoshida, S. Nishizaki, T. Fujita, J. G. Bednorz, and F. Lichtenberg. "Superconductivity in a layered perovskite without copper". *Nature*, 372(6506):532–534, December 1994. doi: 10.1038/372532a0. URL http://www.nature.com/nature/journal/v372/n6506/abs/372532a0.html.

[113] G. M. Luke, Y. Fudamoto, K. M. Kojima, M. I. Larkin, J. Merrin, B. Nachumi, Y. J. Uemura, Y. Maeno, Z. Q. Mao, Y. Mori, H. Nakamura, and M. Sigrist. "Time-reversal symmetry-breaking superconductivity in Sr_2RuO_4". *Nature*, 394(6693):558–561, August 1998. ISSN 0028-0836. doi: 10.1038/29038. URL http://dx.doi.org/10.1038/29038.

[114] Yoshiteru Maeno, T. Maurice Rice, and Manfred Sigrist. "The Intriguing Superconductivity of Strontium Ruthenate". *Physics Today*, 54(1):42, 2001. ISSN 00319228. doi: 10.1063/1.1349611. URL http://link.aip.org/link/PHTOAD/v54/i1/p42/s1&Agg=doi.

[115] H Suderow, V Crespo, I Guillamon, S Vieira, F Servant, P Lejay, J P Brison, and J Flouquet. "A nodeless superconducting gap in Sr_2RuO_4 from tunneling spectroscopy". *New Journal of Physics*, 11(9):093004, September 2009. ISSN 1367-2630. doi: 10.1088/1367-2630/11/9/093004. URL http://iopscience.iop.org/1367-2630/11/9/093004.

[116] S. Kashiwaya, H. Kashiwaya, H. Kambara, T. Furuta, H. Yaguchi, Y. Tanaka, and Y. Maeno. "Edge States of Sr_2RuO_4 Detected by In-Plane Tunneling Spectroscopy". *Physical review letters*, 107(7):77003, 2011. URL http://link.aps.org/doi/10.1103/PhysRevLett.107.077003.

[117] K. Ishida, H. Mukuda, Y. Kitaoka, K. Asayama, Z. Q. Mao, Y. Mori, and Y. Maeno. "Spin-triplet superconductivity in Sr_2RuO_4 identified by ^{17}O Knight shift". *Nature*, 396(6712):658–660, December 1998. ISSN 0028-0836. doi: 10.1038/25315. URL http://www.nature.com/nature/journal/v396/n6712/full/396658a0.html.

[118] A. P. Mackenzie, R. K. W. Haselwimmer, A. W. Tyler, G. G. Lonzarich, Y. Mori, S. Nishizaki, and Y. Maeno. "Extremely Strong Dependence of Superconductivity on Disorder in Sr_2RuO_4". *Physical Review Letters*, 80(1):161–164, January 1998. doi: 10.1103/PhysRevLett.80.161. URL http://link.aps.org/doi/10.1103/PhysRevLett.80.161.

[119] Keiji Yada, Seiichiro Onari, Yukio Tanaka, and Jun-ichiro Inoue. "Electrically controlled superconducting states at the heterointerface $SrTiO_3/LaAlO_3$". *Physical Review B*, 80(14), October 2009. ISSN 1098-0121, 1550-235X. doi: 10.1103/PhysRevB.80.140509. URL http://link.aps.org/doi/10.1103/PhysRevB.80.140509.

[120] Karen Michaeli, Andrew C. Potter, and Patrick A. Lee. "Superconducting and Ferromagnetic Phases in $SrTiO_3/LaAlO_3$ Oxide Interface Structures: Possibility of Finite Momentum Pairing". *Physical Review Letters*, 108(11), March 2012. ISSN 0031-9007, 1079-7114. doi: 10.1103/PhysRevLett.108.117003. URL http://link.aps.org/doi/10.1103/PhysRevLett.108.117003.

[121] Florian Loder, Arno P. Kampf, and Thilo Kopp. "Superconductivity with Rashba Spin-Orbit Coupling and Magnetic Field". *arXiv:1206.1816*, June 2012. URL http://arxiv.org/abs/1206.1816.

[122] R. A. Hein, J. W. Gibson, B. T. Matthias, T. H. Geballe, and E. Corenzwit. "Superconductivity of Iridium". *Physical Review Letters*, 8(10):408–410, May 1962. doi: 10.1103/PhysRevLett.8.408. URL http://link.aps.org/doi/10.1103/PhysRevLett.8.408.

[123] Bernd T. Matthias, Zachary Fisk, David C. Johnston, and Robert N. Shelton. "High Temperature Superconductivity: A Metallurgical Approach". Technical Report Summer 1980, Los Alamos National Laboratory, February 1978. URL www.fas.org/sgp/othergov/doe/lanl/pubs/00818095.pdf.

[124] John G. Simmons. "Electric Tunnel Effect between Dissimilar Electrodes Separated by a Thin Insulating Film". *Journal of Applied Physics*, 34(9):2581–2590, September 1963. ISSN 00218979. doi: 10.1063/1.1729774. URL http://jap.aip.org/resource/1/japiau/v34/i9/p2581_s1.

[125] R.M. Feenstra, Joseph A. Stroscio, and A.P. Fein. "Tunneling spectroscopy of the Si(111)2 × 1 surface". *Surface Science*, 181(1–2):295–306, March 1987. ISSN 0039-6028. doi: 10.1016/0039-6028(87)90170-1. URL http://www.sciencedirect.com/science/article/pii/0039602887901701.

[126] C. Julian Chen. "Theory of scanning tunneling spectroscopy". *Journal of Vacuum Science Technology A: Vacuum, Surfaces, and Films*, 6(2):319 –322, March 1988. ISSN 0734-2101. doi: 10.1116/1.575444.

[127] D. Tenne, I. Gonenli, A. Soukiassian, D. Schlom, S. Nakhmanson, K. Rabe, and X. Xi. "Raman study of oxygen reduced and re-oxidized strontium titanate". *Physical Review B*, 76(2), July 2007. ISSN 1098-0121, 1550-235X. doi: 10.1103/PhysRevB.76.024303. URL http://link.aps.org/doi/10.1103/PhysRevB.76.024303.

[128] D. Nuzhnyy, J. Petzelt, S. Kamba, T. Yamada, M. Tyunina, A. Tagantsev, J. Levoska, and N. Setter. "Polar phonons in some compressively stressed epitaxial and polycrystalline $SrTiO_3$ thin films". *Journal of Electroceramics*, 22(1):297–301, 2009. ISSN 1385-3449. doi: 10.1007/s10832-008-9494-2. URL http://www.springerlink.com/content/t8183715n5782001/abstract/.

[129] Wilfried Wunderlich. "Phonons in $SrTiO_3$ analyzed by difference bond-length spectrum". *arXiv:0711.0567*, November 2007. doi: 10.1016/j.sse.2008.03.017. URL http://arxiv.org/abs/0711.0567. Solid-State Electronics, 52 (2008) 1082-1087.

[130] G. Shirane and Y. Yamada. "Lattice-Dynamical Study of the 110°K Phase Transition in $SrTiO_3$". *Physical Review*, 177(2):858–863, January 1969. ISSN 0031-899X, 1536-6065. doi: 10.1103/PhysRev.177.858. URL http://link.aps.org/doi/10.1103/PhysRev.177.858.

[131] Narayani Choudhury, Eric Walter, Alexander Kolesnikov, and Chun-Keung Loong. "Large phonon band gap in $SrTiO_3$ and the vibrational signatures of ferroelectricity in $ATiO_3$ perovskites: First-principles lattice dynamics and inelastic neutron scattering". *Physical Review B*, 77(13), April 2008. ISSN 1098-0121, 1550-235X. doi: 10.1103/PhysRevB.77.134111. URL http://link.aps.org/doi/10.1103/PhysRevB.77.134111.

[132] J. L. Servoin, Y. Luspin, and F. Gervais. "Infrared dispersion in $SrTiO_3$ at high temperature". *Physical Review B*, 22(11):5501–5506, 1980. doi: 10.1103/PhysRevB.22.5501. URL http://link.aps.org/doi/10.1103/PhysRevB.22.5501.

[133] H. Vogt. "Hyper-Raman tensors of the zone-center optical phonons in $SrTiO_3$ and $KTaO_3$". *Physical Review B*, 38(8):5699–5708, 1988. doi: 10.1103/PhysRevB.38.5699. URL http://link.aps.org/doi/10.1103/PhysRevB.38.5699.

[134] W. Zhong, R. D. King-Smith, and David Vanderbilt. "Giant LO-TO splittings in perovskite ferroelectrics". *Physical Review Letters*, 72(22):3618–3621, 1994. doi: 10.1103/PhysRevLett.72.3618. URL http://link.aps.org/doi/10.1103/PhysRevLett.72.3618.

[135] Chris Lasota, Cheng-Zhang Wang, Rici Yu, and Henry Krakauer. "Ab initio linear response study of $SrTiO_3$". *Ferroelectrics*, 194(1):109–118, April 1997. ISSN 0015-0193, 1563-5112. doi: 10.1080/00150199708016086. URL http://www.tandfonline.com/doi/abs/10.1080/00150199708016086.

[136] A. I. Lebedev. "Ab initio calculations of phonon spectra in $ATiO_3$ perovskite crystals (A = Ca, Sr, Ba, Ra, Cd, Zn, Mg, Ge, Sn, Pb)". *Physics of the Solid State*, 51(2):362–372, February 2009. ISSN 1063-7834, 1090-6460. doi: 10.1134/S1063783409020279. URL http://www.springerlink.com/index/10.1134/S1063783409020279.

[137] R. A. Cowley. "Lattice Dynamics and Phase Transitions of Strontium Titanate". *Physical Review*, 134(4A):A981–A997, 1964. doi: 10.1103/PhysRev.134.A981. URL http://link.aps.org/doi/10.1103/PhysRev.134.A981.

[138] Wikipedia. "Oxygen — Wikipedia, The Free Encyclopedia", 2012. URL http://en.wikipedia.org/w/index.php?title=Oxygen&oldid=506162892. [Online; accessed 11-August-2012].

[139] J. Lambe and R. C. Jaklevic. "Molecular Vibration Spectra by Inelastic Electron Tunneling". *Physical Review*, 165(3):821–832, January 1968. doi: 10.1103/PhysRev.165.821. URL http://link.aps.org/doi/10.1103/PhysRev.165.821.

[140] D. J. Scalapino and S. M. Marcus. "Theory of Inelastic Electron-Molecule Interactions in Tunnel Junctions". *Physical Review Letters*, 18(12):459–461, March 1967. doi: 10.1103/PhysRevLett.18.459. URL http://link.aps.org/doi/10.1103/PhysRevLett.18.459.

[141] E L Wolf. "Electron tunnelling spectroscopy". *Reports on Progress in Physics*, 41(9):1439–1508, September 1978. ISSN 0034-4885, 1361-6633. doi: 10.1088/0034-4885/41/9/002. URL http://iopscience.iop.org/0034-4885/41/9/002.

[142] Wikipedia contributors. "Inelastic electron tunneling spectroscopy", July 2012. URL http://en.wikipedia.org/w/index.php?title=Inelastic_electron_tunneling_spectroscopy&oldid=456754019. Page Version ID: 456754019.

[143] Won-joon Son, Eunae Cho, Bora Lee, Jaichan Lee, and Seungwu Han. "Density and spatial distribution of charge carriers in the intrinsic n-type $LaAlO_3$-$SrTiO_3$ interface". *Physical Review B*, 79(24):245411, June 2009. doi: 10.1103/PhysRevB.79.245411. URL http://link.aps.org/doi/10.1103/PhysRevB.79.245411.

[144] Ariando, X. Wang, G. Baskaran, Z. Q. Liu, J. Huijben, J. B. Yi, A. Annadi, A. Roy Barman, A. Rusydi, S. Dhar, Y. P. Feng, J. Ding, H. Hilgenkamp, and T. Venkatesan. "Electronic phase separation at the $LaAlO_3$/$SrTiO_3$ interface". *Nature Communications*, 2:188, February 2011. ISSN 2041-1723. doi: 10.1038/ncomms1192. URL http://www.nature.com/ncomms/journal/v2/n2/full/ncomms1192.html.

[145] Manan Mehta, Dimitry Dikin, Chung Wung Bark, Chad Folkman, Chang-Beom Eom, and Venkat Chandrasekhar. "Hysteretic magneto-resistance at the $LaAlO_3$-$SrTiO_3$ interface - interplay between superconducting and ferromagnetic properties". In *Bulletin of the American Physical Society*, volume Volume 56, Number 1. American Physical Society, March 2011. URL http://meetings.aps.org/link/BAPS.2011.MAR.A34.12.

[146] D. Dikin, M. Mehta, C. Bark, C. Folkman, C. Eom, and V. Chandrasekhar. "Coexistence of Superconductivity and Ferromagnetism in Two Dimensions". *Physical Review Letters*, 107(5), July 2011. ISSN 0031-9007, 1079-7114. doi: 10.1103/PhysRevLett.107.056802. URL http://link.aps.org/doi/10.1103/PhysRevLett.107.056802.

[147] Andrew J. Millis. "Oxide interfaces: Moment of magnetism". *Nature Physics*, 7(10):749–750, 2011. ISSN 1745-2473. doi: 10.1038/nphys2087. URL http://www.nature.com/nphys/journal/v7/n10/full/nphys2087.html?WT.ec_id=NPHYS-201110.

[148] Julie A. Bert, Beena Kalisky, Christopher Bell, Minu Kim, Yasuyuki Hikita, Harold Y. Hwang, and Kathryn A. Moler. "Direct imaging of the coexistence of ferromagnetism and superconductivity at the $LaAlO_3$/$SrTiO_3$ interface". *Nature Physics*, 7(10):767–771, September 2011. ISSN 1745-2473, 1745-2481. doi: 10.1038/nphys2079. URL http://www.nature.com/doifinder/10.1038/nphys2079.

[149] Peter Fulde and Richard A. Ferrell. "Superconductivity in a Strong Spin-Exchange Field". *Physical Review*, 135(3A):A550–A563, August 1964. doi: 10.1103/PhysRev.135.A550. URL http://link.aps.org/doi/10.1103/PhysRev.135.A550.

[150] A. I. Larkin and Yu. N. Ovchinnikov. "Inhomogeneous State of Superconductors". *Sov. Phys. JETP*, 20:762, 1965.

[151] Yuji Matsuda and Hiroshi Shimahara. "Fulde–Ferrell–Larkin–Ovchinnikov State in Heavy Fermion Superconductors". *Journal of the Physical Society of Japan*, 76(5):051005, 2007. doi: 10.1143/JPSJ.76.051005. URL http://jpsj.ipap.jp/link?JPSJ/76/051005/.

[152] J.-H. Park, E. Vescovo, H.-J. Kim, C. Kwon, R. Ramesh, and T. Venkatesan. "Direct evidence for a half-metallic ferromagnet". *Nature*, 392(6678):794–796, April 1998. ISSN 0028-0836. doi: 10.1038/33883. URL http://www.nature.com/nature/journal/v392/n6678/abs/392794a0.html.

[153] L. Fidkowski, H. C. Jiang, R. M. Lutchyn, and C. Nayak. "Magnetic and Superconducting Ordering at $LaAlO_3/SrTiO_3$ Interfaces". *arXiv preprint arXiv:1206.6959*, 2012. URL http://arxiv.org/abs/1206.6959.

[154] Joshua P. Veazey, Guanglei Cheng, Patrick Irvin, Cheng Cen, Daniela F. Bogorin, Feng Bi, Mengchen Huang, Chung-Wung Bark, Sangwoo Ryu, Kwang-Hwan Cho, Chang-Beom Eom, and Jeremy Levy. "Superconducting $LaAlO_3/SrTiO_3$ Nanowires". *arXiv:1210.3606*, October 2012. URL http://arxiv.org/abs/1210.3606.

[155] Thilo Kopp and Jochen Mannhart. "Calculation of the capacitances of conductors: Perspectives for the optimization of electronic devices". *Journal of Applied Physics*, 106(6):064504–064504–15, September 2009. ISSN 00218979. doi: 10.1063/1.3197246. URL http://jap.aip.org/resource/1/japiau/v106/i6/p064504_s1.

[156] Judith Leese. "Untersuchung des elektrischen Widerstandes zwischen dem Elektronengas an $LaAlO_3/SrTiO_3$ Grenzflächen und verschiedenen Kontaktmaterialien". Masterarbeit, Institut für Physik, Augsburg, Germany, 2009.

[157] Pfanzelt, Georg. "Verwendung ferroelektrischer $BaTiO_3$-Filme zum Schalten eines zweidimensionalen Elektronensystems". Masterarbeit, Institut für Physik, Augsburg, November 2011.

[158] J. W. Park, D. F. Bogorin, C. Cen, D. A. Felker, Y. Zhang, C. T. Nelson, C. W. Bark, C. M. Folkman, X. Q. Pan, M. S. Rzchowski, J. Levy, and C. B. Eom. "Creation of a two-dimensional electron gas at an oxide interface on silicon". *Nature Communications*, 1:94, October 2010. ISSN 2041-1723. doi: 10.1038/ncomms1096. URL http://www.nature.com/ncomms/journal/v1/n7/abs/ncomms1096.html.

[159] Božidar Mitrović and Lee A Rozema. "On the correct formula for the lifetime broadened superconducting density of states". *Journal of Physics: Condensed Matter*, 20(1):015215, January 2008. ISSN 0953-8984, 1361-648X. doi: 10.1088/0953-8984/20/01/015215. URL http://stacks.iop.org/0953-8984/20/i=1/a=015215?key=crossref.6d894e91c42ff0d67563fbce9df33fd7.

[160] Bin Liu and Xiao Hu. "Local electronic structure of the superconducting interface $LaAlO_3/SrTiO_3$". *Physical Review B*, 81(14), April 2010. ISSN 1098-0121, 1550-235X. doi: 10.1103/PhysRevB.81.144504. URL http://link.aps.org/doi/10.1103/PhysRevB.81.144504.

[161] Y. Hotta, T. Susaki, and H. Y. Hwang. "Polar Discontinuity Doping of the $LaVO_3/SrTiO_3$ Interface". *Physical Review Letters*, 99(23):236805, December 2007. doi: 10.1103/PhysRevLett.99.236805. URL http://link.aps.org/doi/10.1103/PhysRevLett.99.236805.

[162] S. Miyasaka, T. Okuda, and Y. Tokura. "Critical Behavior of Metal-Insulator Transition in $La_{1-x}Sr_xVO_3$". *Phys. Rev. Lett.*, 85:5388–5391, Dec 2000. doi: 10.1103/PhysRevLett.85.5388. URL http://link.aps.org/doi/10.1103/PhysRevLett.85.5388.

[163] Masashige Onoda, Hiroshi Ohta, and Hiroshi Nagasawa. "Metallic properties of perovskite oxide $SrVO_3$". *Solid State Communications*, 79(4):281 – 285, 1991. ISSN 0038-1098. doi: 10.1016/0038-1098(91)90546-8. URL http://www.sciencedirect.com/science/article/pii/0038109891905468.

[164] F. S. Razavi, S. Jamali Gharetape, D. A. Crandles, G. Christiani, R. K. Kremer, and H.-U. Habermeier. "Evidence for random networks of diodes in thin films of $LaVO_3$ on $SrTiO_3$ substrates". *Applied Physics Letters*, 96(4):042110, 2010. ISSN 00036951. doi: 10.1063/1.3293439. URL http://link.aip.org/link/APPLAB/v96/i4/p042110/s1&Agg=doi.

[165] Y. Hotta, Y. Mukunoki, T. Susaki, H. Y. Hwang, L. Fitting, and D. A. Muller. "Growth and epitaxial structure of $LaVO_x$ films". *Applied Physics Letters*, 89(3):031918, 2006. doi: 10.1063/1.2227786. URL http://link.aip.org/link/?APL/89/031918/1.

[166] N.H. Hur, S.H. Kim, K.S. Yu, Y.K. Park, J.C. Park, and S.J. Kim. "Structural and magnetic properties of the anion-deficient $LaVO_{3-\delta}$". *Solid State Communications*, 92(6):541 – 546, 1994. ISSN 0038-1098. doi: 10.1016/0038-1098(94)90494-4. URL http://www.sciencedirect.com/science/article/pii/0038109894904944.

[167] P. Perna, D. Maccariello, M. Radovic, U. Scotti di Uccio, I. Pallecchi, M. Codda, D. Marré, C. Cantoni, J. Gazquez, M. Varela, S. J. Pennycook, and F. Miletto Granozio. "Conducting interfaces between band insulating oxides: The $LaGaO_3/SrTiO_3$ heterostructure". *Applied Physics Letters*, 97(15):152111, October 2010. ISSN 00036951. doi: 10.1063/1.3496440. URL http://apl.aip.org/resource/1/applab/v97/i15/p152111_s1.

[168] D. C. Dube, H. J. Scheel, I. Reaney, M. Daglish, and N. Setter. "Dielectric properties of lanthanum gallate ($LaGaO_3$) crystal". *Journal of Applied Physics*, 75(8):4126–4130, 1994. doi: 10.1063/1.355993. URL http://link.aip.org/link/?JAP/75/4126/1.

[169] S. Nazir, N. Singh, and U. Schwingenschlögl. "The metallic interface between the two band insulators $LaGaO_3$ and $SrTiO_3$". *Applied Physics Letters*, 98(26):262104, June 2011. ISSN 00036951. doi: 10.1063/1.3604020. URL http://apl.aip.org/resource/1/applab/v98/i26/p262104_s1.

[170] D. F. Li, Yan Wang, and J. Y. Dai. "Tunable electronic transport properties of $DyScO_3/SrTiO_3$ polar heterointerface". *Applied Physics Letters*, 98(12):122108, March 2011. ISSN 00036951. doi: 10.1063/1.3570694. URL http://apl.aip.org/resource/1/applab/v98/i12/p122108_s1.

[171] Martina Luysberg, Markus Heidelmann, Lothar Houben, Markus Boese, Tassilo Heeg, Jürgen Schubert, and Martin Roeckerath. "Intermixing and charge neutrality at $DyScO_3/SrTiO_3$ interfaces". *Acta Materialia*, 57(11):3192–3198, June 2009. ISSN 13596454. doi: 10.1016/j.actamat.2009.03.031. URL http://linkinghub.elsevier.com/retrieve/pii/S1359645409001736.

[172] H. Amid, R. Ambo, P. MacDonald, S. Lettich, and S. Stallone. "Blue luminescence in organic polymers", July 1988. URL http://www.youtube.com/watch?v=sQwenCfM6t0&feature=youtube_gdata_player.

[173] Alexey Kalabukhov, Robert Gunnarsson, Johan Börjesson, Eva Olsson, Tord Claeson, and Dag Winkler. "Effect of oxygen vacancies in the $SrTiO_3$ substrate on the electrical properties of the $LaAlO_3/SrTiO_3$ interface". *Physical Review B*, 75(12):121404, 2007. doi: 10.1103/PhysRevB.75.121404. URL http://link.aps.org/doi/10.1103/PhysRevB.75.121404.

[174] S. Gariglio, Marco Salluzzo, Zoran Ristic, Xavier Torrelles, Roberto Felici, and Claudia Cancellieri. "Investigation of non-conducting polar oxide interfaces by GXID measurements". Technical report, ESRF, Grenoble, March 2011. URL http://ftp.esrf.eu/pub/UserReports/43649_A.pdf.

[175] Pouya Moetakef, Jack Y. Zhang, Alexander Kozhanov, Bharat Jalan, Ram Seshadri, S. James Allen, and Susanne Stemmer. "Transport in ferromagnetic $GdTiO_3/SrTiO_3$ heterostructures". *Applied Physics Letters*, 98(11):112110, March 2011. ISSN 00036951. doi: 10.1063/1.3568894. URL http://apl.aip.org/resource/1/applab/v98/i11/p112110_s1.

[176] Bharat Jalan, Roman Engel-Herbert, Nicholas J. Wright, and Susanne Stemmer. "Growth of high-quality $SrTi_3$ films using a hybrid molecular beam epitaxy approach". *Journal of Vacuum Science & Technology A: Vacuum, Surfaces, and Films*, 27(3):461, 2009. ISSN 07342101. doi: 10.1116/1.3106610. URL http://link.aip.org/link/JVTAD6/v27/i3/p461/s1&Agg=doi.

[177] Pouya Moetakef, Tyler A. Cain, Daniel G. Ouellette, Jack Y. Zhang, Dmitri O. Klenov, Anderson Janotti, Chris G. Van de Walle, Siddharth Rajan, S. James Allen, and Susanne Stemmer. "Electrostatic carrier doping of $GdTiO_3/SrTiO_3$ interfaces". *Applied Physics Letters*, 99(23):232116, December 2011. ISSN 00036951. doi: 10.1063/1.3669402. URL http://apl.aip.org/resource/1/applab/v99/i23/p232116_s1.

[178] Umberto Scotti di Uccio, Carmela Aruta, Claudia Cantoni, Emiliano Di Gennaro, Alessandro Gadaleta, Andrew R. Lupini, Davide Maccariello, Daniele Marré, Ilaria Pallecchi, Domenico Paparo, Paolo Perna, Muhammad Riaz, and Fabio Miletto Granozio. "Reversible and Persistent Photoconductivity at the $NdGaO_3/SrTiO_3$ Conducting Interface". *arXiv:1206.5083*, June 2012. URL http://arxiv.org/abs/1206.5083.

[179] Fabio Miletto Granozio. "Conducting interfaces between band insulating oxides", 2011. URL http://www.fisica.unisa.it/phpicalendar/print.php?cal=meetings,seminars,spotlights,tuesday&getdate=20110411&printview=day.

[180] F. Gunkel, K. Skaja, A. Shkabko, R. Dittmann, S. Hoffmann-Eifert, and R. Waser. "Stoichiometry dependence and thermal stability of conducting $NdGaO_3/SrTiO_3$ heterointerfaces". *Applied Physics Letters*, 102(7):071601–071601–4, February 2013. ISSN 00036951. doi: 10.1063/1.4792509. URL http://apl.aip.org/resource/1/applab/v102/i7/p071601_s1.

[181] H. W. Jang, D. A. Felker, C. W. Bark, Y. Wang, M. K. Niranjan, C. T. Nelson, Y. Zhang, D. Su, C. M. Folkman, S. H. Baek, S. Lee, K. Janicka, Y. Zhu, X. Q. Pan, D. D. Fong, E. Y. Tsymbal, M. S. Rzchowski, and C. B. Eom. "Metallic and Insulating Oxide Interfaces Controlled by Electronic Correlations". *Science*, 331(6019):886–889, February 2011. ISSN 0036-8075, 1095-9203. doi: 10.1126/science.1198781. URL http://www.sciencemag.org/content/331/6019/886.

[182] Keisuke Shibuya, Tsuyoshi Ohnishi, Mikk Lippmaa, and Masaharu Oshima. "Metallic conductivity at the $CaHfO_3/SrTiO_3$ interface". *Applied Physics Letters*, 91(23):232106, December 2007. ISSN 00036951. doi: 10.1063/1.2816907. URL http://apl.aip.org/resource/1/applab/v91/i23/p232106_s1.

[183] S. A. Chambers, L. Qiao, T. C. Droubay, T. C. Kaspar, B. W. Arey, and P. V. Sushko. "Band Alignment, Built-In Potential, and the Absence of Conductivity at the $LaCrO_3/SrTiO_3(001)$ Heterojunction". *Physical Review Letters*, 107(20):206802, November 2011. doi: 10.1103/PhysRevLett.107.206802. URL http://link.aps.org/doi/10.1103/PhysRevLett.107.206802.

[184] S. Nazir, M. Upadhyay Kahaly, and U. Schwingenschlögl. "High mobility of the strongly confined hole gas in $AgTaO_3/SrTiO_3$". *Applied Physics Letters*, 100(20):201607, May 2012. ISSN 00036951. doi: 10.1063/1.4719106. URL http://apl.aip.org/resource/1/applab/v100/i20/p201607_s1?ver=pdfcov.

[185] S. Nazir, N. Singh, M. Upadhyay Kahaly, and U. Schwingenschlögl. "Role of the electronegativity for the interface properties of non-polar heterostructures". *EPL (Europhysics Letters)*, 98(2):27007, April 2012. ISSN 0295-5075, 1286-4854. doi: 10.1209/0295-5075/98/27007. URL http://iopscience.iop.org/0295-5075/98/27007.

[186] J. D. Burton and E. Y. Tsymbal. "Highly Spin-Polarized Conducting State at the Interface between Nonmagnetic Band Insulators: $LaAlO_3/FeS_2$ (001)". *Phys. Rev. Lett.*, 107:166601, Oct 2011. doi: 10.1103/PhysRevLett.107.166601. URL http://link.aps.org/doi/10.1103/PhysRevLett.107.166601.

[187] A. D. Caviglia, S. Gariglio, C. Cancellieri, B. Sacépé, A. Fête, N. Reyren, M. Gabay, A. F. Morpurgo, and J.-M. Triscone. "Two-Dimensional Quantum Oscillations of the Conductance at $LaAlO_3/SrTiO_3$ Interfaces". *Physical Review Letters*, 105(23):236802, 2010. doi: 10.1103/PhysRevLett.105.236802. URL http://link.aps.org/doi/10.1103/PhysRevLett.105.236802.

[188] M. El Kazzi, C. Merckling, G. Delhaye, L. Arzel, G. Grenet, E. Bergignat, and G. Hollinger. "Photoemission (XPS and XPD) study of epitaxial $LaAlO_3$ film grown on $SrTiO_3$(001)". *Materials Science in Semiconductor Processing*, 9(6):954 – 958, 2006. ISSN 1369-8001. doi: 10.1016/j.mssp.2006.10.044. URL http://www.sciencedirect.com/science/article/pii/S1369800106002320.

[189] C. Merckling, M. El-Kazzi, G. Delhaye, V. Favre-Nicolin, Y. Robach, M. Gendry, G. Grenet, G. Saint-Girons, and G. Hollinger. "Strain relaxation and critical thickness for epitaxial $LaAlO_3$ thin films grown on $SrTiO_3$(001) substrates by molecular beam epitaxy". *Journal of Crystal Growth*, 306(1):47 – 51, 2007. ISSN 0022-0248. doi: 10.1016/j.jcrysgro.2007.04.048. URL http://www.sciencedirect.com/science/article/pii/S0022024807004411.

[190] Y. Segal, J. H. Ngai, J. W. Reiner, F. J. Walker, and C. H. Ahn. "X-ray photoemission studies of the metal-insulator transition in $LaAlO_3/SrTiO_3$ structures grown by molecular beam epitaxy". *Physical Review B*, 80(24):241107, 2009. doi: 10.1103/PhysRevB.80.241107. URL http://link.aps.org/doi/10.1103/PhysRevB.80.241107.

[191] T. C. Droubay, L. Qiao, T. C. Kaspar, M. H. Engelhard, V. Shutthanandan, and S. A. Chambers. "Nonstoichiometric material transfer in the pulsed laser deposition of $LaAlO_3$". *Applied Physics Letters*, 97(12):124105, 2010. ISSN 00036951. doi: 10.1063/1.3487778. URL http://link.aip.org/link/APPLAB/v97/i12/p124105/s1&Agg=doi.

[192] I. M. Dildar, D. B. Boltje, M. H. S. Hesselberth, Q. Xu, H. W. Zandbergen, and S. Harkema. "Conductivity of $LaAlO_3/SrTiO_3$ Interfaces made by Sputter Deposition". *arXiv:1111.5047*, November 2011. URL http://arxiv.org/abs/1111.5047.

[193] L. J. van der Pauw. "A method of measuring specific resistivity and Hall effect of discs of arbitrary shape". *Philips Research Reports*, 13(1):1–9, February 1958.

[194] C. Cancellieri, N. Reyren, S. Gariglio, A. D. Caviglia, A. Fête, and J.-M. Triscone. "Influence of the growth conditions on the $LaAlO_3/SrTiO_3$ interface electronic properties". *EPL (Europhysics Letters)*, 91(1):17004, July 2010. ISSN 0295-5075, 1286-4854. doi: 10.1209/0295-5075/91/17004. URL http://iopscience.iop.org/0295-5075/91/17004.

[195] Jun Zhang, D. Doutt, T. Merz, J. Chakhalian, M. Kareev, J. Liu, and L. J. Brillson. "Depth-resolved subsurface defects in chemically etched $SrTiO_3$". *Applied Physics Letters*, 94(9):092904, 2009. doi: 10.1063/1.3093671. URL http://link.aip.org/link/?APL/94/092904/1.

[196] James N. Eckstein. "Oxide interfaces: Watch out for the lack of oxygen". *Nature Materials*, 6(7):473–474, July 2007. ISSN 1476-1122. doi: 10.1038/nmat1944. URL http://www.nature.com/nmat/journal/v6/n7/full/nmat1944.html.

[197] Wolter Siemons, Gertjan Koster, Hideki Yamamoto, Walter A. Harrison, Gerald Lucovsky, Theodore H. Geballe, Dave H. A. Blank, and Malcolm R. Beasley. "Origin of Charge Density at $LaAlO_3$ on $SrTiO_3$ Heterointerfaces: Possibility of Intrinsic Doping". *Physical Review Letters*, 98(19):196802, May 2007. doi: 10.1103/PhysRevLett.98.196802. URL http://link.aps.org/doi/10.1103/PhysRevLett.98.196802.

[198] G. Herranz, M. Basletić, M. Bibes, C. Carrétéro, E. Tafra, E. Jacquet, K. Bouzehouane, C. Deranlot, A. Hamzić, J.-M. Broto, A. Barthélémy, and A. Fert. "High Mobility in $LaAlO_3/SrTiO_3$ Heterostructures: Origin, Dimensionality, and Perspectives". *Physical Review Letters*, 98(21): 216803, 2007. doi: 10.1103/PhysRevLett.98.216803. URL http://link.aps.org/doi/10.1103/PhysRevLett.98.216803.

[199] J.-P. Maria, S. Trolier-McKinstry, D. G. Schlom, M. E. Hawley, and G. W. Brown. "The influence of energetic bombardment on the structure and properties of epitaxial $SrRuO_3$ thin films grown by pulsed laser deposition". *Journal of Applied Physics*, 83(8):4373–4379, April 1998. ISSN 00218979. doi: 10.1063/1.367195. URL http://jap.aip.org/resource/1/japiau/v83/i8/p4373_s1.

[200] T. Ohnishi, M. Lippmaa, T. Yamamoto, S. Meguro, and H. Koinuma. "Improved stoichiometry and misfit control in perovskite thin film formation at a critical fluence by pulsed laser deposition". *Applied Physics Letters*, 87(24):241919–241919–3, December 2005. ISSN 00036951. doi: 10.1063/1.2146069. URL http://apl.aip.org/resource/1/applab/v87/i24/p241919_s1.

[201] Tsuyoshi Ohnishi, Keisuke Shibuya, Takahisa Yamamoto, and Mikk Lippmaa. "Defects and transport in complex oxide thin films". *Journal of Applied Physics*, 103(10):103703, May 2008. ISSN 00218979. doi: 10.1063/1.2921972. URL http://jap.aip.org/resource/1/japiau/v103/i10/p103703_s1.

[202] P. R. Willmott, S. A. Pauli, R. Herger, C. M. Schlepütz, D. Martoccia, B. D. Patterson, B. Delley, R. Clarke, D. Kumah, C. Cionca, and Y. Yacoby. "Structural Basis for the Conducting Interface between $LaAlO_3$ and $SrTiO_3$". *Physical Review Letters*, 99(15):155502, 2007. doi: 10.1103/PhysRevLett.99.155502. URL http://link.aps.org/doi/10.1103/PhysRevLett.99.155502.

[203] S.A. Chambers, M.H. Engelhard, V. Shutthanandan, Z. Zhu, T.C. Droubay, L. Qiao, P.V. Sushko, T. Feng, H.D. Lee, T. Gustafsson, E. Garfunkel, A.B. Shah, J.-M. Zuo, and Q.M. Ramasse. "Instability, intermixing and electronic structure at the epitaxial heterojunction". *Surface Science Reports*, 65(10–12):317–352, 2010. ISSN 0167-5729. doi: 10.1016/j.surfrep.2010.09.001. URL http://www.sciencedirect.com/science/article/pii/S0167572910000671.

[204] S.A. Chambers, T.C. Droubay, C. Capan, and G.Y. Sun. "Unintentional F doping of $SrTiO_3$(001) etched in HF acid-structure and electronic properties". *Surface Science*, 606(3–4):554 – 558, 2012. ISSN 0039-6028. doi: 10.1016/j.susc.2011.11.029. URL http://www.sciencedirect.com/science/article/pii/S0039602811004626.

[205] M. Kareev, S. Prosandeev, J. Liu, C. Gan, A. Kareev, J. W. Freeland, Min Xiao, and J. Chakhalian. "Atomic control and characterization of surface defect states of TiO_2 terminated $SrTiO_3$ single crystals". *Applied Physics Letters*, 93(6):061909, 2008. doi: 10.1063/1.2971035. URL http://link.aip.org/link/?APL/93/061909/1.

[206] Yanwu Xie, Yasuyuki Hikita, Christopher Bell, and Harold Y. Hwang. "Control of electronic conduction at an oxide heterointerface using surface polar adsorbates". *Nature Communications*, 2:494, October 2011. ISSN 2041-1723. doi: 10.1038/ncomms1501. URL http://www.nature.com/ncomms/journal/v2/n10/full/ncomms1501.html.

[207] S. Thiel, C. W. Schneider, L. Fitting Kourkoutis, D. A. Muller, N. Reyren, A. D. Caviglia, S. Gariglio, J.-M. Triscone, and J. Mannhart. "Electron Scattering at Dislocations in $LaAlO_3/SrTiO_3$ Interfaces". *Phys. Rev. Lett.*, 102:046809, Jan 2009. doi: 10.1103/PhysRevLett.102.046809. URL http://link.aps.org/doi/10.1103/PhysRevLett.102.046809.

[208] V.V. Lemanov, A.V. Sotnikov, E.P. Smirnova, M. Weihnacht, and R. Kunze. "Perovskite $CaTiO_3$ as an incipient ferroelectric". *Solid State Communications*, 110(11):611 – 614, 1999. ISSN 0038-1098. doi: 10.1016/S0038-1098(99)00153-2. URL http://www.sciencedirect.com/science/article/pii/S0038109899001532.

[209] Eric Cockayne and Benjamin P. Burton. "Phonons and static dielectric constant in $CaTiO_3$ from first principles". *Phys. Rev. B*, 62:3735–3743, Aug 2000. doi: 10.1103/PhysRevB.62.3735. URL http://link.aps.org/doi/10.1103/PhysRevB.62.3735.

[210] H. F. Kay and P. C. Bailey. "Structure and properties of $CaTiO_3$". *Acta Crystallographica*, 10 (3):219–226, Mar 1957. doi: 10.1107/S0365110X57000675. URL http://dx.doi.org/10.1107/S0365110X57000675.

[211] K Ueda, H Yanagi, H Hosono, and H Kawazoe. "Study on electronic structure of $CaTiO_3$ by spectroscopic measurements and energy band calculations". *Journal of Physics: Condensed Matter*, 11(17):3535–3545, May 1999. ISSN 0953-8984, 1361-648X. doi: 10.1088/0953-8984/11/17/311. URL http://iopscience.iop.org/0953-8984/11/17/311.

[212] Yijian Jiang, Ruyan Guo, and A. s Bhalla. "Growth and Properties of $CaTiO_3$ Single Crystal Fibers". *Journal of Electroceramics*, 2(3):199–203, November 1998. ISSN 1385-3449, 1573-8663. doi: 10.1023/A:1009978901009. URL http://link.springer.com/article/10.1023/A:1009978901009.

[213] B.E. Watts, H. Dabkowska, and B.M. Wanklyn. "The flux growth of perovskites ($CaTiO_3$, $CdTiO_3$, $SrZrO_3$, and $LaGaO_3$, $PrGaO_3$, $NdGaO_3$)". *Journal of Crystal Growth*, 94(1):125–130, January 1989. ISSN 0022-0248. doi: 10.1016/0022-0248(89)90611-8. URL http://www.sciencedirect.com/science/article/pii/0022024889906118.

[214] Liliana Goncalves-Ferreira, Simon A. T. Redfern, Emilio Artacho, and Ekhard K. H. Salje. "Ferrielectric Twin Walls in $CaTiO_3$". *Phys. Rev. Lett.*, 101:097602, Aug 2008. doi: 10.1103/PhysRevLett.101.097602. URL http://link.aps.org/doi/10.1103/PhysRevLett.101.097602.

[215] Sandra Van Aert, Stuart Turner, Rémi Delville, Dominique Schryvers, Gustaaf Van Tendeloo, and Ekhard K. H. Salje. "Direct Observation of Ferrielectricity at Ferroelastic Domain Boundaries in $CaTiO_3$ by Electron Microscopy". *Advanced Materials*, 24(4):523–527, January 2012. ISSN 09359648. doi: 10.1002/adma.201103717. URL http://doi.wiley.com/10.1002/adma.201103717.

[216] Liliana Goncalves-Ferreira, Simon A. T. Redfern, Emilio Artacho, Ekhard Salje, and William T. Lee. "Trapping of oxygen vacancies in the twin walls of perovskite". *Phys. Rev. B*, 81:024109, Jan 2010. doi: 10.1103/PhysRevB.81.024109. URL http://link.aps.org/doi/10.1103/PhysRevB.81.024109.

[217] G. Catalan, J. Seidel, R. Ramesh, and J. Scott. "Domain wall nanoelectronics". *Reviews of Modern Physics*, 84(1):119–156, February 2012. ISSN 0034-6861, 1539-0756. doi: 10.1103/RevModPhys.84.119. URL http://link.aps.org/doi/10.1103/RevModPhys.84.119.

[218] Stuart S. P. Parkin, Masamitsu Hayashi, and Luc Thomas. "Magnetic Domain-Wall Racetrack Memory". *Science*, 320(5873):190–194, 2008. doi: 10.1126/science.1145799. URL http://www.sciencemag.org/content/320/5873/190.abstract.

[219] O. N. Tufte and P. W. Chapman. "Electron Mobility in Semiconducting Strontium Titanate". *Phys. Rev.*, 155:796–802, Mar 1967. doi: 10.1103/PhysRev.155.796. URL http://link.aps.org/doi/10.1103/PhysRev.155.796.

[220] G. Binnig, A. Baratoff, H. E. Hoenig, and J. G. Bednorz. "Two-Band Superconductivity in Nb-Doped $SrTiO_3$". *Phys. Rev. Lett.*, 45:1352–1355, Oct 1980. doi: 10.1103/PhysRevLett.45.1352. URL http://link.aps.org/doi/10.1103/PhysRevLett.45.1352.

[221] A. D. Caviglia, S. Gariglio, N. Reyren, D. Jaccard, T. Schneider, M. Gabay, S. Thiel, G. Hammerl, J. Mannhart, and J.-M. Triscone. "Electric field control of the $LaAlO_3/SrTiO_3$ interface ground state". *Nature*, 456(7222):624–627, 2008. doi: 10.1038/nature07576. URL http://dx.doi.org/10.1038/nature07576.

[222] Wikipedia. "Calcium hydroxide — Wikipedia, The Free Encyclopedia", 2012. URL http://en.wikipedia.org/w/index.php?title=Calcium_hydroxide&oldid=483952094. [Online; accessed 28-March-2012].

[223] Wikipedia. "Strontium hydroxide — Wikipedia, The Free Encyclopedia", 2012. URL http://en.wikipedia.org/w/index.php?title=Strontium_hydroxide&oldid=483534809. [Online; accessed 28-March-2012].

[224] Antonello Tebano, Emiliana Fabbri, Daniele Pergolesi, Giuseppe Balestrino, and Enrico Traversa. "Room-Temperature Giant Persistent Photoconductivity in $SrTiO_3/LaAlO_3$ Heterostructures". *ACS Nano*, 6(2):1278–1283, February 2012. ISSN 1936-0851. doi: 10.1021/nn203991q. URL http://dx.doi.org/10.1021/nn203991q.

[225] D. C. Johnston. "Stretched exponential relaxation arising from a continuous sum of exponential decays". *Phys. Rev. B*, 74:184430, Nov 2006. doi: 10.1103/PhysRevB.74.184430. URL http://link.aps.org/doi/10.1103/PhysRevB.74.184430.

[226] W.J. de Haas, J. de Boer, and G.J. van dën Berg. "The electrical resistance of gold, copper and lead at low temperatures". *Physica*, 1(7-12):1115–1124, May 1934. ISSN 00318914. doi: 10.1016/S0031-8914(34)80310-2. URL http://www.sciencedirect.com/science/article/pii/S0031891434803102.

[227] Arjan Jeroen Houtepen. *A revised variable-range hopping model explains the peculiar T-dependence of electronic conductivity in ZnO quantum-dot solids.* PhD thesis, Utrecht University, Utrecht, 2007. URL http://igitur-archive.library.uu.nl/dissertations/2007-0626-203806/cp7.pdf.

[228] Nevill Francis Mott and Edward Arthur Davis. *Electronic processes in non-crystalline materials.* International series of monographs on physics. Clarendon Press ; Oxford University Press, New York, 1979. ISBN 0198512880.

[229] Andreas Schmehl. *Transporteigenschaften dünner $LaTiO_{3+\delta}$-Schichten und Heterostrukturen.* PhD thesis, Universität Augsburg, 86159 Augsburg, 2003.

[230] Reina Ohtsuka. *Transport properties of embedded $LaTiO_3$ Layers.* PhD thesis, University of Tokyo, 2010. URL http://id.nii.ac.jp/0021/00021892.

[231] Heiko Gross, Namrata Bansal, Yong-Seung Kim, and Seongshik Oh. "In situ study of emerging metallicity on ion-bombarded $SrTiO_3$ surface". *Journal of Applied Physics*, 110(7):073704, 2011. doi: 10.1063/1.3650254. URL http://link.aip.org/link/?JAP/110/073704/1.

[232] M.L. Reinle-Schmitt, C. Cancellieri, D. Li, D. Fontaine, M. Medarde, E. Pomjakushina, C.W. Schneider, S. Gariglio, Ph. Ghosez, J.-M. Triscone, and P.R. Willmott. "Tunable conductivity threshold at polar oxide interfaces". *Nature Communications*, 3:932, July 2012. ISSN 2041-1723. doi: 10.1038/ncomms1936. URL http://www.nature.com/doifinder/10.1038/ncomms1936.

[233] Wolter Siemons, Gertjan Koster, Hideki Yamamoto, Theodore Geballe, Dave Blank, and Malcolm Beasley. "Experimental investigation of electronic properties of buried heterointerfaces of $LaAlO_3$ on $SrTiO_3$". *Physical Review B*, 76(15), October 2007. ISSN 1098-0121, 1550-235X. doi: 10.1103/PhysRevB.76.155111. URL http://link.aps.org/doi/10.1103/PhysRevB.76.155111.

[234] Frank Schoofs, Mehmet Egilmez, Thomas Fix, Judith L. MacManus-Driscoll, and Mark G. Blamire. "Impact of structural transitions on electron transport at $LaAlO_3/SrTiO_3$ heterointerfaces". *Applied Physics Letters*, 100(8):081601, February 2012. ISSN 00036951. doi: 10.1063/1.3687706. URL http://apl.aip.org/resource/1/applab/v100/i8/p081601_s1.

[235] K. A. Müller, W. Berlinger, and F. Waldner. "Characteristic Structural Phase Transition in Perovskite-Type Compounds". *Physical Review Letters*, 21(12):814–817, September 1968. doi: 10.1103/PhysRevLett.21.814. URL http://link.aps.org/doi/10.1103/PhysRevLett.21.814.

[236] J. F. Scott and H. Ledbetter. "Interpretation of elastic anomalies in $SrTiO_3$ at 37 K". *Zeitschrift für Physik B Condensed Matter*, 104(4):635–639, 1997. URL http://www.springerlink.com/index/U8WUVCL8F5ENCG1F.pdf.

List of Figures

List of Tables

Acknowledgement/Danksagung

Meinem Doktorvater Jochen Mannhart danke ich für die tolle Zeit und die vielen Erfolge, die wir zusammen feiern durften. Ihr Riecher für interessante Physik und lohnende Zusammenarbeiten hat uns weit gebracht. Danke auch für die Möglichkeit, meine Doktorarbeit als Exilstuttgarter in Augsburg beenden zu können – das war sicher nicht selbstverständlich und hat mir und meiner Familie viel bedeutet. Abgesehen davon waren die neuen Möglichkeiten am Max Planck Institut natürlich auch eine große Bereicherung für meine Doktorarbeit.

Vielen Dank auch an meinen Zweitgutachter Herrn Achim Wixforth für die bereitwillige Einwilligung, meine Arbeit zu bewerten.

Lu Li, you have contributed to this thesis in major parts. I have always enjoyed to collaborate with you and Ray. Thank you so much!

I am much obliged to Lena Fitting Kourkoutis and Dave Muller for the wonderful STEM/EELS images and analyses. Danke, Lena!

Thank you, John Kirtley, for teaching me the basics of inelastic tunneling. You have equipped me with all the basic equations, the fundamental interpretation of my inelastic tunneling spectra, and the confidence that even complicated formulae are there to be used – by a computer, that is.

I am thankful to Darrell Schlom, who has provided me with the $CaTiO_3$ substrates as well as the opportunity for many interesting collaborations, notably with Maitri Warusawithana, whom I would also like to thank.

I am also debtful to Stefano Gariglio for low-temperature $R(T)$ measurements and Jean-Marc Triscone and his Geneva group in general for great collaborations.

Die Zusammenarbeit mit Ralf Claessen und seiner Würzburger Gruppe, insbesondere mit Götz Berner und Michael Sing war ebenfalls ein wichtiger und schöner Teil dieser Arbeit, für den ich sehr dankbar bin.

Herrn Werner Dietsche danke ich für die praktische Einweisung und die viele Hilfe am Mischkryostaten. Sie haben mich quasi als Vorhut der Abteilung Mannhart freundlichst am Max Planck Institut willkommen geheißen. Danke dafür und auch für den Beistand während der langen spannenden Tage und Nächte im 3C2 auf der Suche nach dem Gap.

Hans Boschker, der diese Rolle dann in späteren Messrunden übernommen hat, danke ich für die vielen interessanten Gespräche und die verrückten Messsitzungen, die wir hatten. Ich habe von Dir und mit Dir viel gelernt, Hans. Dank je wel!

Ich möchte mich auch bei Christof Schneider bedanken, zum einen für die $SrTi^{18}O_3$ Substrate, vor allem aber für sein stetes Interesse an mir und meiner Arbeit und viele hilfreiche Tipps und Infos.

Dem Lehrstuhl Experimentalphysik VI der Uni-Augsburg, insbesondere Thilo Kopp und German Hammerl, danke ich für die vielen schönen Jahre, die ich hier an der Uni hatte, besonders aber auch für die „Gastfreundschaft“ in meinem letzten Jahr als Stuttgarter im Augsburger Exil. Zum Lehrstuhl gehören natürlich noch viele andere besondere Menschen. Klaus und Lore, ohne Euch wär's hier nicht halb so schön – Ihr haltet diesen Lehrstuhl zusammen. Danke dafür! Alex, ohne Dich würde hier auch nichts laufen, v.a. technisch gesehen. Vielen Dank für die unzähligen Reparaturen und die technischen Tips beim Basteln von Probenstäben, Messverstärkern und Doktorhüten! Allen Masteranden, Doktorbrüdern und -schwestern, insbesondere Rainer Jany, gilt ein besonders großes Dankeschön für helfende Hände und Köpfe, Lektorat und v.a. für die tolle Atmosphäre und den vielen Spaß hier am Lehrstuhl.

Bei meinen Eltern und Brüdern möchte ich mich dafür entschuldigen, dass ich mich in der letzten (langen) Zeit so sehr ausgeklinkt habe. Danke, dass Ihr trotzdem so sehr zu mir haltet! Gleiches gilt natürlich für viele Freunde und meine Schwiegerfamilie.

Und dann gibt es da noch zwei Menschen, deren unschätzbar großer Anteil an dieser Arbeit vor allem darin bestand, mich von der Arbeit abzuhalten. Nanny, Josephin, ohne Euch wäre ich verrückt geworden und verzweifelt. Danke, Nanny, für Deine unendliche Geduld, Deinen Beistand und Deine Liebe. Du hast mir während der ganzen Zeit den Rücken freigehalten und mich trotzdem nie vergessen lassen, dass es Wichtigeres im Leben gibt als Physik und Doktortitel.